Cost-effective monitoring of structural risk of bridges supported by cutting-edge technologies

Published version
DOI:10.60576/poliba/iris/calo-mirko_phd2025

Publisher: Politecnico di Bari

Politecnico di Bari

LIBERATORIA PER L'ARCHIVIAZIONE DELLA TESI DI DOTTORATO

Al Magnifico Rettore
del Politecnico di Bari

Il sottoscritto **Mirko Calò** nato a **Taranto** il **15/09/1995** residente a **Bari** in **Traversa al n, 126 di Via Giovanni Amendola, 14**, e-mail: **mirko.calos3@gmail.com**.

iscritto al 3° anno di Corso di Dottorato di Ricerca in **Rischio e Sviluppo Ambientale, Territoriale ed Edilizio**, ciclo **XXXVII**.

ed essendo stato ammesso a sostenere l'esame finale con la prevista discussione della tesi dal titolo:

"Cost-effective monitoring of structural risk of bridges supported by cutting-edge technologies"

DICHIARA

1) di essere consapevole che, ai sensi del D.P.R. n. 445 del 28.12.2000, le dichiarazioni mendaci, la falsità negli atti e l'uso di atti falsi sono puniti ai sensi del codice penale e delle Leggi speciali in materia, e che nel caso ricorressero dette ipotesi, decade fin dall'inizio e senza necessità di nessuna formalità dai benefici conseguenti al provvedimento emanato sulla base di tali dichiarazioni;
2) di essere iscritto al Corso di Dottorato di ricerca in **Rischio e Sviluppo Ambientale, Territoriale ed Edilizio**, ciclo **XXXVII**, corso attivato ai sensi del "*Regolamento dei Corsi di Dottorato di ricerca del Politecnico di Bari*", emanato con D.R. n.286 del 01.07.2013;
3) di essere pienamente a conoscenza delle disposizioni contenute nel predetto Regolamento in merito alla procedura di deposito, pubblicazione e autoarchiviazione della tesi di dottorato nell'Archivio Istituzionale ad accesso aperto alla letteratura scientifica;
4) di essere consapevole che attraverso l'autoarchiviazione delle tesi nell'Archivio Istituzionale ad accesso aperto alla letteratura scientifica del Politecnico di Bari (IRIS-POLIBA), l'Ateneo archivierà e renderà consultabile in rete (nel rispetto della Policy di Ateneo di cui al D.R. 642 del 13.11.2015) il testo completo della tesi di dottorato, fatta salva la possibilità di sottoscrizione di apposite licenze per le relative condizioni di utilizzo (di cui al sito http://www.creativecommons.it/Licenze), e fatte salve, altresì, le eventuali esigenze di "embargo", legate a strette considerazioni sulla tutelabilità e sfruttamento industriale/commerciale dei contenuti della tesi, da rappresentarsi mediante compilazione e sottoscrizione del modulo in calce (Richiesta di embargo);
5) che la tesi da depositare in IRIS-POLIBA, in formato digitale (PDF/A) sarà del tutto identica a quelle **consegnate**/inviate/da inviarsi ai componenti della commissione per l'esame finale e a qualsiasi altra copia depositata presso gli Uffici del Politecnico di Bari in forma cartacea o digitale, ovvero a quella da discutere in sede di esame finale, a quella da depositare, a cura

dell'Ateneo, presso le Biblioteche Nazionali Centrali di Roma e Firenze e presso tutti gli Uffici competenti per legge al momento del deposito stesso, e che di conseguenza va esclusa qualsiasi responsabilità del Politecnico di Bari per quanto riguarda eventuali errori, imprecisioni o omissioni nei contenuti della tesi;

6) che il contenuto e l'organizzazione della tesi è opera originale realizzata dal sottoscritto e non compromette in alcun modo i diritti di terzi, ivi compresi quelli relativi alla sicurezza dei dati personali; che pertanto il Politecnico di Bari ed i suoi funzionari sono in ogni caso esenti da responsabilità di qualsivoglia natura: civile, amministrativa e penale e saranno dal sottoscritto tenuti indenni da qualsiasi richiesta o rivendicazione da parte di terzi;
7) che il contenuto della tesi non infrange in alcun modo il diritto d'Autore né gli obblighi connessi alla salvaguardia di diritti morali od economici di altri autori o di altri aventi diritto, sia per testi, immagini, foto, tabelle, o altre parti di cui la tesi è composta.

Luogo e data: Bari, 10/03/2025 Firma ____________________

Il sottoscritto, con l'autoarchiviazione della propria tesi di dottorato nell'Archivio Istituzionale ad accesso aperto del Politecnico di Bari (POLIBA-IRIS), pur mantenendo su di essa tutti i diritti d'autore, morali ed economici, ai sensi della normativa vigente (Legge 633/1941 e ss.mm.ii.),

CONCEDE

- al Politecnico di Bari il permesso di trasferire l'opera su qualsiasi supporto e di convertirla in qualsiasi formato al fine di una corretta conservazione nel tempo. Il Politecnico di Bari garantisce che non verrà effettuata alcuna modifica al contenuto e alla struttura dell'opera.
- al Politecnico di Bari la possibilità di riprodurre l'opera in più di una copia per fini di sicurezza, back-up e conservazione.

Luogo e data: Bari, 10/03/2025 Firma ____________________

POLITECNICO DI BARI

D.R.S.A.T.E.

Doctor in Risk And Environmental, Territorial And Building Development

11

2025

Coordinator: Prof. Vito Iacobellis

XXXVII CYCLE
CEAR-07/A – Structural Engineering

DICATECh
Department of Civil, Environmental, Building Engineering and Chemistry

Mirko Calò

Cost-effective monitoring of structural risk of bridges supported by cutting-edge technologies

Prof. Giuseppina UVA
Dr. Sergio RUGGIERI
Dr. Andrea NETTIS
DICATECh, Politecnico di Bari

Prof. Josè M. ADAM
ICITECH, Universitat Politècnica de València

D.R.S.A.T.E.

POLITECNICO DI BARI

11

Dottorato di Ricerca in Rischio e Sviluppo Ambientale, Territoriale ed Edilizio

2025

Coordinatore: Prof. Vito Iacobellis

XXXVII CICLO
CEAR-07/A – Tecnica delle costruzioni

DICATECh
Dipartimento di Ingegneria Civile, Ambientale, del Territorio, Edile e di Chimica

Mirko Calò

Monitoraggio cost-effective del rischio strutturale dei ponti per mezzo di tecnologie avanzate

Prof. Giuseppina UVA
Dr. Sergio RUGGIERI
Dr. Andrea NETTIS
DICATECh, Politecnico di Bari

Prof. Josè M. ADAM
ICITECH, Universitat Politècnica de València

EXTENDED ABSTRACT (eng)

The socio-economic development of humankind has always required connecting routes, and technological development has led to the construction of increasingly complex and extensive transportation networks. One of the most critical components of roadway and railway networks is represented by bridges and viaducts and recent chronicles have shown the potential economic losses and the possible casualties occurring after their collapse. Taking Italy as a reference, a virtuous example on the principle of prevention is the new guidelines (IG) issued in 2020 for the structural safety of existing bridges. The IG propose a comprehensive multi-level strategy to be applied on the national bridge stock, to identify structures exhibiting the most critical conditions and, for such cases, implement appropriate monitoring and maintenance strategies (e.g., service limitations, demolition/reconstruction).

Although effective for both bridge risk classification and assessment a national scale, and the rational administration of resources, IG propose traditional monitoring procedures (necessary and hardly replaceable), involving time- and cost-consuming activities. These characteristics make them difficult to apply on a large scale in a short period of time given the existence of tens of thousands of facilities. Indeed, during their service life, bridges and viaducts are subjected to actions (e.g., combination of traffic and dead loads), natural hazards, environmental conditions and phenomena inducing displacements, material degradation and structural decay (e.g., steel rebar corrosion, spalling in concrete elements, bearing malfunctioning) that affect their safety and functionality. The IG emphasise the need for a continuous monitoring of these structures opening up the possibility of using cutting-edge technologies. Focusing on the most spread bridge typology in Italy, that is single/multi-span simply supported concrete girder bridge both

reinforced (RC) and prestressed (PSC) concrete, and on the objective to employ cost-effective technologies for large scale near-continuous structural risk assessment of these structures, Interferometry via satellite-based Synthetic Aperture Radar (InSAR), Unmanned Aerial Vehicle (UAV) photogrammetry and Machine Learning (ML) are investigated among the emerging technologies in the field of civil engineering.

The first Chapter discusses InSAR algorithms that exploits large-scale complex images acquired remotely at discrete time intervals (near continuous). Such images are characterized by few meters resolution, and their processing allows reconstructing displacement time series of scatterers associated with parts of man-made structures with millimetre accuracy. Considering the integration of InSAR data with poor structural information and other easily accessible data, and simple static schemes describing the bridge behaviour under service conditions, a structural risk early-warning framework is proposed. Displacement time series characterizing bridge vertical and longitudinal axis are compared with appropriate thresholds activating potential early warnings aimed at supporting road managers in undertaking future surveillance actions based on the recognized displacement scenario. As a main advantage, the proposed framework presents a standardized and scalable series of steps, enclosed in a Python module, to apply for the purpose of large-scale monitoring. Its effectiveness as early-warning system is demonstrated through the application on two case-studies affected by different pathologies (e.g., increasing material degradation/gravity loads, differential displacements and subsidence). Regardless the simplifications introduced in the framework and its applicability on a single bridge typology this is one of the fewest examples in the scientific literature on the use of InSAR data for structural interpretation of remote-sensed displacements. In addition, to facilitate the application of the framework by practitioners and spread the use of monitoring using SAR data, BAS-MTInSAR, a user-friendly GIS plugin with a graphical user interface, is developed.

In the second Chapter, UAV photogrammetry is proposed as a dual cost-effective technology to InSAR for bridge assessment. Indeed, while InSAR data is used to monitor structural displacements at millimetre scale, UAV photogrammetry through Digital Surface Models (DSMs) is exploited to compensate for the absence of scatterers in the surroundings of the structure. DSMs can be used to evaluate vertical displacements in the surroundings of a focused structure for geo-hazard monitoring purpose (e.g., subsidence). Considering the centimetre accuracy obtained through DSM, and thus the difference in accuracy between the two monitoring techniques, a probabilistic framework based on statistical distributions of the spatiotemporal velocities of both is proposed. Statistical distributions, evaluated towards predefined limit states to compute their probability of exceedance, are classified under different scenarios to reveal the occurrence of possible subsidence phenomena in the structure surrounding and their possible interaction with it. The proposed methodology is firstly validated on the Pomarico landslide and later tested on one of the simply supported bridges evaluated in the previous Chapter for risk prediction. From its application, a satisfying capacity of providing warnings to employ in risk mitigation plans is found, although a qualitative and not quantitative information on the geological risk affecting the focused structure is given.

In the last Chapter the focus is no longer on the use of remote sensing techniques for structural risk assessment of bridge portfolios, but on the use of a sensor-based system for the same objective. In particular, the prestressing force reduction is discussed among one of the most important degradation phenomena affecting prestressed concrete bridges. Literature SHM sensor-based systems struggle in pointing out the reduction of prestressing force, especially in case of unbounded tendons inside box-girder bridges. Among these systems, strain-gauges and ML regression algorithms could be combined to achieve this goal. Also in this case, a framework is proposed accounting for the combination of a ML surrogate model with sensor-based measurements. Artificial Neural Network, Random Forrest Regressor and Support Vector Regression algorithms are trained on sample data generated from a nonlinear modelling approach considering mechanical and geometrical characteristics of the bridge deck. The proposed modelling strategy represent a trade-off between computational effort and accuracy, which represent an important requirement when dealing with the generation and analysis of thousands of models. This result was achieved by numerically validating vertical displacements recorded from an experimentally tested scaled PSC box bridge. The

results of the best ML surrogate model, selected considering statistical metrics, are discussed through an eXplainability approach to identify new insights which could be used in the design of an optimized sensor-based SHM. The framework is applied on a scaled PSC box bridge experimentally tested in the ICITECH laboratories of the Universitat Politècnica de València.

Keywords

Existing Bridges, Bridge Assessment, Structural Risk, Reinforced Concrete Bridges, Prestressed Reinforced Concrete Bridges, Cutting-edge Technologies, Multi-Temporal Interferometry Synthetic Aperture Radar, Unmanned Aerial Vehicle, Photogrammetry, Machine Learning.

EXTENDED ABSTRACT *(ita)*

Lo sviluppo socio-economico dell'umanità ha sempre richiesto vie di collegamento e lo sviluppo tecnologico ha portato alla costruzione di reti di trasporto sempre più complesse ed estese. Una delle componenti più critiche delle reti stradali e ferroviarie è rappresentata da ponti e viadotti e le cronache recenti hanno mostrato le potenziali perdite economiche e le possibili vittime che si verificano in seguito al loro crollo. Prendendo come riferimento l'Italia, un esempio virtuoso sul principio della prevenzione è rappresentato dalle nuove linee guida (LL.GG.) emanate nel 2020 per la sicurezza strutturale dei ponti esistenti. Le LL.GG. propongono una strategia globale multi-livello da applicare al parco ponti nazionale, per identificare le strutture che presentano le condizioni più critiche e, per questi casi, implementare adeguate strategie di monitoraggio e manutenzione (es., limitazioni di servizio, demolizione/ricostruzione).
Sebbene siano efficaci sia per la classificazione e la valutazione del rischio dei ponti su scala nazionale, sia per l'amministrazione razionale delle risorse, le LL.GG. propongono procedure di monitoraggio tradizionali (necessarie e difficilmente sostituibili), che comportano attività dispendiose in termini di tempo e di costi. Tali caratteristiche le rendono difficilmente applicabili su larga scala in tempi brevi data l'esistenza di decine di migliaia di strutture. Infatti, durante la loro vita utile, i ponti e i viadotti sono soggetti ad azioni (ad esempio, combinazione di carichi di traffico e carichi morti), pericoli naturali, condizioni ambientali e fenomeni che inducono spostamenti, degrado dei materiali e decadimento strutturale (es., corrosione delle armature, espulsione del copriferro, malfunzionamento degli apparecchi di appoggio) che ne influenzano la sicurezza e la funzionalità. Le LL.GG. sottolineano la necessità di un monitoraggio continuo di queste strutture, aprendo la possibilità di utilizzare tecnologie all'avanguardia. Focalizzando

l'attenzione sulla tipologia di ponte più diffusa in Italia, ovvero i ponti a travata semplicemente appoggiati in calcestruzzo armato (RC) o precompresso (PSC), e sull'obiettivo di impiegare tecnologie economicamente vantaggiose per una valutazione del rischio strutturale quasi-continuo su larga scala di queste strutture, tra le tecnologie emergenti nel campo dell'ingegneria civile sono state prese in esame l'Interferometria satellitare Radar ad Apertura Sintetica (InSAR), la fotogrammetria con veicoli aerei senza pilota (UAV) e l'apprendimento automatico (ML).

Nel primo capitolo vengono discussi gli algoritmi InSAR che sfruttano immagini complesse di grande estensione acquisite da remoto ad intervalli discreti di tempo (quasi-continuo). Tali immagini sono caratterizzate da una risoluzione di pochi metri e la loro elaborazione permette di ricostruire le serie temporali di spostamento degli scatterer associati a parte delle strutture antropiche con una precisione millimetrica. Considerando l'integrazione dei dati InSAR con informazioni strutturali e altri dati facilmente accessibili, e semplici schemi statici che descrivono il comportamento del ponte in condizioni di esercizio, viene proposto un quadro di allerta precoce del rischio strutturale. Le serie temporali di spostamento che caratterizzano l'asse verticale e longitudinale del ponte sono confrontate con soglie appropriate che attivano potenziali allerte precoci volti a supportare i gestori delle strade nell'intraprendere azioni di sorveglianza sul funzionamento del ponte in base allo scenario di spostamento riconosciuto. Come vantaggio principale, il quadro proposto presenta una serie di passaggi standardizzati e scalabili, racchiusi in un modulo Python, da applicare ai fini del monitoraggio su larga scala. La sua efficacia come sistema di allerta precoce è dimostrata attraverso l'applicazione a due casi studio affetti da diverse patologie (es., crescente degrado dei materiali/carichi gravitazionali, spostamenti differenziali e cedimenti). A prescindere dalle semplificazioni introdotte nel quadro e dalla sua applicabilità a una singola tipologia di ponte, questo è uno dei pochi esempi nella letteratura scientifica sull'uso dei dati InSAR per l'interpretazione strutturale degli spostamenti rilevati a distanza. Inoltre, per facilitare l'applicazione del framework da parte dei professionisti e diffondere l'uso del monitoraggio tramite dati SAR, è stato sviluppato BAS-MTInSAR, un plugin GIS di facile utilizzo con interfaccia grafica.

Nel secondo capitolo, la fotogrammetria UAV viene proposta come tecnologia duale ed economicamente vantaggiosa rispetto ai dati InSAR per la valutazione dei ponti. Infatti, mentre i dati InSAR vengono utilizzati per monitorare gli spostamenti strutturali su scala millimetrica, per compensare l'assenza di scatterer nell'ambiente circostante la struttura viene sfruttata la fotogrammetria UAV attraverso i Modelli Digitali di Superficie (DSM). Questi ultimi possono essere utilizzati per valutare gli spostamenti verticali nell'intorno di una struttura focalizzata per il monitoraggio dei rischi geologici (es., la subsidenza). Considerando l'accuratezza centimetrica ottenuta con i DSM, e quindi la differenza di precisione tra le due tecniche di monitoraggio, viene proposto un quadro probabilistico basato sulle distribuzioni statistiche delle velocità spazio-temporali di entrambe. Le distribuzioni statistiche, valutate verso stati limite predefiniti per calcolarne la probabilità di superamento, sono classificate in diversi scenari per rivelare l’occorrenza di possibili fenomeni di subsidenza nell'intorno della struttura e la loro possibile interazione con essa. La metodologia proposta è stata dapprima validata sulla frana di Pomarico e successivamente testata su uno dei ponti semplicemente appoggiati, valutato nel capitolo precedente, per la previsione del rischio. Dalla sua applicazione è emersa una soddisfacente capacità di fornire avvertimenti da impiegare nei piani di mitigazione del rischio, sebbene venga fornita un’informazione qualitativa e non quantitativa sul rischio geologico che interessa la struttura.

Nell'ultimo capitolo l'attenzione non è più rivolta all'uso di tecniche di telerilevamento per la valutazione del rischio strutturale dei portafogli di ponti, ma all'uso di un sistema basato su sensori per lo stesso obiettivo. In particolare, la riduzione della forza di precompressione è discussa tra i più importanti fenomeni di degrado che interessano i ponti in calcestruzzo armato precompresso. I sistemi basati su sensori SHM presenti in letteratura faticano ad evidenziare la riduzione della forza di precompressione, soprattutto nel caso di cavi di precompressione non aderenti all’interno di ponti a travi scatolari. Tra questi, i sensori di deformazione e gli algoritmi di regressione ML potrebbero essere combinati per raggiungere questo obiettivo. Anche in questo caso, viene proposto un framework che prevede la combinazione di un modello surrogato di ML con misure basate su sensori. Gli algoritmi di reti neurali artificiali, di regressione a

foresta casuale e di regressione vettoriale di supporto sono stati addestrati su dati campione generati da un approccio di modellazione non lineare che considera le caratteristiche meccaniche e geometriche dell'impalcato del ponte. La strategia di modellazione proposta rappresenta un compromesso tra sforzo computazionale e accuratezza, che rappresentano un requisito importante quando si tratta di generare e analizzare migliaia di modelli. Questo risultato è stato ottenuto convalidando numericamente gli spostamenti verticali registrati da un ponte scatolare PSC testato sperimentalmente. I risultati del miglior modello surrogato di ML, selezionato in base a metriche statistiche, sono discussi attraverso un approccio di eXplainability per identificare nuove intuizioni che potrebbero essere utilizzate nella progettazione di un sistema SHM ottimizzato basato su sensori. L'approccio è applicato a una trave PSC scatolare in scala, testata sperimentalmente nei laboratori ICITECH dell'Università Politecnica di Valencia.

Keywords

Ponti esistenti, Valutazione dei ponti, Rischio strutturale, Ponti in calcestruzzo armato, Ponti in calcestruzzo armato precompresso, Tecnologie all'avanguardia, Interferometria Multi-Temporale Radar ad Apertura Sintetica, Veicolo aereo senza pilota, Fotogrammetria, Apprendimento automatico.

INDEX

INTRODUCTION

Since the earliest civilizations, humans have adapted the environment to their needs and desires. With early inventions and applications, they began to reshape the environment with farms, villages, roads, and eventually large cities. However, socioeconomic progress brought new challenges that required more complex solutions, such as connecting two cities located on opposite sides of a river. To meet this need, bridges were built to cross obstacles such as depressions in the ground, rivers, or other roads. One of the oldest examples in Italy is the S. Angelo Bridge, located in Scigliano, Cosenza, built in the 2nd century B.C. to cross the Savuto River (Fondo Ambiente Italiano, 2022). Over time, the discovery of new materials and construction techniques led to the creation of more complex and functional structures, resulting in transportation networks (both road and rail) that stretch for thousands of kilometres.

In Italy, transportation networks are under the authority of Concessionaries (e.g., Azienda Nazionale Autonoma delle Strade, ANAS S.p.A.) whose goal is to keep them functional through a timely maintenance. Particular attention must be paid to bridges, which are a core structures of these systems, whose collapses result in economic losses and casualties as shown by the recent chronicles of the Polcevera viaduct (Calvi *et al*., 2018; Lanari *et al*., 2020; Milillo *et al*., 2019; Fig. 1), or the Albiano-Magra viaduct (Farneti *et al*., 2022; Fig. 2). Therefore, the technical and political debate about infrastructural safety cannot focus only on the causes that generate collapses and losses but must converge on the main principle of prevention. To practice prevention for existing bridges, it should be considered that during their service life, these structures are subjected to actions and phenomena inducing displacements, material degradation and structural decay. Among the main actions to consider, natural hazardous events can be mentioned, such as landslides, subsidence motions, earthquakes, and floods (e.g.,

Fig. 1 - Collapse of the Polcevera bridge in Genova (Italy), 14th August 2018, (Sbarbaro, 2018).

Fig. 2 - Collapse of a bridge in Albiano Magra (Massa-Carrara, Italy), 8th April 2020, (Delle Luche, 2022).

Borzi *et al*., 2015; Fiorillo and Ghosn, 2017; Nettis *et al*., 2022; Sangiorgio *et al*., 2022). On the other hand, within the service life of bridges, other exogenous actions may affect safety and serviceability of bridges, such as the combination of traffic and dead loads, which increase gravitational actions on bridges. Moreover, the environmental conditions (e.g., temperature, solar radiation, wind, rain) represent a silent enemy of structures leading to a slow but steady evolution of degradation phenomena, peculiar to the construction typology and material of the bridge (e.g., steel rebar corrosion and spalling in reinforced concrete, RC, and prestressed concrete, PSC, elements, rusted surfaces on steel elements, bearings malfunctioning).

Motivations

Although governments and transportation management authorities are aware of the necessity of the need for infrastructure maintenance, this is still a difficult task considering large portfolios of these assets and limited economical and human resources. To give a dimension to the abovementioned issue, ANAS S.p.A. manages around 32.000 km of roads and motorways in which 18.720 bridges are placed (ANAS, 2024a). In this context, is becoming increasingly important to define a standardized methodology at a national scale for bridge risk classification. The aim is the rational administration of resources for safety assessment, risk mitigation strategies and recovery actions homogeneously and uniformly across different types of infrastructures. Some examples can be found in the technical and scientific literature for the operation and management of bridges as reported in AASHTO, 2018. Taking as reference the Italian case, the Italian Ministry of Infrastructures and Transportation (MIT) issued in 2020 the “Guidelines for risk classification, safety assessment and structural health monitoring of existing bridges” (ANSFISA, 2022; MIT, 2020). The Italian guidelines (IG) proposed a multilevel approach, Fig. 3 from Level 0 to Level 4, for the risk classification of bridges based on census (Level 0), field survey and visual inspections (Level 1), preliminary risk assessment (Level 2, to achieve a total warning class based on

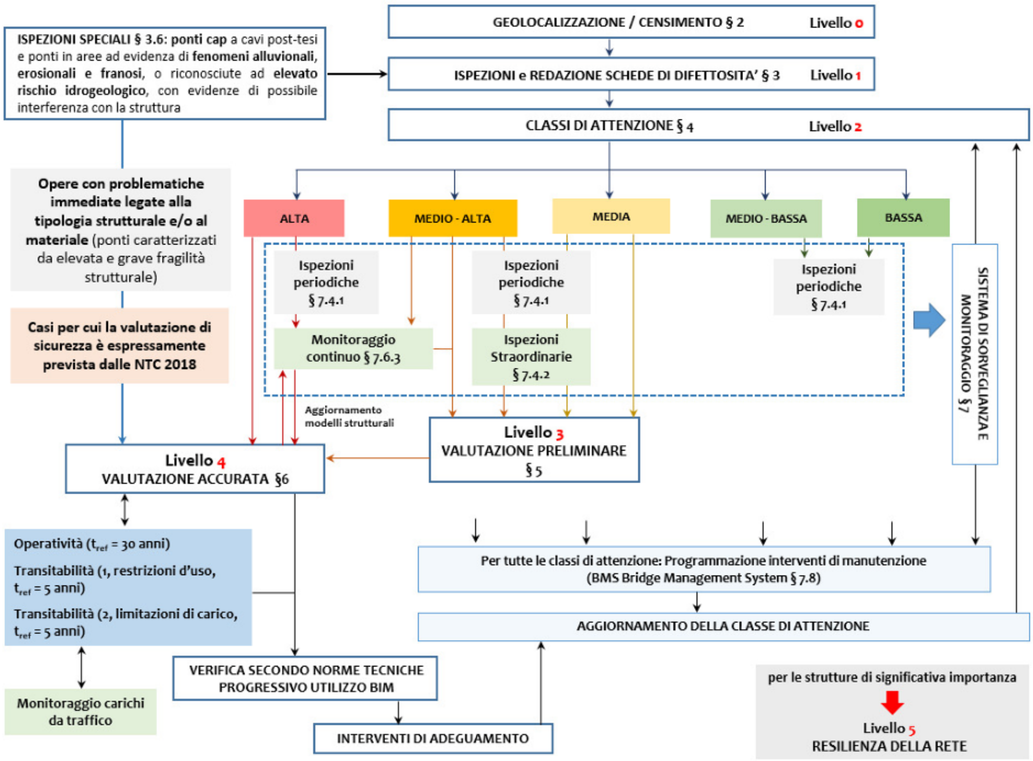

Fig. 3 - Multilevel approach and relationships between levels of analysis (MIT, 2020).

structural-foundational, seismic, hydrological, and geological risks assessment), preliminary structural analyses (Level 3) and safety checks (Level 4).

Since the issuing of IG, many Concessionaries have been implementing the IG methodology and, thanks to their collaboration with the Fabre Consortium (Fabre, 2024), data about Level 0, 1 and 2 are available to draw some considerations. The database is composed by more than 400 bridges (Salvatore *et al.*, 2024) representing structures with a total length higher than 6 m as required by IG for its application. Considering census data (Level 0) reported in the database, an initial classification of the bridge inventory is presented according to geometrical (i.e., total length, Fig. 4a, number of spans, Fig. 4b, maximum span length, Fig. 5a) and typological parameters (i.e., static scheme, Fig. 4c, superstructure material, Fig. 5b and structural scheme, Fig. 5c). Most

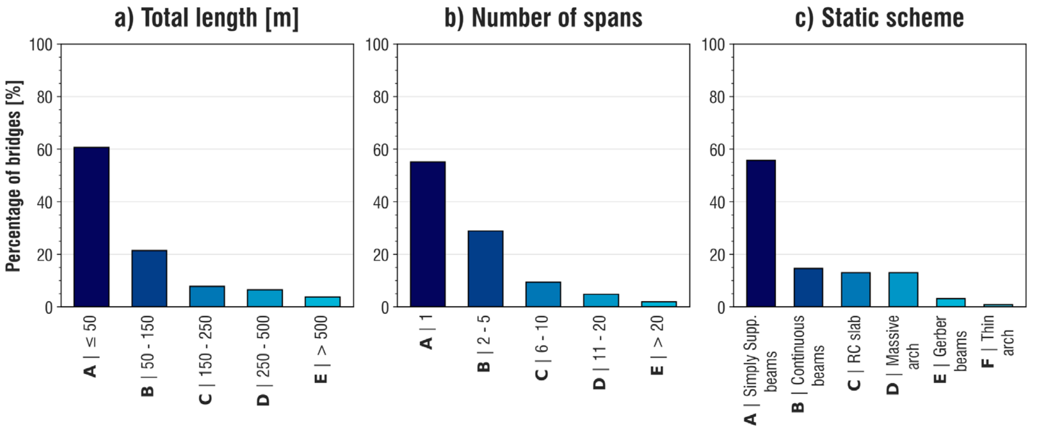

Fig. 4 - Bridge classification based on a) total length [m], b) number of spans and c) static scheme. Capital letters in x-axis labels refer to the columns of the table that shows the number of bridges and the percentage value.

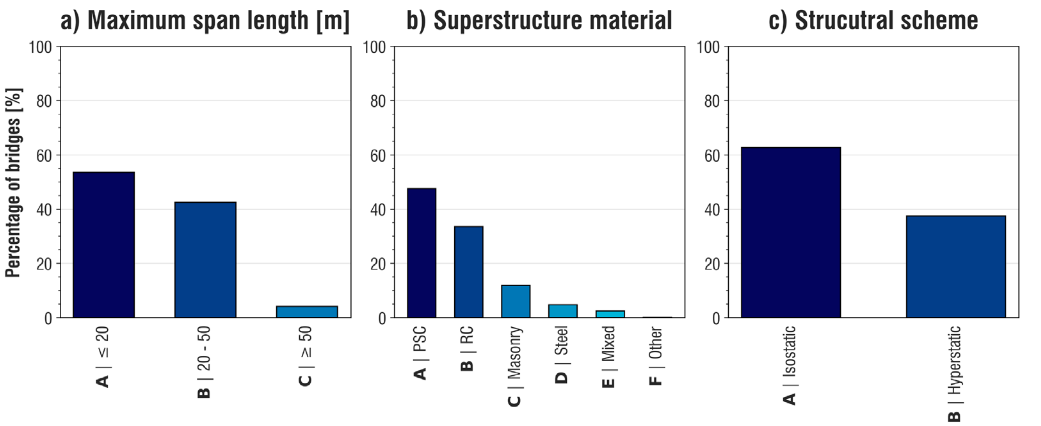

Fig. 5 - Bridge classification based on a) maximum span length [m], b) superstructure material and c) structural scheme (isostatic or hyperstatic). Capital letters in x-axis labels refer to the columns of the table that shows the number of bridges and the percentage value.

of bridges are less than 50 m long (60.6%), have less than 2 spans (55.1%), and the deck consist of simply supported or continuous beams (70.1%). Furthermore, only a small sample of the dataset is characterized by maximum span length greater than 50

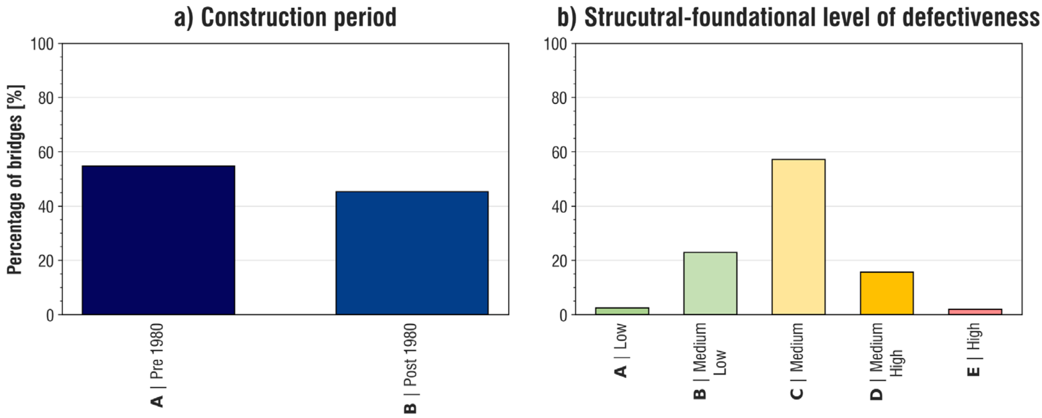

Fig. 6 - Bridge classification based on a) construction period and b) structural-foundational level of defectiveness. Capital letters in x-axis labels refer to the columns of the table that shows the number of bridges and the percentage value.

m (4.1%). Regarding superstructure of bridges, PSC and RC are the most used construction materials (47.5% and 33.5%, respectively) and two bridges out of three show an isostatic structural scheme. Looking at construction period, Fig. 6a, there is a balance between before and after 1980 in bridge construction and more than half, Fig. 6b, is reported to have a level of structural defectiveness equal to Medium or higher (74.6%). At Level 2 every parameter collected so far in Level 1 is combined according to the logical operator approach provided by IG to classify different aforementioned risks (Fig. 7a and Fig. 7b show only structural-foundational and seismic warning classes, respectively). Later, each risk class is jointed in a total warning class, Fig. 7c, spanning from High to Low. According to the IG, bridges characterized by a High total warning class (22.6% of the total) are addressed to Level 4 (accurate assessment, ordinary and extraordinary periodic inspections), while those ascribed to Medium-High total warning class (25.8% of the total) are assessed through Level 3 (preliminary assessments) and later through Level 4. This approach is intended to update the total warning class based on the results of each step. Furthermore, for these bridges, periodic or continuous structural health monitoring (SHM) systems are considered when required.

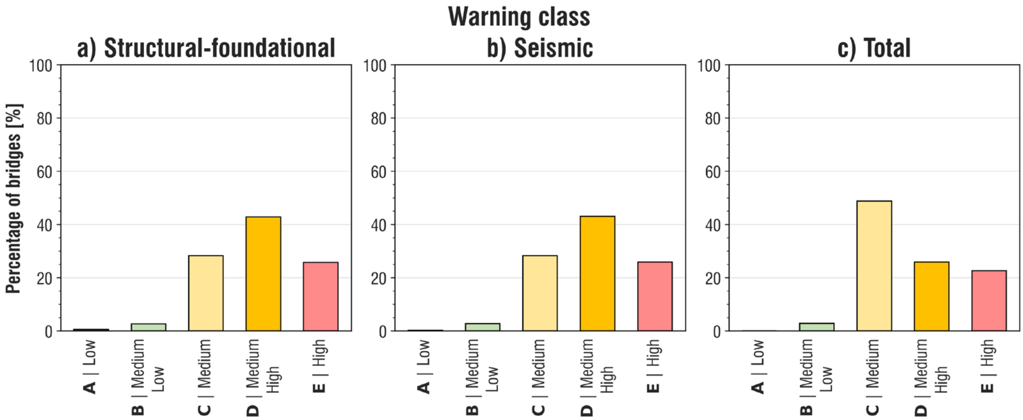

Fig. 7 - Bridge classification based on warning classes a) structural-foundational, b) seismic and c) total. Capital letters in x-axis labels refer to the columns of the table that shows the number of bridges and the percentage value.

Although effective as standardized methodology at a national scale for bridge risk classification and assessment and the rational administration of resources, IG relies on traditional monitoring procedures (necessary and hardly replaceable) which involve time- and cost-consuming activities that cannot be widely applied to a bridge portfolio scale in a short timely given the numbers before presented. Still, new cutting-edge technologies, new if compared to the well consolidated traditional monitoring techniques, can be explored with the goal of: (i) lightening management costs; (ii) supporting reliable prioritization schemes of the IG; (iii) providing a near-continuous cost-effective monitoring strategy of structural risk.

Objectives

This research work is aimed at identifying such cutting-edge technologies and techniques for structural risk evaluation to support the application of the multi-level approach on a bridge portfolio scale focusing on the most recurrent bridge typologies in Italy and based on the guidance provided by the IG. Starting from Section 7.6 of the IG where requirements of such systems are defined, the goal of a SHM can be dual, depending on the specific health state of the bridge. In case of recognized degradation phenomena/damages a periodic or permanent SHM system can be used to study evolutionary trends or determine their causes through the correlation between monitored parameters (e.g., strain measures of structural elements through embedded strain-gauges). Moreover, a SHM system can be installed to detect any anomalies or structural damages in real time before these produce obvious manifestations. Such systems, whatever their periodic or permanent nature, can be considered effective if they are part of a process of analysis and management of data also capable, where necessary, of determining immediate traffic restriction measures that can also be implemented through suitable traffic interdiction equipment. Furthermore, it is clear that the technologies involved in SHM are profoundly interdisciplinary and thus their dissemination depends on the sensitivity of the technical-scientific context to knowledge, other than that of the cultural matrix of origin, and the more or lesser aptitude to assimilate its innovation content. In this framework Synthetic Aperture Radar (SAR) sensors and their image processing algorithms (e.g., Multi-Temporal Interferometry Synthetic Aperture Radar, MTInSAR), Unmanned Aerial Vehicles (UAVs) photogrammetry and Machine Learning (ML) could meet the requirements demanded by IG and are studied and implemented in this research work for SHM applications regarding structural risk. This dissertation is organised in several studies regarding the abovementioned technologies corresponding to different Chapters. The proposed studies are focused on specific objectives (SO).

- **SO1: Exploiting MTInSAR data as early warning system in simply supported concrete girder bridges**

  The potential of innovative remote-sensing approaches for continuous and near-real time displacement monitoring of existing structure is discussed. The applicability to existing bridge portfolios is evaluated and conceptualized in a framework for early warning evaluations, along with a GIS plugin to ease its adoption by practitioners. The framework is discussed with advantages and shortcomings of the technique.

- **SO2: Combination of UAV photogrammetry and MTInSAR on existing built heritage**
  The study aims to investigate how to overcome MTInSAR limitations by the combination with other data sources (i.e., UAV photogrammetry). Starting from a literature review of UAV photogrammetry, its potentials and weaknesses are discussed together with main digital products derived by this technology. A probabilistic-based assessment framework is proposed to leverage structural displacements recorded by MTInSAR and surrounding area displacements obtained by UAV photogrammetry.

- **SO3: Application of ML algorithms to traditional sensor-based SHM**
  Traditional sensor-based SHM systems for prestressing force monitoring purpose are studied, considering limitations regarding the use on specific structural typologies (i.e., internal unbonded tendons). Literature ML algorithms for regression analysis are studied and evaluated proposing a methodology to predict prestressing force reduction in PSC bridges based on traditional SHM sensor measurements. The physical evaluation of ML surrogate models through an eXplainability approach is used to explore the best strategy in the implementation of a sensor-based SHM system.

Outline and organization of the thesis

In the first part of Chapter 1, a section on the state-of-the-art on Earth observation based on remote-sensing technologies focusing on satellite constellations and SAR sensors is presented, together with the main principles of SAR technique and their image processing algorithms as Differential Interferometry Synthetic Aperture Radar (DInSAR) and MTInSAR. Then, a literature review section is proposed on the application of MTInSAR data for structure and infrastructure monitoring. Based on the available

literature, pros and cons of structures monitoring through SAR data are presented to explore their use as near-continuous monitoring system in a cost-effective manner (Calò *et al.*, 2023). Considering the objectives of the thesis, an early warning system for structural risk assessment on the most spread bridge typology in Italy and Europe (i.e., simply supported concrete girder bridges) is proposed. The use of MTInSAR data is codified in a completely automated framework through Python modules (Calò *et al.*, 2024a) which exploits poor structural information (already at disposal by transportation management authorities, for example via Level 0 and Level 1 of IG) and temperature data to describe the bridge structural behaviour over the time under service conditions. The output provides displacement profiles characterizing bridge in vertical and longitudinal directions, which are compared with new displacement thresholds evaluated through simple analytical models of the investigated bridge typology. Moreover, different displacement scenarios associated to displacement components are proposed to identify their causes, providing a structural interpretation of remote-sensed measurements. The procedure is tested on two different case studies, affected by different pathologies, demonstrating its effectiveness.
Moreover, to promote the use of this remote-sensing technology, a GIS plugin named BAS-MTInSAR, developed for QGIS in Python language, is presented (Calò *et al*., 2024b; Calò *at al*., 2024c). BAS-MTInSAR implements the proposed MTInSAR framework along with other innovations achieved during its development (e.g., additional thresholds). Through the developed Graphic User Inter-face (GUI), practitioners can manage input data required and automatically detect displacement scenarios. Moreover, BAS-MTInSAR allow to manage bridge portfolios by storing results on previous analysed bridges.
In Chapter 2, UAV and their working principles as additional remote-sensing technology are presented, exploring the main digital products derived from UAV photogrammetry with a focus on Digital Surface Models (DSMs). Then, a literature review section on the use of UAV photogrammetry, as a cost-effective technology for existing built heritage (both buildings and infrastructures) and landslide monitoring is proposed to point out potentials and weaknesses. Based on the acquired knowledge, the advantages of both

remote-sensing technologies (i.e., MTInSAR data and UAV photogrammetry) are leveraged in a probabilistic-based approach (Calò *et al*., 2024d). Indeed, MTInSAR data can be used to monitor displacements of structures, while UAV photogrammetry to monitor displacements of the surrounding area. Given a structure to monitor and a period of observation, the idea consists of retrieving MTInSAR data about the structure and of performing UAV flight surveys on the surrounding area at the beginning and end of the considered period. From both surveys, statistical distributions of the spatiotemporal velocities (only the vertical component is assessed) can be processed and evaluated towards a predefined limit state. The obtained results are classified under different scenarios to reveal the occurrence of possible subsidence phenomena. The proposed methodology is firstly validated on a real landslide and subsequently is tested on one of the case studies showed in Chapter 1 for risk prediction, showing a satisfying capacity of providing warnings to employ in structural risk mitigation plans.

In Chapter 3, the focus of the study moves from a large-scale to the structure specific assessment. Bridges, especially aged ones, are characterized by different degradation phenomena (peculiar to the construction typology and material of the bridge) induced by exogenous actions (e.g., increasing traffic and dead loads) and environmental conditions (e.g., temperature, solar radiation, rain). A common structural defect for PSC structures is the corrosion and break of wires of tendons of the prestressing system reducing the bearing capacity of the structure (Nettis *et al*. 2024). In literature there are several examples of SHM sensor-based systems to monitor prestressing system of PSC bridges, although affected by some limitations highlighted in this Chapter. Considering the cost-effective solution represented by strain-gauges, ML algorithms already at disposal by literature for regression analysis are explored, proposing a methodology combining strain-gauges measurements and other structural information to predict prestressing force reduction in PSC bridges (Calò *et al.*, 2024e). Artificial Neural Network (ANN), Random Forrest Regressor (RFR), Support Vector Regression (SVR) are trained and tested on a dataset generated by a simplified nonlinear modelling strategy. The ML surrogate model, able to predict the prestressing force reduction based on the required input data, is selected among the trained ones based on statistical metrics. The effectiveness of the methodology is tested on a scaled PSC box bridge experimentally tested in the ICITECH laboratories of the Universitat Politècnica de València. The physical evaluation of ML surrogate models through an eXplainability approach is used to explore the best strategy in the implementation of a sensor-based SHM system.

CHAPTER 1

AN MTINSAR-BASED EARLY WARNING SYSTEM TO APPRAISE DEFORMATIONS IN SIMPLY SUPPORTED CONCRETE GIRDER BRIDGES

In this Chapter, an overview on Earth observation (EO) in presented, focusing on SAR sensors and main principles of the acquisition system. SAR images, processed with specific algorithms early discussed, are used in a remote sensing technique called Interferometry Synthetic Aperture Radar (InSAR) in which displacement time series of points on the Earth surface (called scatterers) are reconstruct. After a literature review on the applications and the potentials of this technique as a cost-effective tool for structure monitoring (Calò *et al*., 2023), an engineering bridge-oriented framework is proposed exploiting Multi-Temporal Interferometry Synthetic Aperture Radar (MTInSAR) data, poor structural information (already at disposal by transportation management authorities) and temperature data to describe the bridge behaviour over the time (Calò *et al*., 2024a). The output of the framework, providing comparisons of longitudinal and vertical displacements of the bridge with new displacement thresholds defined for specific scenarios, aims to identify the causes of such displacements with the goal to provide structural interpretation of remote-sensed measurements. The procedure, which applies to simply supported concrete girder bridges (most spread bridge typology in Italy as demonstrated in the Introduction), is tested on two different case studies affected by different pathologies, demonstrating its effectiveness as early warning system for purpose of bridge portfolio analysis and risk prioritization, also according to the framework proposed by the recent Italian guidelines (MIT, 2020). Lastly, a new developed GIS Plugin named BAS-MTInSAR (Calò *et al*., 2024b; Calò *et al*., 2024c) is presented to ease the application of MTInSAR data by practitioners for structural risk management of bridges.

1.1. Fundament

1.1.1. Earth observation and satellites

EO is a branch of science that uses remote sensing technologies, sensors in ground-based, or airborne platforms to gather information about physical, chemical, and biological systems of the Earth (Paravano *et al.*, 2024). Hence, EO encompasses both remotely sensed and on-site data. The outstanding advantage in the field of the EO that has led researchers to develop remote sensing observation technologies is the ability to carry out remote observations through optical and multispectral imagery of the Earth's surface for reconnaissance, mapping and monitoring with a high coverage, both spatial (i.e. thousands of km^2) and temporal (from a few hours up to tens of days). Furthermore, compared to traditional on-site methods this technology has a very low environmental impact, limited costs, and other many advantages compared to on-site methods. For instance, on the same survey area or observation period, although traditional on-site methods provide very accurate measurements, they require direct access to the areas, sometimes difficult to reach due to adverse climatic and environmental conditions (e.g. polar ice caps, volcanic craters, landslide areas). Among the remote sensing technologies employed for monitoring applications, satellites deserve special attention due to their increasingly widespread use in the literature. Before discussing about this topic is important to describe EO satellites and their operating principles.

EO satellites can be classified in several ways considering, for example their payloads and their orbits. Regarding this latter, an orbit is the curved path that an object in space, as a satellite, takes around another object, such as a planet, due to gravity (ESA, 2020a). The orbits of the satellites differ in altitude above the Earth's surface and path, Fig. 8. Polar orbit (PO) is an orbit at low altitudes between 200 to 1000 km. Satellites in PO usually travel past Earth from North (N) to South (S) rather than from West (W) to East (E), passing roughly over the Earth's poles. Even a deviation within 20 to 30 degrees is still classified as a polar orbit and called near polar orbit (NPO). Sun-synchronous orbit (SSO) is another polar orbit where satellites are synchronous with the Sun. This means they are synchronised with the relative position of the Sun over a place. Thus, the observation of a spot happens at the same local time and is used in several applications where it is important to compare how somewhere changes over time, fixed some characteristics. A satellite in an SSO is usually at an altitude between 600 to 800 km. A low Earth orbit (LEO) is an orbit at low altitudes between 160 km to 1000 km. LEO satellites do not always have to follow a particular path around Earth and then their plane can be tilted from the equatorial plane. For this reason, LEO is a very commonly used orbit because there are more available routes for satellites. Geostationary orbit (GEO) allows satellites to circle the Earth above the equator from W to E following Earth's rotation. Hence, satellites in GEO are called geostationary for their fixed position. To perfectly match Earth's rotation of 23 hours 56 minutes and 4 seconds, *T*, the altitude, *h*, of GEO is about 35786 km.

$$T = 2\pi(R + h)\sqrt{\frac{(R + h)}{gR^2}} \tag{1}$$

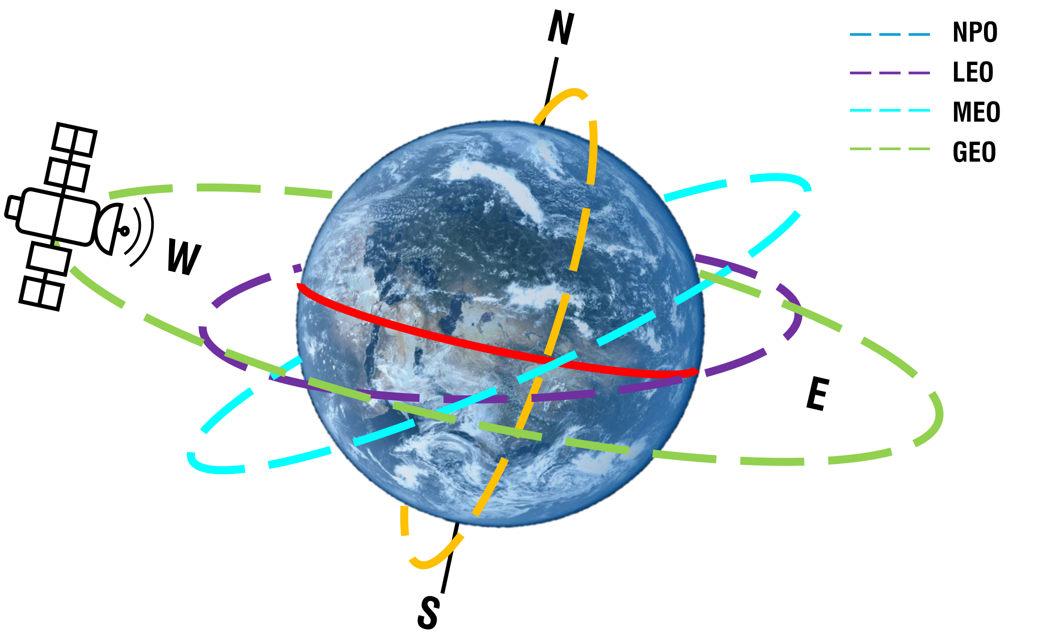

Fig. 8 - Schematic representation of different satellite orbits. Black line shows Earth's rotation axis and red line the equator. Dashed lines describe the orbits: orange is the near polar orbit (NPO), purple is the low Earth orbit (LEO), cyan is the medium Earth orbit (MEO) and green is the geostationary orbit (GEO).

Where g is the acceleration due to gravity near Earth's surface and R is the Earth's radius ($\approx$ 6380 km). GEO is used, for example, by telecommunication satellites and weather monitoring satellites. There is also a wide range of orbits, with any path, between LEO and GEO called medium Earth orbits (MEO). Like satellites travelling in LEO, those travelling in MEO do not need to follow specific paths around the Earth and are also used for many different applications. For example, the European Galileo system powers navigation communications across Europe to get directions on our smartphones. In summary, EO satellites are placed in LEO for a high data resolution or SSO to have consistent lighting and obtain a total view of the Earth: other satellites are placed in GEO for an uninterrupted coverage.
Continuing with the description of the satellites operating principles, their payloads (i.e., sensors) are used to acquire the electromagnetic energy. Electromagnetic radiation, known as the propagation of the energy of the electromagnetic field in space, consists of an electric (E_l) and a magnetic (B) field. E_l and B are orthogonal to each other and always perpendicular to the direction of propagation Z, Fig. 9. The electromagnetic radiation is characterized by three types of propagation, Fig. 10:

- Transmission, a fraction of the radiation penetrates the surface of certain medium, for example water.

- Absorption, a fraction of the radiation is absorbed through molecular or electronic interactions with the medium it passes through.

- Reflection, a fraction of the radiation is reflected (and scattered) by the target at different angles (depending on the "roughness" of the surface and the orientation of the direction of incidence of the solar radiation with respect to the inclination of the surface).

The satellite payload can be divided into two categories, based on their acquisition mode: passive (e.g., optical) and active (e.g., Synthetic Aperture Radar, SAR). Passive

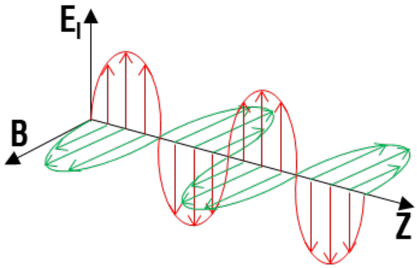

Fig. 9 - A linearly polarized electromagnetic wave going in the Z-axis, with E_I denoting the electric field and perpendicular B denoting magnetic field.

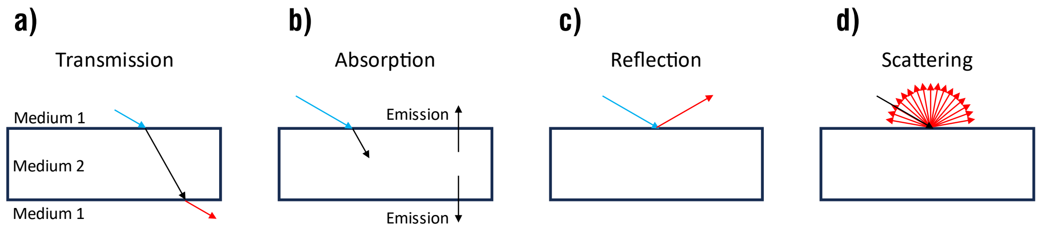

Fig. 10 - Types of propagation of the electromagnetic radiation: (a) transmission, (b) absorption, (c) reflection, (d) scattering.

sensors measure the radiation that is available, whether it is emitted or reflected (i.e. solar radiation) by objects on the Earth's surface depending on their reflectivity or reflectance. Instead, active sensors emit an electromagnetic wave towards the object to investigate and thus independent from other forms of lighting (e.g., solar). The radiation backscattered by the object, along the direction of the sensor carrying out the observation, is then recorded and measured by the sensor itself. Each sensor is designed to operate among one or more bands of the electromagnetic spectrum, each characterized by certain wavelengths, λ, and frequency, f_λ. These quantities are mutually connected. Indeed, traveling sinusoidal waves can be represented mathematically in terms of their velocity, v_λ, (in the Z- direction and influenced by the medium it passes), f_λ and λ as:

$$y(Z,t) = A\cos\left(2\pi\left(\frac{Z}{\lambda} - f_\lambda t\right)\right) = A\cos\left(\frac{2\pi}{\lambda}(Z - v_\lambda t)\right) \quad (2)$$

where y is the value of the wave at Z and time t, and A is the amplitude of the wave. Equation (2) expresses traveling sinusoidal wave both in terms of angular frequency, ω_λ, and wavenumbers, k_λ.

$$y(Z,t) = A\cos(k_\lambda Z - \omega_\lambda t) = A\cos\big(k_\lambda(Z - v_\lambda t)\big) \tag{3}$$

From Equation (2), ω_λ and k_λ are related to v_λ and f_λ as:

$$k_\lambda = \frac{2\pi}{\lambda} = \frac{2\pi f_\lambda}{v_\lambda} = \frac{\omega_\lambda}{v_\lambda} \tag{4}$$

$$\lambda = \frac{2\pi}{k} = \frac{2\pi v}{\omega} = \frac{v}{f} \tag{5}$$

The electromagnetic spectrum, NASA 2022, is the set of all possible λ over which the energy associated with an electromagnetic wave propagating in space can be distributed (Fig. 11 values are referred to electromagnetic waves travelling in the void). Exploring the electromagnetic spectrum and its bands, the component between 380 nm (violet) and 700 nm (red), perceivable by the human eye, is called the visible spectrum.

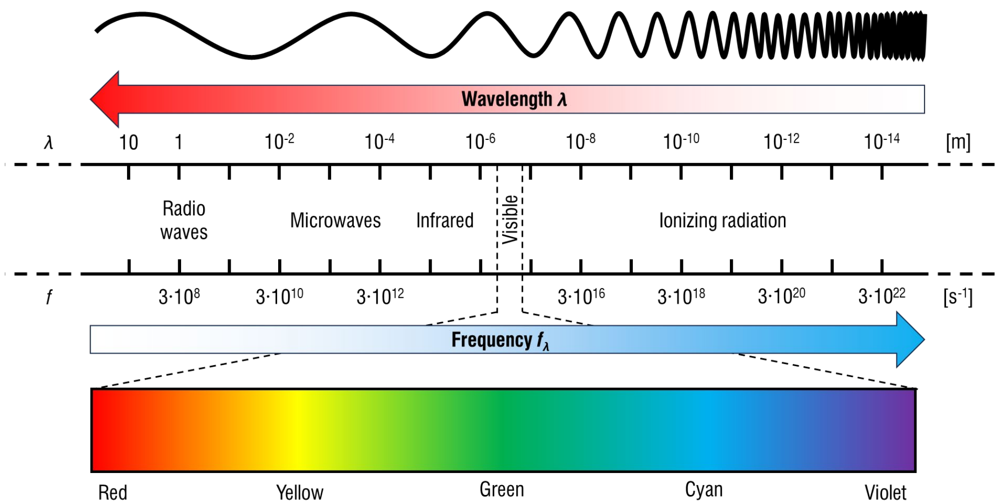

Fig. 11 - Electromagnetic spectrum.

Table 1 - Microwaves class.

Class	Band	Frequency f_λ	Wavelength λ
	Ka	40 – 27 GHz	7.50 mm – 1.11 cm
	K	27 – 18 GHz	1.11 cm – 1.67 cm
	Ku	18 – 12 GHz	1.67 cm – 2.50 cm
Microwaves	X	12 – 8 GHz	2.50 cm – 3.75 cm
	C	8 – 4 GHz	3.75 cm – 7.50 cm
	S	4 – 2 GHz	7.50 cm – 15 cm
	L	2 – 1 GHz	15 cm – 30 cm

The region below the violet, between 10 nm and 380 nm, is called ultraviolet (UV), and the region above the red, between 700 nm and 1 mm, is called infrared (IR). This latter, in the range of 750 nm and 15 μm is defined as thermal infrared. Thermal infrared is related to the thermal emission of bodies and is used for example by FLIR sensors. Electromagnetic waves with λ lower than 400 nm (UV, X, and gamma rays) are not used for remote sensing applications. Instead, the region of the microwave, shown in detail in Table 1, including λ between 1 mm and 10 cm, is used by SAR systems. The main property of the radiation at these λ is to penetrate clouds, making the acquisition independent from the cloud cover. Beyond microwaves, radio waves are used in remote sensing for the management and control of satellites and on-board instrumentation and not for EO. **Table 2** reports a summary of the bands of the electromagnetic spectrum.

Table 2 - Electromagnetic spectrum classes.

Class	Band	Name	Frequency f_λ	Wavelength λ
Ionizing radiation	γ	Gamma rays	30 EHz	10 pm
	HX	Hard X-rays	3 EHz – 30 EHz	100 pm – 10 pm
	SX	Soft X-rays	30 PHz – 3 EHz	10 nm – 100 pm
	EUV	Extreme ultraviolet	3 PHz – 30 PHz	121 nm – 10 nm
	NUV	Near ultraviolet	750 THz – 3 PHz	380 nm – 121 nm
Visible spectrum		Violet	670 THz – 750 THz	450 nm – 380 nm
		Blue	620 THz – 670 THz	485 nm – 450 nm
		Cyan	600 THz – 620 THz	500 nm – 485 nm
		Green	530 THz – 600 THz	565 nm – 500 nm
		Yellow	510 THz – 530 THz	590 nm – 565 nm
		Orange	480 THz – 510 THz	625 nm – 590 nm
		Red	400 THz – 480 THz	700 nm – 625 nm
Infrared	NIR	Near infrared	480 THz – 300 THz	1 µm – 700 nm
	MIR	Mid infrared	300 THz – 30 THz	10 µm – 1 µm
	FIR	Far infrared	30 THz – 3 THz	100 µm – 10 µm
Microwaves	EHF	Extremely high frequency	3 THz – 300 GHz	1 µm – 100 µm
			300 GHz – 30 GHz	1 cm – 1 mm
	SHF	Super high frequency	30 GHz – 3 GHz	1 dm – 1 cm
Radio waves	UHF	Ultra high frequency	3 GHz – 300 MHz	1 m – 1 dm
	VHF	Very high frequency	300 MHz – 30 MHz	10 m – 1 m
	HF	High frequency	30 MHz – 3 MHz	100 m – 10 m
	MF	Medium frequency	3 MHz – 300 KHz	1 km – 100 km
	LF	Low frequency	300 KHz – 30 KHz	10 km – 1 km
	VLF	Very low frequency	30 KHz – 3 KHz	100 km – 10 km
	ULF	Ultra low frequency	3 KHz – 300 Hz	1 Mm – 100 km
	SLF	Super low frequency	300 Hz – 30 Hz	10 Mm – 1 Mm
	ELF	Extremely low frequency	30 Hz – 3 KHz	100 Mm – 10 Mm

1.1.2. Synthetic Aperture Radar

One of the most common active sensors mounted as payload on EO satellites is the SAR. SEASAT was a NASA oceanography experimental mission launched on 28 June 1978 which ceased operations the same year, and on-board there was the first-ever spaceborne SAR system for science applications (ESA, 2021). After this first EO experiment with a SAR sensor, the 1980s saw the birth of SAR systems placed on board shuttle craft. Since the early 1990s, almost all space agencies have included among their programs the launch of platforms carrying SAR sensors on-board. Among these are: the ESA ERS1/2 program (ESA, 2020b), the NASDA JERS (ESA, 2020c), the Canadian RADARSAT (CSA, 2024). Nowadays, some of the active SAR satellites are Sentinel-1 (ESA, 2024), RADARSAT, TerraSAR-X (DLR, 2024), COSMO-SkyMed (ASI, 2017), others are being launched (e.g., COSMO-SkyMed, CSK, second generation has two out of four satellites in orbit as reported in ESA 2022a), and more are planned as IRIDE (Planetek, 2023). Some details about past and current satellite missions are provided in Table 3 (SERVIR Global Science, 2019).

Table 3 - List of past and current and upcoming spaceborne SAR sensors with their properties (F&O: Free & open, Re: Restrained, Co: Commercial, A-D: Application-dependent, RS: Restrained scientific, SP: Scientific proposal, TDB: To be decided).

Satellite	Start/End	Band	Polarization	Resolution	Frame size	Cycle	Access
SEASAT	1978/ 1978	L	Single	25 m	100 km	-	F&O
ERS-1	1991/ 2001	C	Single	6 – 30 m	100 km	35 d	Re
JERS-1	1995/ 1998	L	Single	8 m	75 km	44 d	Re
ERS-2	1995/ 2011	C	Single	6 – 30 m	100 km	35 d	Re
ENVISAT	2002/ 2012	C	Single, Cross, Dual	28 m	100 km	35 d	Re
ALOS-1	2006/ 2011	L	Single, Cross	10 – 30 m	30 – 350 km	46 d	F&O
RADARSAT-1	1995/ 2013	C	Single	9 – 100 m	45 – 510 km	24 d	Re, C
TerraSAR-X	2007/ -	X	Single, Dual, Cross	0.25 – 40 m	3 – 200 km	11 d	A-D, RS, C
TanDEM-X	2010/ -	X	Single, Dual, Cross	0.25 – 40 m	3 – 200 km	11 d	A-D, RS, C
Radarsat-2	2007/ -	C	Single, Dual, Quad	1.5 – 100 m	8 – 500 km	24 d	C
CSK	2007/ -	X	Single, Dual	0.7 – 100m	10 – 200 km	16 d	C, PS

Satellite	Start/End	Band	Polarization	Resolution	Frame size	Cycle	Access
ALOS-2	2014/ -	L	Single, Dual, Quad	1 – 100m	25 – 355 km	14 d	C, PS
PALSAR-2	2014/ -	L	Single, Dual, Quad	1 – 100m	25 – 355 km	14 d	C, PS
Sentinel-1	2014/ -	C	Single, Dual	5 – 40m	250 – 400 km	12 d	F&O
SAOCOM	2018/ -	L	Single, Dual	10 – 100m	65 – 320 km	16 d	TBD
PAZ SAR	2018/ -	X	Single, Dual, Cross	0.25 – 40 m	3 – 200 km	11 d	C
RCM	2019/ -	C	Single, Dual, Quad	3 – 100 m	20 – 500 km	12 d	TBD
NISAR	2021/ -	L	Single, Dual, Quad	3 – 20 m	250 km	12 d	F&O
TanDEM-L	2023/ -	L	Single, Dual, Quad	12 m	350 km	16 d	F&O

Satellites with this payload travel in NPO orbits, half of the path from S to N (i.e., ascending track, ASC) and half from N to S (i.e., descending track, DSC), Fig. 12b. Their orbits are constrained within an Earth-fixed orbital tube with respect to a reference orbit at every orbital point, over any repeat cycle (Prats-Iraola *et al.*, 2015). The ability of the satellite to move within this region provides an increased sensitivity of the terrain height. Specifically, CSK satellites, which are guaranteed to be within ± 1 km from the reference ground track, can reduce the errors in the estimate of the terrain height under 1 m. Travelling in the azimuth direction, SAR sensor transmit, in the Line-of-Sight (LoS) direction, electromagnetic pulses towards the Earth's surface with their moving side-looking antenna. The active sensor can detect and record, for each resolution cell, intensity of the return pulse (amplitude, A_{mp}) and the time it takes to travel forward and back to the antenna, in terms of phase, φ. The characteristic side-looking view with respect to the azimuth direction allows to overcome the left/right ambiguity of possible targets that are at the same distance from the sensor (Franceschetti and Lanari, 1999). The coordinate system of the acquisition geometry of a radar satellite can be referred to as a cylindrical coordinate system (azimuth, slant range, and incidence angle), Fig. 12a. Incidence angle, ϑ, is measured from the vertical direction to the LoS. The projection of the slant range direction on the Earth's surface is called the ground range (α, is the azimuth angle, that is the angle between E and ground range direction) and the footprint, black box in Fig. 12a, has a width called swath width. The swath width depends on both λ and acquisition mode of the SAR sensor. Regarding the resolution in slant range and azimuth, is defined as the minimum distance between two points to be distinguishable. Slant range resolution, Δ_{range}, is described by the following equation:

$$\Delta_{range} = \frac{c}{2\Delta f} \tag{6}$$

and depends on λ and the power of the signal, (Franceschetti and Lanari,1999). Instead, azimuth resolution $\Delta_{azimuth}$, is described by the following equation:

$$\Delta_{azimuth} = \frac{L_{beam}}{2} \tag{7}$$

Where L_{beam} is the length of the antenna. According to Equation (7) the azimuth resolution is linearly dependent on L_{beam}. This would imply the need to have particularly long antennas to obtain resolutions comparable to those in range. To overcome this the antenna steers during flight synthesizing an array of antennas, which is like an

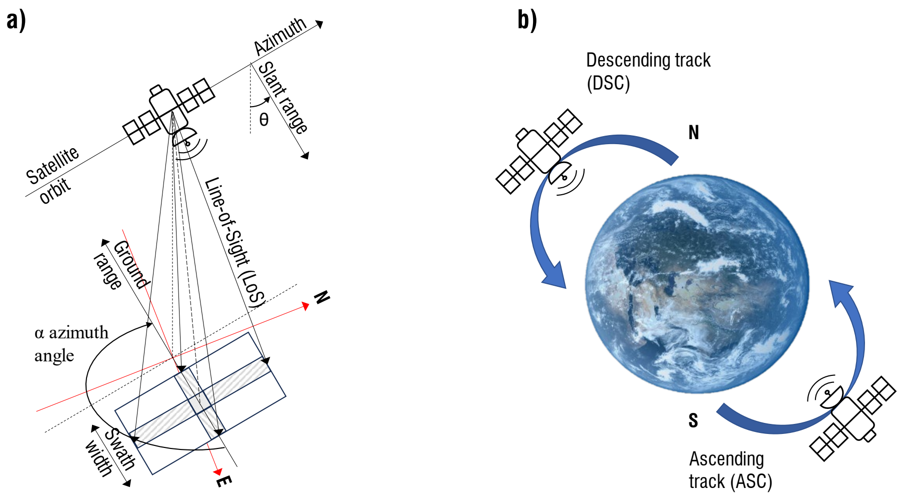

Fig. 12 - Description of satellites acquisition geometries. (a) Geometric definition of azimuth, slant range and LoS, (b) ascending and descending track.

alignment of elementary antennas of length L_{beam} along the LoS. This difference, compared to Real Aperture Radar (RAR) where the antenna is fixed and the resolution depends both on the distance of the target, λ, and L_{beam}, ensures a greater spatial resolution in the azimuth direction, leaving the resolution unchanged in the orthogonal ground range direction, Fig. 13.

Going deep in the discussion of the acquisition geometry, ϑ plays a key role in the acquired images. Unlike optical images taken from a vertical position with respect to the scene, the side view of the antenna introduces some geometrical distortions. This distortion must be considered when a SAR image is evaluated. First, the antenna looks to the scene in a beam and ϑ changes a bit trough each range of the beam. This means that going from slant range to ground range, the same measured quantity in range has different size in ground range, (Fig. 14a). Other distortions are introduced by the relation between ground slope, ϑ_G (measured from horizontal plane), and ϑ angle (Fig. 14). In detail:

- Foreshortening, (Fig. 14b), corresponds to pixel dilatation/compression, depending on ϑ_G value. Compressed pixels look brighter due to the high energy of the backscattered signal related to the number of backscattering objects placed in the pixel.

- Layover, (Fig. 14c), is a particular foreshortening case which occurs when $\vartheta_G > \vartheta$. The uppermost part (point 2 in Fig. 14c) is found to be closer to the satellite and is therefore represented in radar coordinates in a wrong position, reversed in slant range compared to the lower part (1);

- Shadowing, (Fig. 14d), involves regions (point 3 in Fig. 14d) hidden by other regions (point 2 in Fig. 14d).

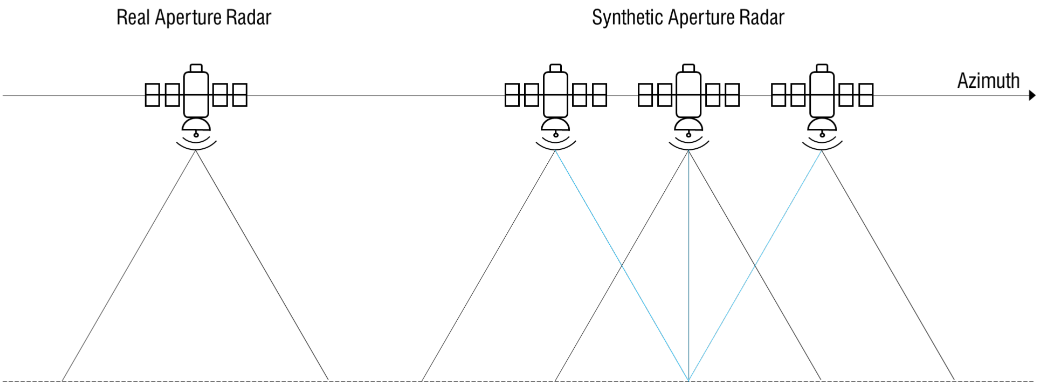

Fig. 13 - RAR with fixed beam and SAR with steering beam.

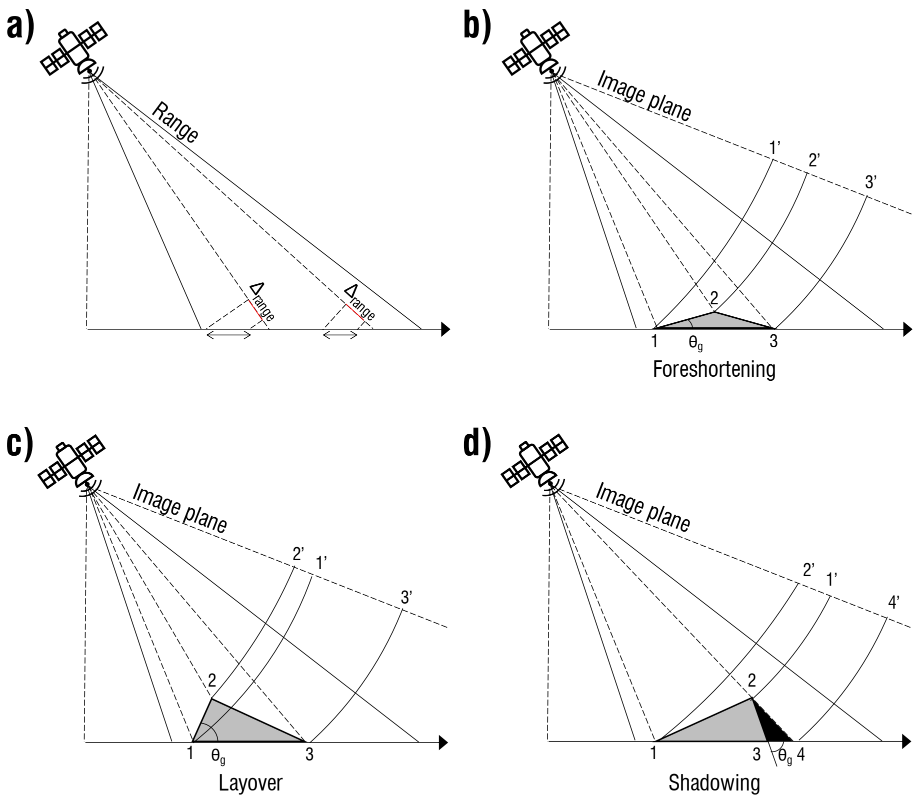

Fig. 14 - Distortions induced by a side-looking view of SAR sensor: (a) Effect of the variability of θ in a beam range; (b) Foreshortening; (c) Layover; (d) Shadowing.

Polarization, reported in Table 3, also has a key role in SAR imagery. Polarization describes the orientation of the plane of oscillation of a propagating signal (SERVIR Global Science, 2019). Most of today's SAR sensors are linearly polarized, meaning that the plane of oscillation of the propagated signal is constant along the propagation path of the electromagnetic wave, Fig. 9. Older SAR satellites (e.g., SEASAT, ERS-1, ERS-2 in Table 3) carried single-polarized sensors, which support only HH- (horizontal polarization on transmit and on receive) or VV-polarization (vertical polarization on transmit and on receive). However, most recent sensors provide dual- or quad-polarization abilities. In this configuration, the sensor alternates between transmitting H- and V-polarized waveforms and receives both H and V simultaneously, thus providing HH-, HV-, VH- and VV-polarized imagery. The acquired scene can be characterized by different scatterers like rough surface scatterers, (e.g., low-vegetation fields and paved surfaces), double-bounce scatterers (e.g., buildings and vertical structures), and volume scatterers (e.g., vegetation canopies). These scattering types do not contribute to all polarimetric channels equally. Indeed, signals at different polarizations interact differently with objects on the ground, affecting the recorded radar brightness in a specific polarization channel, (e.g., HH polarization tends to have better penetration in dense plant cover than VV according to Zalite *et al*., 2014). Thus, in general the choice of polarization depends on the specific application, the characteristics of the terrain of interest and the required spatial resolution.

The most important characteristics reported in Table 3 for the research work described in this chapter are the SAR image resolution, the frame size and the revisit time. SAR image resolution is a key parameter to take into account when dealing with SAR imagery applications because, as later discussed in Section 1.1.3 and 1.1.6, the smaller the resolution cell, the more accurate is the location of the scatterers providing more accurate results for structure investigation. On the other hand, the frame size is important with respect to large-scale assessment of bridge portfolios given that SAR images are not always free and thus a larger frame reduces the number of images to cover larger areas. Lastly, revisit time depends on the number of satellites deployed in the constellation. Revisit time is defined as the time interval between two acquisitions of the same scene. Different from the repeat cycle, reported in Table 3, which is only relevant to the satellite orbits, the revisit time is relative to both orbit and payload of the satellite, such as ϑ and swath width (Luo *et al*., 2017). For example, Sentinel-1 (SEN1) satellites, Fig. 15a, have a revisit time of 6 days, while CSK satellites, Fig. 15b, have a revisit time ranging from 1 to 16 days. Unfortunately, on 23 December 2021 Copernicus Sentinel-1B experienced an anomaly related to the instrument electronics power supply provided by the satellite platform, leaving it unable to deliver radar data (ESA, 2022b). Therefore, the revisit time of this constellation is equal to the recycle time of Sentinel-1A satellite (12 days). Thus, give the time interval between two acquisitions, SAR images can be effectively used for near-continuous monitoring. Furthermore, since SAR images are stored by spaceborne companies can be used to look back in the past from the deploying of the constellation throughout its entire period of activity.

In summary, the reasons behind SAR wide employment are manifold: (i) as active sensor, the acquisition is independent from the illumination of the scene; (ii) microwaves

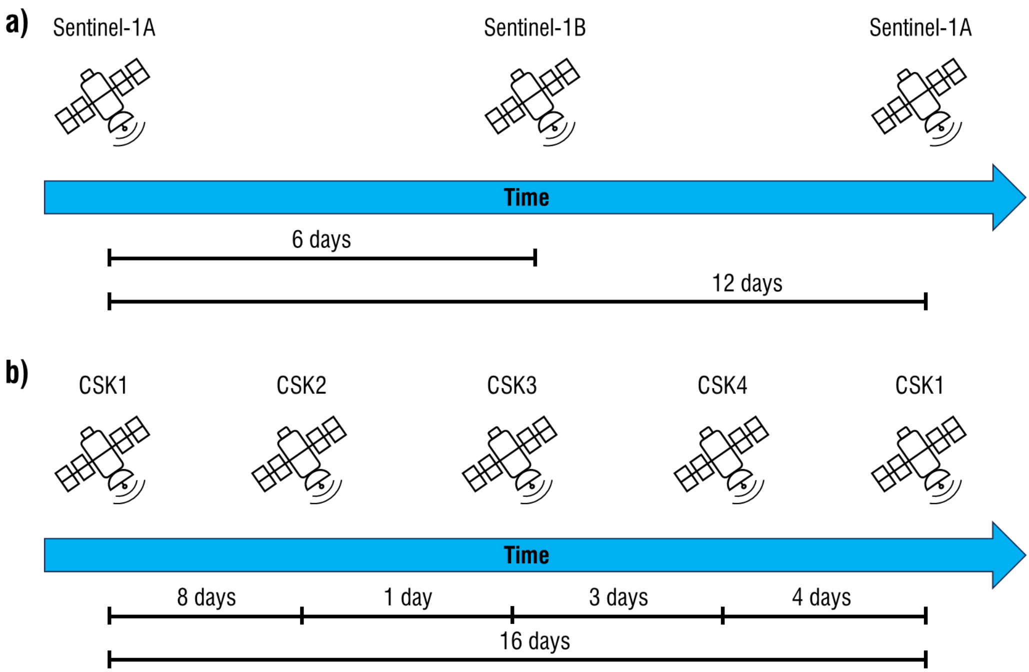

Fig. 15 - Revisit time of (a) SEN1 and (b) CSK constellations.

allow to acquire data beyond the cloud cover, which makes the acquisition as independent also on the atmospheric conditions; (iii) its steering movement during flight enhances the resolution in the azimuth direction compared to RAR; (iv) image resolution and frame size are adequate for single structure observation in a large-scale portfolio application; (v) short revisit time and SAR image storage can be used for near-continuous monitoring from the deploying of the constellation throughout its entire period of activity.

1.1.3. Data types and applications

The variety of data types provided by a SAR system are related to the diverse flavours of information that are captured in every SAR acquisition. In every pixel of a SAR image, sensor stores signal amplitude, phase, and polarization, all of which are related to different physical quantities of the observed scene. SAR data providers offer their imagery in a range of different processing levels to ease the use of such information, not always straightforward to extract and utilize. Level 0 stands for the SAR raw data which is the base for further processing levels. Not every satellite operator has decided to make his RAW data products available to the community. Single-Look Complex (SLC) images, categorized as Level 1 data, are SAR data provided at the full native resolution (single look) with both A and φ information stored in each pixel. SLC products are typically provided in the original slant-range observation geometry (Fig. 12a) and are therefore not geocoded or terrain-corrected. At this level, the φ information can be used for InSAR processing (see next Section 1.1.4), to map surface topography or surface deformation. In addition, SLCs are also used for higher level image products such as amplitude images (Fig. 16), polarimetric products, and geocoded images. At the end, Level 2 consists of geo-located geophysical products derived from Level 1.

Regarding displacement mapping, which is the starting point for further considerations and elaborations in the MTInSAR framework proposed in this Chapter, Level 1 SLC images are sufficient. Analytically, a SLC image expression $\hat{\gamma}(x', r')$ can be expressed as (Franceschetti and Lanari, 1999):

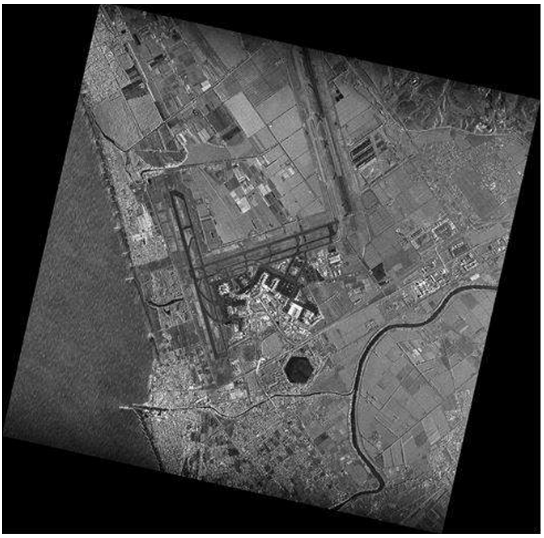

Fig. 16 - SAR amplitude image acquired in Spotlight mode by CSK constellation (Fiorentino and Virelli, 2016).

$$\hat{\gamma}(x', r') \approx \gamma(x', r') \cdot \left[-j\frac{4\varphi}{\lambda} r(x', r')\right] \tag{8}$$

where *x'* and *r'* are azimuth and range directions, respectively. The first term, *γ(x', r')*, is a complex one and is related to the reflectivity of the scene and is used for amplitude images. These images, Fig. 16, are in a gray colour scale and the colour is related to the backscattered signal intensity, which depends on both physical properties of the object and acquisition geometry of the sensor. Flat surfaces like water bodies, paved roads, and runways appear as dark areas in an amplitude image because the radar pulses are mirror reflected, Fig. 10c. Instead, vegetation is usually rough and is typically visualized as a gray area (Fig. 10d). Surfaces inclined toward the sensor are very clear in images because show greater backscatter than surfaces that slope away from the radar.

Buildings and many man-made structures appear very clear too, because of the double-bounce effect. The radar pulse bounces off the horizontal ground towards the target, and then is reflected, slightly weakened, from one vertical surface of the target back to the sensor. Regarding bare soil, the brightness of these areas may vary from very dark

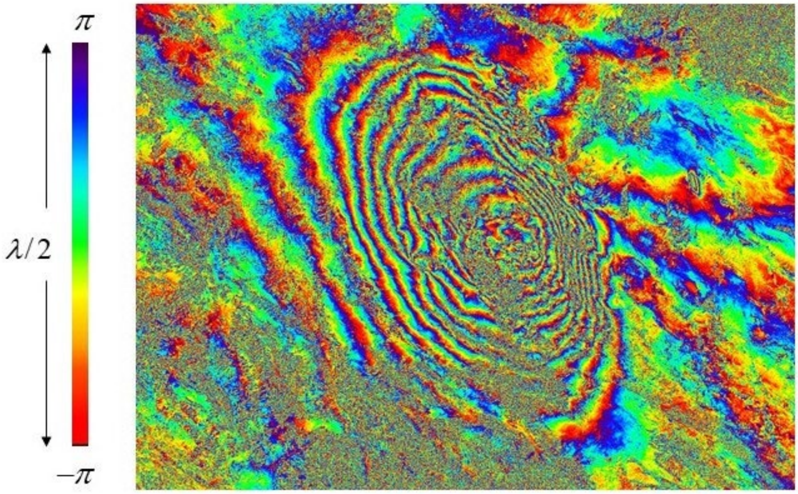

Fig. 17 - Co-seismic interferogram relating to the earthquake that struck the city of L'Aquila on 6 April 2009 and obtained with CSK SAR images acquired on 4 and 12 April 2009 along ascending orbits, (REA-CNR, 2021).

to very bright depending on their roughness and moisture content. Typically, rough soil appears bright in the image and for similar soil roughness, the surface with a higher moisture content will appear brighter. Hence, as a good rule of thumb, the higher the backscattered intensity, the rougher is the surface imaged. Moreover, amplitude images are characterized by the discussed distortions, Fig. 14, due to the acquisition geometry and geometrical characteristics of the scene. Thus, exploiting A_{mp} is possible, through InSAR algorithms, to recognize specific points on the Earth surface called Scatterers. There are two types of Scatterers, named Persistent Scatterers (PSs on plural, PS on singular) and Distributed Scatterers (DSs on plural, DS on singular). PSs and DSs are single, or group of scatterers placed on the Earth surface, respectively, characterized by high phase coherence over time. PSs generally refer to parts of buildings or structures and can be used to monitor the behaviour of a specific structure.

The second term in Equation (8), specifically $\frac{4\pi}{\lambda} \cdot r(x', r')$, is the phase information and is used to generate interferograms. The interferogram is the data matrix obtained from the comparison between two SAR acquisitions of the same area and contains, for each unit, the phase difference information related to the various contributions that generate the phase value in each image. These products allow to estimate the displacement of the Scatterers through specific algorithms named Differential Interferometry Synthetic Aperture Radar (DInSAR) and Multi-Temporal Interferometry Synthetic Aperture Radar (MTInSAR).

1.1.4. DInSAR algorithms

The most important information for InSAR techniques is φ. Its value is considered as the sum of few components:

$$\varphi = \psi + \frac{4\pi}{\lambda} r + \alpha_{atm} + n_{noise} \tag{9}$$

where ψ, is due to the reflectivity of the target, r, is the distance between the target and the sensor, α_{atm}, is the atmosphere component, and n_{noise}, is the noise component due to the acquisition system. φ of a single SAR image is pointless because it is impossible to discriminate one contribution from another to define the distance between the sensor and the target. However, if two SAR acquisitions relating to the same area are available it is possible to use the phase information contained in them to calculate the displacement of a scatterer in a time interval (i.e., the time shift between the two acquisitions, called temporal baseline). This technique is known as DInSAR. Indeed, by subtracting φ of one image (slave image) from the other one (master image) an interferogram is generated in the (x',r') plane. The phase difference $\Delta\varphi$ can be written as the sum of different contributions:

$$\begin{gathered} \Delta\varphi = \Delta\varphi^{topography} + \Delta\varphi^{noise} + \Delta\varphi^{atmosphere} + \\ + \Delta\varphi^{orbit} + \Delta\varphi^{displacement} \end{gathered} \tag{10}$$

$\Delta\varphi^{topography}$ is related to the topography and is accounted considering the perpendicular baseline of the interferogram (the distance between the two satellite orbits of the acquisitions is called perpendicular baseline) and an accurate digital elevation model (DEM) of the scene. $\Delta\varphi^{noise}$ is the decorrelation noise and can be divided into spatial and temporal decorrelation. Spatial decorrelation happens for high perpendicular baseline values, while temporal decorrelation for different electromagnetic properties of the in slave and master images. $\Delta\varphi^{atmosphere}$ accounts for different atmospheric conditions, and $\Delta\varphi^{orbit}$ regards the inaccurate orbit knowledge. $\Delta\varphi^{displacement}$ is obtained by removing the stated contributes and is equal to:

$$\Delta\varphi^{displacement} \approx \frac{4\pi}{\lambda}\Delta_r(x', r') = \frac{4\pi}{\lambda} \cdot d_{LoS} \tag{11}$$

From Equation (11) the displacement of a point in the image along the LoS, d_{LoS}, is equal to:

$$d_{LoS} = \frac{\Delta\varphi^{displacement}}{2\pi} \cdot \frac{\lambda}{2} \tag{12}$$

Equation (12) suggests that InSAR technique can track displacements up to a quarter of λ, for $\Delta\varphi$ equal to 2π, because φ value of the interferogram is in $[-\pi; +\pi]$ range. This is reflected in a measurement ambiguity, as explained in Fig. 18. In this figure, d is the distance travelled by the wave in a complete cycle, d_M is the displacement measured in the $[-\pi; +\pi]$ range, and d_{LoS} is the displacement along the LoS. In case (1), $d_{LoS} = d_M < d$ and the system capture d_{LoS} without ambiguity. In case (2), $d_{LoS} = d_M + d > d$ but φ is useful to capture the d_M value only and this is called measurement ambiguity. Hence, case (1) and (2) are equivalent because the system registers only a d_M value. To avoid mistakes in evaluating the displacement of the target d_{LoS} it is necessary that between the master and the slave images the target does not undergo displacements greater than d. This means that DInSAR techniques applied to data acquired by the CSK constellation, $\lambda \approx 3.1$ cm, is capable to measure d of 0.78 cm for two consecutive images. To solve this ambiguity, due to the so called “wrapped” interferogram, another step named “phase unwrapping” is required to recover the absolute value of $\Delta\varphi$.

The displacement measurements gathered from the interferometric analysis are differential in both time and space domain. Indeed, any measured movement is calculated with respect to the date of the master image (i.e., Reference Date) and with respect to

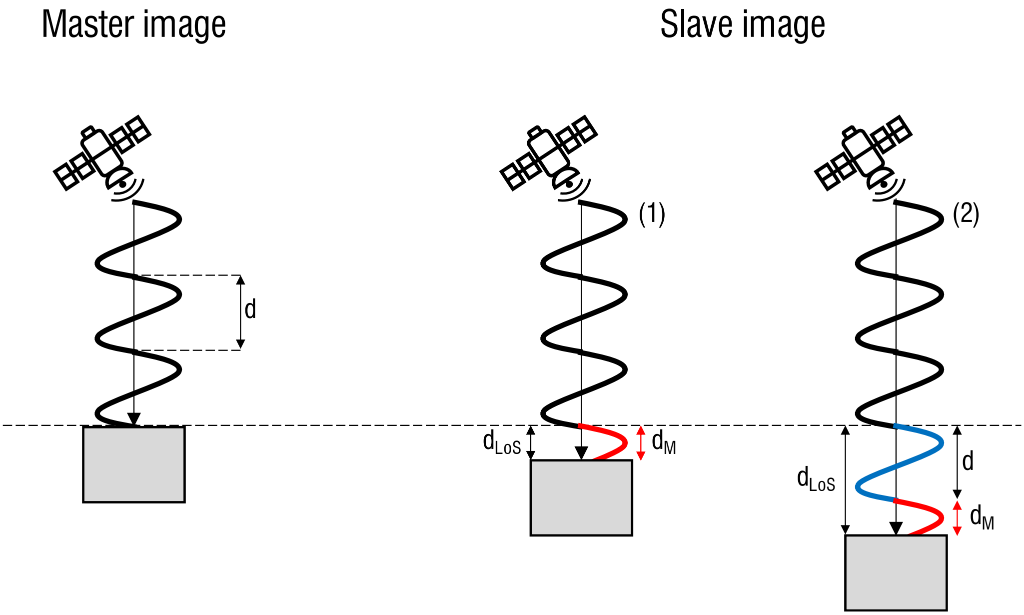

Fig. 18 - DInSAR displacement ambiguity.

a pixel (Reference Point), chosen in an area considered stable or of known deformation. Despite the ability to capture displacements in a millimetre scale, some limitations affect the DInSAR technique. DInSAR algorithms are susceptible to temporal decorrelation and atmospheric disturbances, which can degrade the quality of deformation measurements. To overcome these limitations, MTInSAR algorithms are used.

1.1.5. MTInSAR algorithms

MTInSAR algorithms, compared to DInSAR algorithms where input data is a couple of SAR images, take advantage of large SAR imagery datasets of the same area. The main differences between the several literature MTInSAR algorithms are the selected scatterers, PSs or DSs (in some cases both, as in Bovenga *et al*., 2004), and the selection criteria of the interferograms based on the temporal and perpendicular baseline. Each algorithm returns a displacement time series along the LoS for each scatterer. MTInSAR techniques can be classified into PS approaches, as PSInSAR, SqueeSAR, StaMPS, and Small Baseline (SB) approaches as SBAS-DInSAR.

Persistent Scatterer Interferometry Synthetic Aperture Radar, PSInSAR (Ferretti *et al*., 2001), is a PS technique based on the observation that a small subgroup of radar targets, the PSs, is immune to spatial and temporal decorrelation. These targets preserve phase coherence and are used to reduce the atmospheric phase contribution. PSInSAR technique assumes a single master image for the entire dataset, between M SAR images, and M – 1 slave images to generate M – 1 interferograms. Considering a dataset of 40 SAR images over a 2-year period, the d_{LoS} values are affected by an error of ± 5 mm and the average velocity along the LoS, V_{LoS}, by a ± 1 mm/y error if the reference point is closer than 1 km from the PS (TRE ALTAMIRA, 2009).

SqueeSAR (Ferretti *et al*., 2011) is an evolution of PSInSAR and provides an increased coverage of ground points, especially over non-urban areas where DSs are considered too along with PSs. The precision of the measurements provided by this technique are substantially consistent with those reported for the PSInSAR technique.

StaMPS (Hooper et al., 2004) and its evolution STAMPS/MTI (Hopper *et al*., 2013) is based on the scatterers with stable phase characteristics independent of amplitudes associated with man-made objects and is applicable to areas where conventional InSAR fails due to complete decorrelation of most scatterers.

SBAS-DInSAR (Berardino *et al*., 2002) relies on an appropriate combination of many interferometric pairs obtained from SAR with small perpendicular and temporal baselines. This assumption allows to minimize the spatial and temporal decorrelation and to increase the number of coherent points per unit area for which a reliable displacement measure can be provided. This technique is suitable for local- and large-scale analysis and thus takes full advantage of satellite data. The d_{LoS} values are affected by an error of ± 5 mm and the V_{LoS} by a ± 1 mm/y error.

Stable Point INterferometry even over Un-urbanized Areas, SPINUA (Bovenga *et al*., 2004), analyses input SLC images and a coarse DEM of the area under investigation. Slave images are co-registered, hence superimposed on the master image by using precise orbit information and the input DEM (Nitti *et al*., 2011). SPINUA adopts the MTInSAR processing chain, which is applied to generate a stack of differential interferograms calibrated to detect potential scatterers, both for PSs and DSs (Ferretti *et al*., 2001). After, an atmospheric phase filtering is applied to remove atmospheric and orbital artefacts. The obtained phase information for PSs and DSs candidates is combined with a robust kriging-based interpolation (Belmonte *et al*., 2017), providing a resulting image stack that is analysed to identify final scatterers and to estimate the height and LoS displacement time series. The reliability of the estimation is determined by inter-image coherence (or temporal coherence). Proper thresholds are identified on the base of the monitoring period, the number of images and their distribution in the perpendicular/temporal baseline plane. In the end, for each scatterer the main parameters and attributes are obtained (i.e., Latitude, Lat, Longitude, Lon, and V_{LoS}). An accurate parameter setting (e.g., the ones regarding the atmospheric phase contribute) allows for reaching an accuracy of 1÷2 mm/y for the V_{LoS} output, for points 5 km far from the reference point.

PS and SB techniques have some advantages and disadvantages. First, PS techniques use SLC images, at full resolution, while SB typically use multi-look characterized by a lower resolution. Second, PS techniques discard considerations about the temporal and perpendicular baseline, at the expense of the number of scatters, but SB techniques, although require an extra computation effort to proper select master and slave images for interferogram generation and combination of the interferogram stacks to obtain a displacement time series, can achieve a higher number of scatterers. Given the purpose of portfolio scale assessment, where wide areas are analysed, PS techniques are suggested to reduce the computational effort.

Concluding this section, each point PS/DS is characterized by the following attributes: georeferenced position, defined through Lat, Lon, and Height, according to the WGS84 geodetic reference system, LoS displacement time series, average velocity along the LoS, V_{LoS}, for the entire period and calculated as the slope of the Least Squares Regression line on d_{LoS} time series, and coherence. This latter parameter quantifies the consistency of the estimated LoS displacement time series with a mathematical model based on φ used in the specific algorithm. Coherence value ranges between 0 (low coherence, not reliable result) and 1 (high coherence). In structural monitoring applications, to avoid unreliable estimates, a threshold should be fixed for this attribute,

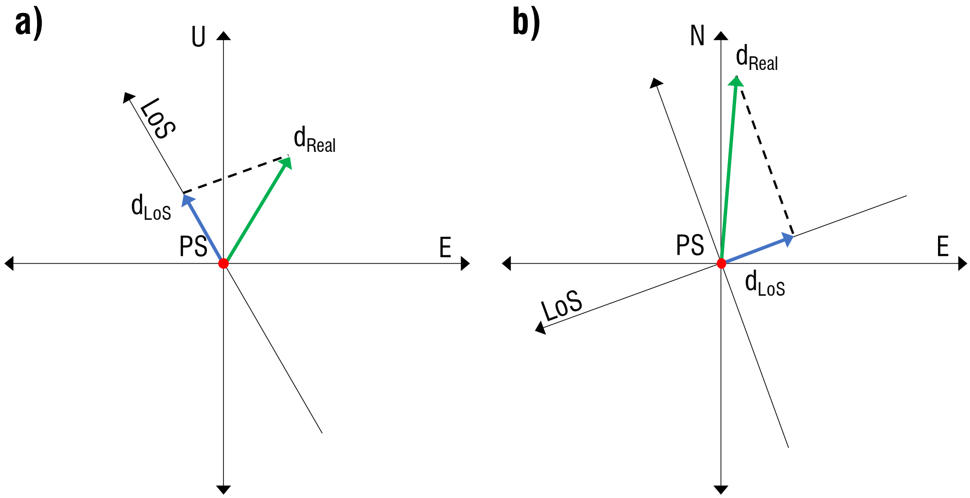

Fig. 19 - Projection of the real displacement, d_{Real}, along the LoS d_{LoS}. View on (a) Up-East plane (U-E, *U* is the Vertical direction in WGS84), and (b) N-E plane.

depending on the type and the quantity of data at disposal. the LoS displacement represent the projection of the real displacement along the LoS itself (Fig. 19). Hence, due to satellite near polar orbits, it is not possible to evaluate displacements occurred along the N-S direction (Fig. 19b), while results can be reliably obtained in W-E direction. Finally, for convention of sign, a positive value of the LoS displacement is assigned if the detected motion approaches the satellite along the LoS direction.

1.2. MTINSAR for structures and infrastructures

In this section, a short description on the applications of MTInSAR for structural near-continuous monitoring is provided. As the main field of application, MTInSAR procedures are suitable for studying slow kinematic phenomena, such as landslides (Infante *et al*., 2019; Luo *et al*., 2021) and subsidence (Blasco *et al*., 2019; Orellana *et al*., 2022) occurring in large areas. Several studies apply MTInSAR to monitor transportation infrastructure networks. For example, Fiorentini *et al.* (2020) focused on mapping and predicting the surface movement of road infrastructures over a wide area in the Province of Pistoia, Italy. Macchiarulo *et al*. (2022) proposed a semi-automatic GIS integrated methodology, whose capability was demonstrated on two real case studies in United Stated and Italy. MTInSAR is also used to identify the effects of landslides and subsidence on the existing building stock. Di Carlo *et al*. (2021) discussed about the settlement evaluation of two case studies of RC buildings in Rome, Italy, by means of CSK imagery collected along ASC and DSC orbits. Miano *et al*. (2021) and Infante *et al*. (2019) use numerical models for infilled RC frame buildings to find a numerical correspondence between the landslide-induces displacements measured via MTInSAR and the damages detected on the buildings. Other studies deal with MTInSAR monitoring of critical structures such as dams (Milillo *et al*., 2016; Scaioni *et al*., 2018). On the other hand, of interest for the scope of this paper are the works using MTInSAR for bridge monitoring.

Moving on bridge SHM, and looking at bridge portfolios, Peduto *et al*. (2018) formulated a procedure to investigate bridge settlement-induced damages via empirical fragility curves in Amsterdam city which are calibrated by using MTInSAR measurements and damages detected on site. Nettis *et al*. (2022) proposed a methodology based on an automatic geoprocessing pipeline, aimed at automatically interpreting bridge-specific displacement scenarios and for providing monitoring/assessment priority classes via MTInSAR. The methodology was applied to two highway networks in Italy by using SEN1 and CSK satellite datasets. Del Soldato *et al*. (2016) monitored a roadway multi-span RC bridge in the harbour of Valencia, due to opened joints and damaged pavement in the abutment-embankment transition area. The InSAR analysis was used to show values of displacements higher than 20 mm in a four-year range period. Hoppe *et al*. (2019) presented two post-tensioned bridges in Virginia, U.S., monitored through TerraSAR-X data. The results of the investigation showed that there was not any evidence of permanent bridge deformations. Giordano *et al*. (2022) used satellite data and principal component analysis for purpose of bridge damages detection. Authors developed a framework, which evaluated displacement time histories by removing environmental conditions. The effectiveness of the method was assessed by applying the proposed methodology on a real steel truss bridge located in the Rome area, which was subjected to subsidence-induced deformations. Markogiannaki *et al*. (2022) investigated MTInSAR potentialities to support bridge visual inspections, through an application on a bridge located in Greece. D-TomoSAR advanced technique was employed to achieve crucial conclusions on the performance and traffic capacity of the asset. Decoupled displacements suggested an evolving deformation of 1.8 mm/year for an absolute value of 9.5 mm that, according to authors, can be related to evolving degradation phenomena, as confirmed by on-site inspections.

Other studies focus on analysing the thermal behaviour of a given bridge based on MTInSAR measurements (Huang *et al*., 2017; Huang *et al*., 2018; Lazecky *et al*., 2017; Jung *et al*., 2019). For instance, Cusson *et al*. (2018) and Cusson *et al*. (2021) applied RADARSAT-2 data and on-site sensor-recorded temperature to evaluate the structural behaviour of a bridge located in Canada. The bridge finite element (FE) model was used to apply recorded temperature data for evaluating the bridge thermal sensitivity to longitudinal displacements. Using a linear regression, the same parameter was also evaluated on satellite displacements. The InSAR displacement thermal sensitivity data was then evaluated and matched between the two elaborations.

Some studies focus on the identification of displacement precursors of bridge collapse. For example, Selvakumaran *et al*. (2018) analysed an arch bridge in U.K., partially collapsed after a period of severe rainfall and flooding. Analysing the LoS displacement time series of the points located near the collapsed pier, authors identified as displacement outliers the last two acquisitions before collapse. The outlier definition was based on the statistical analysis of the displacement data, giving high relevance to the values exceeding three times a fixed interquartile range. Farneti *et al*. (2022) dealt with a framework to evaluate displacements in multi-span bridges by means of MTInSAR. Starting from the decomposition of LoS displacements to longitudinal and vertical components, they accounted for systematic and random errors, depending on the precision of the first LoS measurements and the plane in which the deformation was assumed. The methodology was applied to the Albiano-Magra Bridge, exploiting a five-year period of satellite data. Macchiarulo *et al*. (2022) identified several PSs with V_{LoS} values lower than - 6 mm/y in the area near the Himera viaduct, which partially collapsed in 2015. Of interest are some studies about the Polcevera Viaduct (Genova, Italy) collapse. Milillo *et al*. (2019) and Milillo *et al*. (2020) employed a modified version of a MTInSAR algorithm to evaluate relative displacements, observed over the five-year period before the collapse and referred to a reference point belonging to the bridge deck. In this way, authors focused on differential displacements along the suspended part of the bridge, which resulted to present a maximum velocity of 14.1 ± 7.5 mm/y. Instead, Lanari et al. 2020 recorded, by a different algorithm, a lack of coherent scatterers in the central part of the bridge affected by nonlinear displacements, evidence attributed to vibration effects and wind.

At the end of the literature review, the reasons provided at the end of section 1.1.3 are confirmed motivating the use of InSAR for bridge monitoring. First, this approach requires a relatively low-cost information source, considering that, for example, SEN data are completely free (Copernicus, 2020). Second, depending on the microwave sensor band, X or C, a different spatial resolution and measurements accuracy can be achieved, which make the InSAR techniques suitable for both large and local scale analysis. Finally, a multi-year stock of data is available for analysis (limited by constellation activity period), which allows users to assess possible events on the focused area counting on an acquisition frequency spanning from 6 to 14 days. Most of the reported research studies focus on well-known or well-defined case studies to investigate the use of SAR data from a single facility perspective. Hence, such techniques might not be extensively generalizable for bridge portfolios monitoring applications. For this reason, with the aim to overcome these limitations, an early warning system is proposed and implemented in a Python module, to be used on a specific bridge typology, simply supported concrete girder bridges, as the most spread in Italy.

1.2.1. MTINSAR-based early warning system: a framework proposal

In this Section, the framework of the proposed MTInSAR-based early warning system for purpose of bridge monitoring is reported. The main aim of the procedure is to provide a support for the structural near-continuous monitoring via MTInSAR, by exploiting and elaborating other poor data. This can confer a standardized and reproducible approach for the considered structural typology (i.e., simply supported concrete girder bridges). The proposed framework is structured as reported in Fig. 20. The

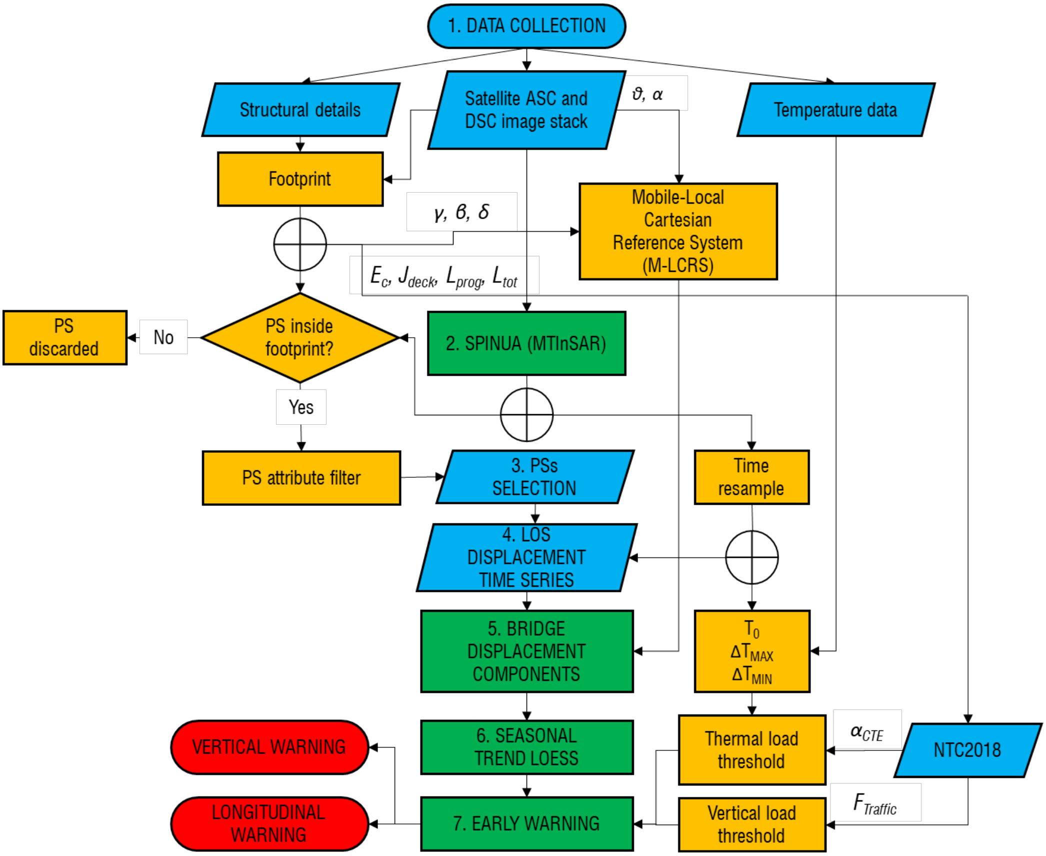

Fig. 20 - Workflow of the proposed MTInSAR-based early warning system framework.

idea behind the procedure is also covered by the Italian patent request n. 102024000002389, entitled "Metodo di early-warning per predire il comportamento strutturale di ponti esistenti basato su dati MTInSAR", date of filing 06 February 2024.

1.2.1.1. Data collection

Single or multi-span simply supported RC girder is the most spread constructive typology for existing bridges built in the period 1950-1990 in Italy as shown in the Introduction (Fig. 4c and Fig. 6a). Span length can extend up to 40-50 m, and they are built through cast-in-place elements (generally) up to 30 m, while prestressed beams are used for longer span length. Usually, the superstructure is characterized by longitudinal girders connected by transverse beam elements (diaphragms) and an RC slab. To transfer forces and displacements from superstructure to substructure components, such as piers and abutments, bearings devices are used. In simply supported girder bridges, expansion joints allow relative displacements and rotations between adjacent decks under service loads, while guaranteeing continuity of the road surface for the comfort of travellers. Considering service conditions, as the ones in which no hazards occur, simply supported RC girder bridges present deformations in longitudinal, transverse, and vertical directions. With a certain degree of simplification, the vertical displacements can be related to traffic loads acting on the slab, and gravity loads, while longitudinal and transverse displacements are mainly related to the environmental conditions (e.g., temperature and solar radiation). Longitudinal displacements are mostly concentrated in the support zones, while the transverse displacements can occur from the bridge centreline to the end of the transverse section.

The proposed framework is based on the analysis of such displacement patterns which are characteristics for simply supported girder bridges. To develop the proposed framework, some initial information is required. In detail, satellite data are required as well as a generic MTInSAR algorithm. With this regard, image stacks acquired according to both ASC and DSC acquisition geometries are needed for a given period at disposal. Since bridge monitoring via satellite data requires a high level of spatial detail and displacement accuracy, the use of satellite imagery acquired with the highest available resolution is recommended (e.g., CSK X-band sensor data working in StripMap HIMAGE mode) as in Hoppe *et al*. (2019).

Still, to apply the framework to a specific bridge, the knowledge of poor, easily accessible, structural details is required. As minimum requirements about the information to gather, it is necessary to dispose of (a) the bridge coordinates, to match satellite data with the position of the structure; (b) the height above sea level (a.s.l.); (c) the number of spans and the longitudinal-transverse dimensions of each span, to identify the planimetric extension of the structure; (d) the deck cross-section geometry, to identify the distribution of beam elements; (e) the number of bearings and their arrangement as movable and fixed supports. In the case in which beams are placed on unbonded old elastomeric supports, the higher the rubber layer, the greater its stiffness at the translation (with the same *G*), and then a smaller displacement is allowed. This information is easily accessible if original design documents and drawings are available. Indeed, from the management companies' point of view, such data should be available before to perform any type of prioritization procedure, as recommended by the Italian guidelines, IG (MIT, 2020). When the abovementioned structural data are lacking, some limitations can characterize the proposed approach and then some hypotheses must be introduced, by employing other sources of data. For example, beam RC cross sections could be assumed through a fast on-site survey. Obviously, the lack of information could reduce the reliability of the framework output, considering the necessity to account for some hypotheses.

Close to structural data, the last source of information to retrieve regards the temperature data, which is required to describe the bridge thermal behaviour (see Section 1.7.6). As showed in Fig. 20, temperature data are used to define the temperature on the first acquisition date, T_{start}, and the maximum and minimum temperature delta, ΔT_{MAX} and ΔT_{MIN} respectively. These constant temperature deltas, calculated as difference between T_{MAX} (or T_{MIN}) and T_{start}, are referred to the hottest and coldest satellite acquisition day. Ideally, this information should be captured by sensors placed on bridges to recreate the real temperature profile along the vertical section of the deck, possibly one acquisition for each span considering the different environmental conditions induced by the shade of the vegetation, which could reduce the solar radiation impact. In addition, the sensor sampling frequency should be equal to the satellite one. Since few bridges are equipped with these types of sensors, another source of temperature data could be explored, that is the one obtained from close weather stations. To define reliable estimates, the distance between the station and the facility should not exceed the 10 km, to foster the representativeness of data, especially for complex topographic areas. This solution is less accurate than the sensors-based one, because air temperature is different from the one registered on the road pavement, and the solar radiations influence the deck temperature profile. A third option is given by the application mathematical models, as the cosine temperature model (Mahaffy, 2012). This latter, fitted over weather station data, could help to reconstruct the temperature values along the interested period.

1.2.1.2. SPINUA Interferometry analysis

For the application of the proposed framework in this research work, results of SPINUA results of SPINUA algorithm were used. Nevertheless, as explained in Section 1.1.5, PS techniques are suggested. Furthermore, the use of only PSs is suggested given that: (a) DSs refers to more pixels than PSs and is not sure that MTInSAR algorithm groups pixels of bridge areas characterized by the same structural behaviour (i.e., those close to pinned and roller supports); (b) considering the overall dimensions of the bridges, very few DSs belonging to the bridge could usually be identified, making the further analyses statistically inconsistent.

1.2.1.3. Bridge footprint definition and PS selection

Once satellite images are elaborated and PSs are recognized through an MTInSAR algorithm, this step of the procedure aims to select a subset of PSs for extracting bridge deformation information. The first PS attribute to evaluate is the planimetric position, which is identified by Lat and Lon. Such quantities can be used under the, herein named, '*POS'* criterion, which aims to recognize if the PS is placed inside or outside of the bridge footprint. This operation is not straightforward, considering possible errors in the geolocalization of the PSs and of the footprint. In general, the footprint localization and its dimensions should be available on the original design drawings. Otherwise, a free repository of geospatial data collected via shapefiles, e.g., OpenStreetMap (OSM, 2024), can be used to effectively retrieve the bridge position (Macchiarulo *et al*., 2022; Nettis *et al*., 2022). The same database can be used to find the bridge width. Indeed, each line feature stored in the OSM database is provided with the width of the street, which can be assumed, with a satisfying degree of approximation, equivalent to the bridge deck. The position of the footprint and the position of the PSs are characterized by inaccuracies, which are different for the two data sources. Hence, to manage this matching operation, it is assumed for simplicity that the footprint position is correctly identified, and a homothetic buffer zone can be fixed, by using a width equal to the resolution of the cell dimension. This choice is justified by the definition of a PS, because it is unique within the resolution cell and its real position can be somewhere inside the pixel (Calò *et al*., 2023). According to Peduto *et al*. (2018) and to REA-CNR (2023), a 3 m buffer for CSK dataset is suggested when for StripMap HIMAGE mode is used (resolution cell of 3 x 3 m is denoted). Comparing the PS position with the buffered footprint may lead to select PS that do not actually belong to the bridge. This phase is paramount especially in urban contexts, where high PS densities are achieved. To refine the PSs selection, other attributes contained in the dataset can be employed (see Section 1.1.5), to complete the selection through other criteria:

- '*H_GEO*', which compares the height attribute of each PS to the bridge information about height a.s.l. As pointed out by Talledo *et al*. (2022), since PS position is evaluated with respect to that of the reference point, a potential uncertainty in its estimation has a uniform impact on all PS. Hence, all pixels could be affected by the same rigid translation whose value can be different for ASC and DSC dataset. This height shift is computed as the difference between the bridge height a.s.l. (or its average value if it is sloping) and the PS average height. The PS is selected if its biased height value is comprised between the bridge height above computed, added and subtracted from a quantity related to PS height uncertainty, as explained in Section 1.2.1.1. For CSK datasets, this value amounts to 1 m.

- '*COH*', which excludes PS characterized by coherence values lower than a fixed threshold. This threshold should be empirically set up by considering the characteristics of the processed image dataset, such as the number of SAR acquisitions, the overall time interval, and the sampling time of the available acquisitions (Mele et al., 2022). The available literature suggests assuming coherence threshold values ranging from 0.45 to 0.8 (Milillo et al., 2019; Di Carlo et al., 2021; Lazecky et al., 2017; Cusson et al., 2018; Cusson et al., 2021; Milillo et al., 2020).

- '*V_LOS*', which evaluates the distribution of V_{LoS} attribute and returns only points whose V_{LoS} value is between 5% and 95% percentile. With this regard, Giordano *et al*. (2022), assuming the V_{LoS} standard deviation (σ_{LoS}), employed a threshold of $\pm\ 2\sigma_{VLoS}$ to discriminate PS belonging to the structure. The σ_{VLoS} value was referred to the V_{LoS} values estimated over 2 years for which the bridge is considered in a healthy state. Since neither prior information are required nor preliminary evaluations are performed about bridge healthy state, a larger threshold is fixed to prevent information loss gained by PS characterized by high V_{LoS} values.

A combination of the presented criteria could also be considered for densely populated datasets, paying attention to not excluding representative points and not excessively reducing the number of available PS for the applicability of the next steps. The authors suggest linking all the above criteria in a hierarchical order as follows: '*H_GEO*', '*COH*' and '*V_LOS*'. The '*H_GEO*' criterion is considered as important as the '*POS*' one because it is also related to the bridge location, and for this reason should be used as first. Secondly, a coherence threshold equal to 0.65, according to the specific SPINUA recommendations, must be fixed to avoid PS do not adhering to the adopted φ model in the MTInSAR algorithm. Lastly, '*V_LOS*' could be used to exclude PSs characterized by high-velocity values, which are reasonably not representative of the possible undergoing phenomena (e.g., values ten times higher than the average). It is worth noting that the proposed approach to select PSs does not involve specific clustering techniques (e.g., K-means), which could be especially used for large-scale monitoring of structures in urbanized areas. For example, Mele *et al*. (2022) proposed the Density-Based Spatial Clustering of Applications with Noise clustering technique, which allows a sub-optimally attribution of PSs to specific buildings in aggregate contexts.

1.2.1.4. LoS displacement time series

Once the PS candidates are selected, the phase for computing displacement time series can be initialized. The first step involves the interpretation and the combination of the ASC and DSC dataset acquisitions, which are available for different PSs. Indeed, the PSs from ASC and DSC geometry are different because the points recognized by the MTInSAR algorithm on these image stacks do not overlap. This happens for at least two reasons. First, the satellite images are different due to the satellite right look view in both geometries which makes the scene different. Second, image distortions are different, as well as the ϑ angle. Therefore, the identification of unique PS pairs is required to represent the same point in the scene. Di Carlo *et al*. (2021) suggested comparing the mutual distance between PSs with the position accuracy and selecting PSs presenting the first parameter lower than the second one. This approach was provided for the purpose of building applications, but it cannot be applied to the bridge case. Indeed, in the case of mismatched points, despite the mutual distance is lower than positioning accuracy, the PSs could belong to some parts of the bridge, which may be characterized by a different displacement behaviour (e.g., one PS is located above a fixed bearing, and one is located above a movable one). To overcome this problem, a position-based clustering method is proposed, which neglects PS geopositioning errors. The footprint is divided according to the span positions concentrating half extra bridge length, due to *'POS'* criterion, to the side spans (or to the only one if a single-span bridge is analysed). Then, the span is considered as a reference unit and its centroid is characterized by the average displacement time series of all previous selected PSs falling within it. In this way, the influence of the false-positive PSs representing points outside of the bridge is minimized.

Depending on the number of PSs in each dataset and on their spatial distribution, a more refined subdivision can be processed, as shown in Farneti *et al*. (2022) and Giordano *et al*., (2022). This subdivision can be processed to define homogeneous sub-regions in terms of expected structural behaviour. Hence, the footprint of each span should be divided along the side of the longitudinal axis into sub-regions, with a minimum of 3 parts. Given the investigated structural typology, of interest are the parts close to the bearings, which behave in a certain way under service conditions and the central parts (e.g., middle-span), which differently behave from the previous ones (see Section 1.2.1.7). Obviously, the resulting sub-region size cannot be lower than the satellite image resolution since PS is unique within the resolution cell. In the case of high PS density, a further subdivision can be performed, orthogonally to the one just defined. Again, this additional subdivision must be avoided for a deck having a width lower than twice the resolution of the cell. The main difference between these analysis solutions lies in the hypothesis on the transverse behaviour of the viaduct. In the case of transverse subdivision only, the flexural behaviour of the deck is assumed to be described by the hypothesis of infinite flexural stiffness of transverse diaphragms in their own plane. This implies the absence of differential displacements between the two outer regions of the transverse subdivision. Conversely, also considering the longitudinal subdivision it is possible to assume that differential displacements occur.

Another aspect to highlight is the time shift occurring among ASC and DSC acquisitions. This is due to the operativity of the adopted sensors, which is characterized by two orbits that do not revisit the same scene on the same day. To address this difference in terms of time, the first solution is the one proposed by Talledo *et al*. (2022), which resampled one time series on the temporal baseline of the other one, by using a linear interpolation of the missing values. This solution is reliable for two datasets presenting a low time lag between them (e.g., SEN datasets with six-days of time interval) and a regular sampling frequency without missing values. A second option is provided by Nyquist-Shannon theorem, which can be applied to resample a non-uniform sampled series, starting from the average sampling time. The main disadvantage of the above techniques lies in the loss of real acquisitions from one of the two datasets. To overcome this limitation, another resampling approach can be mentioned, where both acquired time series are merged to consider an “enlarged” temporal baseline. This latter extends from the further last acquisition to the closer first acquisition and missing values are estimated through a linear interpolation among consecutive measures. The criterion to select the first and the last dates is not random, and it is formulated to avoid interpolations where data are missing (e.g., back interpolation from closer to further dates). In this way, the information contained in all the acquisitions is preserved and the new values are coherent with the acquisitions. This approach was adopted in the proposed framework, and it also considers the possibility that the initial acquisition, in one of the resampled time series, is characterized by a non-null displacement value. As suggested by Di Carlo *et al*. (2021), in this case, the entire time history can be depurated from this non-null displacement value.

At this point, ASC and DSC displacement time series could be combined, but some considerations should be highlighted starting from LoS values. Assuming for the sake of simplicity, that both acquisition geometries present the same ϑ angle, if V_{LoS} values have the same magnitude and the same sign, the PS is moving upwards or downwards, depending on the LoS acquisition sign and the abovementioned sign convention. Instead, in case of opposite signs between measures, the movement is along E or W. In most cases, ASC and DSC displacement vector modules are not characterised by the same values and the result is like the one shown in Fig. 21. This observation can be used with ASC and DSC V_{LoS} values to estimate the prevalent displacement component over the observation period, although not very accurate.

Finally, it is worth specifying that each displacement measure (along the LoS, for both acquisition geometries, and the ones derived from further elaborations) is referred to the master image, which, in turn, reflects an initial specific deformed shape that is unknown. If on one side, the information about the initial deformed shape could be important, on the other side, the proposed procedure aims at assessing the evolution of the deformation over time. Hence, as can be observed later (see Section 1.2.1.7), the comparison of the deformation with the proposed limits could reveal the occurrence of permanent anomalies, which do not depend on the initial deformed shape.

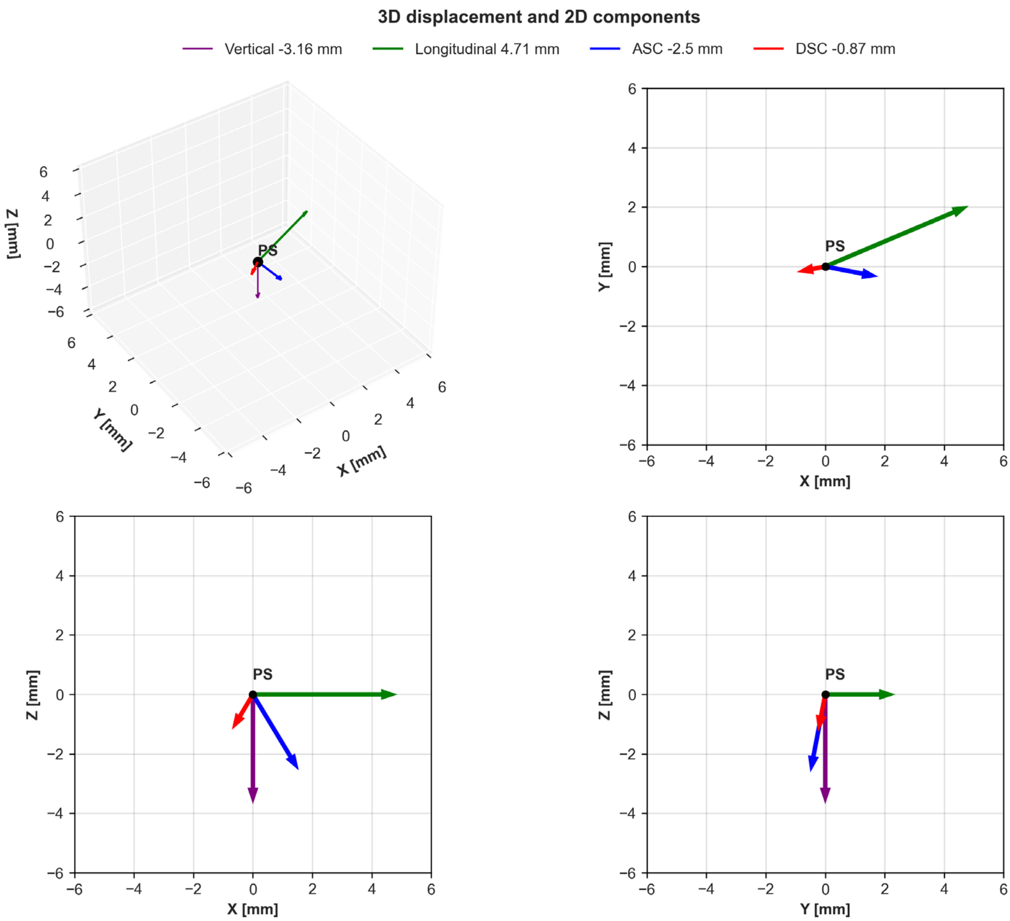

Fig. 21 - ASC (blue vector) and DSC (red vector) LoS displacement vectors combination resulting in longitudinal (green vector) and vertical (purple vector) components. Although cartesian reference system is drawn, X is referred to West-East (W-E) direction, Y to North-South (N-S), and Z to Vertical (U) direction. On top-left corner is shown a 3D representation of the mentioned vectors, on the top-right the 2D projection on X-Y plane. On the bottom, from left to right the 2D projections on X-Z and Y-Z planes.

1.2.1.5. Displacement time series analysis for bridge monitoring

Having at disposal ASC and DSC satellite imagery, the MTInSAR technique is used to retrieve the LoS displacement, d_{LoS}, whose magnitude is the result of the real displacement, d_{Real}, projected along satellite LoS, as shown in Fig. 19. It is worth strengthening the necessity to combine the two acquisition geometries for the purpose of structural performance assessment via MTInSAR data. In fact, considering only one acquisition geometry, the only presence of different V_{LoS} values (e.g., positive and negative) for spans with the same geometry and orientation is not enough to identify an evolving undesired structural behaviour possibly related to subsidence or landslide. As for example, in the case of Albiano-Magra Bridge (Farneti *et al*., 2022), the V_{LoS} values of PSs located on the last two spans on the right-hand side had a greater magnitude compared to the other ones, but this information did not provide a reliable identification of an evolving deformation pattern which can be connected to a specific structural anomaly. Instead, by combining the two geometries, an upward displacement was identified, and it was related to a specific slow ground movement due to the activation of a landslide (that is probably the potential cause of the Albiano-Magra Bridge collapse). For the case at hand, LoS displacements, d_{LoS}, can be referred to the Reference System defined by W-E, N-S, and U directions. Equation (13) shows d_{LoS} as the product of its components along the above-mentioned Reference System, d_{Real} vector, and directional cosines of the LoS direction in the Reference System, stored in the $\hat{u}_{LoS}$.

$$d_{LoS} = \hat{u}_{LoS} d_{Real} \tag{13}$$

$$\hat{u}_{LoS} = [sin\theta cos\alpha; -sin\theta sin\alpha; cos\theta] \tag{14}$$

$$d_{Real} = [d_E; d_N; d_U]^T \tag{15}$$

Hence, substituting Equation (14) and (15) in Equation (13), d_{LoS} is equal to:

$$d_{LoS} = d_E sin\theta cos\alpha - d_N sin\theta sin\alpha + d_U cos\theta \tag{16}$$

where α is assumed positive clockwise from E to ground range and ϑ is the angle between U and LoS direction (Fig. 12a). On this base, some assumptions can be fixed to derive the displacements of the bridge superstructure under service conditions. First, assuming to neglect thermal transverse displacements (in most cases transverse displacements are negligible with respect to longitudinal ones), the possible degrees of freedom for the bridge are defined in a vertical plane described by the bridge vertical and longitudinal directions. Second, in view of developing an output-only methodology, no information about geo-hazards, like landslides phenomena, is known prior to the assessment. If such phenomena have occurred during the observation period or are still active, the proposed approach will provide a deviation between the monitored behaviour of the bridge and the expected one. Hence, under this second hypothesis, the real displacement can be assumed along the directions defined by bridge service conditions (e.g., thermal and traffic/gravity loads). d_{LoS} can be described with respect to a Mobile-Local Cartesian Reference System (M-LCRS) fixed in the centroid of the considered reference unit and below described. This M-LCRS is created by assuming the Longitudinal (L) direction parallel to bridge/sub-region main longitudinal axis, the Vertical (V) direction defined by a normal vector to road pavement (Fig. 22), and the Transverse (T) direction to complete a right-handed cartesian reference system. The change of reference system from E-N-U to L-T-V, leads to re-write Equation (15) in:

$$[d_E; d_N; d_U]^T = R_V R_T R_L [d_L; d_T; d_V]^T \tag{17}$$

where:

$$R_V = \begin{bmatrix} cos\gamma & sin\gamma & 0 \\ -sin\gamma & cos\gamma & 0 \\ 0 & 0 & 1 \end{bmatrix} \tag{18}$$

$$R_T = \begin{bmatrix} cos\beta & 0 & sin\beta \\ 0 & 1 & 0 \\ -sin\beta & 0 & cos\beta \end{bmatrix} \tag{19}$$

$$R_L = \begin{bmatrix} 1 & 0 & 0 \\ 0 & cos\delta & sin\delta \\ 0 & -sin\delta & cos\delta \end{bmatrix} \tag{20}$$

Hence, d_{LoS} is equal to:

$$d_{LoS} = \hat{u}_{LoS} R_V R_T R_L [d_L; d_T; d_V]^T \tag{21}$$

Equation (21) presents three unknown terms, that is, d_L, d_T, and d_V. These latter represent the components of the assumed real displacement along the new reference system axes. To find the three unknown values, three LoS acquisition datasets from different geometries should be required (e.g., imagery corresponding to a higher incidence angle or left-looking geometry, in addition to conventional ASC and DSC acquisitions). Considering that only two datasets (e.g., ASC and DSC) are usually available, one of

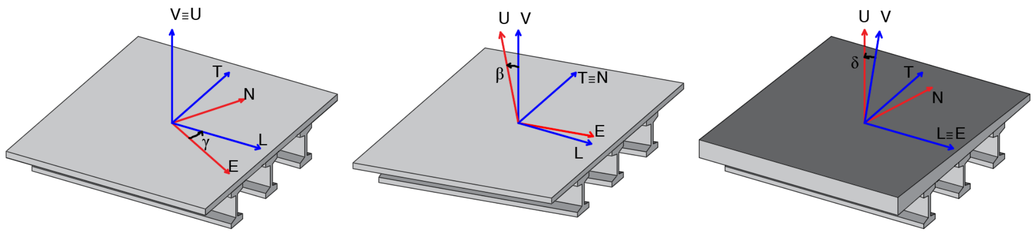

Fig. 22 - Coordinate Reference System (blue lines) and M-LCRS (red lines). Left span shows *γ* definition (roll), middle span shows *β* definition (pitch) and the right span *δ* definition (yaw).

the displacement components can be neglected to solve the system. Among the candidates, the negligible component is assumed the transverse one (d_T) since temperature effects are prevalent along the longitudinal direction (L). The two remaining unknows are calculated for each sub-region updating rotational matrices values (Equations 18, 19, and 20), according to sub-region directions, defined by the angles γ, β, and δ (Fig. 22). The above matrices describe the rotations R_V, R_T, and R_L along the local axis V, T and L, respectively. γ is considered positive from E to L clockwise, or negative if accounted counterclockwise, as well for β and δ from V to U. These angles are limited between 0° and 180°. The use of rotational matrices to project d_{LoS} along M-LCRS instead of simpler E-W direction allows estimating more accurate time series components of the bridge displacements, because are referred to the main axes of the bridge (REA-CNR, 2020). To conclude this step, the hypothesis of transverse negligible displacement is not valid in the cases of N-S orientation (or nearly N-S) since the LoS projection of the longitudinal displacements is almost equal to 0, due to the satellite acquisition geometry. In these cases, the transverse displacements can be evaluated and compared with proper thresholds referred to the abovementioned service condition. The described steps can be then repeated for each acquisition, to obtain L and V time series.

1.2.1.6. Seasonal trend decomposition

Given displacement time series in L and V directions for each sub-region, some considerations about the use of the data should be highlighted. To estimate bridge seasonal fluctuations, the magnitude of the displacements, and the trend of each component, a seasonal trend decomposition method is employed. Cleveland *et al*. (1990) proposed the method, herein named STL (seasonal trend decomposition based on LOESS) and depicted in Fig. 23. Using the STL approach, it is possible to derive from a displacement time series the trend T_r, the seasonal S_{eas}, and the remainder R_{es} components, according to an additive model, mathematically described as:

$$x(t) = T_r(t) + S_{eas}(t) + R_{es}(t) \tag{22}$$

To estimate all seasonal contributions, an iterative procedure is involved, whose main steps are reported as follows:

- Perform a weighted moving average (LOESS) on the original time series, to estimate the local trend.
- Depurate the estimated trend from the original time series and estimate the seasonality and noise components. This step can be iteratively performed to improve the accuracy of the seasonal estimation.
- Apply the LOESS algorithm to the seasonality and noise components, to estimate the local seasonality component. The local component represents trends that may differ from year to year, adapting to the specific conditions of the data under review.
- Derive the noise component, as the difference between the estimated seasonality component and the ones obtained from the previous step. The difference represents the residual decomposition error, named the remainder component.

Considering that STL method is applied to historical series characterized by a regular sampling frequency, but MTInSAR algorithms could provide irregular sampling frequency, a time resampling is required. Hence, to prevent data loss and simplify the definition of the next parameter, a one-day linear resampling is suggested. Moreover,

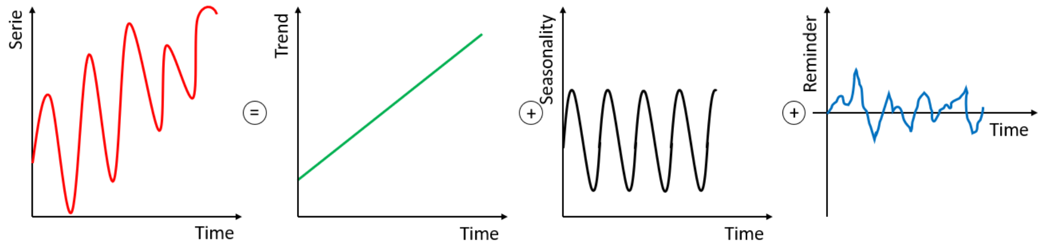

Fig. 23 - STL decomposition.

the number of observations describing the seasonal component is the second parameters to define and its value is fixed according to the sampling frequency of the time series.

Without evident structural damage, landslide or subsidence phenomena, the displacement time series should present seasonal fluctuations under service conditions (e.g., thermal and traffic/gravity loads), with an average value that can be assumed equal to zero (Giordano *et al*., 2022). However, since landslide and subsidence are common phenomena, part of the measured displacements can be related to the above geo-hazard components. Hence, the seasonal component is useful for understanding the bridge behaviour concerning service conditions, while trend components could give information regarding geo-hazards or ongoing structural damage.

1.2.1.7. Definition of early warning thresholds

Once displacement time series for bridge regions in both the bridge main directions are available together with their components, such outcomes can be compared with appropriate displacement thresholds. Those thresholds are defined to automatically check if the focused bridge conditions present an unexpected behaviour. Those thresholds are assumed for defining a sort of limit for the displacement components. It is worth noting that the output of the proposed procedure cannot be mistaken for a structural analysis of bridges in the investigated portfolio, but it can provide insights towards the ideal behaviour that bridges should exhibit during their service life. In addition, considering the impossibility of knowing prior real input loads, the output of the proposed methodology reveals the current performance and the displacement trend to compare with the imposed limit (i.e., threshold).

Looking in detail at the structural behaviour, satellite SAR sensors are not able to provide information about temperature (e.g., measure bridge surface temperature), as described by Goel *et al*. (2014), and the acquired imagery cannot provide traffic information (Hoppe *et al*., 2019). For this reason, external data sources are needed. As discussed on Section 1.2.1.7, temperature information regarding the bridge can be retrieved from on-site sensors (Cusson *et al*., 2018), weather stations located near the investigated facility (Cusson *et al*., 2018; Cusson *et al*., 2021), or calculated by mathematical models. Assuming this latter option, the model indicated as *T(m)* can be described as:

$$T(m) = A_T + B_T \cdot \cos\big(\omega \cdot (m - \phi_T)\big) \tag{23}$$

where A_T is the average annual temperature, B_T is the amplitude, ω is the frequency and it is obtained by assuming a reference period equal to 12 months, ϕ_T is the phase shift, and m is a day of the year expressed in months. B_T, ω and ϕ_T are equal to the average of their values obtained from one-year fittings for the length of the satellite temporal baseline. In each fitting, the average daily temperature is used. The average daily temperature is considered a good approximation of the bridge temperature since no sensor data are available or reliable acquisitions at the local solar time of the satellite pass.

The obtained values from the mathematical model in Equation (23), and T_{start}, T_{MAX} and T_{MIN}, as defined in Section 1.2.1.1, are used to calculate the displacements threshold due to temperature. This threshold can be compared with the seasonal longitudinal displacement component. Indeed, it can be derived from simple considerations related to the structural typology investigated. As a matter of fact, an analytical model related to simple supported beams can be employed and, according to the Italian Technical code (MIT, 2018), the threshold can be defined by means of the coefficient of thermal expansion for the concrete, named α_{CTE}, and usually assumed equal to 10E-06 °C^{-1} for the considered material. Assuming a constant temperature profile along the vertical section, the maximum thermal displacement, d_{Term}, is equal to:

$$d_{Term} = \alpha_{CTE} \cdot \Delta T \cdot L_{prog} \tag{24}$$

where L_{prog} is the progressive length of the sub-region from the fixed support and ΔT is the considered temperature delta. This threshold is computed for both temperature delta, ΔT_{MAX} and ΔT_{MIN}. The warning is raised if the longitudinal seasonal displacement time series of a span sub-region exceeds one of the values obtained from Equation (23). It is worth noting that traffic loads were not accounted for in the longitudinal seasonal threshold. Generally, traffic loads can induce a displacement in the longitudinal direction, especially when considering vehicle braking action. On the other hand, this effect depends on both the number of vehicles involved (e.g., resultant force to compute according to number of vehicles, the intensity of braking, the direction of vehicles) and the position/mechanical features of mobile supports. The above data are usually derived from specific sources of information (e.g., average daily traffic for the types of vehicles and periodic on-site surveys for supports), not always available, especially for the purpose of bridge portfolio assessment (that is, the main aim of the proposed procedure). In addition, it is worth reminding that: (a) SAR imagery cannot provide traffic information (see Hoppe *et al.*, 2019); (b) the traffic flow is uncertain with regard to satellite acquisitions. Both above points suggest that the two aspects cannot be neither statistically nor physically related for longitudinal seasonal components. Regarding the assumption of the simple analytical model described by Equation (24) and shown in Fig. 24a and Fig. 24b is clear that it completely ignores some structural details, such as the bearing stiffness. Although longitudinal displacement thresholds defined by the simple analytical model are greater than a FE model estimate that accounts for the stiffness of the bearings, some advantages are clear, such as the typical conservativism in a large-scale analysis and the no need to perform detailed FE models. Another useful information to describe the bridge health state is the alignment of seasonal longitudinal displacements component of span sub-regions. Indeed, for simply supported bridges, the mentioned seasonality is the same for sub-region upon fixed and mobile supports. It is worth noting that the above assumptions could be subjected to modifications, when considering deformable structures (e.g., Ponzo *et al.*, 2024), because

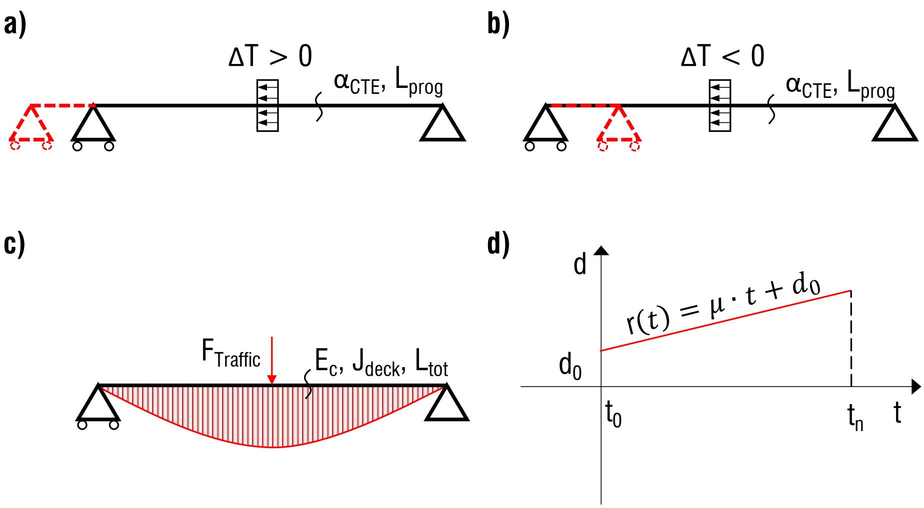

Fig. 24 - Thresholds analytical models: (a) longitudinal seasonal displacement threshold for positive temperature delta (in red the beam elongation); (b) longitudinal seasonal displacement threshold for negative temperature delta (in red the beam contraction); (c) vertical trend component threshold for material degradation, damage, and gravity loads, calculated with a concentrated force ($F_{Traffic}$) in the middle of the span and in red its deformed shape; (d) vertical trend component threshold for uniform and differential displacements.

the elevated deformability implies a reduction of the number of detected PSs and a loss of accuracy of the average displacement time series.

About vertical displacements, as just stated they are related to loads acting in the vertical direction (e.g., self-weight, traffic loads) and are influenced by material degradation and environmental conditions (e.g., temperature, subsidence). Exploring in detail each factor, gravity loads increase during the bridge service life and usually the effect for the considered structural typology is a higher vertical deflection at mid-span. Some causes could be identified for the increment of gravity loads, such as the replacement of old road barriers with new concrete jersey ones, or addition of new bitumen layers to the road pavement. At the same time, the increase in material degradation affects the vertical deflection of gravity loads, amplifying the vertical component of the time series. Also, environmental conditions could change the vertical deformation of the bridge, as occurs for the temperature excursion that produces a seasonal upwards or

downwards of the vertical deflection at mid-span in summer and winter, respectively. This effect is due to a non-uniform temperature profile along the vertical deck section and to the variation of the stiffness characterizing bearings. For the investigated bridge typology, the variation of the vertical component due to the temperature is limited and is also influenced by the solar radiation excursion. It is clear that this kind of information can be retrieved via a specific sensors-based system able to measure temperature variation over the vertical section of the deck, and this is not always possible. In addition, other boundary conditions affecting the bridges (e.g., subsidence, hydro-geomorphological actions) can produce uniform or differential displacements between the sub-regions of the same span (Cusson *et al*., 2018; Del Soldato *et al*., 2016). The observation of differential displacements can highlight the presence of other phenomena, such as discontinuities between abutment and embankment, or between the decks of two adjacent spans. Instead, uniform displacements reveal vertical discontinuity on structural elements.
Considering the different displacement scenarios and the impossibility to a-priori know the real input loads, two thresholds can be defined, associated to three bridge-specific displacement scenarios. First, for each sub-region a linear trend is fitted, according to the Least Squares Regression method, on the vertical trend component, T_r, as retrieved from Section 1.2.1.6. Then, the slope of the regression line, μ, is multiplied for the acquisition time interval to obtain a vertical cumulative displacement, δ_i, to be evaluated for each i^{th} sub-regions of each span.

Once defined δ_i and Δ_i, as the difference between δ_{i+1} and δ_i, the three bridge-specific displacement scenarios are:

- Increasing mid-span vertical deflection, $\delta_{mid\,span}$, due to material degradation and gravity loads described by $\Delta_{sx} = \sum_{i=1}^{(n-1)/2} \Delta_i \geq 0$, $\Delta_{dx} = \sum_{i=(n+1)/2}^{n-1} \Delta_i \leq 0$ and $\frac{(\sum_i |\delta_i|)}{n} \leq \frac{2|\delta_{mid\,span}|}{3}$. The last condition is necessary to differentiate this Scenario with the next one, where in this case (Scenario 1) the parabolic deformation of the span is more emphasized as observed in Fig. 25a.

- Subsidence, shown in Fig. 25b, where a uniform vertical displacement profile is described by $\Delta_{sx} \geq 0$, $\Delta_{dx} \leq 0$ and $\frac{(\sum_i |\delta_i|)}{n} > \frac{2|\delta_{mid\,span}|}{3}$. In this case the last condition is used to describe a quasi-linear deformation of the span.

- Differential displacement Fig. 25c) where Δ_{sx} and Δ_{dx} are both higher or lower than 0.

The output of the three above scenarios (Fig. 25) can be compared with the two thresholds. The first threshold, shown in Fig. 24c, is calculated as follows:

$$d_{service} = \frac{F_{Traffic} \cdot L_{tot}^3}{48 \cdot E_C \cdot J_{deck}} \tag{25}$$

where E_C is the concrete Young Modulus, J_{deck} is the moment of inertia around deck transverse axis, L_{tot} is the span length and $F_{Traffic}$ equal to 600 kN (established according to the Italian Technical code, MIT, 2018). The value of $F_{traffic}$ is the one used to perform structure-specific assessment for serviceability limit states. Still, the self-weight was not considered, because it is intrinsically considered in every satellite image. The second threshold, shown in Fig. 24d, is equal to 2 mm/y (as proposed in Nettis *et al.*, 2022), multiplied by the acquisition time interval. Regarding Equation (25), if information about material degradation and structural defectiveness is available, modified values of E_C and J_{deck} could be defined and the value of $d_{service}$ could vary. Nevertheless, two main aspects can be highlighted: (a) the quantification of the material degradation cannot be identified without results by a sensors-based system, which in turn makes the proposed procedure useless; (b) lower values E_C and J_{deck} would increase the value of $d_{service}$, making the threshold more conservative than the proposed value (especially in the case of Scenario 1).

Scenario 1 is compared with the first threshold, whose value considers the occurrence of both damage and material degradation. This displacement, which occurs under service conditions, is considered critical if recognized as inelastic deformation due to ageing, material degradation and gravity loads. Hence a warning is raised if $\delta_{mid\,span}$ observed by Scenario 1 exceeds $d_{service}$. Scenario 2 is achieved when the average value

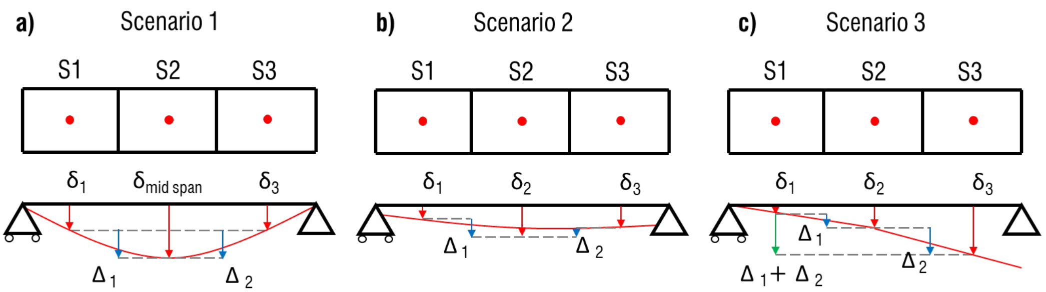

Fig. 25 - Vertical bridge-specific displacement scenarios. Each sub-region, named S1, S2 and, S3 (for a 3-transverse subdivision) is characterized by its centroid together with a vertical displacement δ_i. Differential displacements Δ_i are used on early warning evaluations.(a) Scenario 1, material degradation, aging, gravity loads; (b) Scenario 2, uniform vertical displacement (e.g., subsidence); (c) Scenario 3, differential vertical displacement.

of $|\delta_i|$ for a single span exceeds the second threshold. An average value of $|\delta_i|$ lower than the threshold highlights that the bridge is not subjected to critical displacements. Finally, a warning is raised for Scenario 3 when $\sum_i |\Delta_i|$ overcomes the value estimated for the second threshold.

In conclusion, it is worth specifying how the proposed system can be employed in practical applications. Considering that the entire framework (see Fig. 20) was developed in an automated Python module, the tool can be used for each bridge belonging to a focused road network. In particular, the comparison between the displacement time series and the proposed threshold can be checked every time a new satellite acquisition is available (by updating the input data), and the occurrence of warnings can be assessed. It is important to specify that the occurrence of an isolated warning could not be a real concern, given that some approximations and elaborations were proposed. On the other hand, if the same warning persists for consecutive runs, the user can proceed with specific investigations (e.g., on-site survey) and undertake specific actions according to the detected Scenario. The system could be also implemented in a bridge management system as an additional module at disposal to road management companies.

1.2.2. Application of the proposed early warning system

This section is aimed at providing an illustrative application of the proposed framework. The proposed early warning system was applied to two prestressed RC girder bridges, one multi-span (Section 1.2.2.1) and one single-span (Section 1.2.2.2). About the case studies, it is worth noting that the satellite data have been collected and elaborated on bridges for which some details (e.g., name, location) cannot be disclosed. The bridges should be considered archetype structures, as its constructive and structural features are representative of simply supported bridges built in Italy in the period 1950-1990.

1.2.2.1. Multi-span bridge

According to the first step, the structural information is collected. It is made of four spans supported by single-shaft piers and seat-type abutments. Each span is characterized by four prestressed RC T beams, transversely connected by RC cast-in-place diaphragms and by an RC slab whose thickness is equal to 0.2 m thick. The bridge superstructure is connected to the piers and abutments through elastomeric bearings. The length of the spans ranges from 32 m to 33 m. The bridge longitudinal axis is inclined by an angle equal to - 33° with respect to the E-W direction. The deck width is equal to 13.00 m. The bridge presents a 7° slope and it was hypothesized to be located at a height of about 560 m a.s.l. for its highest point and about 550 m a.s.l for its lowest point. The distribution of elastomeric bearings was assumed as repetitive along the bridge: longitudinal mobile bearings at the beginning of each span and fixed mobile bearings at the end of each span, going from the first (AB1) to the second (AB2) abutment, according to the indication in Fig. 26 Regarding the deck section, geometric and mechanical features were available. In particular, the value of E_c was assumed equal to 31000 MPa, while the J_{deck} was assumed equal to 4.12 m^4. Although these values are assumed as fixed along the bridges, they could be considered accounting for

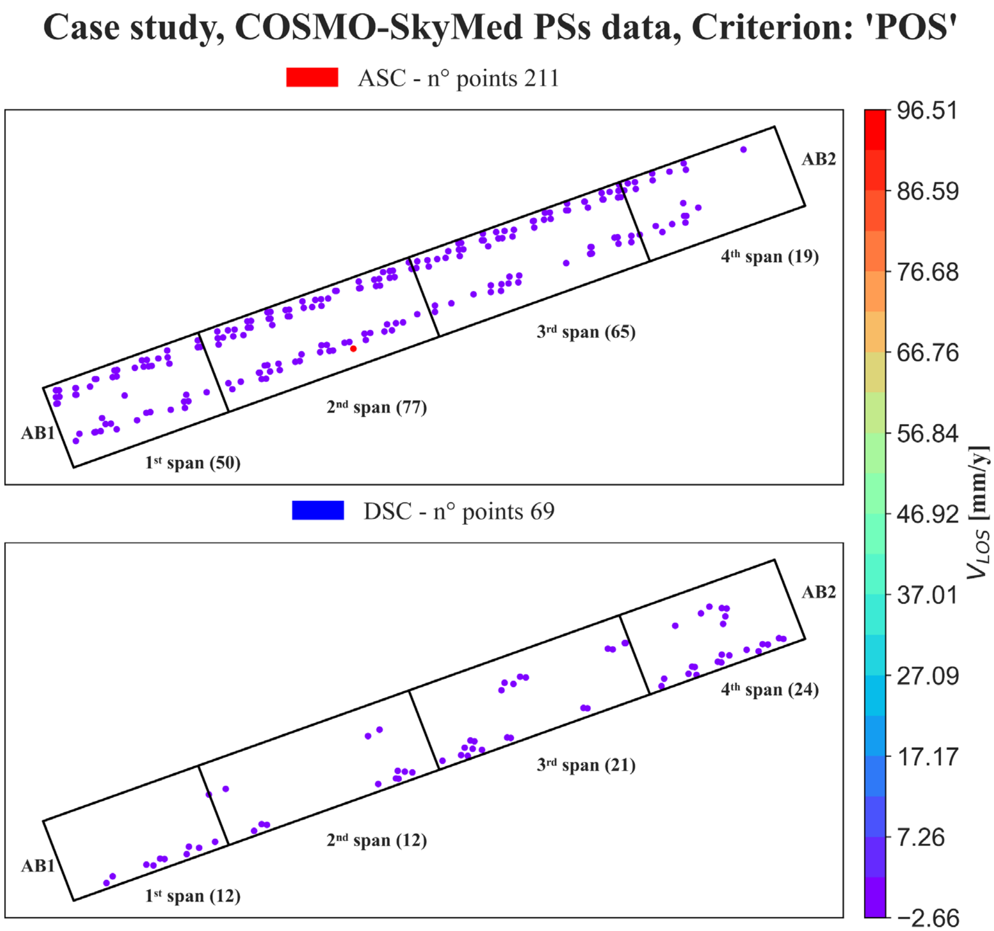

Fig. 26 - Multi-span bridge footprint, accounting for geo-coding errors, divided in spans. On the top ASC PSs are displayed, on the bottom DSC PSs ones are reported. In each span, the selected PSs are reported, and counted in the round brackets, according to the '*POS*' criterion. AB1 refers to the first abutment while AB2 refers to the second one. The colours of PSs match the V_{LoS} colormap on the right.

uncertainty (especially for E_C when estimated through mechanical tests) and this can produce a set of seasonal vertical thresholds (e.g., a spindle). Nevertheless, this is not of interest for purpose of the proposed procedure application.
Regarding satellite data, both ASC and DSC imagery were collected by CSK constellation on StripMap HIMAGE mode, for which detailed features are reported in Table 4.

Table 4 - Characteristics of the employed SAR datasets for the multi-span prestressed RC bridge.

Satellite	Mode	Spatial resolution	Pass type	Time span	Incidence angle θ [°]	Azimuth angle α [°]
CSK	StripMap HIMAGE	3 m x 3 m	ASC	02 January 2015 24 December 2020	31.143	169.155
CSK	StripMap HIMAGE	3 m x 3 m	DSC	01 September 2015 03 January 2021	30.781	10.894

Image resolution suits well for this application considering the bridge footprint dimension (Section 1.2.1.1). Fig. 26 reports the numbering of the spans and, for each span, the distribution of ASC and DSC PSs. Each PS is coloured by matching a common colormap defined according to V_{LoS} values. The number of points for each span is also indicated in the brackets.

Satellite data were processed by the SPINUA algorithm to retrieve PSs and the related attributes. The selected ones in Fig. 26 are obtained by defining the bridge and the span footprints according to the *'POS'* criterion (a 3 m buffer around the real footprint is fixed to consider geo-positioning errors).

Once the buffered footprint was divided in spans, the PSs were selected. Table 5 summarizes the number of PSs selected according to each criterion described in Section 1.2.1.3, reporting results for the whole bridge footprint. PS height values were corrected considering the difference between the bridge mean height a.s.l and mean height attribute of each PS falling within the enhanced footprint. Hence, PSs are subjected to a rigid translation of 7.8 m and 7.5 m for ASC and DSC dataset, respectively, and a ± 1 m tolerance is considered for geo-positioning errors. It is worth noting that, using *'H_GEO'* criterion, among the points a PS was discarded (L20968P02259, red dot in the ASC geometry of Fig. 26 and black line in Fig. 27, left), which is characterized by a very high V_{LoS} value (96.51 mm/y) over the whole period and that completely disagreed with V_{LoS} of the closer PSs (Fig. 27, right). The results of the retained PSs from *'H_GEO'* criterion are illustrated in Fig. 28 and given both the low variability of V_{LoS} attribute on *'H_GEO'* criterion and the lack of PSs from DSC geometry on 3rd span with *'V_LOS'* criterion, the *'H_GEO'* criterion was chosen to continue the analysis.

Table 5 - Number of PS selected for each formulated criterion (multi-span prestressed RC bridge).

Criterion	PSs - ASC	PSs - DSC
POS	211	69
H_GEO	191	61
V_LOS	190	55
COH	211	69
H_GEO + COH	191	61
H_GEO + COH + V_LOS	187	55

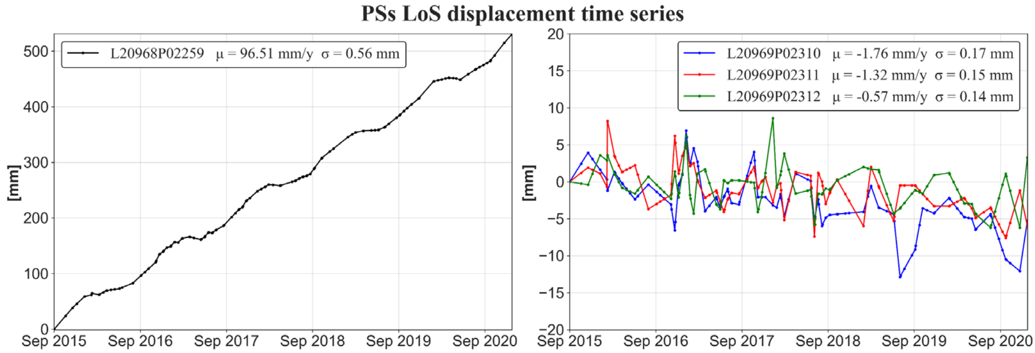

Fig. 27- Time series of discarded PS, black line in left chart, compared to the ones of some neighbour PSs displayed in the right chart. μ is the V_{LoS} value, slope of the Least Squares Regression line, while σ represents the standard deviation.

Fig. 28 shows the division of the spans in sub-regions for the 1st and 3rd spans (S11, S12, S13 for the 1st span and S31, S32, S33 for the 3rd span), according to the minimum requirements defined in Section 1.2.1.3. The performed subdivision has the goal to describe the behaviour of lateral and central span regions, where the first ones could be affected by more sensitive longitudinal displacements (e.g., due to thermal effects) and the second one could be affected by vertical displacements (e.g., due to traffic/gravity loads). Temporal and spatial consistency was evaluated before computing longitudinal and vertical displacement time series. Spatial consistency was evaluated on the PS distribution along each span. As observed in Fig. 28, although 1st and 3rd spans present a good spatial consistency, a different situation can be observed on the

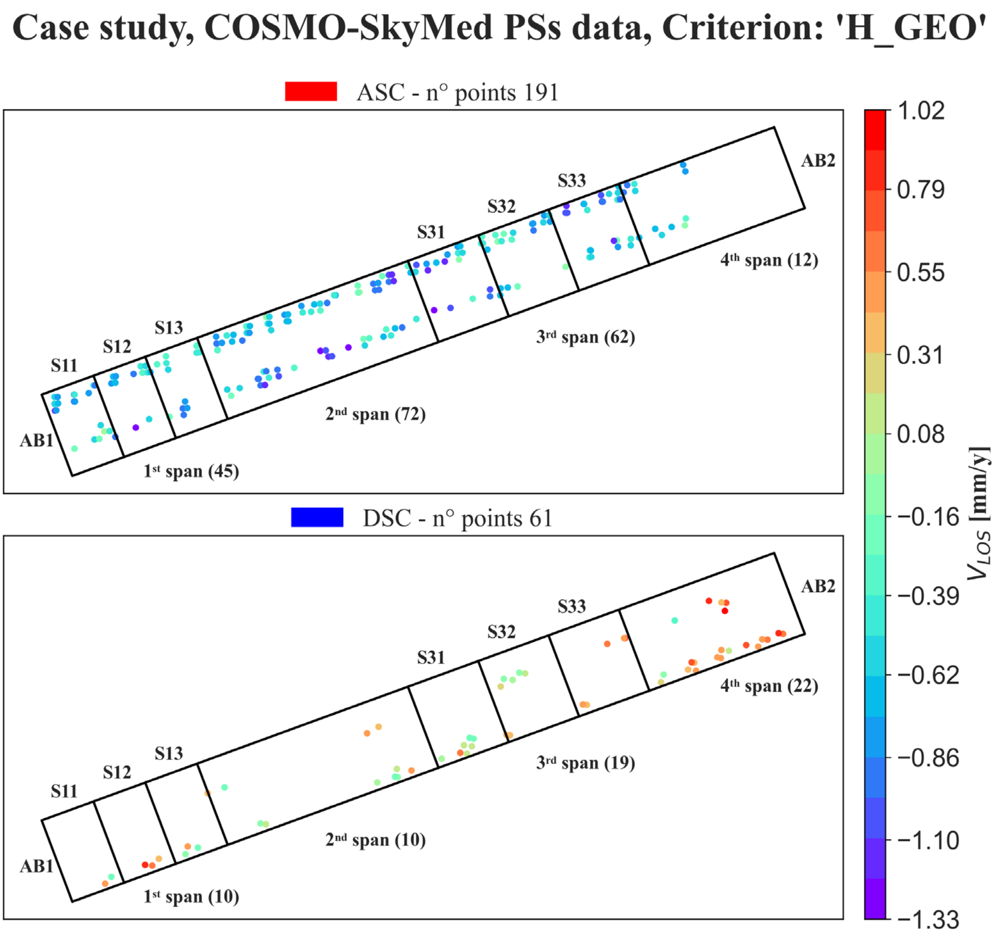

Fig. 28 - Case study bridge footprint, accounting for geo-coding errors, together with transverse sub-regions of 1st (S11, S12 and S13) and 3rd (S31, S32 and S33) spans. On the top ASC PSs are displayed, on the bottom DSC PSs ones are reported. The PSs, counted for each span in the round brackets, are selected according to the '*H_GEO*' criterion. AB1 refers to the first abutment while AB2 refers to the second one. The colours of PSs match the V_{LoS} colormap on the right.

remaining spans. As a matter of fact, the 2nd span does not present PSs in the central part of the DSC dataset, even without PSs filtering, as in the *'POS'* criterion shown in Fig. 26, while the 4th span is partially covered by the ASC dataset. The lack of PSs from the DSC dataset could be caused by the presence of vegetation on the bridge left side coupled with the DSC side view geometry. The absence of points remains an open issue, which limits the application of the proposed methodology. In general, improvements for spatial consistency, obtainable through a further longitudinal division, are recommended as proposed by Miano *et al*. (2021). This is worth only in the cases in which larger datasets are available to analyse the differences among structural parts, especially regarding vertical displacements (as for example shown for the Himera viaduct in Ferretti *et al*., 2022). Talking about the temporal consistency, time series associated with each PS should be manipulated. First, it is necessary to eliminate the first ASC acquisition (02 January 2015), because it is extremely far from the second acquisition of the same dataset (01 September 2015). To this scope, the entire ASC time series must be purified from the data related to its first acquisition. After, the common temporal baseline was defined according to Section 1.2.1.4.

With the data at disposal, Fig. 29 shows the average LoS displacement time series evaluated in the centroid of each span. As observed, a negative trend component, defined as the slope of the Least Squares Regression line, characterizes ASC average LoS displacement time series, with V_{LoS} values ranging from - 0.61 mm/y to - 0.67 mm/y. Instead, a positive trend describes the average DSC LoS displacement time series, with V_{LoS} values ranging from 0.11 mm/y to 0.44 mm/y. A marked displacement seasonality is highlighted by ASC acquisition of 3rd and 4th spans (green and yellow lines, respectively), while a less pronounced seasonality is observed for 1st and 2nd spans (blue and red lines, respectively). A more accurate evaluation can be derived from the decomposition of the LoS displacement vector by applying and inverting Equation (21). Assuming a M-LCRS with L axis coincident with the bridge centreline, using the slopes of the bridge (γ = - 33°, δ = 0°, and β = 7°), and neglecting transversal displacements, d_T, the values of d_L and d_V can be obtained:

$$\begin{bmatrix} d_{LoS,ASC} \\ d_{LoS,DSC} \end{bmatrix} = \begin{bmatrix} \begin{matrix} sin\theta^{ASC}cos\beta \cdot \\ \cdot\cos(a^{ASC}-\gamma) \end{matrix} & \begin{matrix} sin\theta^{A}sin\beta\cos(a^{ASC}-\gamma)+ \\ +cos\theta^{ASC}cos\beta \end{matrix} \\ \begin{matrix} sin\theta^{DSC}cos\beta \cdot \\ \cdot\cos(a^{DSC}-\gamma) \end{matrix} & \begin{matrix} sin\theta^{D}sin\beta\cos(a^{DSC}-\gamma)+ \\ +cos\theta^{DSC}cos\beta \end{matrix} \end{bmatrix} \begin{bmatrix} d_L \\ d_V \end{bmatrix} \qquad (26)$$

Results from Equation (26), for each span, can be observed in the bottom graphs of Fig. 29. A reversed sign is assumed for longitudinal displacements to classify positive

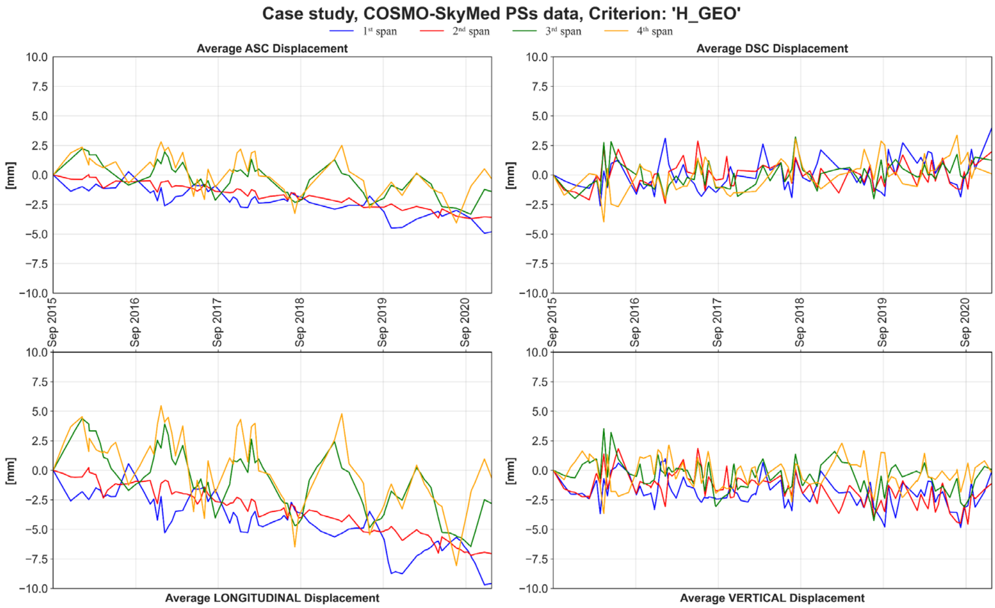

Fig. 29 - Span centroid average time series. On top-left corner the average ASC LoS displacement time series is shown, on the top-right corner the average DSC LoS displacement time series. On the bottom, from left to right the average longitudinal displacement time series and the average vertical displacement time series obtained by applying Equation (26), considering each time step and each span, and starting from ASC and DSC data plotted in the top graphs.

displacements during summer and negative ones during winter. A positive displacement implies a stretching movement toward W direction, while a negative displacement implies a stretching movement toward W direction, while a negative displacement corresponds to an approaching movement to the E direction. According to the estimates of V_{LoS} values in Fig. 29, the longitudinal and vertical displacement trends are found, denoting that the vertical one is less accentuated (i.e., near horizontal). Regarding the longitudinal seasonal component, although it is not possible to quantify an amplitude, it can be observed that the first two spans (1st and 2nd) have a mirrored behaviour compared to the last two spans (3rd and 4th). Hence, during the summer months, the 1st and 2nd spans show positive displacements, while 3rd and 4th spans show negative displacements. Similar outcomes cannot be provided regarding the vertical direction,

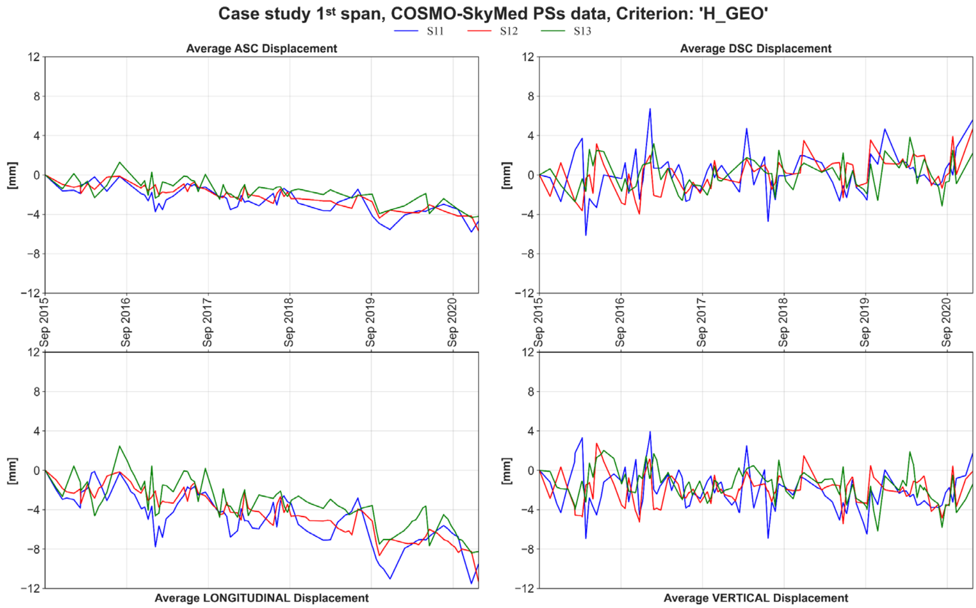

Fig. 30 - 1st sub-regions average time series. On top-left corner is shown the average ASC LoS displacement time series, on the top-right corner the average DSC LoS displacement time series. On the bottom, from left to right the average longitudinal displacement time series and the average vertical displacement time series.

where an unclear seasonal trend can be observed. Fig. 30 and Fig. 31 shows, in the bottom graphs, the time series already discussed for the sub-regions of the 1st (S11, S12 and S13) and 3rd (S31, S32 and S33) span, respectively, denoting the same outcomes. As discussed at the end of Section 1.2.1.4, final insights about average longitudinal displacements-time series in Fig. 29 can be provided. Observing the V_{LoS} values of ASC and DSC acquisition geometry, a quite similar magnitude can be denoted (i.e., -0.64 mm/y for ASC and 0.20 mm/y for DSC on average), but opposite signs were obtained for longitudinal components. This means that, although longitudinal displacements present a trend similar to the one observed for ASC component, it was obtained by the combination of ASC and DSC, and then should be not confused.

To process a systematic analysis of the time series, the application of the decomposition algorithm STL was required. A temporal resampling of the time series was processed, to have a regular sampling frequency. Considering an average frequency of 34

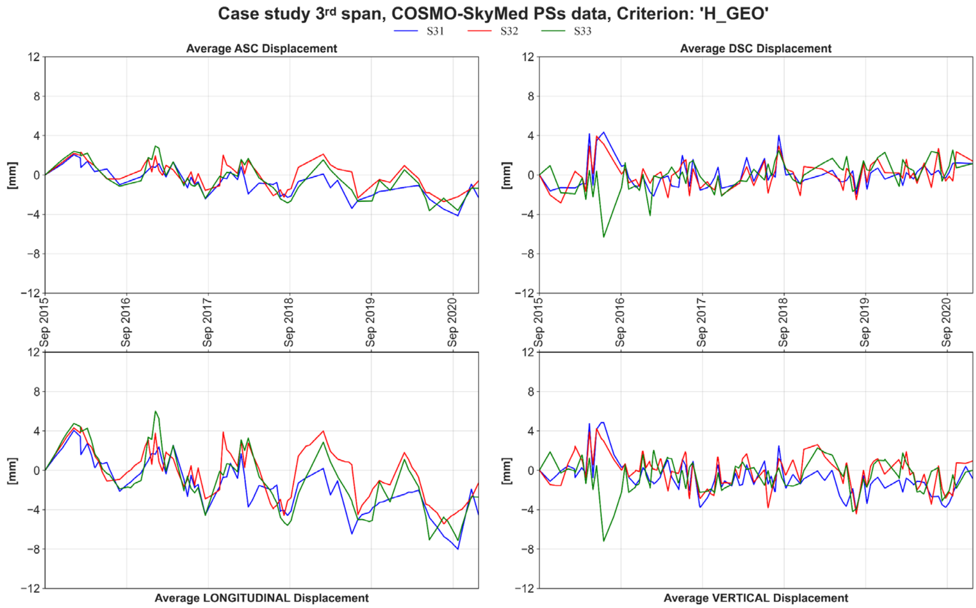

Fig. 31 - 3rd span sub-regions average time series. On top-left corner is shown the average ASC LoS displacement time series, on the top-right corner the average DSC LoS displacement time series. On the bottom, from left to right the average longitudinal displacement time series and the average vertical displacement time series.

days for the case at hand, corresponding to twice the satellite revisit time for CSK constellation, the series were resampled with a daily frequency, to prevent acquisition losses. In addition, an annual seasonality was considered. The obtained trends (seasonal and remainder components) are shown in Fig. 32 for S11, S12, S13 and in Fig. 33 for S31, S32, and S33. Some considerations can be provided by observing the results of obtained displacement components from the STL analysis. As previously stated, from the longitudinal seasonal components, the displacements of the 1st span sub-regions (S11, S12, S13 in the bottom left chart of Fig. 30) are out of phase compared to the ones provided in the 3rd span sub-regions (S31, S32, S33 in the bottom left chart of Fig. 30) are out of phase compared to the ones provided in the 3rd span sub-regions (S31, S32, S33 in the bottom left chart of Fig. 31). Furthermore, as expected for this constructive typology, the displacements of sub-regions close to the

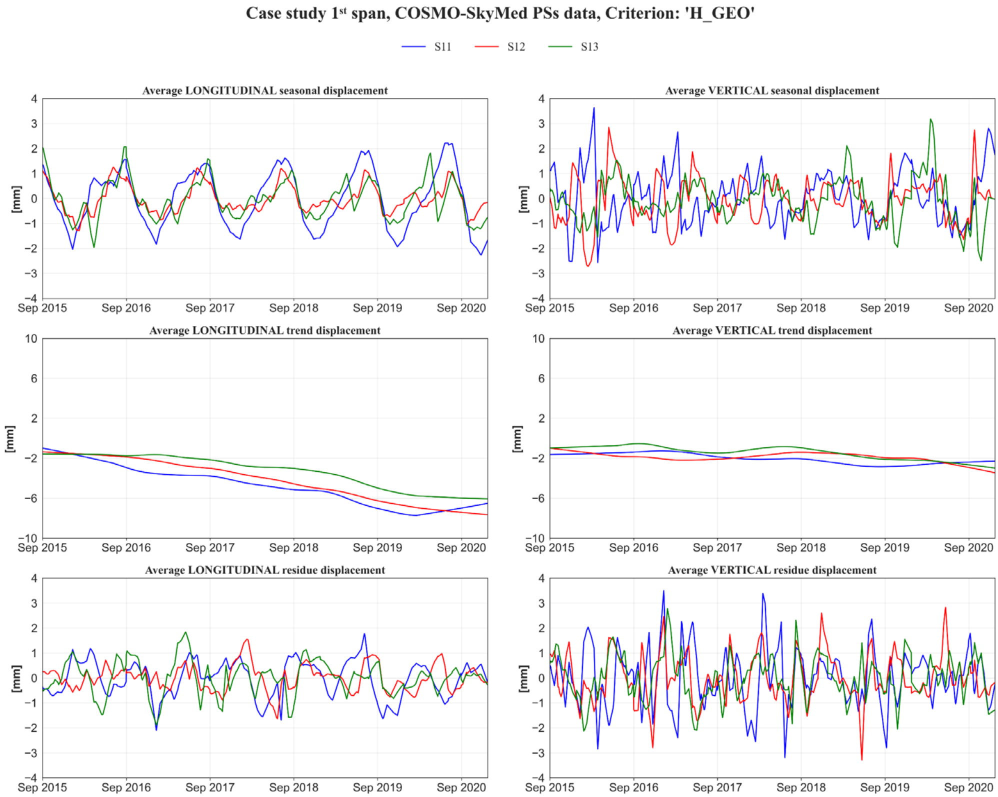

Fig. 32 - 1st span sub-regions STL decomposition of average displacement time-series. The charts on the left refer to the longitudinal displacement components while the ones on the right refer to the vertical displacement component. From top to bottom, the first row depicts the seasonal component, the one below shows the trend component and the last one the remainder component.

sub-regions (S11, S12, S13 in the bottom left chart of Fig. 30) are out of phase compared to the ones provided in the 3rd span sub-regions (S31, S32, S33 in the bottom left chart of Fig. 30) are out of phase compared to the ones provided in the 3rd span sub-regions (S31, S32, S33 in the bottom left chart of Fig. 31). Furthermore, as expected for this constructive typology, the displacements of sub-regions close to the fixed support (S13 and S31, blue lines), are smaller than those of central (S12 and S32, red lines) and last (S11 and S33, green lines) sub-regions (see top left graphs in

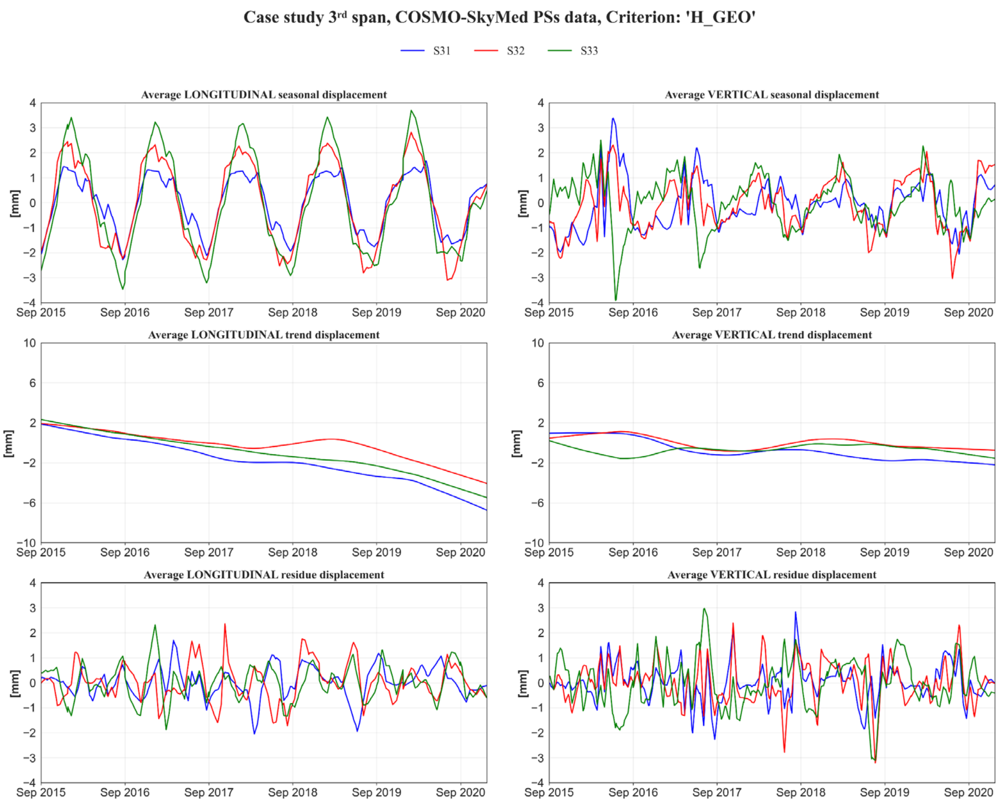

Fig. 33 - 3rd span sub-regions STL decomposition of average displacement time-series. The charts on the left refer to the longitudinal displacement components while the ones on the right refer to the vertical displacement component. From top to bottom, the first row depicts the seasonal component, the one below shows the trend component and the last one the remainder component.

Fig. 32 and Fig. 33). From this observation, some insights can be derived on how bearings are working under service conditions, despite the original design drawings could suggest a different positioning criterion. As a matter of fact, observing the obtained results, it seems that bearings are positioned symmetrically to the central pier and not according to the scheme above declared. The magnitude of the movements is also increasing in both summer and winter months, which cannot imply a wrong functioning of the bearings, but a different behaviour to the expected one (a malfunction of bearings could lock the longitudinal displacements, benefiting the development of greater displacements in the vertical direction).

In addition, looking at the longitudinal displacements, a negative trend can be observed for 1st and 3rd span, which could imply a movement from AB1 to AB2 (see Fig. 28). Nevertheless, this aspect was faced only by considering the vertical displacements because, for the sake of generalization, the effect of the movement can be always detected by the vertical component and not always derived by the horizontal component (i.e., when the horizontal component is in the azimuth direction). Regarding the vertical seasonal component (top right graphs in Fig. 32 and Fig. 33), it shows a lower regularity than the longitudinal component, considering that the expected behaviour of larger vertical displacements in the central sub-regions (S12 and S32, red lines) than the lateral ones (S11, S13 and S31, S33) is not always well described by satellite data.

Regarding trend values, the longitudinal components are almost linear (presenting a high coefficient of determination, R^2, values) and highlight an ongoing deformation along *L* axis (see middle left graphs of Fig. 32 and Fig. 33). For the case at hand, the average value, μ, is equal to -1.2 mm/y and -0.8 mm/y for 1st and 3rd span sub-regions, respectively, as summarized in Table 6 where d_0 is the intercept of the Least Square Regression. Looking the obtained values, average velocities are not alarming for the bridge, also according to the available literature (e.g., Nettis *et al.*, 2023a classified as low deformation scenarios velocities lower than 2 mm/y). Concerning vertical trends (see middle right graphs in Fig. 32 and Fig. 33), although nonlinearities can be observed (low values of R^2), they describe a slightly downward movement characterized by an average value, μ, equal to -0,28 mm/y for both 1st and 3rd span sub-regions.

Finally, the above qualitative considerations about the time series and the velocity values can be quantified and compared with limits. Therefore, as a last step, longitudinal and vertical thresholds were defined according to Section 1.2.1.7. Temperature data were derived from the closest weather station (10 km away). The reference temperature, T_{start}, of the master image, was fixed to 29 °C, from the weather station data, while ΔT_{MAX} and ΔT_{MIN} were calculated from T_{MAX} and T_{MIN}, defined through the temperature

Table 6 - Slope μ, intercept d_0, and R^2 of Least Squares Regression method applied to longitudinal and vertical trend component of subregions retrieved from the application of STL algorithm. δ_i describes the vertical differential displacement for each i^th subregion."

Sub-region	Longitudinal			Vertical			
	μ [mm/y]	d_0 [mm]	R^2	μ [mm/y]	d_0 [mm]	R^2	δ_i [mm]
S11	-1.23	-1.47	0.95	-0.28	-1.25	0.75	-1.5
S12	-1.34	-0.66	0.98	-0.18	-1.42	0.34	-0.96
S13	-1.01	-0.60	0.92	-0.38	-0.44	0.77	-2
S31	-1.36	1.77	0.97	-0.61	0.88	0.86	-3.32
S32	-0.83	1.93	0.80	-0.25	0.65	0.40	-1.32
S33	-1.25	2.24	0.98	0.03	-0.78	0.01	0.16

cosine model, Equation (23), fitted on the few data provided by the same station. The fitting parameters, from a nonlinear least squares method, were $B_T = 11$ °C, $\phi_T =$ -4.6 assuming $A_T = 23.1$ °C. Hence, ΔT_{MAX} is found equal to 4.3 °C and ΔT_{MIN} to -7.5 mm (dark blue lines on top graphs in Fig. 34 and Fig. 35) for both S11 and S33, respectively. Later, the two vertical thresholds were calculated and compared with the observed Scenario. The first threshold, $d_{service}$, was equal to 3.5 mm for both 1^st and 3^rd span, Equation (25), while the second threshold was quantified as equal to 10.6 mm. The scenarios value to be compared with thresholds, as described in Section 1.2.1.7 and reported in Table 7, were defined through the vertical cumulative displacement δ_i reported in Table 6. As a result, the 1^st span falls under Scenario 1 (material degradation, Fig. 36) while the 3^rd span falls under Scenario 3 (differential displacement). From the comparison of descriptive characteristics with the threshold values, no span was subject to warnings.

In summary, considering a five-year observation period, the proposed framework allowed for retrieving, discussing, and comparing seasonal and trend displacement components for the focused bridge. As a first result, the longitudinal seasonal component highlighted a different behaviour between the hypothesized and the real bridge behaviours, regarding the supports operation. Considering a constant temperature range

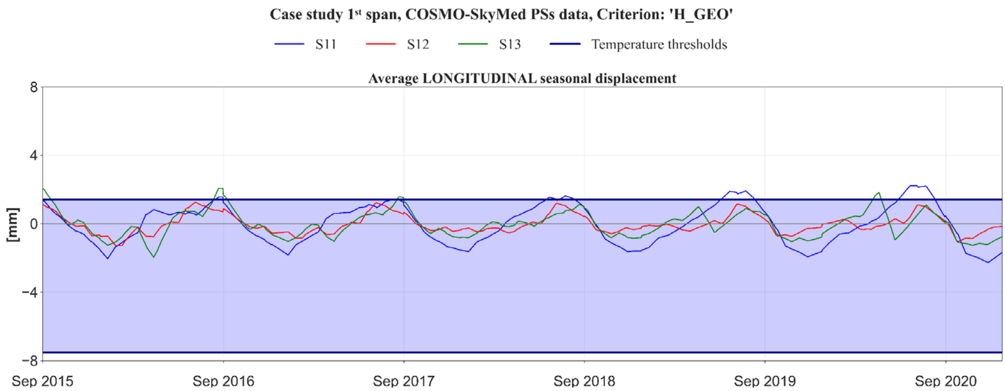

Fig. 34 - 1st span sub-regions seasonal displacement time-series and thresholds. The chart shows the average longitudinal displacements time series of S11 (blue line), S12 (red line) and S13 (green line) sub-regions and two dark blue lines representing the calculated temperature thresholds (1.4 and -7.5 mm).

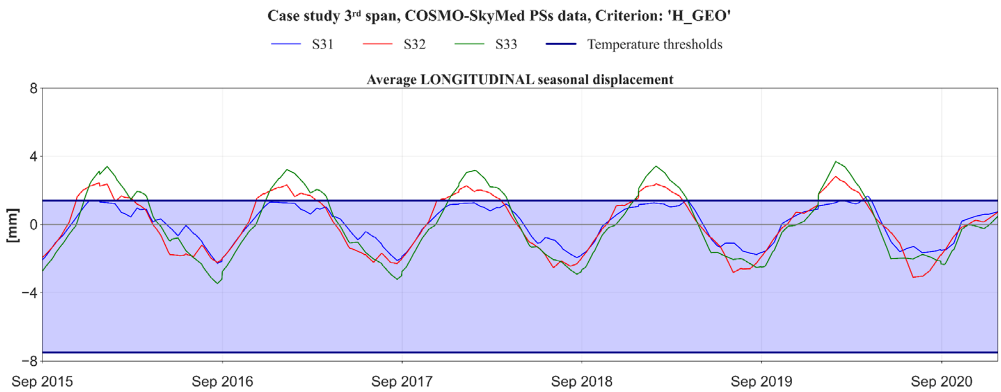

Fig. 35 - 3rd span sub-regions seasonal displacement time-series and thresholds. The chart shows the average longitudinal displacements time series of S31 (blue line), S32 (red line) and S33 (green line) sub-regions and two dark blue lines representing the calculated temperature thresholds (1.4 and -7.5 mm).

Table 7 - Scenario evaluation and thresholds.

Span	Δ_{sx} [mm]	Δ_{dx} [mm]	$\delta_{mid\ span}$ [mm]	Average $\lvert\Delta_i\rvert$ [mm]	$2\lvert\delta_{mid\ span}\rvert/3$ [mm]	Scenario	Threshold [mm]
1st	0.54	-1.04	-0.96	0.25	0.64	1	-3.5
3rd	1.91	1.48	-1.32	1.7	0.88	3	10.6

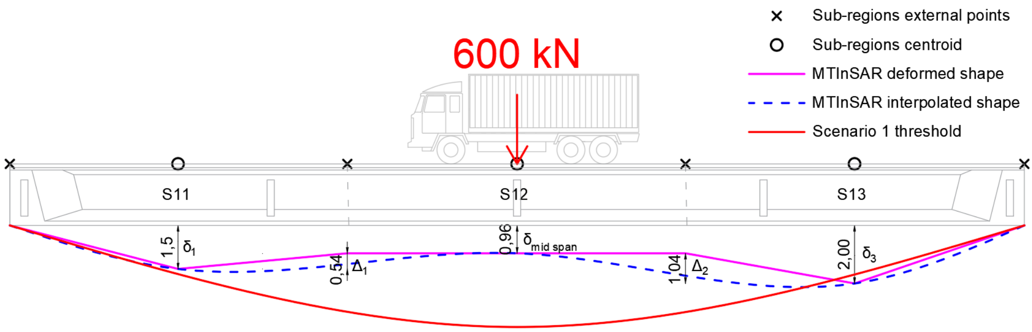

Fig. 36 - 1st span bridge-specific displacement scenario 1. On background, the assumed configuration of the 1st span on 01 September 2015. Cross signs refer to sub-regions (S11, S12 and S13) external points, while circle signs refer to sub-regions' centroid. Magenta line connects the vertical cumulative displacement of centroids of the sub-regions, δ_i, estimated according to the proposed framework (Section 1.2.1.7). Blue dashed line interpolates the vertical cumulative displacement of centroids of the sub-regions, δ_i. Red line shows the deformed shape of 1st span as simply supported beam under $F_{Traffic}$ equal to 600 kN. All the values are expressed in millimeters; therefore, all vertical deformed shapes are in 1000:1 scale with respect to 1st span length Although the MTInSAR deformed shape exceeds the Scenario 1 threshold in a point, the warning is not triggered, because the reference point to check is the mid-span one.

along transverse deck section, thresholds were evaluated and compared to seasonal displacements, showing that the imposed limit was always exceeded by the 3rd span. Regarding vertical displacements two different deformation scenarios were identified, material degradation and subsidence, but no warnings were noticed. Longitudinal trends presented small velocity values but, in the absence of further analysis, material degradation and aging cannot be excluded as possible causes of displacement increment. In the end, considering the tolerances and the limited precision of the displacement time series for the reasons more times above stated, the specific exceedance of the thresholds is not worrying, but it is worth paying attention in the cases of constant exceedance and of relative velocity increasing.

1.2.2.2. *Single-span bridge*

As second case study, a single-span bridge characterized by eighteen pre-stressed RC double-T beams located in Fiumicino, Rome (Italy) is analysed (Fig. 37). This area is subject to subsidence which has been documented by several studies (Nettis *et al*., 2023a; Orellana *et al*., 2020). Table 8 shows the main features of CSK datasets, while Table 9 summarizes the main characteristics of the bridge.

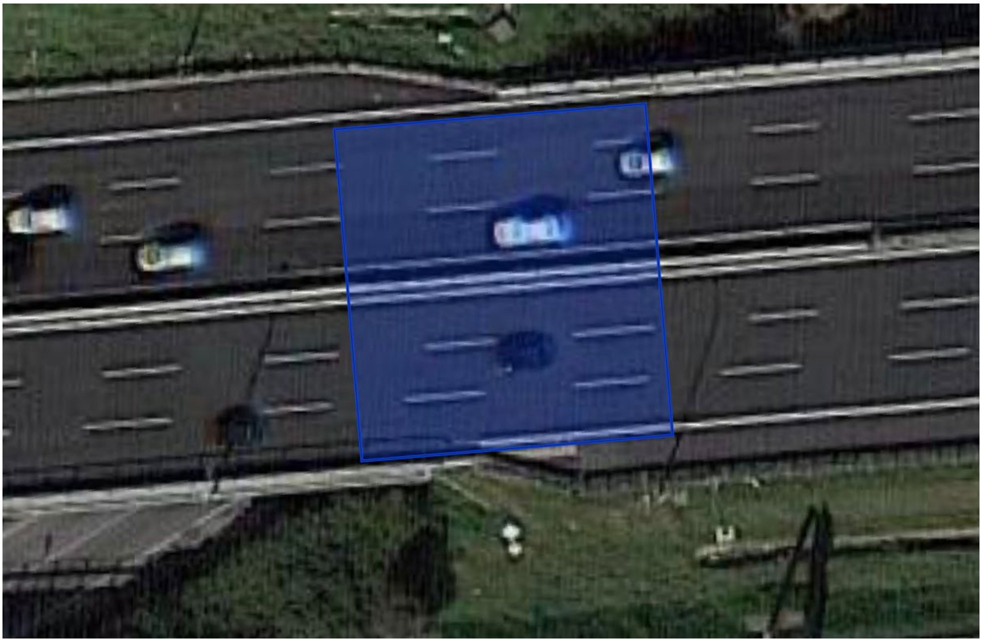

Fig. 37 - Single span simply supported concrete girder bridge, Fiumicino, Rome (Italy).

Table 8 - Characteristics of the employed SAR datasets for the single-span prestressed RC bridge.

Satellite	Mode	Spatial Resolution	Pass type	Time span	Incidence angle θ [°]	Azimuth angle α [°]
CSK	StripMap HIMAGE	3 m x 3 m	ASC	Jan 2015 - Aug 2021	33.282	169.373
CSK	StripMap HIMAGE	3 m x 3 m	DSC	June 2015 - July 2022	29.550	11.026

Table 9 - Characteristics of the single-span bridge.

Num. spans	Span length [m]	Span width [m]	Height [m]	Bearings typology	J_Y [m^4]	E [MPa]	M-LCRS γ [°]	M-LCRS β [°]	M-LCRS δ [°]
1	22	24	4	Elastomeric	3.43	31000	~ 4	~ 0	~ 0

Each span is characterized by four prestressed RC T-beams, transversely connected by RC cast-in-place diaphragms and by an RC slab whose thickness is equal to 0.2 m thick. The bridge superstructure is connected to the piers and abutments through elastomeric bearings.

For the footprint definition, a 3 m buffer around the real footprint was fixed to consider for geo-positioning errors. For the same reason, a $\pm$ 1 m tolerance was considered for heights as well. According to these assumptions, a sub-region scale analysis was performed considering the '*H_GEO*' criterion. To characterize the behaviour of the zones near to the bearings (1st and 3rd) and of the middle part (2nd), three transverse sub-regions were considered, as reported in Fig. 38. For each of them, an average LoS displacement time series was defined (Fig. 39 upper charts), for a period spanning going from October 2015 to November 2020, and the decomposition was performed according to the criteria defined in Sections 1.2.1.5 (Fig. 39 bottom charts) and 1.2.1.6 (Fig. 40). The results are shown in Fig. 39 for the sub-region analysis. Starting from average LoS displacement time series (Fig. 39 upper charts), negative values were observed from both ASC and DSC geometries, which means that the scene is moving away from the satellite. The missing information concerns the extent of the displacements along the assumed directions, that is, the longitudinal and vertical axes of the viaduct, which are orthogonal to each other. Therefore, a null displacement component was supposed along transversal direction. Considering Equation (21), the assumptions, and the angle values reported in Table 9, the system of equations to characterize d_L and d_V are reported:

$$\begin{bmatrix} d_{LoS,ASC} \\ d_{LoS,DSC} \end{bmatrix} = \begin{bmatrix} sin\theta^{ASC} \cdot \cos(a^{ASC} - \gamma) & cos\theta^{ASC} \\ sin\theta^{DSC} \cdot \cos(a^{DSC} - \gamma) & cos\theta^{DSC} \end{bmatrix} \begin{bmatrix} d_L \\ d_V \end{bmatrix} \tag{27}$$

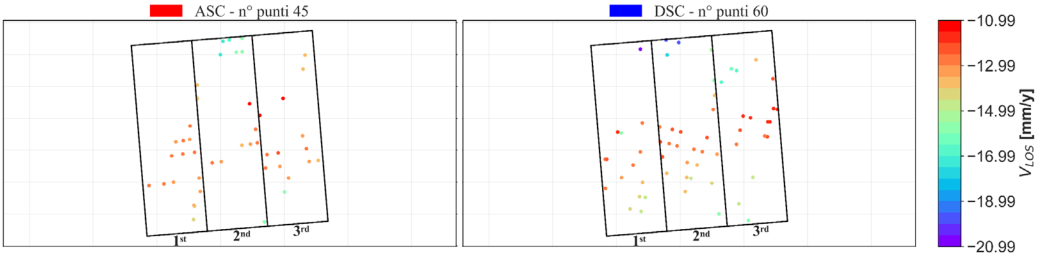

Fig. 38 - Single-span bridge footprint, accounting for geo-coding errors, and selected PSs through '*H_GEO*' criterion. On the left ASC PSs are displayed, on the right DSC PSs ones are reported.

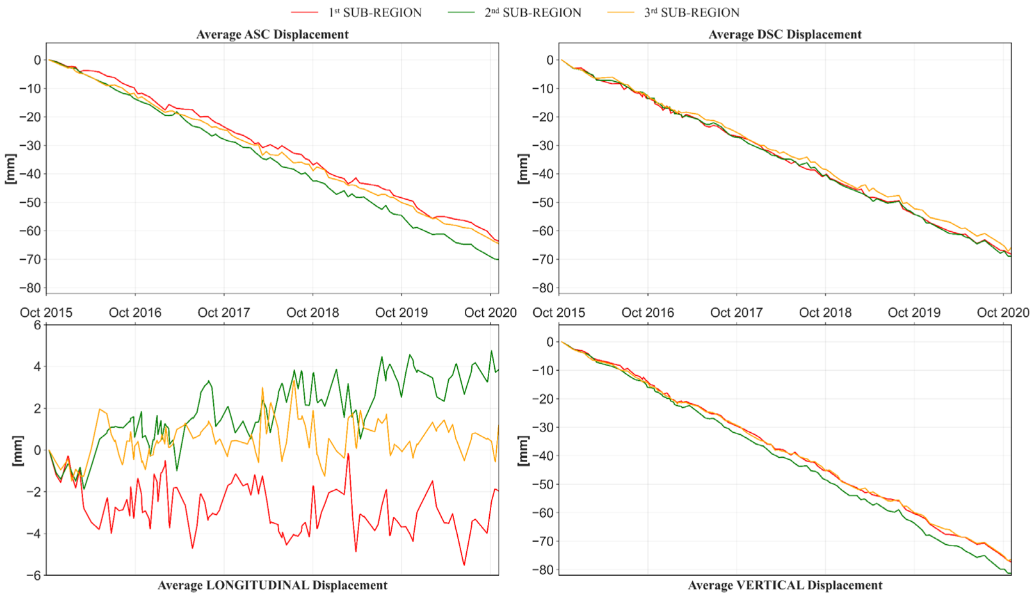

Fig. 39 - Single-span centroid average time series. On top-left corner the average ASC LoS displacement time series is shown, on the top-right corner the average DSC LoS displacement time series. On the bottom, from left to right the average longitudinal displacement time series and the average vertical displacement time series obtained by applying Equation (27), considering each time step and each span, and starting from ASC and DSC data plotted in the top graphs.

The longitudinal and vertical displacement time series were defined, and they are characterized by a trend and a seasonal component, as shown in bottom charts of Fig. 39. To evaluate the obtained results, the STL technique was applied and average displacement time series were daily resampled to prevent acquisitions loss, considering their heterogeneous sampling frequency. The three components for both longitudinal and vertical sub-regions displacements are reported in Fig. 40.

Some considerations can be provided by observing the resulting components of the STL analysis. From the longitudinal seasonal component (top left graph in Fig. 40) was observed the displacements of the sub-regions near to the supports, which present reverse phases (1st and 3rd zones in Fig. 40). Their relative displacement values oscillating within ± 1.5 mm. This behaviour is related to a static scheme that provides for longitudinally mobile bearings on both abutments. This behaviour is related to a static scheme that provides for longitudinally mobile bearings on both abutments.

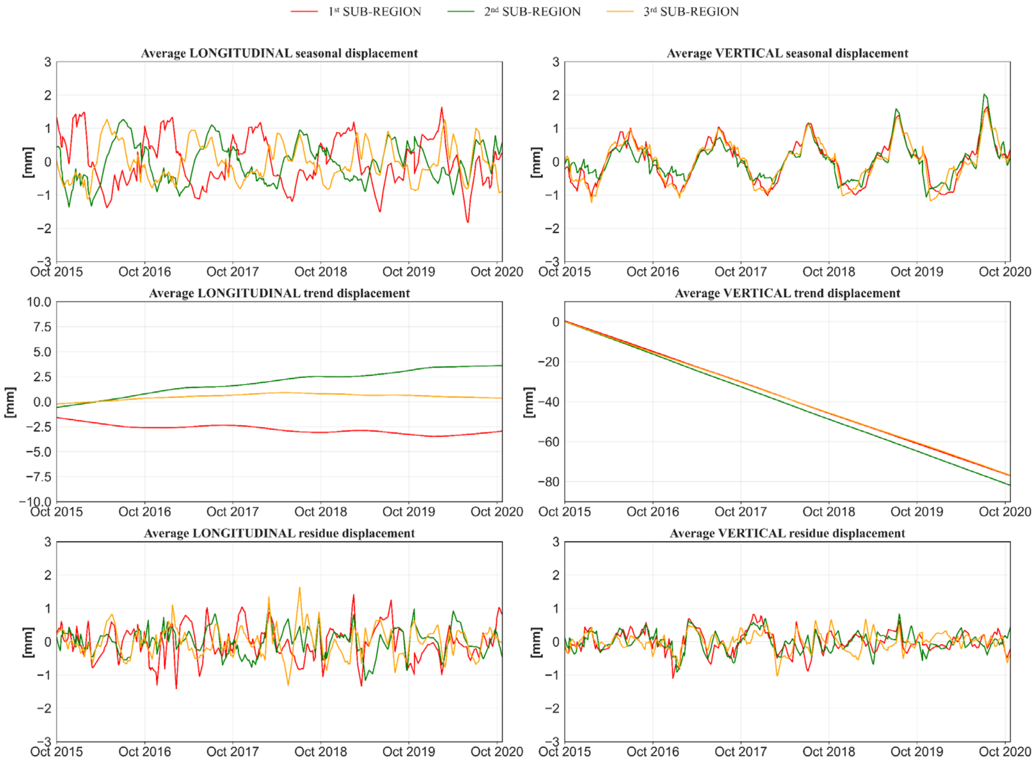

Fig. 40 - Single-span sub-regions STL decomposition of average displacement time-series. The charts on the left refer to the longitudinal displacement components while the ones on the right refer to the vertical displacement component. From top to bottom, the first row depicts the seasonal component, the one below shows the trend component and the last one the remainder component.

Maximum vertical seasonal displacement of the 2nd sub-region (top right graph in Fig. 40) increased to double over 3 years, between 2017 and 2020. The cause of this may be related to a malfunctioning of the bearings.

Regarding the trend components (middle graphs in Fig. 40), a clear value was observed (middle right graph Fig. 40), with vertical displacements presenting value of 15.5 mm/y. The cumulative displacement amounted to 78 mm for the reported vertical linear trend as reported in Table 10. Regarding to the longitudinal trend (middle left graph Fig. 40), the sub-regions near to the bearings were initially moving away from each other with velocity values equal to -0.27 mm/y and 0.42 mm/y for 1st and 3rd sub-regions, respectively. Then, they started moving together towards West direction from mid-2018, with a value of -0.21 mm/y for the 3rd sub-region.

Finally, the above qualitative considerations about the time series and the velocity values can be quantified and compared with limits. Therefore, as a last step, longitudinal and vertical thresholds were defined according to Section 1.2.1.7 and to bridge structural characteristics displayed in Table 9. The temperature data were extracted from the meteorological station closest to the structure. The reference temperature, T_{start}, of the master image was fixed to 16.0 °C, while a minimum value, T_{min}, and a maximum value, T_{max}, were set equal to 0°C and 36 °C, respectively. Constant temperature differences, ΔT_C, were considered for summer and winter, assuming a value of 20.0 °C and -16.0 °C, respectively. According to the proposed framework, the threshold values for the longitudinal seasonal component, d_{Term} (dark blue lines in Fig. 41), were estimated as 1.7 mm and -1.5 mm from Equation (23). The scenarios value to be compared with thresholds, as described in Section 1.2.1.7 and reported in Table 11, were defined through the vertical cumulative displacement δ_i reported in Table 10. Hence, by computing the displacements Δ_{sx} and Δ_{dx}, as summarized in Table 10, it is possible to observe that one is positive, and one is negative. This means that the possible Scenarios are 1 or 2. Of course, the Scenario 2 is the right one because the average of absolute value of δ_i is greater than $2|\delta_{\text{mid span}}|/3$. In the end, the framework has successfully identified Scenario 2, which was expected from the hydro-geomorphological context of the area. In addition, the average value of $|\delta i|$ equal to 78.19 mm exceeds the 10 mm threshold (2 mm/y times 5 years). In the end, no structural damages related to the subsidence should be observed given that the surrounding area around the bridge is moving together with the bridge itself.

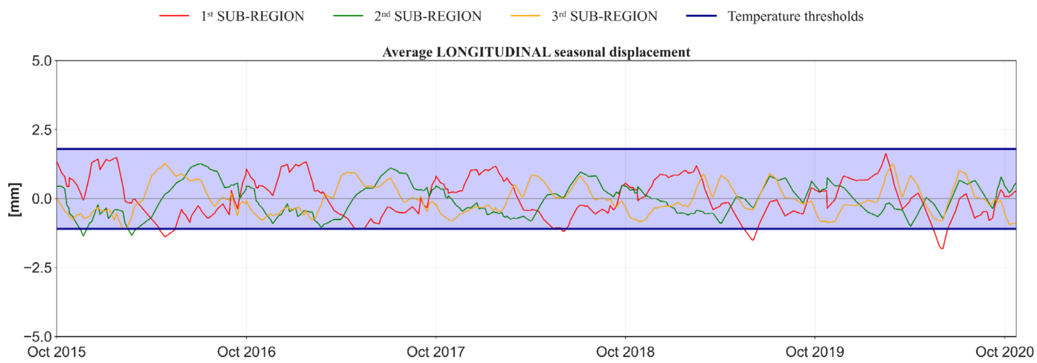

Fig. 41 - 1st span sub-regions seasonal displacement time-series and thresholds. The chart shows the average longitudinal displacements time series of 1st (red line), 2nd (green line) and 3rd (yellow line) sub-regions and two dark blue lines representing the calculated temperature thresholds (1.7 and -1.5 mm).

Table 10 - Slope μ, intercept d_0, and R^2 of sub-regions vertical trend component and vertical differential displacement for each sub-region δ_i.

Sub-region	Vertical			
	μ [mm/y]	d_0 [mm]	R^2	μ [mm/y]
1st	-15.65	0.43	0.98	-78.23
2nd	-16.24	0.35	0.99	-81.20
3rd	-15.63	0.58	0.98	-78.15

Table 11 - Scenario evaluation and thresholds for the single-span bridge.

Span	Δ_{sx} [mm]	Δ_{dx} [mm]	$\delta_{mid\ span}$ [mm]	Average $\lvert\Delta_i\rvert$ [mm]	$2\lvert\delta_{mid\ span}\rvert/3$ [mm]	Scenario	Threshold [mm]
1st	2.97	-3.05	-81.2	78.19	54.13	2	10

1.2.3. BAS-MTInSAR: definition of a new GIS plugin

The framework described in Section 1.2.1 and applied to two real case studies showed its potential in the field of structural risk monitoring of existing bridges. However, several hurdles can be faced in the management and interpretation of data. In fact, a right evaluation of the output depends on the data collection and aggregation (considering different data sources), which require articulated computational steps, often difficult to replicate manually for each bridge within a considered portfolio. Moreover, as declared in the introduction of this research work, the application of MTInSAR data for structural assessment is limited by the interdisciplinary nature of technical knowledge required, reducing the number of potential users, especially in the field of professional practice. A viable option to manage and elaborate georeferenced data as MTInSAR products is represented by Geographic Information Systems (GIS).

GIS is a powerful tool in several research fields and applications for spatial analysis and informed decision-making, through aggregation, management, and visualization of georeferenced data. When referring to displacement monitoring through MTInSAR data, scientific literature proposes different examples showing the combination and analysis of multi-sources data in GIS environment (Bordoni *et al*., 2017; DePrekel, Bouali and Oommen, 2018; Macchiarulo *et al*., 2022; Meisina *et al*., 2008). One of the most popular applications in which MTInSAR data is employed is the ground-motion detection of large areas. Bordoni *et al*. (2017) and Meisina *et al*. (2008) focused on this topic by post-processing InSAR data through a working chain based on different open-source software. In their works, PS displacement time series accuracy was evaluated to improve the reliability of result and the identification of areas characterized by anomalous displacements was achieved by aggregating PS displacement time series with terrain data (i.e. geological, geotechnical, hydrogeological, and land use information) and DEMs through GIS tools. Talking about infrastructure systems, DePrekel, Bouali and Oommen (2018) and Macchiarulo *et al*. (2022) studied deformation of a wide area through MTInSAR data. Using GIS tools, zones of maximum ground-displacement were identified from SAR data and the use of descriptive database of road networks was useful for identifying assets towards local analysis were performed to describe their deformation mechanism (e.g., long-term downward displacements, correlated with the regional subsidence). The application on real case studies demonstrated that the procedures were suitable for the screening of large transportation networks and for the identification of infrastructures requiring further investigations. Other examples on MTInSAR and GIS data integration for infrastructure displacement monitoring can be found in Ciampoli *et al*. (2019) and Vaccari *et al*. (2018).

Although not exhaustive, this brief literature review highlighted the main advantages and shortcomings about the integration of satellite data with GIS software, with the possibility to perform different operations. As main advantage, GIS software allows users to display PS displacement time-series through opensource plugins avoiding the use of external data visualization tools. Furthermore, GIS tools facilitate the geoprocessing of LoS displacements (e.g., projections along desired directions, calculation of displacement velocities) and the integration of free road maps inventories, such as OpenStreetMap (OSM, 2024), allows the user for the proper selection of PS in an easier and automatic way. Close to the above advantages, some issues should be highlighted. Most of the above operations require time and manual actions by users, as well as basic knowledge of programming languages. To facilitate the automation and the assessment of bridge displacements at portfolio scale through MTInSAR data (according to the proposed framework in Section 1.2.1), a new and comprehensive GIS plugin is necessary, able also to automatically check the occurred displacement towards specific thresholds for the purpose of early warning. With this goal in mind, BAS-MTInSAR is developed and herein proposed with a full description of its GUI, functionalities, and working principles.

BAS-MTInSAR (Calò *et al*., 2024b; Calò *at al*., 2024c) was developed for QGIS application and was idealized at this stage for accounting simply supported concrete girder bridges, which, as already discussed, is the most spread bridge typology in Italy and Europe. The framework at the base of BAS-MTInSAR is shown in Fig. 42, while Section 1.2.3.1 reports a summary of the analytical steps of the automated analysis already proposed in Section 1.2.1 and Section 1.2.3.2 presents the GUI.

1.2.3.1. *Analytical steps*

BAS-MTInSAR is designed to automate and guide practitioners towards the application of laborious analytical steps for structural interpretation of bridge displacements. The modules implemented in the plugin GUI take advantage of the most promising techniques reported in scientific literature on the topic (Calò *et al*., 2024a) and extend their content providing an additional displacement scenario and the structural

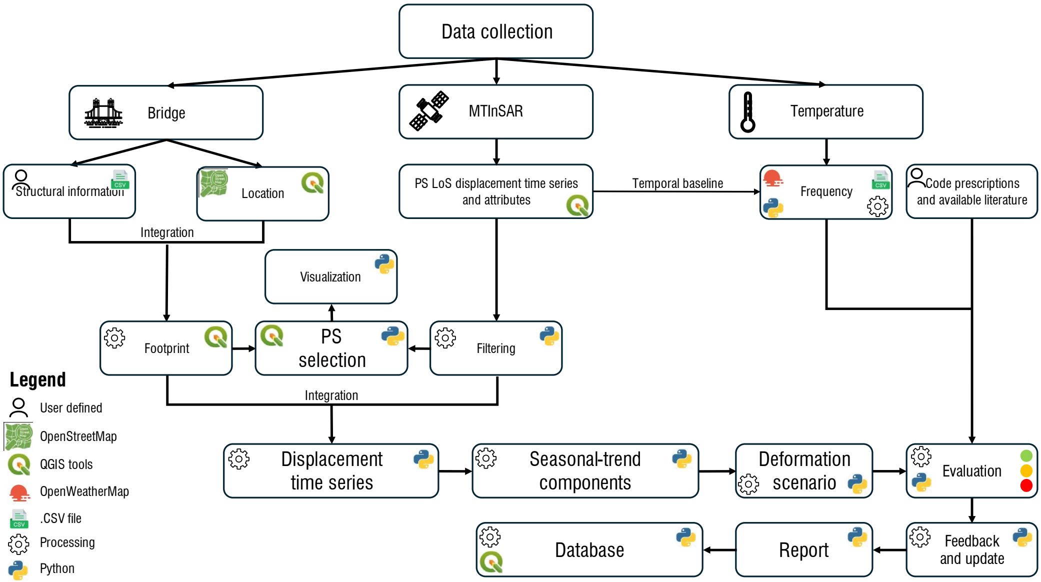

Fig. 42 - Framework of BAS-MTInSAR.

interpretation of bridge displacement time series. The following steps are required to achieve the structural assessment through MTInSAR data.

STEP 1: Data collection and PS selection.

Step 1 regards the collection of input data about the geometrical (e.g., bridge centerline, number of spans, deck and beam section, bearing distribution), mechanical (e.g., E_c and α_{CTE} of concrete) and location (e.g., latitude, longitude, altitude) characteristics of the bridge. Temperature data (e.g., average temperatures recorded at weather stations near the bridge), and satellite data of the COSMO Sky-Med type (i.e., at the best spatial

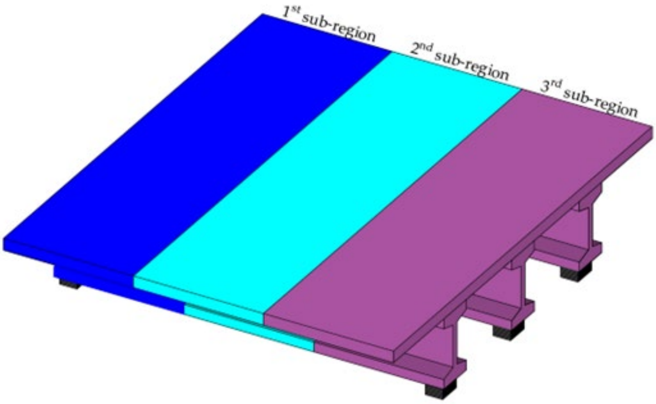

Fig. 43 - Example of simply supported deck divided in three equally distributed sub-regions: 1st sub-region (blue) near the pinned support, 2nd sub-region (cyan) at mid-span, 3rd sub-region (purple) near the roller support. The bearing typology shown in the example is the unbonded elastomeric, where the greater the bearing height, the lower the translation stiffness (i.e., higher displacements).

resolution, 3 x 3 m) from ASC and DSC acquisition geometry are needed as well. The latter, as explained in Section 1.1, can be used in the proposed analysis only if processed by means of MTInSAR algorithms. Location and some geometrical characteristics of the bridge (bridge centreline, deck width, and altitude) are used to define the georeferenced footprint of the structure (Section 1.2.1.3). The other geometrical characteristics like beam and deck sections and the bearing distribution are exploited in combination with mechanical features of the bridge to describe the expected behaviour of the deck under service conditions (see Step 4).

Once the bridge is identified, each span is subdivided into three sub-regions (i.e., the two at the side in correspondence of the bearings, 1st and 3rd sub-regions, and one in the middle at mid-span, 2nd sub-region, Fig. 43) considering their different structural behaviour under service conditions, as shown in Step 4.

After the elaboration of satellite data via MTInSAR algorithm, the obtained PS are carefully selected to provide bridge-related information. For this purpose, hierarchical selection criteria are proposed (Section 1.2.1.3) based on: (i) localization of PS and mutual position with the footprint (in plan and height), considering inaccuracies due to SAR acquisition geometry and MTInSAR algorithms elaborations; (ii) coherence of the

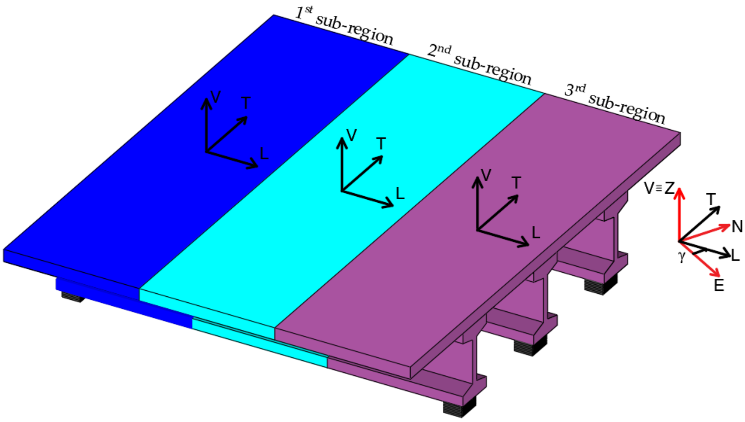

Fig. 44 - Example of simply supported deck together with M-LCRS reference system, in black, for each sub-region. In this case, each sub-region of the bridge is rotated by γ angle with respect to the East direction, reported by the red reference system (i.e., East-North-Zenith).

PS; (iii) V_{LoS}. At the end of this step of the analysis, the centroid of each sub-region is described by two average displacement time series along the LoS derived from the retained PS, one for each acquisition geometry (i.e., ASC and DSC). In addition, time sampling processing of the time series is required to align the data obtained from the ASC and DSC datasets for subsequent combination in Step 2.

STEP 2: Displacement time series along bridge main axes.

Disposing of the two timeseries for each centroid of sub-regions, their combination and projection is preformed according to Equation (21) in a new reference system, named M-LCRS, Fig. 44.

STEP 3: Definition of seasonality and trend for each displacement component.

At this point, d_L and d_V time series obtained from Equation (21), under the assumptions explained in Section 1.2.1.5, can be processed via mathematical models to derive their trend and seasonality. Step 3 is required because, although useful information can be gained by the time series, the strong trend component (e.g., in the case of subsidence

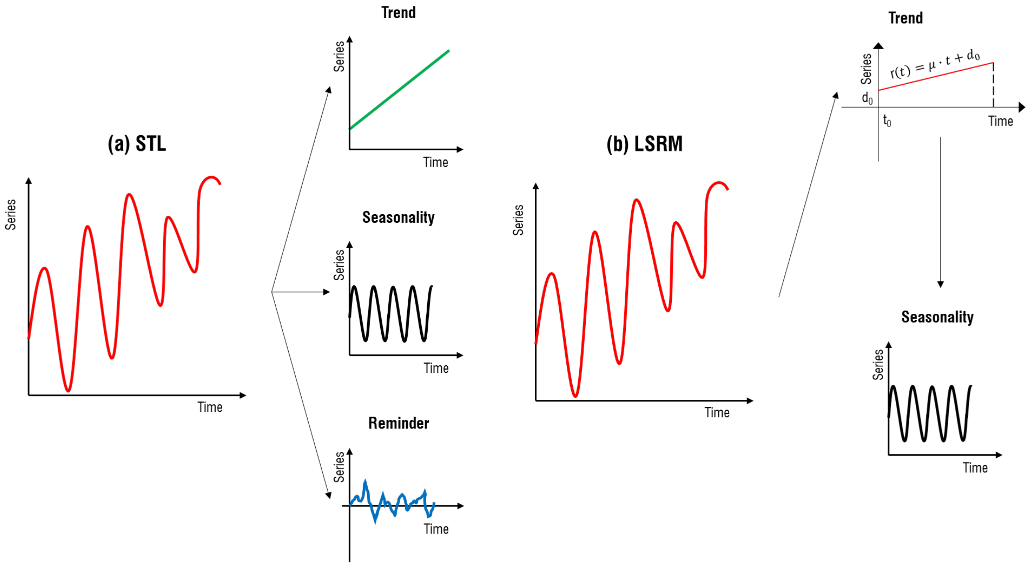

Fig. 45 - Example of (a) STL and (b) LSRM decompositions of a generic time series from Step 2.

for vertical component) could hide the seasonality. As reported in 1.2.1.6, the use of a literature model called STL is suggested, Fig. 45(a). Still, in the case of bridges characterized by many spans, the computational time needed for the decomposition could require faster algorithms, especially in the case of large portfolios screening. Hence, another approach is proposed in which the generic time series is considered as the combination of only trend and seasonality. Specifically, the trend displacement-time series is computed as a sequence of values obtained by multiplying μ, in Fig. 45(b), by the progressive acquisition time. The seasonality is calculated by subtracting the trend component from the original time series. Although less accurate than STL, which uses a moving average algorithm to characterize trend and seasonal components and their variation over time, this option speeds up the evaluation process. The retrieved components are used in the next Step to compare bridge displacements under service conditions and recognize proper displacement scenarios.

STEP 4: Displacement scenarios and structural interpretation.

The information regarding trend and seasonality from Step 3 can be compared with proper thresholds based on the expected behaviour of the bridge under service conditions. Generally, this bridge typology can exhibit longitudinal and vertical seasonal displacements. Seasonal longitudinal displacements are related to a constant temperature gradient, ΔT_C, defined on the daily average temperature during the SAR observation time. The threshold, calculated on the base of the analytical models in Fig. 46(a), consider two extreme configurations of the span: (i) maximum elongation from pinned to roller support under a positive ΔT_C; (ii) maximum shortening from roller to pinned support under a negative ΔT_C. Vertical seasonal displacements are one of the novelties proposed with BAS-MTInSAR and are linked to a linear temperature gradient, ΔT_L, across the deck section. The use of ΔT_C does not account for the temperature difference between the upper and lower sides of the deck. Indeed, these two regions can be characterized by different temperatures due to the solar radiation (road pavement hotter than the lower side of the deck) and to the presence of snow/thin layer of ice (road pavement colder than the lower side of the deck) in summer and winter, respectively.

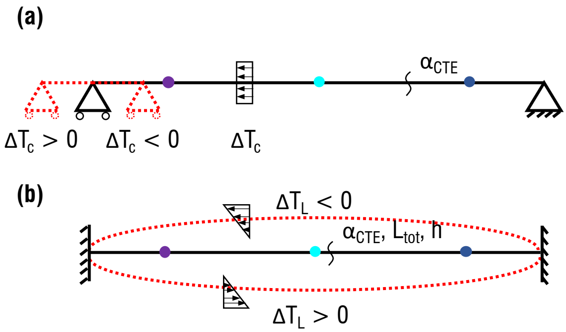

Fig. 46 - Example of displacement scenario and simple analytical model employed (coloured dots represent sub-region centroids): (a) Free longitudinal displacements under constant temperature delta, ΔT_C. Dashed shapes show the deformed configuration of the deck under positive and negative ΔT_C; (b) Vertical displacements under linear temperature delta, ΔT_L. Dashed shaped show the deformed configuration of the deck under positive and negative ΔT_L.

Thus, the additional displacements under ΔT_L are considered only in the vertical direction under a different static scheme reported in Fig. 46(b). In this case, the deformed shape of the bridge is not characterized by progressive elongation/shortening from pinned to roller support as under ΔT_C. The linear temperature gradient ΔT_L induce an upward deflection during summer and a downward deflection during winter. The threshold for the vertical seasonal displacement scenario is computed as:

$$\delta_v = \frac{\alpha_{CTE}\Delta T_L}{2h} L_{tot}^2 \tag{28}$$

where h and L_{tot} are the height and length of the deck defined in Step 1.

Still, other displacements components could characterize the bridge, both longitudinal and vertical, which cannot be considered as service conditions. Regarding vertical trend components, the difference of cumulative displacements of sub-regions is used to discern among three different deformation scenarios (described in Section 1.2.1.7): (1) increasing gravity loads/material degradation; (2) subsidence; (3) differential displacements.

Longitudinal trend component scenario is a novelty proposed with BAS-MTInSAR. In this case, the deformation scenario is related to landslides and the range of velocities for vertical trend scenario (2) and (3) are extended to the longitudinal trend scenario. The threshold is compared to the absolute value of the average velocities of sub-regions.

To provide a structural interpretation of the displacement time series and insights to practitioners and bridge inspectors, the characteristics of bridges collected during Step 1 are considered. In detail, possible bearing malfunctions or wrong information from design documents are recognized starting from longitudinal seasonal component of 1st and 3rd sub-regions and bearing distribution provided to the tool (see Section 1.2.3.2). Given the bridge typology under investigation, bearings are usually roller on one side of the span and pinned on the other one to ensure the longitudinal thermal dilation of the deck. Hence, longitudinal displacement due to ΔT_C are incremental and phase aligned from pinned toward roller bearings for each sub-region. In the case of longitudinal seasonal components of 1st and 3rd sub-regions in reverse phase, bearing can be assumed as both rollers. BAS-MTInSAR, checking the bearing distribution with the longitudinal seasonal displacement time series, provides two different attention messages: (i) bearing malfunctions, in the case of reverse phase; (ii) bearing malfunctions/incorrect design documentation, in case displacements are incremental from roller toward pinned supports. In both cases, a visual survey is suggested. Other attention messages suggesting visual surveys are prompted for longitudinal and vertical trend components. For the longitudinal one, considering the use of thermal joints, e.g., between spans and abutments on the side of roller bearings, the occurrence of increasing longitudinal displacements higher than 2 mm/y could provide damage. For the vertical component, the potential structural damages identified are different depending on the abovementioned differences between cumulative displacements of sub-regions and thus identified displacement scenario: (1) cracks and/or corrosion are expected on girder beams; (2) possible damage on transition zones when the bridge deck and the abutments are moving away from each other in the vertical direction; (3) possible pavements discontinuities due to the vertical relative movement between two adjacent spans or between side span and abutment.

It is worth reminding that the output of the proposed procedure (Section 1.2.1) cannot be confused with a structural analysis of bridges in the investigated portfolio, but it aims to provide insights towards the ideal behaviour that this bridge typology should exhibit during their service life. Furthermore, the obtained results could be integrated with other tools (e.g., Nettis *et al.*, 2024) for the purpose of bridge portfolio assessment.

1.2.3.2. GUI description

As evidenced in the analytical description of Section 1.2.3.1, BAS-MTInSAR is designed to integrate multi-sources data. This is possible thanks to Python modules running on 3.9 version (e.g., Pandas, NumPy, Matplotlib, Shapely, Scikit-learn) and QGIS tools recalled through Python API (i.e., PyQGIS) implementing all the steps described in the previous Section 1.2.3.1. Another strength point of BAS-MTInSAR is its subdivision into separated modules. Each module can be used on its own and extended/integrated with other modules to customize the assessment based on the specific needs. The use of BAS-MTInSAR is proposed with a GUI designed with QT

Designer 5.15.2 and including QGIS widgets coded through Qt Designer Python API (i.e., PyQt5). The main functionalities and the most recurrent elements characterizing the GUI are following listed:

- QDialog, top-level window used to store other elements of the GUI.
- QTabWidget, stack of tabbed widgets.
- QFrame, frame to store and organize elements of the GUI.
- QGroupBox, group box frame with a title.
- QComboBox, combines a button with a dropdown list (mainly layer of the QGIS project in this application).
- QgsFileWidget, provides a dialog that allows users to select files or directories (mainly .CSV files in this application).
- QTableWidget, table to store and visualize numerical and categorical data.
- QSpinBox, spin box widget.
- QCheckBox, checkbox with a text label.
- QPushButton, command button to perform actions when pressed.
- QLineEdit, one-line text editor for textual input.
- QTextEdit, used to edit and display both plain and rich text.

- QLabel, text or image display.

- QStackedWidget, a stack of widgets where only one widget is visible at a time.

- QWidget, base class of all user interface objects.

- QListWidget, list of elements.

The main objects of the GUI, i.e., the most used and recurrent in the tool, are illustrated in Fig. 47, which reports the indication about the look of the tool, without data. BAS-MTInSAR plugin is structured in different QDialog windows to optimize its layout and the distribution of functionalities and information. The main QDialog window is named "Bridge Analysis", Fig. 47, containing a QTabWidget of 6 tabs.
The first tab is named "Data collection" (Fig. 47) and is used by practitioners to define all input information required for the step analysis described in Section 1.2.3.1. Starting from bridge data, organized in three separated QFrame, the minimum requirements to characterize the structure are: (a) geo-localization; (b) beam and deck transverse cross-sections; (c) position and distribution of pinned and roller bearing devices; (d) E_c. All mentioned data are usually available to transportation management companies and stored in various forms depending on their bridge management system. BAS-MTInSAR exploits two ways to import data: (i) shapefiles through QComboBox; (ii) .CSV files through QgsFileWidget. Depending on the completeness of imported data, QTableWidget automatically shows a summary of data, allowing the manual input of missing ones. Other automatic operations performed by BAS-MTInSAR, in this first phase, consists of generating the footprint of the bridge and the subdivision of each span into three sub-regions (**Fig. 43**). This process, based on QGIS tools, leads to generate a new polygon shapefile to store the sub-regions characterized with proper attributes (i.e., the ones in the QTableWidget and Fig. 48). Indeed, each sub-region is characterized, for

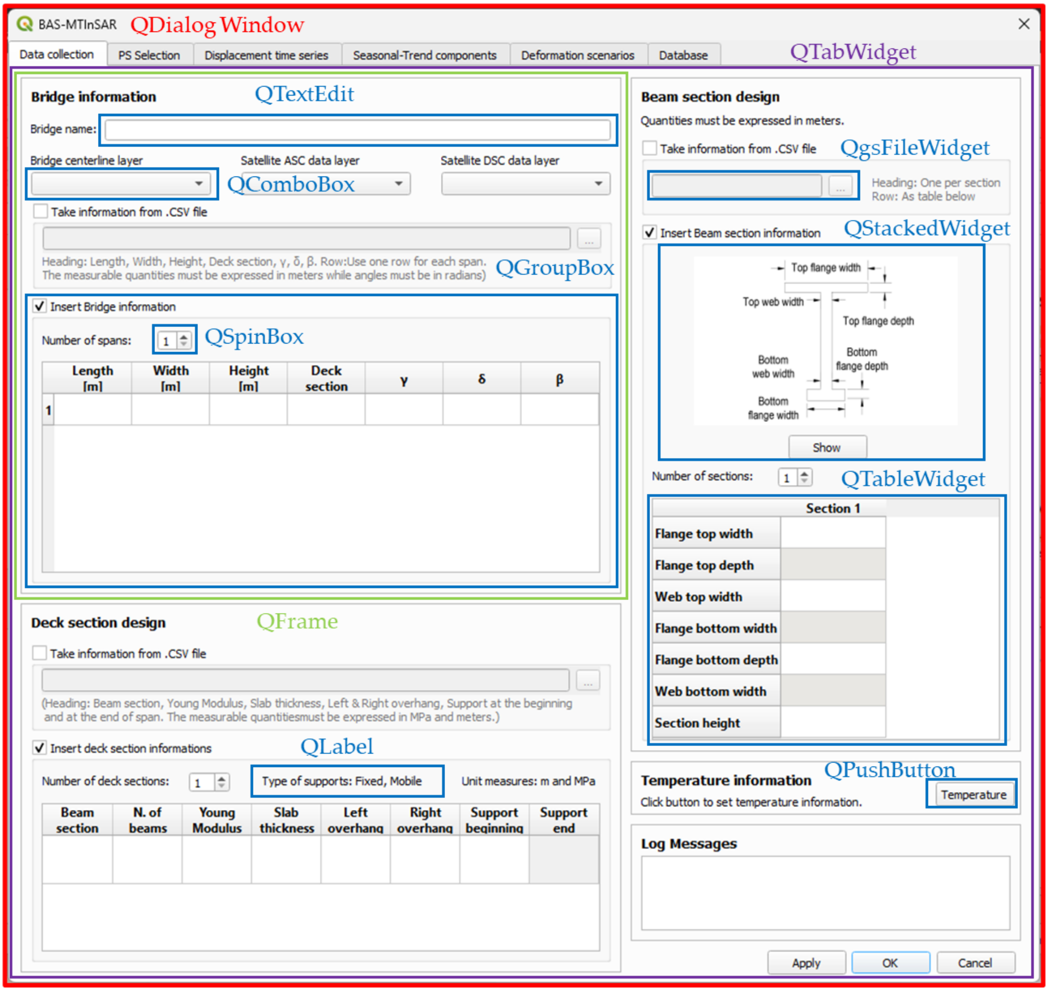

Fig. 47 - QDialog window named “Bridge Analysis” with boxed the most recurrent GUI elements employed in BAS-MTInSAR.

example, by height, bearings distribution, beam sections and by J_{deck}. The latter, calculated from the geometry of beams (“Beam section design” QFrame, only T or double T type) and deck (“Deck section design” QFrame), is required in Step 4 of Section 1.2.3.1 for the threshold definition. Fig. 48 shows the geometrical quantities used for the definition of J_{deck}. At this stage, such beam typologies are the only available for design, which anyway cover a wide range of cases. Further developments of the tool will be aimed at implementing other beam cross-section type definition (e.g. U-shaped, box).

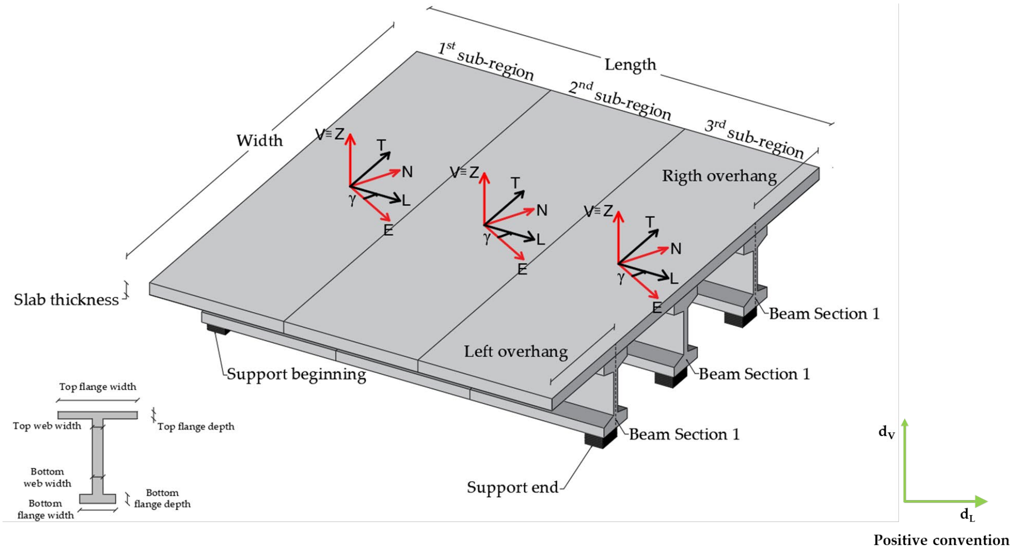

Fig. 48 - Deck and beam information defined in the QTableWidgtes of “Deck section design” and “Beam section design” QFrames for a single span. Green reference system on the right shows the convention sign for bridge displacements of Step 2 and 3 in the case in which the bridge centreline is drawn from the left to the right, which is from the beginning of 1st sub-region to the end of 3rd sub-region in figure.

Regarding the other two sources of data, MTInSAR and temperature, similar options are given for their import (i.e., shapefiles for MTInSAR data, one for each acquisition geometry, and .CSV for temperature data). BAS-MTInSAR extracts information about PS required for Step 1 and 2 of Section 1.2.3.1. Lastly, to ease the data collection process, BAS-MTInSAR provides practitioners the possibility to automatically download and process the temperature records from a free API service named OpenWeatherMap. The temperature data definition, included in the “Temperature” QDialog window (see Section 4), can be combined with the use of a cosine temperature model, Equation (23), in case of missing daily average temperature values in correspondence of the temporal baseline defined by time sampling processing of the two satellite acquisition geometries. The fitting process, automated in Python, can be shown by the user in the same QDialog window. All the above steps are tracked in a log messages box, designed with a QTextEdit, containing also warnings due to, for example, mismatching of data types (e.g., strings instead of numbers in QTableWidget of bridge information).

The tab named “PS Selection” allows criterion-based PS selection as described in Step 1 of Section 1.2.3.1. The view, organized by spans and acquisition geometries, can be updated every time a new attribute is considered. To enhance the informed selection of PS, BAS-MTInSAR GUI allows users to observe the PS distribution on the span and by left click on them to examine their attributes on the right of the plots. Moreover, by right-clicking with the cursor on a PS, its LoS displacement time series is prompted in a new QDialog window. Once the practitioner is satisfied with the selection of PS, the average displacement time series is computed and can be observed in the tab named “Displacement time series”. In this latter, organized by spans as the previous one, BAS-MTInSAR shows LoS (two Qframe on top) and projected (two Qframe on bottom) average displacement-time series of centroids of sub-regions and related quantitative information (i.e., velocities, standard deviation of velocities and cumulative displacements calculated as velocities in a time interval). It is worth specifying the sign convention of projected displacements. These components are assumed positive in the direction from the start to the end of the span (this depends on the direction in which the bridge centerline is drawn), projected vertical components are assumed as positive when upwards (Fig. 48).

To derive additional information about trend and seasonality of displacements, the tab named “Seasonal-Trend component” is designed. Both STL and LSRM algorithms described in the Step 3 of Section 1.2.3.1 are available. Results, also in this case organized by spans, are divided in QFrame: (i) the two on the top pertain to the seasonal components, longitudinal and vertical from left to right; (ii) the two on the bottom pertain to the trend components, in the same order as for the seasonal ones. In this case, QTableWidget records different computed quantities, that is, slope, standard deviation, coefficient of determination of LSRM, and the cumulative displacements.

The evaluation of the deformation scenarios and asset management is the core element of BAS-MTInSAR and all data previously elaborated are used in the two tabs named “Deformation scenarios” and “Database”. In “Deformation scenario”, a summary of the required data for the evaluation of scenarios, presented in Step 4 of Section 1.2.3.1, and related results are displayed in different QFrame (i.e., one for each displacement component). Also in this case, the representation is provided separately for each span, to preserve coherence in the GUI. Near to each threshold value, a graphic symbol (green check, yellow triangle, or red triangle) is shown and, to make results checking easier and faster, thresholds QLabel are coloured as the graphic symbol. The scenario assessment is considered positive (green check) if the thresholds are not overcome in the last two years of observation. Otherwise, an attention (yellow triangle) or warning (red triangle) message is issued, depending on the number of years in which the thresholds are exceeded for seasonal components, or on the magnitude of velocities (classified in three ranges) for trend components. The attention message includes a description based on the structural assessment explained in Step 4 of Section 1.2.3.1. It is worth specifying that possible false alarms could arise due to the inaccuracies of satellite data and their manipulations. For this reason, the deformation scenario results should not be used to detect possible damage, but to only for supporting the operation of onsite surveys.

The tab named “Database”, Fig. 49, is designed to navigate through the evaluated bridges and to update results. A list of available bridges is designed to select the desired structure and the information automatically saved through shapefiles are recalled and shown (e.g., observation period, status of each deformation scenario, as the worst through the entire bridge, and its summary). Deformation scenario status can be changed through “Change status” QPushButton, which opens a new QDialog window named “Inspection report”, Fig. 50. In this window, users can declare the date of onsite visual inspection, confirm or clean attention and warning alerts. In the bottom part, a QTableWidget was given for summarizing the number of passed checks, attention and warnings marks for each displacement component through the entire database. The “Show on map” QPushButton was used to locate them in the QGIS visualization environment.

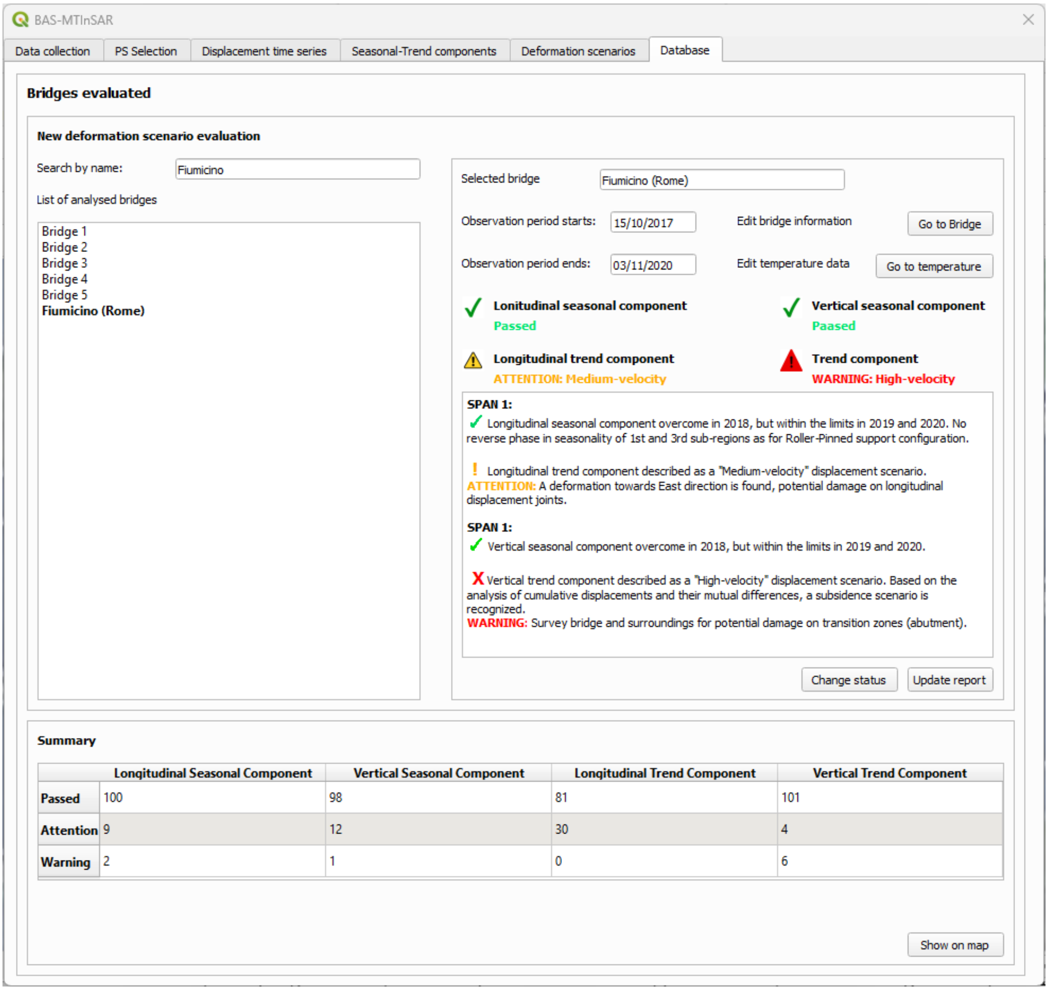

Fig. 49 - "Database" QTabWidget of "Bridge analysis" QDialog window. Listed bridges (e.g., Bridge 1 in QListWidget) and numbers in the Summary QTableWidget are fictitious and added by the author for demonstration purpose only. Fiumicino (Rome) bridge is the one discussed in Section 1.2.2.2.

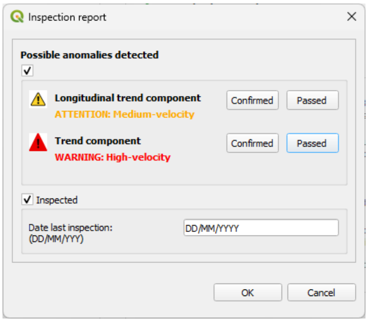

Fig. 50 - "Inspection report" QDialog window.

1.2.3.3. Application of the proposed BAS-MTInSAR plugin

This section is aimed at providing an illustrative and technical application of the proposed BAS-MTInSAR plugin on a single-span simply supported concrete girder bridge, the same described in Section 1.2.2.2 and showed in Fig. 51.

To begin the assessment, a new QGIS project was opened and saved in a directory containing shapefiles of the bridge centerline and of the SPINUA elaborations for ASC and DSC acquisition geometries (main features of CKS datasets in Table 12). After importing the shapefiles into the project, BAS-MTInSAR was executed. As first

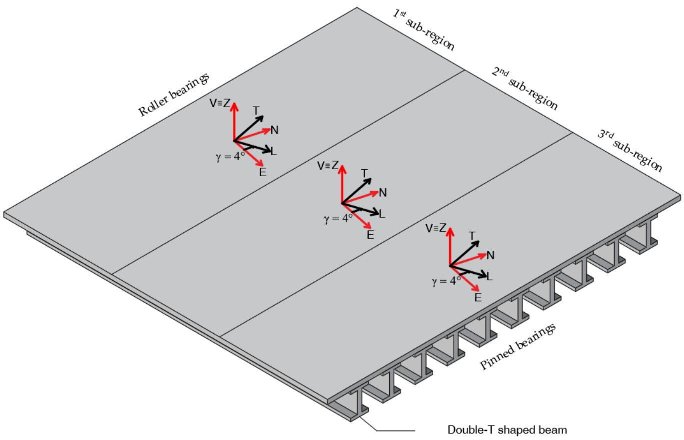

Fig. 51 - Single-span simply supported concrete girder bridge, Fiumicino, Rome (Italy) in a scale axonometric view. The single span bridge, characterized by 10 double-T beams of equal sections is divided into three sub-regions (i.e., 1st, 2nd and 3rd sub-region). The 1st sub-region is characterized by roller bearings, while the 3rd one by pinned bearings.

Table 12 - Characteristics of the employed SAR datasets for the single-span prestressed RC bridge.

Satellite	Mode	Spatial Resolution	Pass type	Time span	Incidence angle θ [°]	Azimuth angle α [°]
CSK	StripMap HIMAGE	3 m x 3 m	ASC	Oct 2017 – Nov 2020	33.282	169.373
CSK	StripMap HIMAGE	3 m x 3 m	DSC	Sept 2017 – Dec 2020	29.550	11.026

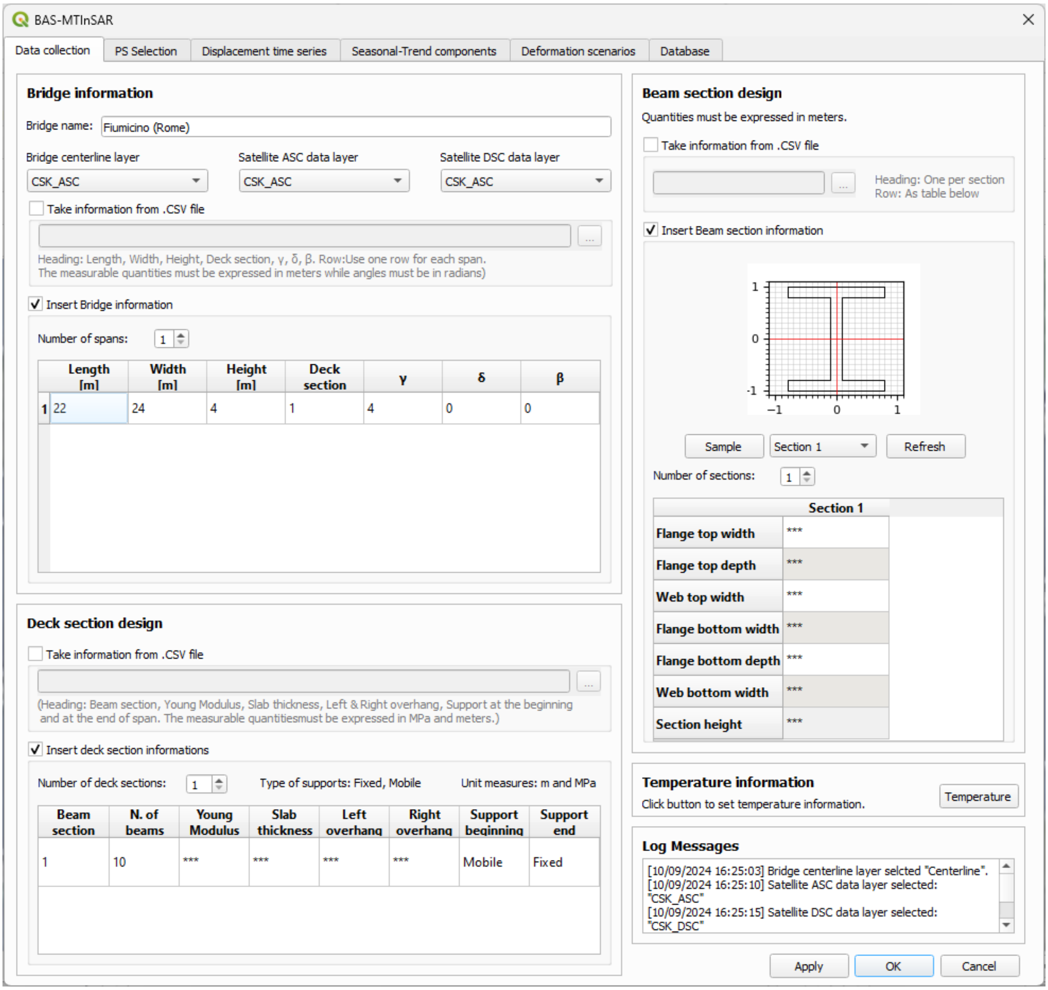

Fig. 52 - Definition of input data through the "Data collection" QTabWidget of "Bridge analysis" QDialog window. "Deck Section design" and "Beam Section design" are defined according to Fig. 44, resulting into Fig. 51.

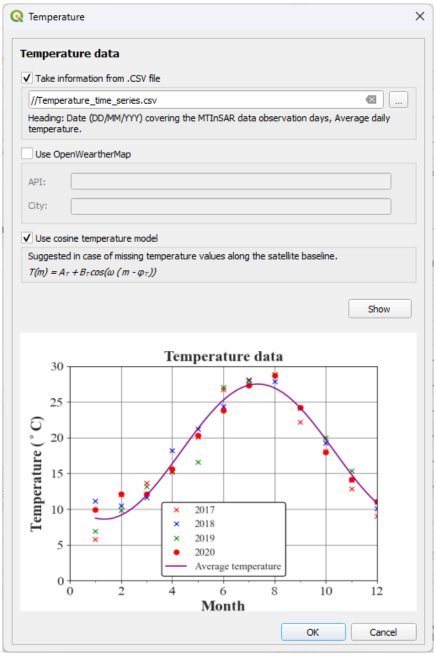

Fig. 53 – Temperature data of the closets weather station. Chart shows monthly average temperature in 2017, 2018, 2019 and 2020 (red cross, blue cross, green cross, red circle respectively) used in the cosine temperature model, Equation (23). Purple line is the cosine model whose parameters are the average of the model itself fitted over each year of temperature acquisition.

step, the abovementioned layers were uploaded, and incomplete structural information contents were implemented, Fig. 52. The double-T beam section was defined and assigned to the deck in a number equal to 10. Environmental temperature data were available from the closest weather station and were processed with the cosine temperature model, Fig. 53, due to many missing values along satellite temporal baseline.
After, the PS selection was performed (Fig. 54), using only height criterion due to the few retained PS in each sub-region (i.e., 1st, 2nd and 3rd) in the case of multi-criteria selection defined in Step 1 of Section 1.2.3.1. All the selected PS were characterized by a negative V_{LoS} value in both acquisition geometries (e.g., L20967P02301 for ASC and L20967P0485 for DSC in Fig. 54). Indeed, observing average displacement time series along the LoS direction in the “Displacement time series” tab (top

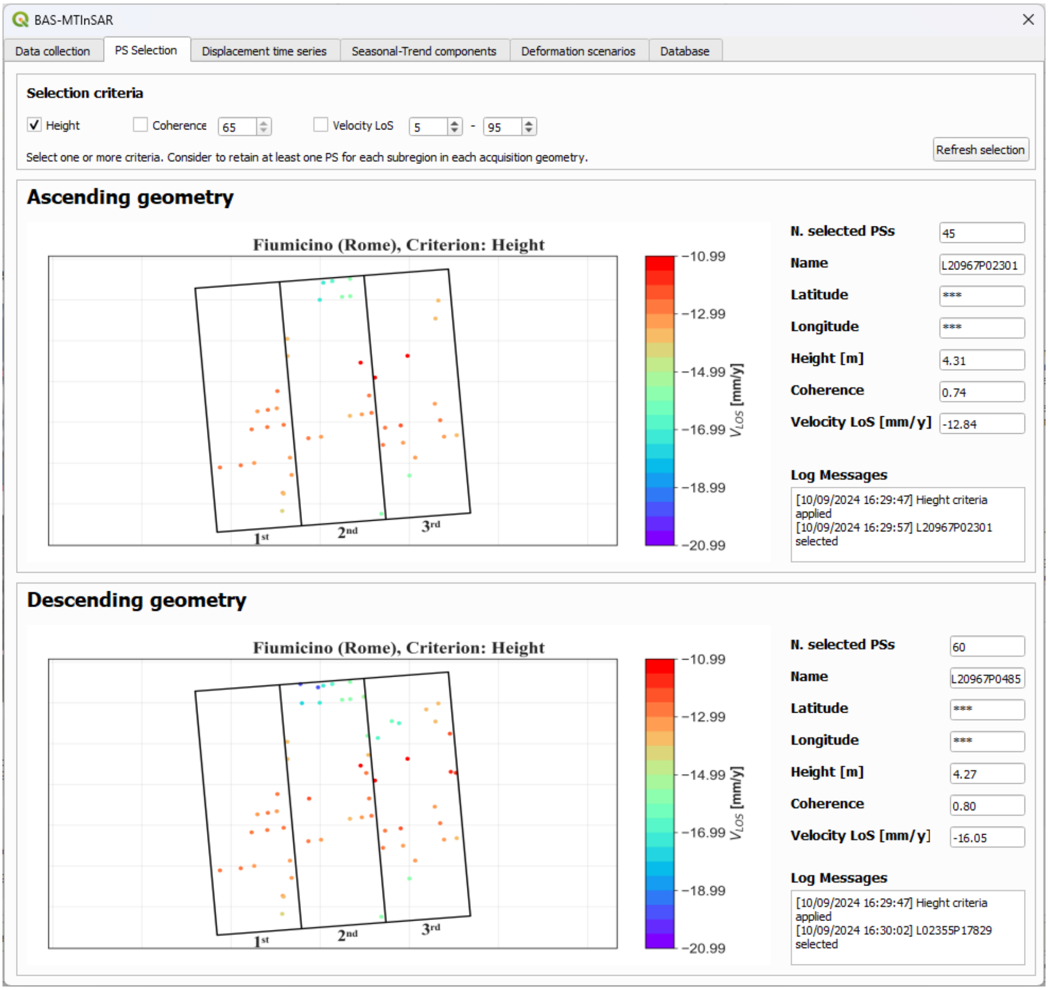

Fig. 54 - "PS Selection" QTabWidget of “Bridge analysis” QDialog window.

QFrame in Fig. 55) only negative V_{LoS} values were reported. They were ranging from -12.40 to -13.72 mm/y, together with negative values of the cumulative displacements, comprised between -37.87 mm and -46.44 mm. Given the convention sign of LoS reported in Section 1.2.1.4, PS are moving away from the satellite in both acquisition geometries.

To gather information regarding the displacement components along bridge axes, the ASC and DSC datasets were combined and projected considering the orientation of the bridge defined by γ angle equal to 4°, Fig. 51 and Table 9. A strong negative

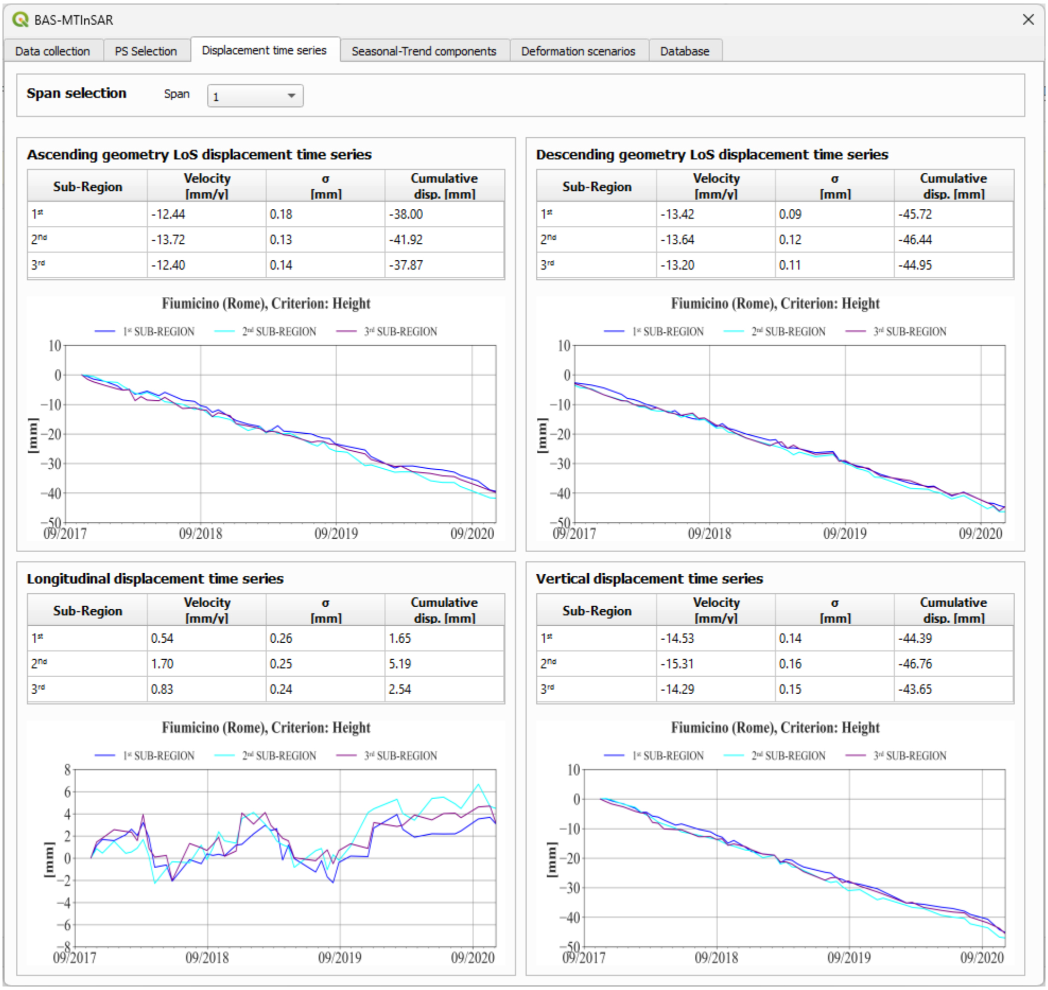

Ascending geometry LoS displacement time series

Sub-Region	Velocity [mm/y]	σ [mm]	Cumulative disp. [mm]
1st	-12.44	0.18	-38.00
2nd	-13.72	0.13	-41.92
3rd	-12.40	0.14	-37.87

Descending geometry LoS displacement time series

Sub-Region	Velocity [mm/y]	σ [mm]	Cumulative disp. [mm]
1st	-13.42	0.09	-45.72
2nd	-13.64	0.12	-46.44
3rd	-13.20	0.11	-44.95

Longitudinal displacement time series

Sub-Region	Velocity [mm/y]	σ [mm]	Cumulative disp. [mm]
1st	0.54	0.26	1.65
2nd	1.70	0.25	5.19
3rd	0.83	0.24	2.54

Vertical displacement time series

Sub-Region	Velocity [mm/y]	σ [mm]	Cumulative disp. [mm]
1st	-14.53	0.14	-44.39
2nd	-15.31	0.16	-46.76
3rd	-14.29	0.15	-43.65

Fig. 55 - "Displacement time series" QTabWidget of “Bridge analysis” QDialog window.

vertical component was identified for each sub-region with similar velocities (between -14.29 mm/y and -15.31 mm/y) and cumulative displacements (between -43.65 mm and -46.76 mm) to the ones along the two LoS (bottom right QFrame in Fig. 55). This result was expected for two reasons: (a) subsidence phenomena affect the area, due to its hydro geomorphological context (Nettis *et al*., 2023a; Orellana *et al*., 2020); (b) SAR data reported negative LoS displacements in both acquisition geometries with similar velocities, which is symptomatic of a strong vertical displacement component for the focused structure (REA-CNR, 2021). Lower values of velocity, 1.7 mm/y, and cumulative displacements, 5.19 mm, were identified for the longitudinal component. Positive values of the longitudinal component were oriented in the West-Est direction, considering the bridge centreline drawn direction from left to right (West to East), Fig. 51.

The seasonality of the vertical projected component was masked by a strong trend, making its evaluation almost impossible as in the case previously shown in Section 1.2.2.2 where a longer observation period was considered. Hence, using STL algorithm in “Seasonal-Trend components” tab, Fig. 56, the two components were disjointed confirming the evidence about the vertical trend component. This latter showed maximum velocity and cumulative displacement values, equal to -15.09 mm/y and -46.12 mm, respectively, in correspondence of the 2nd sub-region. On the other hand, a non-linear longitudinal trend component between 1.06 and 2.34 mm/y was found (from West to East), based on the LSRM over the nonlinear trend. Seasonal components showed almost regular seasonality for longitudinal and vertical component, respectively. This information was used in “Deformation scenario” evaluation tab, Fig. 57, according to the convention sign reported in the green reference system of Fig. 58 (positive d_L from left to right, positive d_V upward).

Starting from seasonal components, the average temperature at the beginning of the observation period (T_{REF}) calculated from the cosine temperature model, Fig. 53, was equal to 17.3 °C. From the same data source, exploiting minimum (T_{MIN}) and maximum (T_{MAX}) temperatures in the observation period, 8.6 and 27.5 °C respectively, two ΔT_C were calculated to define longitudinal thresholds (herein named positive and negative displacement available). For the vertical seasonal component, a linear gradient temperature of 5°C was assumed according to code prescriptions (MIT, 2018). For both seasonal components, the deformation scenario assessment was successful, Fig. 57. In this figure, thresholds values (red patches) were reported and their overcoming was registered only in the case of longitudinal seasonal component in March and June of 2018. Given the assumption of neglecting the overcoming in the last two years of observation, the assessment is considered positive. The same result can be highlighted for the control performed on bearings. Indeed, based on design documents, the bridge

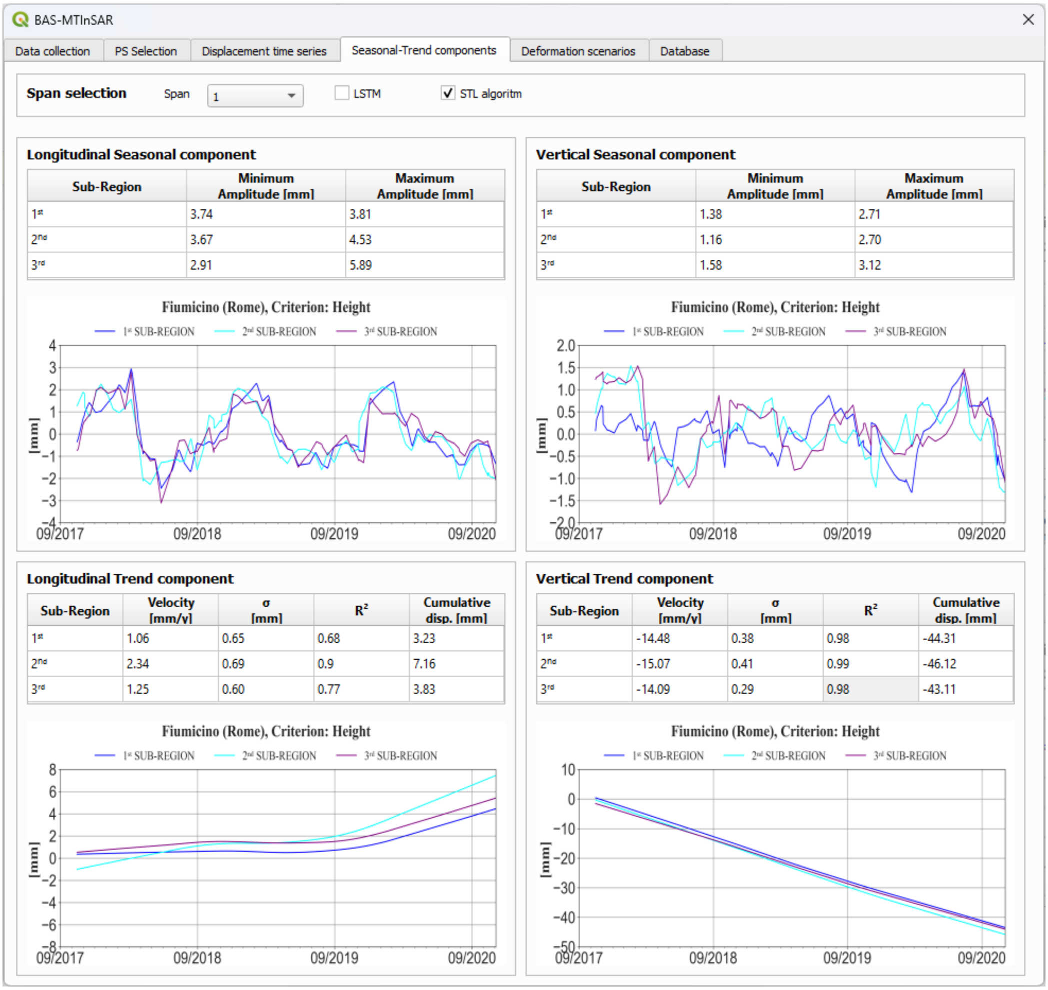

Fig. 56 - "Seasonal-Trend components" QTabWidget of "Bridge analysis" QDialog window.

is characterized by roller supports at the beginning of the span (i.e., 1st sub-region) and pinned at its end (i.e., 3rd sub-region). According to this information and to bridge centerline drawn direction, from which the abovementioned convention sign depends, the maximum (i.e., positive) longitudinal seasonal displacements should occur in the coldest months of the year (in Italy typically from December to February, Fig. 53). The ΔT_C of – 8.7 °C, equal to $T_{MIN} - T_{REF}$, induce a shortening (negative displacement available) of the deck of 1.9 mm from roller to pinned support as reported by the blue dashed lines of Fig. 58(a). On the other hand, during the hottest months of the year (in Italy

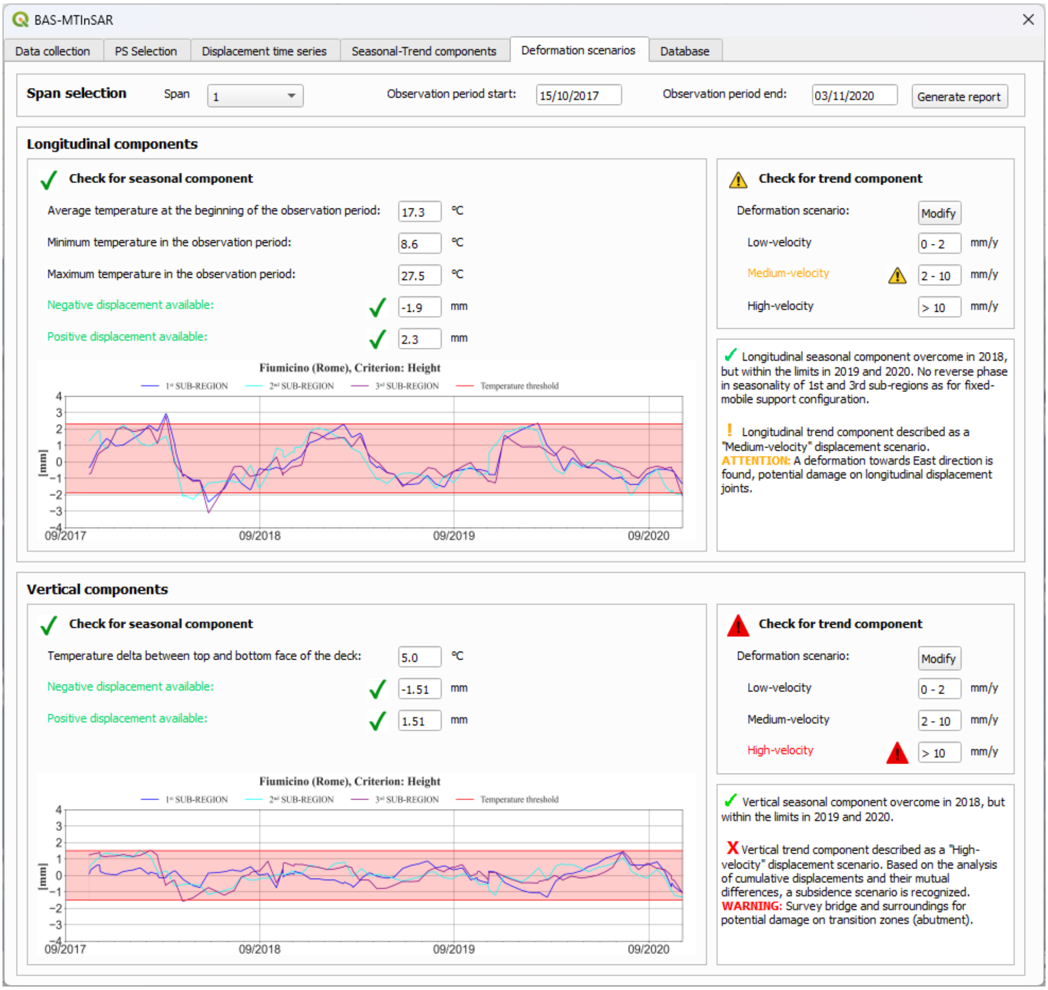

Fig. 57 - "Deformation scenarios" QTabWidget of “Bridge analysis” QDialog window.

typically from June to August, Fig. 53), the ΔT_C of 18.9 °C, equal to $T_{MAX} - T_{REF}$, induce an elongation (positive displacement available) of the deck of 2.3 mm from pinned to roller support as reported by the red dashed lines of Fig. 58(a). The phase of the three seasonal longitudinal displacements time series was aligned, and the shortening (positive displacement) was found around January in each year, Fig. 57. Thus, the bridge is behaving according to the bearing distribution reported in the design documents, finding a coherence in vertical seasonal displacements. Looking at the static scheme in Fig. 46(a) and time series in Fig. 57, a negative ΔT_L of 5°C inducing positive upward

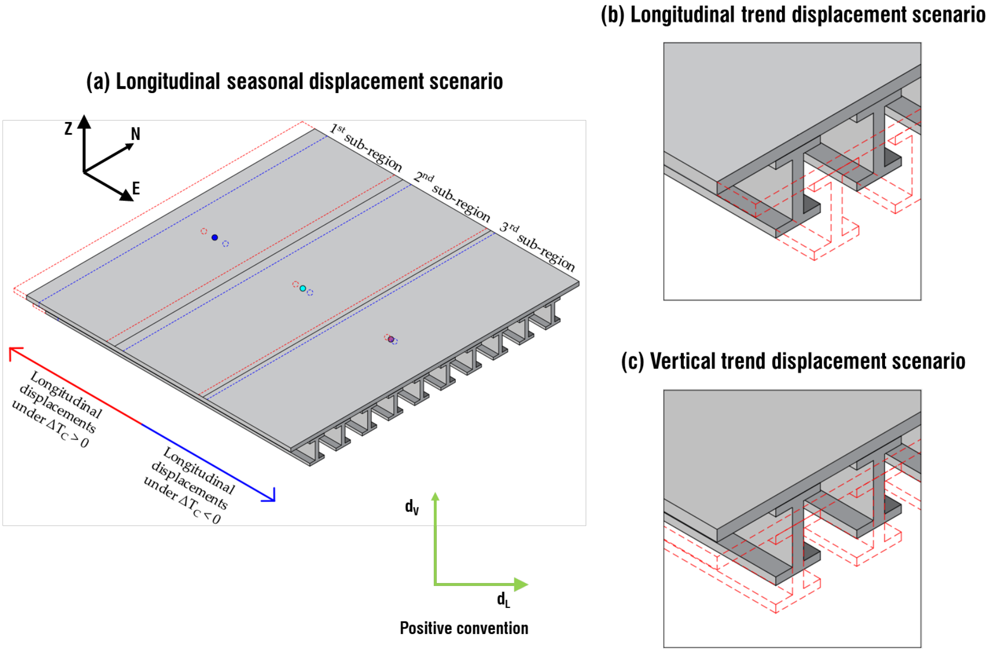

Fig. 58 - Some of the evaluated bridge displacement scenarios on the Fiumicino (Rome) bridge. (a) Longitudinal seasonal displacement scenario, dashed lines represent the deformed shape of the bridge under ΔT_C. Red lines refer to a positive ΔT_C (negative displacement), blue ones to a negative ΔT_C (positive displacement); (b) Longitudinal trend displacement scenario, focus on 3rd sub-region with dashed lines showing a uniform positive displacement toward East (black reference system on top left); (c) Vertical trend displacement scenario, focus on 3rd sub-region with dashed lines showing a uniform downward negative displacement. Deformed shapes of the span are not scaled and represented only for description purpose.

displacement is found in the winter, typical of a deck surface colder than its lower face. Given the confinement of the vertical seasonal displacements within the proposed thresholds for this assessment scenario, the two thresholds proved to be effective and descriptive of the bridge typology under investigation. Different results were obtained for trend components. A medium-low velocity scenario was found for the longitudinal component toward East direction, suggesting the attention for potential damage on longitudinal displacement joints (i.e., in case the bridge deck is moving away from the left abutment in the longitudinal direction). The high-velocity deformation scenario detected on the vertical component was ascribed to subsidence given the negligible difference between cumulative displacements of sub-regions according to its definition in Section 1.2.1.7, with a warning to check potential damage on transition zones (i.e., in case the bridge deck and the abutments are moving away from each other in the vertical direction). Given the extension of the area affected by hydrogeological phenomena, these occurrences may not be found after the onsite survey and the check might be changed to “Inspection report” QDialog window, Fig. 50.

1.3. Conclusions

This Chapter proposed a Multi-Temporal Interferometric Synthetic Aperture Radar- (MTInSAR) based early warning system to investigate structural displacements and slow deformations over time for single/multi-span simply supported prestressed/reinforced-concrete girder bridges. As a main advantage, the proposed framework presents a standardized and scalable series of steps, developed through a Python module, to apply for the purpose of large-scale monitoring of the considered structural typology, one of the most common in bridge portfolios in Italy. The main piece of information employed in the framework are the SAR data, processed by MTInSAR algorithms, demonstrating its effectiveness for near-continuous large-scale monitoring of single structures. The main advantage of SAR data are the image resolution, the frame size, and the short revisit time. However, SAR data are not sufficient for monitoring purposes and therefore need to be supplemented by additional information. Among these, as minimum requirements, environmental temperatures, and structural information from original drawings should be available such as the number of spans, the position, the longitudinal and transversal dimensions, the bearings distribution, and the structural material. Bridge geometrical information and Persistent Scatterers (PSs) attributes are used for PS selection considering both geo-positioning errors and algorithm inaccuracies. After, the bridge spans are considered as homogenous structural units characterized by several Line-of-Sight (LoS) displacement time series, one for each selected PS. Spatial and temporal coherence between the two satellite acquisition geometries must be ensured, and the criteria for performing resampling operations are provided. Each span is then subdivided into sub-regions (at least three parts) to highlight the different structural behaviour between regions close to the bearings and

regions in the middle of the span. Each region is characterized by two average LoS displacement time series, one for each acquisition geometry. Taking advantage from these two and fixing predefined reference directions in the Mobile-Local Cartesian Reference System (M-LCRS), longitudinal and vertical displacements are computed for each sub-region, by employing directional cosines for the LoS vector along the reference directions. The obtained displacement time series can be characterized by a trend and a seasonal component, and both can be evaluated against service conditions (e.g., thermal and traffic/gravity loads). To obtain these seasonal and trend displacement components, a Seasonal Trend LOESS (STL) algorithm is applied. Using straightforward static schemes, likely thresholds for the abovementioned displacement components are established, considering an a-priori unknown deformed shape of the bridge (as systematic over time, starting from the first acquisition).
The framework is applied to two structures representative of the considered structural typology, by using COSMO-SkyMed satellite data retrieved from a five-year observation period. Results were elaborated for each span and the related sub-regions. From longitudinal displacement time series, the related seasonal component revealed unexpected behaviour of the bearings, which differently operates from the ideal situation (i.e., design documents) for both bridges. This is the first valuable piece of information, which could be assessed only through a visual survey. Looking at the results obtained on the remaining displacement components STL model, other considerations can be derived:

- About the multi-span bridge, the temperature threshold is always exceeded during the summer months by sub-regions close to the mobile bearings of 1st and 3rd spans. Moreover, the magnitude of the longitudinal seasonal displacements increased in both summer and winter, which confirmed the above observation on the operation of the supports. Regarding vertical seasonal displacements, no warnings are noticed. Regarding the bridge-specific displacement scenarios, the 1st span falls under Scenario 1 (material degradation) while the 3rd span falls under Scenario 3 (differential displacement). From the comparison of descriptive characteristics with the threshold values, no span was subjected to warnings. Small velocity values are found for longitudinal trend components, which could be due to several causes, such as material degradation or aging.

- On the single-span bridge, a strong trend component related to vertical displacement characterized is found (-15.5 mm/y and a cumulative displacement of almost 80 mm). Regarding the bridge-specific displacement scenarios, Scenario 2 is ascribed to the span (uniform vertical displacement) which was expected from the hydro-geomorphological context of the area. Seasonal temperature displacement components, on the other hand, are observed within limits calculated with simple analytical models. However, no structural damages related to the subsidence should be observed during an onsite survey as the area around the bridge moves along with the bridge itself.

From the application of the proposed procedure, the main pros and cons can be highlighted. As main potentialities, the proposed early-warning system uses SAR data to perform cost-effective long-term structural risk monitoring of existing bridges in a portfolio, by simply elaborating the displacement time series derived by the PSs (i.e., output-only procedure). The identification of possible anomalies, detected comparing displacements along predefined directions with the structural behaviour under service conditions, can be used by transportation management authorities to plan further actions (e.g., specific bridge sensors-based monitoring, traffic limitations). The entire framework is automatic because implemented in a specific Python module, which allows the output to be automatically updated when new input data are available and to perform the monitoring procedure on all bridges belonging to a targeted road network. At this scope, to ease the application of the framework by practitioners, BAS-MTInSAR, a user-friendly GIS plugin with a GUI, was developed.
On the other hand, the main disadvantage is represented by the absence of data. As a matter of fact, if SAR data are not available or the PSs on the focused bridges (or span) are limited, the proposed procedure cannot provide a result. In the end, it is worth noting that the proposed approach cannot replace the traditional monitoring methodologies,

considering the limits characterizing the information contained in the satellite data. Nevertheless, also according to the provisions of the Italian guidelines (MIT, 2020), the approach can be used for large-scale monitoring of bridges within road networks, especially for those phenomena that are difficult to survey through a visual inspection. Future developments will include some enhancements, thanks also to the development of more powerful satellite sensors and to the deployment of new satellite constellations. As first improvement, to acquire more accurate measurements for each sub-region and to characterize regions not covered by PSs, spatial resampling can be pursued. This could be carried out by employing additional models, such as the Inverse Distance Weighted or Kriging techniques. Moreover, due to the deterministic manipulation of both thresholds and displacement time series, a probabilistic approach could be implemented to overcome deterministic risk assessment. Still, other data could be implemented in the proposed framework, considering that it currently works like an "output-only" procedure. For example, information about traffic loads (e.g., average daily traffic, heavy-average daily traffic) could be considered in the procedure as additional input to define more reliable thresholds. Another piece of information, discussed in the following Chapter, can be retrieved by UAV photogrammetry to enhance displacement evaluation on the surrounding area in unurbanized contexts, characterized by a lack of scatterers. Finally, with proper modifications, the method could be extended to other bridge typologies.

CHAPTER 2

PROBABILISTIC-BASED ASSESSMENT OF SUBSIDENCE PHENOMENA ON THE EXISTING BUILT HERITAGE BY COMBINING MTINSAR DATA AND UAV PHOTOGRAMMETRY

In this Chapter, an overview of Unmanned Aerial Vehicles (UAVs) and their applications is presented, focusing on UAV Photogrammetry and related products, such as the Digital Surface Model (DSM). After a literature review about the potentials of this technique as a cost-effective technology for existing built heritage (both buildings and infrastructures) and landslide monitoring, a probabilistic-based approach is presented exploiting the integration of Multi-Temporal Interferometry Synthetic Aperture Radar (MTInSAR) data and UAV photogrammetry (Calò *et al*., 2024d). The idea is to combine the pros of these two techniques while compensating each other's cons. MTInSAR data are used to monitor structural displacements in a millimetre scale and to make up for the absence of scatterers on its surroundings (especially in unurbanized contexts) UAV photogrammetry and derived DSMs are used. Thus, acquiring UAV images at the beginning and end of a fixed observation period, covered by MTInSAR data too, statistical distributions of the spatiotemporal velocities (only the vertical component is assessed) can be processed and evaluated towards a predefined limit state. The obtained results are classified under different scenarios, to reveal the occurrence of possible subsidence phenomena in the structure surrounding and their possible interaction with it. The proposed methodology is firstly validated on a real landslide and, subsequently tested on the multi-span bridge case study described in Chapter 2 for risk prediction. The probability-based framework shows a satisfying capacity of providing warnings to employ in risk mitigation plans, although a qualitative and not quantitative information on the geological risk affecting the focused structure is provided.

2.1. Fundament

2.1.1. Unmanned Aerial Vehicles

An Unmanned Aerial Vehicle or UAV (also known as a drone) is an aircraft without a human pilot on-board and can be piloted remotely or can fly autonomously with predefined paths (Chaurasia and Mohindru, 2021). UAV is a component of an unmanned aircraft system which further includes a remote-control station and a system of communication between the two. UAV is a term mostly referenced to be used in military use cases while in civil it is "drone". A drone is a general term used to refer to the UAVs (Sharma *et al*., 2020). UAVs are becoming increasingly notable because of their applications in several fields and for different scopes (e.g., disaster management and monitoring, Rajan *et al*., 2021; Wang *et al*., 2023, aerial mapping, Samad *et al*., 2013, asset inspection, Montambault *et al*., 2010, precision agriculture, Tsouros *et al*., 2019) depending on the specific payload carrying. Payload is not the only component of a UAV, Fig. 59, but it's the most important one and is chosen depending on the data to be collected during flight and desired output after post-processing. Payloads can include RGB cameras to capture high-resolution optical images, thermal imaging cameras to detect temperature changes, LiDAR sensors to generate detailed

Fig. 59 - Drone (UAV) components. Phantom 4 DJI (DJI, 2024).

three-dimensional maps of terrain and structures, and multispectral sensors. A typical image-based aerial surveying with an UAV platform requires a flight or mission planning and ground control points (GCPs) measurement for geo-referencing purposes. After the acquisitions, images can be used for stitching and mosaicking purposes, or they can be the input of the photogrammetric process to generate a Digital Surface Model (DSM).

2.1.2. UAV Photogrammetry

In general, the UAV photogrammetry consists of the use of a UAV for collecting images about the area to survey, which in turn are processed (e.g., superposition) to generally create a point cloud. This latter can be defined as a set of georeferenced points (i.e., identified in a three-dimensional reference system) representing objects in the investigated area. The first step to attain a UAV photogrammetry product (e.g., DSM) is the flight plan which is as import as the acquisition process (Nex and Remondino, 2014). In this initial phase all interferences and constraints must be considered and in order to do this dedicated software and knowledge of the area of interest are required. Moreover, intrinsic parameters of the UAV (e.g., flight autonomy and size) and of the onboard digital camera must be considered. Indeed, camera field-of-view, shutter speed and resolution are important for the outcome of the photogrammetry. Both influence the resolution of the product and the flight distance from the surveyed object (e.g., a structure) for the consistent overlap of the images (at least 70% depending on the distance of the target, the camera field-of-view and camera shutter speed). The flight is normally done in manual, assisted, or autonomous mode, according to the mission specifications, type of UAV, and environmental conditions. The presence onboard of GNSS/INS navigation devices is usually exploited for the autonomous flight (take-off, navigation, and landing) and to guide the image acquisition in the second step. The image network quality is strongly influenced by the typology of the performed flight. In the manual mode, the image overlap and the geometry of acquisition is usually very irregular, while the presence of GNSS/INS devices, together with a navigation system, can improve the acquisition process. Another important information, automatically acquired by the UAV, is the geo-position of the images to geo-reference the final 3D

product. Advanced and expensive sensors based on single/double-frequency positioning mode can be used or the RTK would improve the quality of positioning to a centimetre level (Remondino *et al*., 2012). If the navigation positioning system cannot be directly used (i.e., signal is strongly degraded or not available as in downtowns or rainforest areas), the orientation phase must rely only on a pure image-based approach (Eugster and Nebiker, 2008), thus requiring GCPs for scaling and geo-referencing.
The image post-processing involves software, like Agisoft Metashape (Agisoft, 2024), which analyse aerial photographs and their tie points, points recognizable from different images thanks to the accurate overlapping zone between the acquired images. By processing images derived for instance by UAV, point clouds with centimeter accuracy can be obtained, achieving same outcomes derivable by other traditional survey techniques (Colomina and Molina, 2014). Generally, by managing mesh and texture operations, point clouds can provide results like the DSM, which is a graphical representation of elevation data about terrain, overlaying objects with both positional and elevation information. Still, from cloud points, orthomosaics can be produced, through projection of raster images composed of coloured pixels resulting from orthorectified images (i.e., warped) within the photogrammetric dataset.
As for other survey techniques, also UAV photogrammetry is characterized by errors, which can be identified in three typologies: (1) photo camera errors; (2) lens system errors; (3) photogram errors, all attributable to construction errors or imperfections.

2.2. UAV photogrammetry for structures and infrastructure monitoring

Concerning the use of UAVs on structures and infrastructures, the scientific literature is oriented on three main research areas: (i) inspection protocols for identifying defectiveness; (ii) inspection protocols for retrieving information for structural assessment; (iii) high-accuracy photogrammetry for surveying built stock and surrounding area.
Based on the characteristics of UAVs, their employment in monitoring and inspection of structures and infrastructure is increasing. Regarding bridge monitoring, UAVs ease the visual inspection process of inaccessible areas due to topography making possible to assess each bridge component (e.g., abutment) or in case of high bridges (i.e., beam

intrados higher than 10-15 meters from ground level). In this case, a by-bridge platform is required to observe structural element defectiveness from a close distance, while drones are both cheaper and easier to find allowing for cheaper and regular inspections. UAV photogrammetry has promising outcomes regarding inspection protocols for identifying defectiveness as demonstrated in recent scientific literature. Kim *et al.* (2018) investigated a crack identification method based on deep learning algorithms, that significantly reduces the computational cost, for crack detection and location. Authors calculated the length and thickness of the cracks using different image processing techniques and validated through field tests. Although the effectiveness of the technique for assessment, difficulties in the quantification of some cracks are found due to the surface contamination of aging concrete. Also, image processing can be affected by the surrounding environment, such as shadows and the intensity of sunlight. Therefore, authors suggest solving these problems through lighting equipment and post-processing. Duque *et al*. (2018) used UAV high quality images to measure crack lengths, thicknesses, and rust stain areas on Keystone Wye glued-laminated timber arch bridge. The proposed protocol evaluated image quality parameters, including sharpness and entropy and feature detection was performed based on both pixel- and photogrammetry-based measurements. Both measurement techniques were accurate when compared to direct measurements and then UAV image-based methods are evaluated efficient in terms of time, expenses, and safety risk reduction. Lie *et al*. (2018) formulated a new crack detection method based on crack central point to address the drawbacks of the traditional edge detection methods and K-means clustering method. The results of the experimental campaign showed a reduced environmental noise and the ability to effectively and accurately extract the cracks of the collected images using small amounts of data.

Regarding the potentialities of creating an accurate 3D model of the scene, this feature can be used for inspection protocols for retrieving information for structural assessment. Castellazzi *et al*. (2015) presented and validated CLOUD2FEM, semi-automatic procedure to transform 3D point clouds, acquired with any kind of technology, of complex objects into a 3D finite element model of a fortress damaged by the 2012 Emilia earthquake. The resulting model contains all the information to use with a FE model, including material mechanical properties. The accuracy of the proposed FE model is validated by a linear natural frequency analysis and results compared with ones gained from a CAD generated model. Results showed very good agreement. Furthermore, an estimation of the time required to generate the same model for both CAD-based and CLOUD2FEM-based is evaluated showing a significant saving of time for the CLOUD2FEM procedure. Barazzetti *et al*. (2015) investigated the use of detailed BIM models generated by dense point clouds for FE Analysis highlighting some of the weaknesses and requirements. Regarding weaknesses of BIM models, it is not straightforward to re-adapt a BIM model to include complex shapes that characterize the load-bearing elements of the historical building without redrawing a new model only for structural analysis. Furthermore, the constructive logic must be incorporated into the model to understand the behaviour of the different structural elements, especially in masonry historic buildings like Castel Masegra, Sondrio (Italy). Morgenthal *et al*. (2018) proposed a framework to automatically acquire tailored image data of bridges with arbitrary geometries using UAV, to process images and to extract as well as to interpret information about the structural condition as a basis for structural condition assessment. The remarkable contribution of authors showed how to match information quality criteria and autonomous flight challenges (e.g., environmental conditions as wind). Wang *et al*. (2023) proposed a framework for rapid seismic risk assessment of bridges using aerial photogrammetric surveys through UAVs. The data acquired by the UAV is used for computer-vision-based automatic extraction of visible geometric features. The 3D reconstruction process is validated by comparing the UAV survey with a laser scanner one. These features are combined in analytical models, more time-efficient if compared to FE model, accounting for bending and shear mechanisms in bridge piers to perform a seismic risk assessment in terms of capacity-to-demand ratios. The feasibility of the proposed framework is demonstrated on a simply supported bridge in the Italian highway network showing potentialities for network-scale bridge management purpose.

High-accuracy photogrammetry for surveying built stock and surrounding area is the research line fitting with the scope of this research work. As emerged from previous literature review, the UAV photogrammetry consists in the use of UAV for collecting images about the area to survey which are post-processed to create, for example DSM. In the context of monitoring landslides, UAV photogrammetry proved of extensive use, as proposed by the scientific literature, exploiting the trade-off between the possibility to monitor wide areas and an information requiring different elaborations to be extremely accurate. For example, in Devoto *et al.* (2020) authors evidenced the pros of UAV-based digital photogrammetry by investigating the slow-motion of coastal landslides in the northwestern of Malta. The authors aimed to analyse models and orthomosaics to assess and categorize coastal megaclast deposits. On the other hand, the use of UAV surveys for monitoring landslides and their effects on structures is of interest to the scope of this research work. In this field, limited literature exists, as reported in Özcan and Özcan (2021), in which a study was conducted by observing different surveys of the Turkish Bogacay lagoon plain area including a bridge near the river. The authors performed a high-resolution topographic survey over two consecutive years using UAVs to identify morphological changes in the river channel. Data from repeated UAV acquisition were compared to estimate parameters like deposition and erosion volumes.

Finally, few works can be mentioned about the combination of UAV photogrammetry and Synthetic Aperture Radar (SAR) data to assess landslide impacts on structures and infrastructures. Events like the 2022, Casamicciola landslide (Romeo *et al*., 2023), demonstrate the paramount importance of monitoring terrain motions (which in turn are dependent on other atmospheric phenomena, such as rains as shown in Vassallo *et al*., 2016; Galeandro *et al*., 2013) for ensuring safety of the existing built heritage. Especially when referring to landslide action, continuous monitoring systems constitute safe approaches, which can reveal real-time motions of specific areas, directly attributable to ongoing phenomena and leading to the definition of potential losses in surrounding structures and infrastructures. On the other hand, traditional structural health monitoring systems (i.e., sensors-based) can be expensive, as well as their use implies high management costs, which discourage this practice unless strictly necessary or if the focused structures assume social relevance (e.g., strategic structures). An alternative option can be represented by the involvement of a pool of experts who periodically monitor the focused area. Nevertheless, also this possibility is difficult to pursue, since not very efficient and, at the same time, possibly very expensive. Streamlining the options and choosing the cheapest route, it is possible to appeal to new cost-effective technologies that, despite showing some limitations, can improve the current practices of risk assessment. Meng *et al*. (2021) investigated the evolution at large-scale of a landslide in northwestern China, identifying erosion and accumulation zones on the base of elevation model differences obtained from surveys. Casagli *et al*. (2017) exploited the synergic use of UAV photogrammetry and ground-based Interferometry Synthetic Aperture Radar (InSAR) (together with other techniques, such as laser scanning and infrared thermography) for the purpose of landslide analysis. The authors showed applications of the above techniques on some case studies, showing pros and cons, and proposing some ideas for employing these approaches in the field of landslides risk mitigation. Martins *et al*. (2020) employed Differential Interferometry Synthetic Aperture Radar data and UAV photogrammetry for monitoring ground deformations in the Borbonaro region of Timor-Leste, showing good potentialities of the two techniques, especially when facing movements in a very large area, as the focused one. Eker and Aydin (2021) used InSAR data and UAV photogrammetry to monitor the slow-moving Devrek landslide (Turkey), demonstrating that the combination of the two approaches is adequate for a long-term monitoring and for developing risk mitigation plans.

At the end of the literature review, advantages and shortcomings can be summarised. UAV allow to remotely acquire images of a scene reducing the effort needed for a field survey while ensuring a centimetre accuracy for 3D reconstructions and measurements. On the other hand, flight planning is a big issue that requires expertise thus limiting the use of UAVs to manual flights in most cases. This occurrence limits the applicability of UAV photogrammetry for continuous monitoring but at the same time a near-continuous monitoring can be planned in case of risks as landslides.

On this basis, the next section presents a method to assess geological risks (and in particular, subsidence phenomena) affecting a structure, by exploiting the output provided by two of the currently most attractive cost-effective technologies: (a) MTInSAR; (b) UAV photogrammetry. MTInSAR data can provide long-term monitoring with a millimetre accuracy as showed in Chapter 2, while UAV photogrammetry can provide a DSM of the area around the focused structure. For this latter, by performing surveys in different moments, it is possible to assess variations of DSMs over time, with a centimetre accuracy. Given the different accuracy and the uncertainties related to the measures, this research work proposes the minimum requirements to perform a probabilistic-based approach, which aims at comparing the statistical distributions of the spatiotemporal velocities (i.e., a normalized measure of the displacements) given by both techniques, to assess the evolution of an ongoing phenomenon affecting the focused structure. By comparing the above statistical distributions with a threshold value through a limit-state (LS) function, the probabilities of exceeding (PoEs) the imposed limit can be defined. By comparing the PoE obtained from MTInSAR data ($PoE_{MTInSAR}$) and the ones obtained from UAV photogrammetry (PoE_{UAV}), different scenarios are identified, which can reveal possible ongoing undesired phenomena on the focused structure (e.g., subsidence effects). Together with the description of the probabilistic approach, the application on two real-life cases studies is proposed (i.e., real landslide and multi-span bridge described in Section 1.2.2.1). The first one is used for validating the hypotheses of the proposed scenarios and the second one for the purpose of subsidence risk assessment.

2.2.1. Probabilistic-based approach for MTInSAR and UAV photogrammetry integration: a framework proposal

The proposed approach is graphically shown in Fig. 60, which reports each step of the procedure. A detailed description of each phase is reported in the next Subsections.

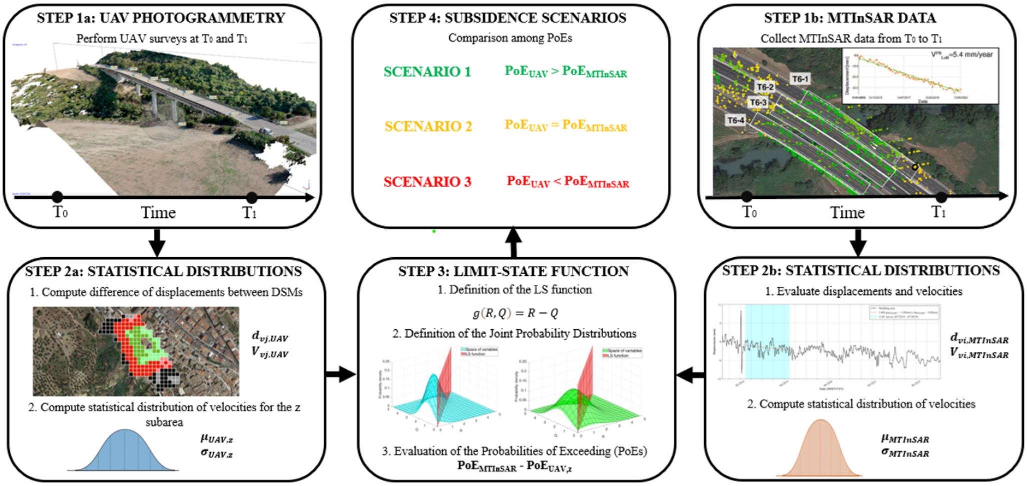

Fig. 60 - Framework of the proposed probabilistic-based approach.

2.2.1.1. Data collection

The first step of the procedure consists of identifying the structure (or infrastructure) on which assessing subsidence phenomena, and the surrounding area, which is usually characterized by a rural context. It is worth noting that the proposed procedure aims to combine the output of the different survey techniques (i.e., MTInSAR and UAV), where it makes sense to combine them. In fact, if the focused structure is located in an urbanized area, a higher number of PSs could be found and, given the higher accuracy than UAV photogrammetry, this latter could be useless. Hence, the proposed procedure, initially conceptualized for existing bridges, which are usually isolated structure, is strongly recommended for single structures within a near-free field. The second aspect to fix is the period of observation on which employing the further elaborations. Considering that the phenomenon under observation (i.e., subsidence) belongs to the slow kinematic motion families, a period of observation ranging from six to twelve months is suggested to appreciate the occurrence of variations. Let us assume that the period of observation begins at time T_0 and finishes at time T_1. After identifying the focused area and period of observation, the surveys can be carried out by elaborating data from the two involved techniques, i.e., MTInSAR data and UAV survey.

Regarding satellite data, the time-displacement series (and velocities) over the period of observation are required (already processed with MTInSAR algorithms, Section 1.1.5), by using the constellations presenting the highest available temporal and spatial resolutions. Considering that X-band constellations provide higher spatial resolution, while C-band constellations provide higher temporal resolution, the choice falls on the most comprehensive dataset for the case under investigation. The data are localized in some points on the focused structure, identified as Persistent Scatterers (PSs), in which single or double acquisition geometries can be found (i.e., ASC and DSC in Fig. 12b). Given the positioning accuracy of the PSs (see for example Calò et al., 2023), the identification of all points characterizing the structure is of fundamental importance. Hence, as a good practice, a buffer area around the focused structure can be considered, by imposing a minimum offset equal to the resolution of the considered satellite data (as in Section 1.2.1.3). For each identified PS, if both acquisition geometries are available and present the same temporal frequency, both horizontal and vertical displacements can be estimated (as in Section 1.2.1.5). Unfortunately, this occurrence does not always happen, because the revisit time of ASC and DSC acquisition geometries is different. In fact, to obtain a homogeneous temporal baseline for both acquisition geometries, a temporal resampling of one component is required. However, for the sake of generalization and for avoiding additional elaborations of MTInSAR data, authors focused only on the vertical components of displacements (and velocity), by only referring about subsidence phenomena. As a matter of fact, as the output of the PSs selection, displacement- or velocity-time series oriented along the LoS are obtained, which are elaborated to estimate vertical components through a mono-dimensional decomposition. To this scope, assuming the availability of one acquisition geometry along the LoS, vertical components of displacements ($d_{vi,MTInSAR}$) and velocities ($V_{vi,MTInSAR}$) for the i^{th} PS can be derived from the measures along the LoS (i.e., d_{LoS} and V_{LoS} vectors), given the incidence angle ϑ (Fig. 12a):

$$d_{i,LoS} = d_{vi,MTInSAR} \cdot cos\theta \tag{29}$$

$$V_{i,LoS} = V_{vi,MTInSAR} \cdot cos \tag{30}$$

The velocity along the LoS, V_{LoS}, is considered a synthetic parameter of the PS displacement-time series, and it can be evaluated as the slope of the least squares regression line of the displacements over the period of observation. To define the value of $V_{vi,MTInSAR}$ in the period of observation, the closest dates to T_0 and T_1 in which a satellite acquisition is available should be considered.

Concerning UAV surveys, two on-site campaigns are performed at the start and end of the period of observation, at the times T_0 and T_1. The UAV system to use must be equipped with an internal multi-constellation GPS. Flights should be performed by assuming a fixed camera direction and same altitude, to ensure a regular and continuous sequence of observation points for the entire duration of the acquisition time. Automatic flights are desirable to ensure that the same flight paths and camera acquisition parameters are adopted during the surveys. The choice of the same GCPs for both flights should be imposed, these are acquired through a real-time kinematic system to guarantee a systematic geolocalization of the entire area. Once flights are performed, DSMs are required. The first action to take on DSMs at T_0 and T_1 (i.e., DSM_1 and DSM_2) is to filter the vegetation (where present), in order to avoid bias on the differences between the two elaborations (i.e., higher displacements due to tree movements). To this scope, a tree cover density (TCD) map can be employed (e.g., for the Italian case, TCD can be retrieved by ISPRA website), by adapting the DSM resolution to the TCD one. Afterwards, the area covered by the focused structure is not accounted for, because it is investigated through MTInSAR data, which present higher accuracy than UAVs. DSM_1 and DSM_2 can be compared cell-by-cell, where given the j^{th} cell, the values of vertical displacements ($d_{vj,UAV}$) and velocities ($V_{vj,UAV}$) can be estimated as:

$$d_{vj,UAV} = d_{vj,DSM1} - d_{vj,DSM2} \tag{31}$$

$$V_{vj,UAV} = \frac{d_{vj,UAV}}{T_1 - T_0} \tag{32}$$

where the subscripts DSM1 and DSM2 indicates the DSMs at T_0 and T_1, respectively.

2.2.1.2. Statistical distributions of measurements

The measures of the vertical displacements and velocities for the focused structure (i.e., $d_{vi,MTInSAR}$ and $V_{vi,MTInSAR}$) and for the surrounding area ($d_{vj,UAV}$ and $V_{vj,UAV}$), can be elaborated in statistical terms, by computing distributions of available data. However, some aspects need to be pointed out. Firstly, although displacements are available, the two employed techniques present different accuracies. On the other hand, velocities represent normalized values of the displacements and can reveal the occurrence of an ongoing phenomena. Thus, the proposed procedure accounts for velocities, which can provide a qualitative indication of the relative displacement scenarios of the structure (measured through MTInSAR data) and the surrounding area (measured through UAV photogrammetry). Secondly, regarding the sign of the vertical displacements, the subsidence is identified when displacements are positive. To obtain the necessary values, $V_{vi,MTInSAR}$ can be derived through a regression of positive and negative values of $d_{vi,MTInSAR}$, while $V_{vj,UAV}$ can be derived by elaborating positive values of $d_{vj,UAV}$. It is worth noting that, if the value of $d_{vj,UAV}$ is positive, it means that the vertical quote at T_1 is lower than the one at T_0 and then, subsidence occurs. This implies that, to investigate subsidence, only the positive values from DSMs should be considered to estimate $V_{vj,UAV}$, while others can be discarded.

According to the above information, statistical distributions of velocities $V_{vj,UAV}$ and $V_{vi,MTInSAR}$ can be estimated, by assuming normality of data. For the two measures, a different computation algorithm must be employed, considering that the real focus of the proposed procedure is the structure and the possible subsidence effects on it. For MTInSAR data, given a total of m_{PSs} PSs, the mean ($\mu_{MTInSAR}$) and the standard deviation ($\sigma_{MTInSAR}$) can be computed as:

$$\mu_{MTInSAR} = \frac{\sum_{i=1}^{m_{PSs}} V_{vi,MTInSAR}}{m_{PSs}} \tag{33}$$

$$\sigma_{MTInSAR} = \sqrt{\frac{\sum_{i=1}^{m_{PSs}} \left(V_{vi,MTInSAR} - \mu_{MTInSAR}\right)^2}{m_{PSs}}} \tag{34}$$

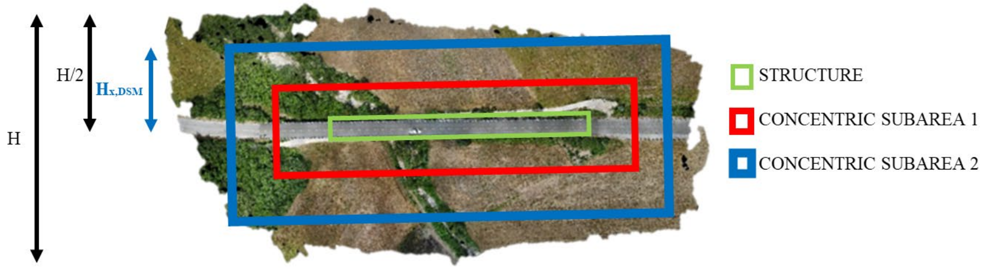

Fig. 61 - Definition of concentric subareas around the structure (in this case, a bridge), and the distances of interest for weighing measures on DSM. *H* is the shorter side of DSM, while $H_{x,DSM}$ indicates the shortest distance from the external side of the subarea to the centroid of the structure.

Instead, different formulations should be used for data from DSMs. In fact, especially if the UAV surveys are performed on a wide area around the focused structure, the displacements (and then the velocities) observed on the closer cells to the structure are more important than the ones observed on the farther ones, which implies the necessity to weigh these measures. For generalizing the selection of the cells and their weights, systematic concentric subareas can be traced around the structure, with a thickness assumed at the discretion of the user and according to his/her sensibility (e.g., similar to the size of the structure), up to cover the entire DSM area, as explicated in Fig. 61.

From the mathematical point of view, given *H* the shorter side of DSM, the weight to apply on the displacement of the z^{th} subarea is defined as:

$$w_z = 1 - \frac{H_{x,DSM}}{H/_2} \tag{35}$$

where $H_{x,DSM}$ is the shortest distance from the external side of the subarea to the centroid of the structure. The weight w_z ranges from 0 to 1, showing higher values for closer subareas to the structures. Using the obtained values of w_z on the related subarea containing a total of *n* cells, the weighted mean ($\mu_{UAV,z}$) and the standard deviation ($\sigma_{UAV,z}$) for the z^{th} subarea can be computed as:

$$\mu_{UAV,z} = \frac{\sum_{j=1}^{n} V_{vj,UAV} \cdot w_z}{\sum_{j=1}^{n} w_z} \tag{36}$$

$$\sigma_{UAV,z} = \sqrt{\frac{\sum_{j=1}^{n} w_z \cdot \left(V_{vj,UAV} - \mu_{UAV}\right)^2}{\frac{(n-1)}{n} \cdot \sum_{j=1}^{n} w_z}} \tag{37}$$

For each subarea, a proper distribution is defined. Some comments need to be provided about the hypothesis of normal distributions for the involved variables. If the number of points is not high, normality could be a strong assumption. On the other hand, other kinds of distributions can be converted into normal ones using the principle of equivalent normalization. Still, in some cases, high values of standard deviation could be obtained, which implies that the mean of data is not representative of the measures in the area. In this case, data should be managed by eliminating outliers or, in the worst cases, by removing the tails of the normal distributions.

2.2.1.3. Definition of limit-state function

Having the measures of the ongoing subsidence phenomenon for the structure and the surrounding area, expressed as two different random variables containing velocities, to establish if the obtained values suggest the occurrence of an undesired event, a failure criterion can be fixed, by defining a LS function (Novak and Collins, 2013). Generally, a LS function, g, can be defined as:

$$g(R,Q) = R - Q \tag{38}$$

where, for a failure mode, *R* represents the capacity of the system and *Q* indicates the demand to which the system is subjected. If *g(R,Q)* is higher than or equal to 0, the system can be defined as safe, while if *g(R,Q)* is lower than 0, the system can be defined as unsafe. Statistical distributions by MTInSAR data ($\mu_{MTInSAR}$ and $\sigma_{MTInSAR}$) and by UAV photogrammetry ($\mu_{UAV,z}$ and $\sigma_{UAV,z}$) represent two different values of *Q*, because they express the demand in terms of subsidence required in the period of observation. Regarding *R*, the capacity can be fixed on the base of the user's sensibility and of the situation under investigation. Given the absence of a universal value representing a threshold for subsidence phenomena, the statistical distribution of *R* can be assumed according to the guidelines in REA-CNR (2021) and other literature works (e.g., Nettis *et al.*, 2023a), which suggest a limit of 2 mm/y on structures and infrastructures when satellite data are employed, with a standard deviation of 1 mm/y. Assuming a normal distribution of *R* having mean, μ_R, equal to 2 mm/y and a standard deviation, σ_R, equal to 1 mm/y, each distribution of *Q* can be compared with *R*, providing different joint probability distributions (JPDs) on which investigate safe and unsafe domains. For each JPD, PoE related to the LS can be derived, i.e., $\mathrm{PoE}_{\mathrm{MTInSAR}}$ for MTInSAR data and $\mathrm{PoE}_{\mathrm{UAV,z}}$ for UAV photogrammetry of each identified subarea (by generically identifying with μ_Q and σ_Q the statistical distributions provided by both methodologies). To this end, concepts of structural reliability need to be retrieved where, according to Novak and Collins (2013), the reliability index, β_{index}, can be computed. Assuming *R* and *Q* uncorrelated, β_{index} indicates the shortest distance from the origin of the standardized abovementioned random variables, according to the following expression:

$$\beta_{index} = \frac{\mu_R - \mu_Q}{\sqrt{{\sigma_R}^2 + {\sigma_Q}^2}} \tag{39}$$

By estimating β_{index} for the MTInSAR data ($\beta_{MTInSAR}$) and for each subarea identified in the DSMs differences ($\beta_{UAV,z}$), PoE can be estimated as the complementary of the reliability index:

$$\beta_{MTInSAR} = -\Phi^{-1}(PoE_{MTInSAR}) \tag{40}$$

$$\beta_{UAV,z} = -\Phi^{-1}\left(PoE_{UAV,z}\right) \tag{41}$$

where Φ represents the cumulative distribution function. Once obtained values of PoE, they can be compared to determine the subsidence scenarios reported in Section 2.2.1.4. It is worth noting that the reliability index herein involved is the one initially proposed by Cornell (and after by Hasofer and Lind, as stated in Novak & Collins, 2013), by assuming a linear function of LS. In the case in which the statistical distributions are not normal, the reliability index (and the consequent probability of exceeding) can be estimated through the modification proposed by Rackwitz-Fiessler (as suggested by the Joint Committee of Structural Safety, 2001).

2.2.1.4. Definition of subsidence scenarios

Given $PoE_{MTInSAR}$ and $PoE_{UAV,z}$, this latter for each concentric subarea, subsidence scenarios can be established. Counting from 1 to z the subareas starting from the one closer to the structure, three different scenarios are defined (with the related actions to take):

- Scenario 1: $PoE_{MTInSAR}$ is lower than $PoE_{UAV,1}$. In this case, the structure is not affected by subsidence phenomena, even though detected in the surrounding area. If external subareas present $PoE_{UAV,z}$ (e.g., $PoE_{UAV,2}$ $PoE_{UAV,3}$) higher than $PoE_{UAV,1}$, monitoring of the surrounding area is required, considering that possible future motions could affect the structure. Instead, if external subareas present $PoE_{UAV,z}$ (e.g., $PoE_{UAV,2}$ $PoE_{UAV,3}$) lower than $PoE_{UAV,1}$, the structure is not affected by possible slow kinematic displacements.

- Scenario 2: $PoE_{MTInSAR}$ is similar to $PoE_{UAV,1}$. In this case, the structure and the surrounding area are behaving accordingly, and the effects of a possible subsidence can be observed. Namely, no discontinuity problems should be observed (e.g., differential settlements). If external subareas present $PoE_{UAV,z}$ (e.g., $PoE_{UAV,2}$ $PoE_{UAV,3}$) higher than $PoE_{UAV,1}$, monitoring of the surrounding area is required, considering that possible future motions could affect the structure. Instead, if external subareas present $PoE_{UAV,z}$ (e.g., $PoE_{UAV,2}$ $PoE_{UAV,3}$) lower than $PoE_{UAV,1}$, the subsidence prevalently regards the structure and the closer surrounding area, and the evolution in the external areas should be observed.

- Scenario 3: $PoE_{MTInSAR}$ is higher than $PoE_{UAV,1}$. In this case, the motion to which the structure is subjected is higher than the motion of the surrounding areas, which can be due to structural problems (e.g., differential settlements). Hence, independently of the values of all $PoE_{UAV,z}$, structural monitoring is required, while lower attention should be paid to the surrounding area.

It is evident once again that, although a quantitative measure of velocities is estimated (from both involved cost-effective techniques), the proposed procedure does not provide quantitative feedback about the ongoing phenomena, considering that displacements are not involved as well as a clear threshold in terms of subsidence is not available (*R* can be varied case-by-case). On the other hand, the outcome of the proposed procedure (i.e., scenario identification) can provide some insights about the relative behaviour between the structure and the surrounding area, giving a warning that can be employed in risk mitigation plans.

2.2.2. Validation of the proposed procedure: effects of Pomarico landslide on building

For validation purpose of the proposed procedure, the case study of the Pomarico landslide, Basilicata, Southern Italy, is investigated. According to the detailed description in Doglioni *et al*. (2020), from January 25th to January 29th, 2019, after an extended period of continuous although not intense rainfall, a substantial portion of the southwestern hillslope on the urban side of Pomarico started a progressive displacement. A complex movement, composed of a roto-translative slide and an earthflow downstream, retrogressively evolved during those 4 days, causing the collapses of several buildings and extensively damaging some roads. Fig. 62 reports the aerial views of Pomarico landslide, which caused extended damages and losses on the structures and infrastructures facing the hill. Further details of this event are in Doglioni *et al*. (2020). According to the proposed procedure, only the quantification of the vertical component (i.e., subsidence) characterizing the buildings facing the hill and the surrounding area is focused. It is worth noting that, with the proposed procedure it is not possible to predict or quantify a fast motion like the one that occurred in the landslide days, but it is possible to assess in a period of reference going from before to after January 29th, 2019, the velocity measures given by MTInSAR data and UAV photogrammetry. For the case under investigation, two aerial surveys are available around the event, one in July 2018 and one in July 2019. For the sake of completeness, the survey made in July 2018 was performed through a LiDAR survey from which, besides

Fig. 62 - Areal views of the Pomarico landslide (left) and focus on damaged structures and infrastructures (right). The red polygon indicates the focused structures.

Monitoring geological movements (e.g., faults and subsidence), it allows to derive a DSM with a sub-centimetre accuracy. Although there are different accuracies between UAV and LIDAR surveys, the choice of the velocities allows overcoming these differences. At the same time, some PSs are available on the buildings affected by the event, which show the occurrence of the subsidence (and then, of the subsidence). Only DSC geometry by Sentinel-1 (SEN1) constellation was retrieved (spatial resolution of 5 m x 20 m), in the time span from January 3rd, 2018, to December 20th, 2022, presenting ϑ equal to 37.319° and α equal to 191.26°. Fig. 63 shows the aerial view of the buildings in aggregate (red polygon), the distribution of the PSs and a time-displacement series of one PS.

According to the observed damages on buildings (see Fig. 64), the application of the proposed procedure should reveal the occurrence of the Scenario 2, that is, $PoE_{MTInSAR}$ is similar to $PoE_{UAV,1}$. In fact, the expected result should reveal that both the considered structures and their surrounding area were subjected to the same phenomenon and then, a similar PoE the LS should be obtained. In quantitative terms, although experienced vertical displacements are different between the focused buildings and surrounding area, the expected velocities over the period of observation (1 year for the case at hand) should be similar, also considering the weights assigned to velocities on the surrounding area.

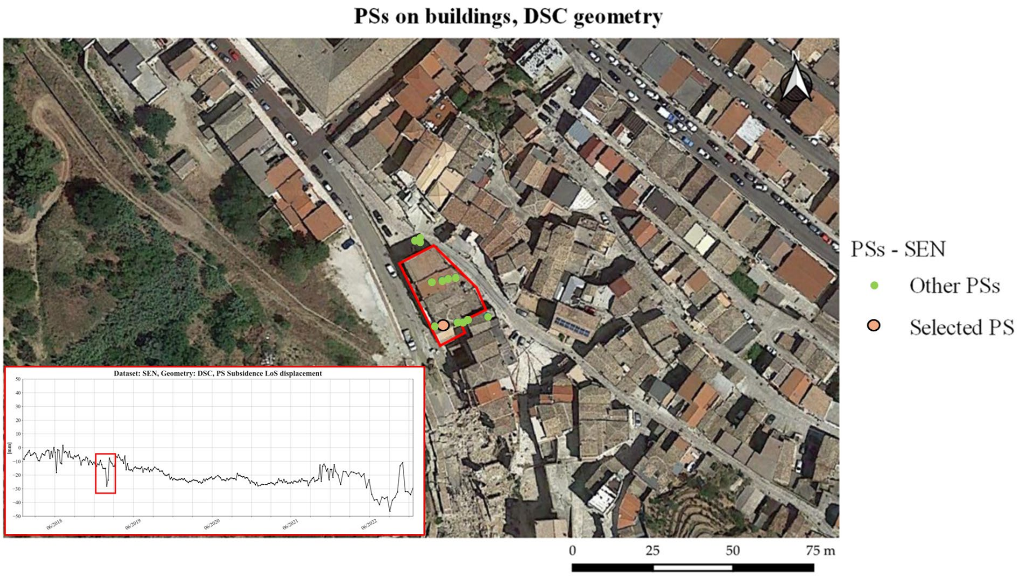

Fig. 63 - Identification of the structures object of subsidence (red polygon), distribution of PSs, and time-displacement series of on PS.

Fig. 64 - Observed damages on buildings and roads.

According to the procedure reported in Sections 2.2.1.1 and 2.2.1.2, statistical distributions of velocities can be defined. First, the buffer zones were identified, by subdividing the surrounding area into 3 concentric subareas of 20m, 50m, and 70m. Fig. 65 reports this subdivision, besides reporting PSs on the building footprint. Looking at MTInSAR data, assuming as positive the values downwards, in the period of observation the maximum displacements along the LoS and the vertical directions were 1.32 mm and

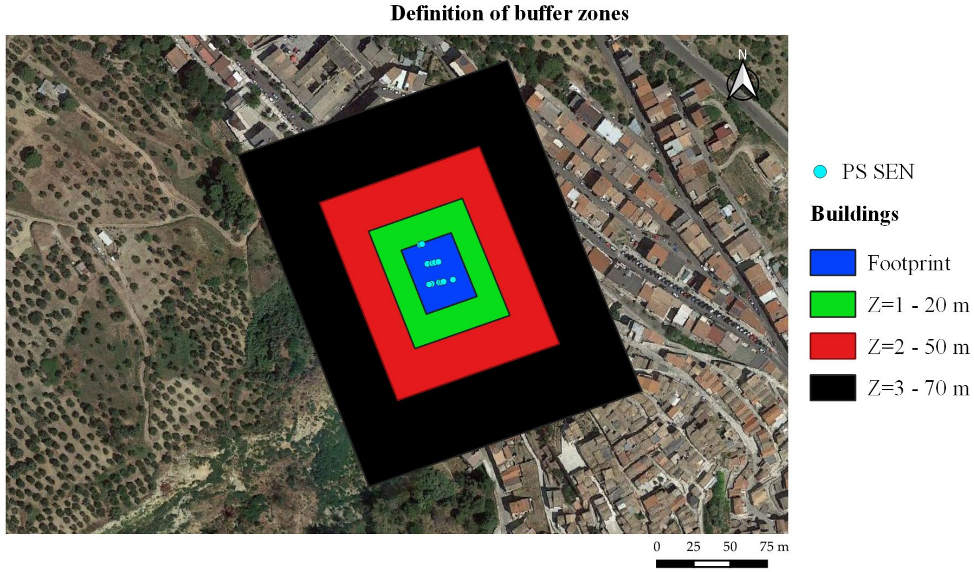

Fig. 65 - (Pomarico landslide) Identification of three different buffer zones (z=1,2,3) of increasing width around the structure footprint, and distribution of PSs.

1.05 mm, respectively, while the minimum displacements along the LoS and the vertical directions were -6.99 mm and -5.56 mm, respectively. After, the mean values of velocities along the LoS and the vertical directions were 1.35 mm/y and 1.09 mm/y, respectively. For all PSs, using Equations (32) and (33), values of $\mu_{MTInSAR}$ and $\sigma_{MTInSAR}$ were defined, as shown in Fig. 66, by referring only to the vertical components of displacements.

After, given DSM1 and DSM2 with a cell resolution of 10m x 10m, values of subsidence displacements were identified (i.e., positive values), to quantify $\mu_{UAV,z}$ and $\sigma_{UAV,z}$ for the three subareas. Considering that the landslide occurred only in the southwestern part, the displacements in the opposite part were ignored. This means that the concentric subareas were cut, and only the cells on the landslide side were considered. The result of the comparison between DSM1 and DSM2 can be observed in Fig. 67, which reports with different colours the cells of each subarea (according to Fig. 65) positive (of subsidence) and negative displacements. In quantitative terms, by using Equation (31), in the period of observation, the values of maximum displacements for the first, second,

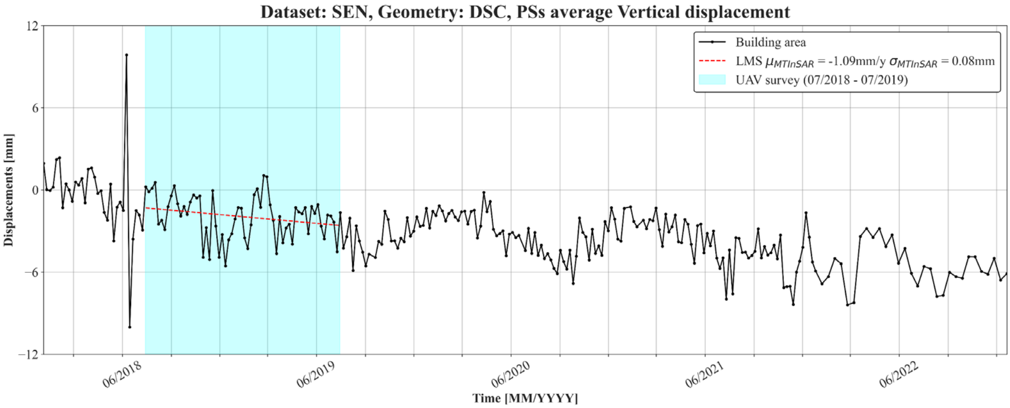

Fig. 66 - (Pomarico landslide) Time-vertical displacement series and definition of $\mu_{MTInSAR}$ and $\sigma_{MTInSAR}$ for velocities (red line), taking as reference the period of observation (light blue band).

and third subareas were 2.12 cm, 5.41 cm, and 10.6 cm, respectively, while the values of minimum displacements for the first, second, and third subareas were -0.57 cm, -0.57 cm, and -0.35 cm, respectively. Using positive displacements, statistical parameters for the three subareas were computed, as well as the relative values of w_z. A summary of the obtained results is reported in Table 13.

Taking each measure separately, JPD functions were generated and, assuming as LS function the one reported in Equation (38) and as *R* the normal distribution proposed in Section 2.2.1.3, both *β* indexes and PoE the LS were estimated. Fig. 68 reports the above elaborations, where the JPD functions for MTInSAR data and UAV photogrammetry (first subarea) were carried out and overlapped on the plane identifying the LS function. According to Equation (39), $\beta_{MTInSAR}$ and $\beta_{UAV,z}$ (z=1, 2, 3) were evaluated, from which $PoE_{MTInSAR}$ and $PoE_{UAV,z}$ (z=1, 2, 3) were computed, and reported in the last row of Table 13. In particular, $PoE_{MTInSAR}$ was equal to 25.65%, while $PoE_{UAV,1}$ was equal to 21.30%. As expected, the two values are similar, thus falling back into Scenario 2. Still, the values of $PoE_{UAV,2}$ and $PoE_{UAV,3}$ were equal to 77.8% and 69.6%, respectively (note that the high standard deviation obtained in the third subarea brings to obtain $PoE_{UAV,3}$ lower than $PoE_{UAV,2}$, despite $\mu_{UAV,3}$ is strongly higher than μ_R). Also in this case, as expected, a monitoring of the surrounding area is required, considering that possible future motions could affect the structure. The obtained results overall confirm the good

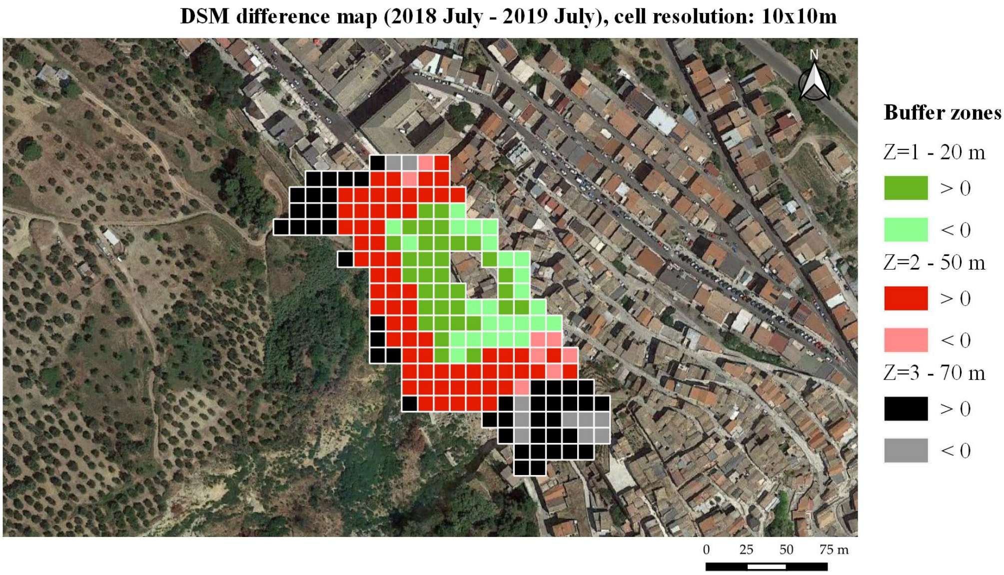

Fig. 67 - (Pomarico landslide) DSM difference map for the surrounding area to the focused buildings subdivided into the three concentric subareas. Different colours were used for each subarea and different colour tones were used for positive (< 0) and negative (> 0) displacements.

Table 13 – (Pomarico landslide) Statistical parameters of velocities obtained by MTInSAR data and UAV photogrammetry on Pomarico landslide (reference to the subsidence component). Values of $\mu_{UAV,z}$ and $\sigma_{UAV,z}$ are reported as already weighted for w_z. The last row reports the values of $PoE_{MTInSAR}$ and $PoE_{UAV,1}$, $PoE_{UAV,2}$, $PoE_{UAV,3}$.

MTInSAR data		**UAV photogrammetry**					
$\mu_{MTInSAR}$ (mm/y)	1.09	$\mu_{UAV,1}$ (mm/y)	1.20	$\mu_{UAV,2}$ (mm/y)	3.20	$\mu_{UAV,3}$ (mm/y)	7.00
$\sigma_{MTInSAR}$ (mm/y)	0.80	$\sigma_{UAV,1}$ (mm/y)	0.10	$\sigma_{UAV,2}$ (mm/y)	1.20	$\sigma_{UAV,3}$ (mm/y)	9.70
		w_1	0.80	w_2	0.50	w_3	0.30
$PoE_{MTInSAR}$ [%]	25.65	$PoE_{UAV,1}$ [%]	21.30	$PoE_{UAV,2}$ [%]	77.8	$PoE_{UAV,3}$ [%]	69.6

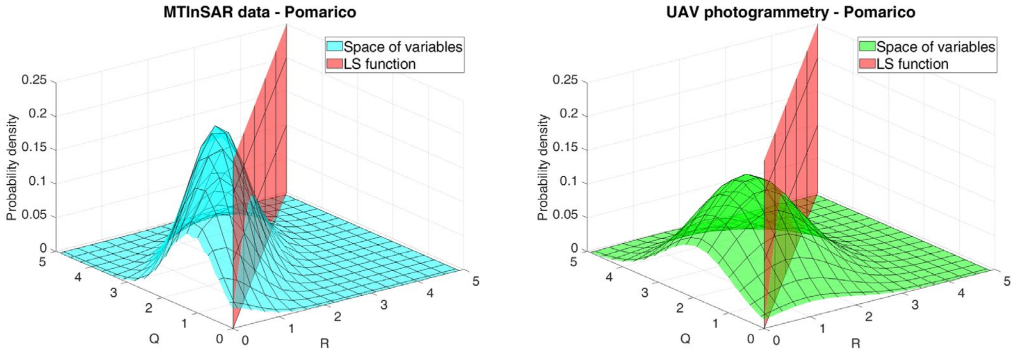

Fig. 68 - (Pomarico landslide) JPD functions for MTInSAR data and UAV photogrammetry (z=1) statistical distributions for the Pomarico landslide (reference to the subsidence component), by fixing a linear LS function (see Section 2.2.1.3). Unsafe domain is placed at the right of the red plane (i.e., LS function).

capacity of the proposed procedure to predict the relative subsidence behaviour between structures and surrounding areas, and in the next Section, the approach was used for the purpose of risk prediction.

2.2.3. Application of the proposed procedure for the purpose of risk prediction to a multi-span bridge

After validating the proposed procedure, it is tested for predicting subsidence risk on an existing reinforced concrete (RC) bridge already described in Section 1.2.2.1. Some photos of the bridge are reported in Fig. 69, comprising a partial aerial view and a lateral shot. For the case at hand, a period of observation of about one year and a half was set, starting from October 2021 up to July 2023. In the established period, MTInSAR data were available, with only a DSC imagery by SEN1 constellation, which resulted in 42 PSs on the structure. These latter are characterized by spatial resolution of 5 m x 20 m, time span from April 12th, 2017, to August 21st, 2023, and present ϑ equal to 41.218° and α equal to 189.724°. Fig. 73 reports the distribution of PSs on the bridge. With regard to numerical values by MTInSAR data, assuming positive the values downwards, in the period of observation the maximum displacements along the LoS

Fig. 69 - Photos of the focused existing bridge, reporting comprising a partial aerial view (left) and a lateral shot (right).

and the vertical directions were 4.30 mm and 3.23 mm, respectively, while the minimum displacements along the LoS and the vertical directions were -5.93 mm and -4.46 mm, respectively. After, the mean values of velocities along the LoS and the vertical directions were -0.11 mm/y and -0.08 mm/y, respectively. Concerning UAV flights, the aerial surveys were performed through a consumer DJI mini 2, equipped with a 12MP camera and an internal multi-constellation GPS. In both flights, specific GCPs were identified and materialized to ensure accurate localization, by using road signs on the bridge and selected points near the pier. Fig. 70 shows the initial phase of UAV flight (second survey) and the phase of GCPs acquisition. Both flights were automatically performed, in order to have a systematic and continuous sequence of photos, covering the entire designated area. The camera direction and flight altitude were kept fixed throughout the acquisition process. After elaborating data and providing DSM1 and DSM2 (depurated by the TDC) with a cell resolution of 10m x 10m, three different buffer zones were identified, by subdividing the surrounding area into three concentric subareas, where the first and the second ones were of 20m and 50m, respectively, while the third one was constituted by the remaining part of the DSM. In quantitative terms, by using Equation (31), in the period of observation, the values of maximum displacements for the first, second, and third subareas were 0.75 cm, 3.79 cm, and 6.13 cm, respectively, while the values of minimum displacements for the first, second, and third subareas were -0.03 cm, -0.10 cm, and -0.22 cm, respectively. Fig. 71

Fig. 70 - UAV system used for surveying the bridge and acquisition of GCPs by the third author of Calò *et al*. (2024d).

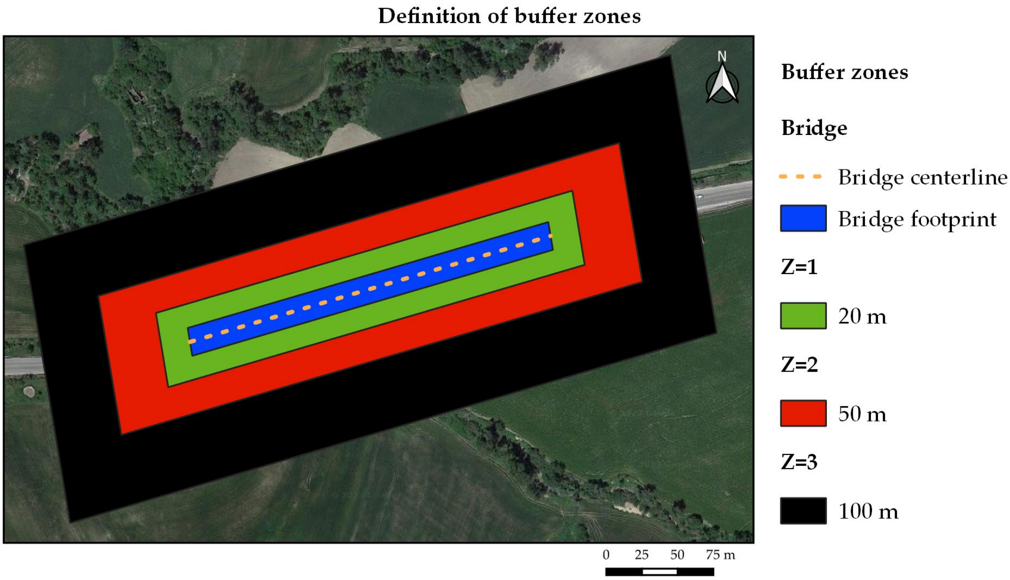

Fig. 71 - (Multi-span RC bridge)Identification of three different buffer zones (z=1,2,3) of increasing width around the bridge footprint. Note that the subarea z=3 is not concentric, according to the available total area of the DEM.

shows the surrounding area subdivision. In this case, differently from the case described in Section 2.2.2, the structure is isolated, and all data contained in the concentric subareas were considered.

According to the proposed framework, using data of all PSs on the bridge, values of $\mu_{MTInSAR}$ and $\sigma_{MTInSAR}$ were defined, as shown in Fig. 72, by referring only to the vertical components of displacements. Analogously, values of subsidence displacements were identified (i.e., positive values) and the quantities $\mu_{UAV,z}$ and $\sigma_{UAV,z}$ for the three subareas were defined. The obtained results are reported in Fig. 73, by using different colours for the cells of each subarea (according to Fig. 71) and distinguishing colour tones for positive (of subsidence) and negative displacements. By estimating the values of w_z, the final statistical parameters for the three subareas were derived, as reported in Table 2. The $\mu_{MTInSAR}$ is lower than $\mu_{UAV,1}$ (and $\mu_{UAV,2}$, $\mu_{UAV,3}$) of about four times, which implies that while the surrounding area is manifesting some vertical displacements, the bridge seems to be safe. In addition, it is worth noting the high standard deviation of the second and third subareas, which implies a high dispersion of data. This aspect could be improved by varying the type of statistical distribution. Nonetheless, considering the good values in the first subarea, normal distributions were always employed.

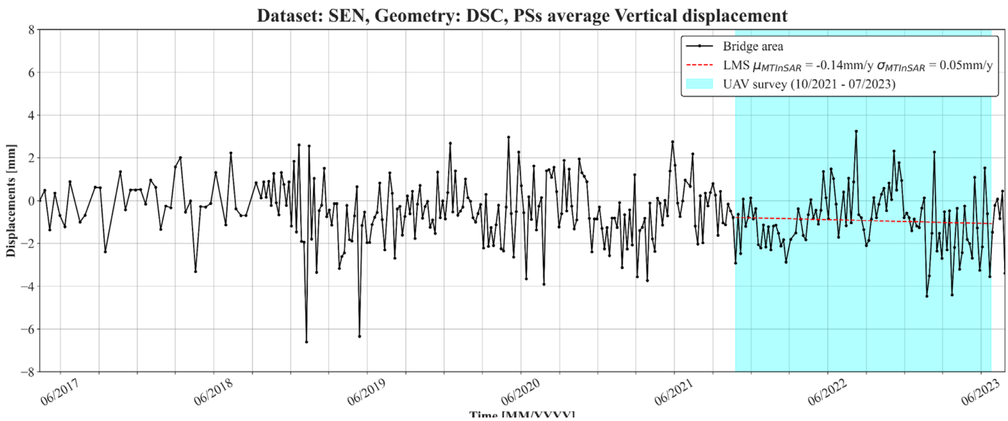

Fig. 72 - (Multi-span RC bridge)Time-vertical displacement series and definition of $\mu_{MTInSAR}$ and $\sigma_{MTInSAR}$ for velocities (red line), taking as reference the period of observation (light blue band).

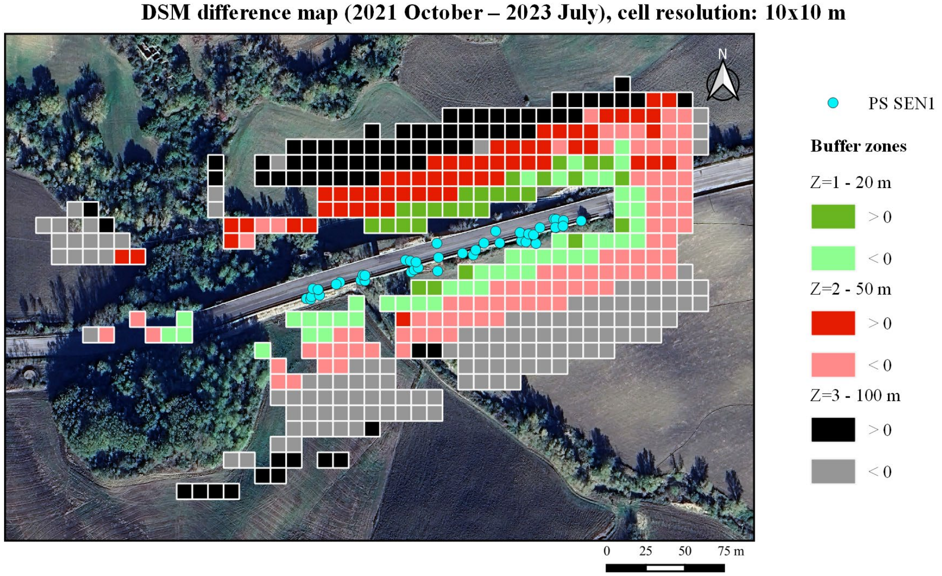

Fig. 73 - (Multi-span RC bridge) DSM difference map for the surrounding area to the focused bridge, subdivided in the three concentric subareas and distribution of PSs. Different colours were used for each subarea and different colour tones were used for positive (< 0) and negative (> 0) displacements.

Using the moments of statistical distributions, specific JPD functions were created and, assuming the linear LS function and the above-described normal distribution of *R*, both *β* indexes and PoE were estimated. Fig. 74 presents the above elaborations, for MTInSAR data and UAV photogrammetry (with reference to the first subarea), by comparing the JPDs and the plane materializing the LS function. Values of PoE are reported in the last row of Table 14. Comparing $PoE_{MTInSAR}$ with $PoE_{UAV,1}$, values of 2.75% and 33.21% were obtained, respectively, bringing to classify the case study into Scenario 1. Still, the values of $PoE_{UAV,2}$ and $PoE_{UAV,3}$ were estimated, and they were equal to 50.04% and 51.27%, respectively, suggesting monitoring the surrounding area, to avoid possible future motions affecting the structure. The results obtained by the proposed procedure were also confirmed by the visual on-site inspections, in which the expert did not detect any subsidence problem on the base of the bridge.

Table 14 - Statistical parameters of velocities obtained by MTInSAR data and UAV photogrammetry on the bridge case study. Values of $\mu_{UAV,z}$ and $\sigma_{UAV,z}$ are reported as already weighted for w_z. The last row reports the values of $PoE_{MTInSAR}$ and $PoE_{UAV,1}$, $PoE_{UAV,2}$, $PoE_{UAV,3}$.

MTInSAR data		**UAV photogrammetry**					
$\mu_{MTInSAR}$ (mm/y)	0.08	$\mu_{UAV,1}$ (mm/y)	0.30	$\mu_{UAV,2}$ (mm/y)	2.28	$\mu_{UAV,3}$ (mm/y)	10.48
$\sigma_{MTInSAR}$ (mm/y)	0.04	$\sigma_{UAV,1}$ (mm/y)	3.79	$\sigma_{UAV,2}$ (mm/y)	29.61	$\sigma_{UAV,3}$ (mm/y)	265.58
		w_1	0.85	w_2	0.62	w_3	0.23
$PoE_{MTInSAR}$ [%]	2.75	$PoE_{UAV,1}$ [%]	33.21	$PoE_{UAV,2}$ [%]	50.04	$PoE_{UAV,3}$ [%]	51.27

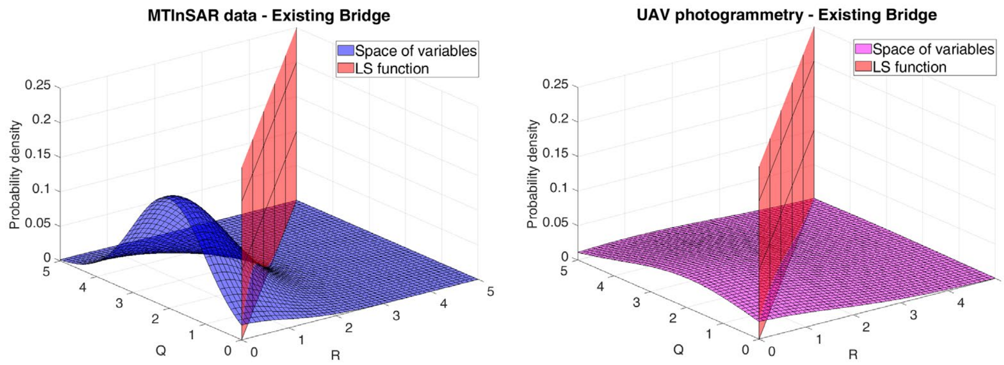

Fig. 74 - JPD functions for MTInSAR data and UAV photogrammetry (z=1) statistical distributions for the existing bridge, by fixing a linear LS function (see Section 2.2.1.3). The unsafe domain is placed at the right of the red plane (i.e., LS function).

2.3. Conclusions

This Chapter presented a probabilistic-based approach to assess the occurrence of possible subsidence phenomena affecting existing structures and infrastructures. Usually, the occurrence of these phenomena is monitored by using specific sensor-based systems or, alternatively, by engaging a domain expert to periodically observe the occurrence of ongoing phenomena. Both strategies could be time-consuming and costly. Instead, to address this issue, the information provided by two of the most attractive cost-effective technologies for structural risk monitoring: (a) Multi-Temporal

interferometry via Synthetic Aperture Radar (MTInSAR) data; (b) Unmanned Aerial Vehicle (UAV) photogrammetry. MTInSAR and UAV photogrammetry data in a predefined observation period can be elaborated, in terms of vertical velocities, combined and evaluated for structural risk assessment purpose. From the MTInSAR data point of view (i.e., structure), Persistent Scatterers (PSs) displacement time series of high accuracy are used. The projection of LoS displacements in the vertical direction is needed together with least square regression to obtain velocities. On the other side (i.e., structure surroundings) Digital Surface Models (DSMs) obtained with UAV photogrammetry at the beginning and at the end of the observation period are considered, although less accurate, after excluding cells characterized by dense vegetation. This time, velocities are retrieved dividing, for each cell, the height difference times the observation time interval. Once velocities are obtained from both technologies, statistical analysis are performed under two assumptions: (a) normal distribution of data; (b) displacements recorded by UAV photogrammetry closer to the structure are more likely to influence it. Then, statistical distributions of the spatiotemporal velocities are processed separately and compared with a threshold value by means of a limit-state (LS) function. Performing this step for each technique, the probabilities of exceeding (PoE) the LS can be computed, and the comparisons between those probabilities are framed within three scenarios, which can suggest the occurrence of subsidence phenomena. The proposed approach was firstly validated on the case study of Pomarico landslide, Southern Italy, and then applied for the purpose of risk prediction on an existing bridge.
Although the proposed procedure does not provide a detailed quantitative measure of a possible subsidence phenomena and its effect on a focused structure, which represents the main disadvantage of the approach, several advantages can be highlighted: (a) the obtained results provide a qualitative information on the evolution of a geological risk affecting the focused structure (i.e., subsidence); (b) the obtained results provide a warning, which can be implemented in reliable structural risk mitigation plans in areas prone to widespread terrain motions, accounting for geological risks and highlighting the necessity (or not) of new detailed monitoring campaigns; (c) the entire process is simple and economic (MTInSAR data could be free, as for the case of Sentinel-1

constellation, while UAV surveys can be performed by using low-cost drones) and can improve the current practices of on-site inspections, by ensuring continuous monitoring for the existing built stock. Further developments will aim to improve the proposed approach, by increasing the current accuracy of the employed survey techniques (e.g., by using new UAVs equipped with LiDAR). Moreover, besides considering subsidence effects, the use of a second acquisition geometry for MTInSAR data, elaborated with a temporal sampling to achieve a homogeneous temporal baseline, is required to estimate the other displacement component (i.e., horizontal), to overall assess landslide risks on the existing built heritage.

CHAPTER 3

AN ML-BASED FRAMEWORK FOR PREDICTING PRESTRESSING FORCE REDUCTION IN REINFORCED CONCRETE BOX-GIRDER BRIDGES

In Chapter 3, the focus of the study moves from large-scale portfolio to structure specific assessment. As pointed out in the introduction, bridges, especially aged ones, are characterized by different types of degradation phenomena induced by exogenous actions as the combination between increasing traffic and dead loads, and the environmental conditions (e.g., temperature, solar radiation, wind, rain). A common problem for prestressed reinforced concrete (PSC) structures is the corrosion and break of wires of tendons of the prestressing system reducing the bearing capacity of the structure (Nettis *et al*. 2024). In literature there are several examples of Structural Health Monitoring (SHM) sensor-based systems to monitor the prestressing system, but with some limitations explained in this Chapter after a description of the PSC technique. Considering the cost-effective solution represented by strain-gauges sensors and literature Machine Learning (ML) algorithms for regression analysis (described in their principles) they are combined in a framework to predict prestressing force reduction in PSC bridges. The effectiveness of the methodology, based on the training of ML algorithms on a sample dataset generated from a nonlinear modelling approach, is validated on experimental tests performed on scaled PSC box bridge in the ICITECH laboratories of the Universitat Politècnica de València. Results are analysed through an eXplainability approach indicating new insights which could be used in the design of an optimized sensor-based SHM for the most relevant structural parts.

3.1. Prestressed reinforced concrete bridges

Post-tensioning is a technique widely used in existing bridges, through the use of tensioned harmonic steel for wires and strands of tendons to generally mitigate the effect of bending moment induced by external loads and the tensile stress in reinforced concrete (RC) sections. This construction technique brings additional advantages such as a high torsional stiffness (especially for curving bridges and for high eccentric loads), the possibility to reduce the deck height while ensuring long spans and an hyperstatic scheme increasing the robustness of the infrastructure (Tyson, 2009). The superstructure of this bridge typology is not only designed with T (Section 1.2.2.1) or double-T beams (Section 1.2.2.2), but other shapes exist, such as the box-girder ones (Fig. 75). Nevertheless, different issues characterize the assessment of this bridge typology. The first issue regards the onsite inspection of the box-girder, in which the external surface can be directly surveyed as for other PSC bridges, while special inspections are required inside the box. This area is characterized by specific problems, such as defects on the internal concrete surface, corrosion on the steel tendons, presence of water deriving from malfunctioning longitudinal joints (if present, Naito *et al.*, 2010). Still, special inspections are not always possible, unless manholes are planned

Fig. 75 - Inside view of typical box-girder bridge (Ledesma and WSP USA, 2019).

the design phase (Corven, 2015).The second issue consists of assessing the prestressing force and the related reduction over time. Several studies investigated this problem (e.g., Bažant *et al*., 2019; Chávez *et al*., 2024; Kim *et al*., 2023; Sconocchia *et al*., 2024), showing objective difficulties in assessing its effective value on existing bridges, due to time-dependent phenomena, environmental parameters, and the interaction among degradation processes (Yang *et al*., 2020). As pointed out by Huang *et al.* (2018) and reported in building codes both concrete and harmonic steel used in PSC structures are affected by long-term deformations. Concrete is subjected to volume changes due to shrinkage and creep, with different time rates. Shrinkage is influenced by concrete curing conditions and affects the elastic modulus of concrete, while creep is dependent on the stress level of the section and the bridge configuration during construction phases. Strain increments induced by creep phenomenon must be considered for each different cross-section of the box-girder where geometrical characteristics of the beam changes along its longitudinal development (e.g., the number of tendons and section depth). On the other side, long-term relaxation of prestressing tendons, when axially deformed by a tensile force (Tu *et al*., 2019), must be addressed through proper analysis, involving constitutive material laws (e.g., viscoplastic constitutive relation proposed by Bažant and Yu, 2012), environmental factors, and construction quality of the prestressing process (e.g., partial grouting Losanno *et al*., 2023a; Losanno *et al*., 2023b). All the above phenomena reduce the initial prestressing force applied to the tendons, and this reduction is estimated around 20% during an average period of 50 years after the end of the bridge construction, as reported in Zia *et al*. (1979). Phenomena characterizing the service life of bridges, such as corrosion can still reduce both the mechanical properties (i.e., ultimate strength and ultimate strain) and the cross-sectional area and mass of the steel strands (Franceschini *et al*., 2023), leading in worst cases to wires rupture, which reduces the total prestressing force of tendons at the anchorage and thus the bearing capacity of structural elements (Nettis *et al*., 2024; Ministerio de Transportes Y Movilidad Sostenible, 2022).

3.2. Monitoring of post-tensioning systems in existing bridges: from traditional to ML-based approaches

Given the paramount importance of the prestressing system in PSC bridges different SHM strategies are present in literature exploiting traditional and ML-based approaches to monitor the prestressing force prestressing force of tendons and its reduction.

3.2.1. Traditional SHM approaches

A viable option to monitor the prestressing force reduction over time could be the design and predisposition of a specific SHM system (e.g., He *et al*., 2021; Sousa *et al*., 2014), able to reveal the variation of the force level and simulate the current service life of PSC bridges in a model updating process (Huang *et al*., 2018). Regarding PSC box-girder, a third issue is the difficulty of setting up an effective SHM system, for different technical reasons. Depending on the physical, chemical, and dynamic parameters of interest, specific sensors are required, and their number and position must be evaluated case-by-case (Comisu *et al*., 2017). In addition, a large amount of data should be stored and processed to ensure quasi-real-time monitoring (He *et al*., 2022). Over time, several SHM approaches were proposed by scientific literature. Starting from the most traditional approaches, Sousa *et al*. (2011), employed sensors to monitor deterioration mechanisms over time of the Lezíria Bridge. After providing some general rules for designing the monitoring system, the authors evaluated the serviceability, the reliability of the structure, and the remaining service life of the bridge in terms of durability, also accounting for the prestressing force level. Dall'Asta and Dezi (1996) analysed a class of PSC beams characterized by unbonded internal strands via vibration method. Frequencies of the first vertical and horizontal bending vibration modes were slightly modified by the variations of stress and profile of the strands, while a stronger influence was observed for the first twisting vibration mode. Similar outcomes were obtained in other studies (Abraham *et al*., 1995; Bonopera *et al*., 2018; De Angelis *et al*., 2024; Hamed and Frostig, 2006; Limongelli *et al*., 2016) showing that vibration methods were not effective in detecting prestressing losses, especially if other effects were not considered (e.g. concrete cracking, material degradation, and variation of environmental conditions). Another monitoring approach to detect prestressing force reduction was represented by impedance-based methods, in which load cells like piezoelectric sensors are used to monitor the variation of prestressing force through the electrical charge produced by mechanically stressing the tendons or the region where are applied (Park *et al.*, 2003). Although impedance-based methods showed good potentialities (e.g., Rabelo *et al*., 2015; Huynh and Kim, 2014), several limitations were identified, such as the strong sensitivity of the adopted device to temperature and difficulties in reaching tendon anchorages for sensor application. Modern approaches are represented by the strain-based method, which allows long-term monitoring of both concrete and tendon strain. Different types of strain sensors can be used, such as in-strand fiber Bragg gratings (FBG) sensors (Chen *et al.*, 2017; Kim *et al*, 2015; Mckeeman *et al*, 2015) and concrete strain sensors (Liu *et al*, 2015; Jo *et al.*, 2013). Nevertheless, there are some limitations for existing bridges. In fact, in-strand FBG sensors can be effective only if equipped in the construction phase. On the other hand, concrete strain sensors can be placed in each desired section and in variable number (e.g., bottom and top part of the section). These are more effective in the case of linear strain distribution and a perfect bond between the prestressing strands and surrounding concrete (Abdel-Jaber, 2017). In the case of unbonded strands, as occurs for PSC box-girder bridges, it is not possible to establish a direct correlation between the strain of strands and of concrete fibers around the strand. Another promising investigation method proposed by Bonopera and Chang (2021) is based on static deflections under three-point bending test. Following the vertical load application, the method estimates the prestressing force by measuring the vertical deflection at a quarter or at the midspan of the PSC girder-bridge. Interested readers can reference to Abdel-Jaber and Glisic (2019) for a deeper discussion about methods used in the assessment of prestressing force and the related reduction over time.

3.2.2. ML-based SHM approaches

In the last years, with the advent of new technologies, ML algorithms were often employed in combination with different phases of bridge health management, such as

visual inspections (e.g., Xiong *et al*, 2024; Wan *et al*, 2023), SHM (e.g., Mei *et al*., 2019; Sakiyama *et al.*, 2022; Svendsen *et al.*, 2021) and risk assessment (e.g., Chen *et al*., 2021, Mangalathu *et al*., 2018; Mo *et al.*, 2023; Opabola and Mangalathu, 2022; Soleimani and Liu, 2021). Scientific literature proposes some applications regarding the combination of ML algorithms to SHM data for PSC girder bridge assessment. Dang *et al*. (2023) presented a hybrid method relating Finite Element (FE) model and Artificial Neural Networks (ANNs) to assess strand relaxation in post-tensioned systems. ANNs were trained with numerical strain datasets obtained by FE model and the method was tested on a nine-strand anchorage, showing good potentialities for onsite implementation. Mariniello *et al*. (2021) used a FE model for damage simulation and data extraction, aimed at training a specific ANN to detect tendon malfunctions in PSC bridges. The obtained results, compared with other ML algorithms like Random Forrest Regressor (RFR) and Support Vector Regression (SVR), showed the higher suitability of ANN model for the case studied. Kim and Park (2019) proposed an ANN trained on experimental datasets to estimate the tensile stress on a 50-m real-scale PSC girder with embedded elasto-magnetic sensors. Results suggested that the method could be a good solution for supporting SHM in on field applications. Nguyen *et al*. (2022) employed a Convolutional Neural Network to automatically extract the optimal features of damage from the raw impedance signals of piezoelectric sensors, demonstrating how to successfully estimate the prestress-loss in a PSC girder.
This literature review about ML showed promising support in estimating the prestressing losses of unbonded tendons and in indicating the best practices to design sensors-based SHM systems. On this basis, this paper presents a new ML surrogate model, able to predict the prestressing force reduction in PSC box-girder bridges characterized by an unbonded post-tensioning system. In detail, the methodology described in Section 3.3 is designed to predict the variation of the prestressing force (F_1), starting from its initial value (F_0) and other mechanical features at the time of onsite strain-sensors installation (henceforth referred to as the time of the investigation, and herein indicate as “initial state”). Three of the most common supervised regression ML algorithms (i.e., ANN, RFR and SVR) are proposed as ML surrogate models of the structure. These

algorithms were trained and tested over sample data generated with a nonlinear FE modelling approach, while the ML surrogate model was selected based on proper statistical metrics. To address the proper design of a sensors-based SHM system, the physical description of results is performed through an eXplainability approach, named Shapley Additive exPlanation (SHAP), Lundberg and Lee, 2017. The effectiveness of the framework and of the nonlinear FE modelling strategy was validated in Section 3.4 by the results derived by experimental tests on a scaled beam specimen made in the ICITECH laboratories of the *Universitat Politècnica de València* (ICITECH, 2024). ANN was identified as the best ML surrogate model for this application task and the most influent parameters on the prestressing force reduction were derived by the SHAP approach. From the obtained results, new insights were derived, which could be used in the design of an optimized sensor-based SHM for the most relevant structural parts. Finally, Section 3.5 draws the main conclusions of the study.

3.3. ML surrogate model: a framework proposal

The proposed ML surrogate model is based on a model-driven approach, accounting for both physical and mathematical methods to establish the input-output relationship. The output of the model is the estimation of the current prestress level F_1 value, given some input variables: the prestressing force (F_0) and the elastic modulus of concrete (E_c) at the time of onsite strain-sensors installation, and the values of strain variations ($\Delta\varepsilon^{(i,j)}$) for different fibers (indicated with the superscript $^{(j)}$) of different sections of the girder, (indicated with the superscript $^{(i)}$). It is worth specifying that input quantities are referred to at the time in which the deformation sensors are installed, and for this reason, the proposed model can predict the prestressing losses from that time onwards. The adopted model is not aimed at estimating prestressing losses occurred during the whole bridge lifetime, unless the bridge was not monitored and characterized from the end of the construction phase. The general framework of the proposed procedure is shown in Fig. 76, and all steps are detailed in the next Sections.

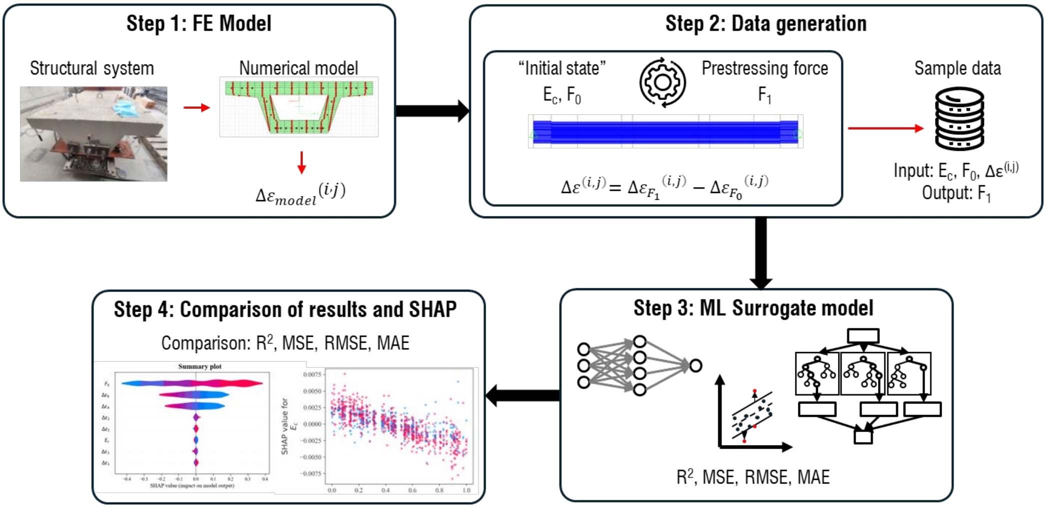

Fig. 76 - Workflow of the proposed ML surrogate model.

3.3.1. FE modelling strategy

The first step of the proposed framework consists of defining a nonlinear FE model of the structure, given: (i) geometry of the PSC box-girder bridge (i.e., length of the spans, dimensions of the sections, position of the steel rebars and tendons in each section); (ii) information about prestressing force, i.e., value of F_0 and moment due to the eccentricity of F_0 from geometric centre of each section; (iii) mechanical properties of structural materials (i.e., concrete, harmonic and mild steel) and the related constitutive laws. The choice of the type of numerical FE model represents a trade-off between accuracy and simplicity of the simulation. In fact, accurate models, as the ones proposed by Hou *et al*. (2024) and Pérez-Sala and Ruiz-Teran (2023), can ensure higher fidelity with the ground truth, but simpler models are desired when modelling and analysing thousands of models, as occurs when defining a sample data for training a ML model. If a detailed modelling strategy (e.g., micro-modelling through solid elements) was adopted it can also imply the characterization of other parameters not herein considered, such as the variation of the density of the concrete along the bridge development, or the effective stiffness of the supports. A good compromise ensuring both simplicity and accuracy of the FE model consists of using frame elements, characterized by correct boundary conditions (e.g., external restraints) accounting for both mechanical and geometrical nonlinearities. Given the different locations of unbonded tendons over the longitudinal development of the PSC box-girder bridge, a diffused plasticity approach is suggested, in which different sections are simulated through a fiber approach. In addition, this modelling approach dealing with the necessity to capture the evolution of strains in fibers located in different sections (i.e., $\Delta\varepsilon^{(i,j)}$), is suitable for providing some insights about the design of effective SHM strategies. Obviously, the numerical model should record the strain values induced on the sections, *i*, and fibers *j*, subjected to sensor-based monitoring. It is worth noting that the numerical simulation of a prestressed beam could also be processed through a linear (or nonlinear) elastic model, considering the beneficial effects of the prestressing in reducing cracking and crushing phenomena. On the other hand, a nonlinear modelling approach was preferred, in this study, to account for low cracking and for extreme situations (e.g., low prestressing force values) in data generation and for geometric nonlinearities. Regarding the typology of plasticity to implement in the FE model, a deformation-controlled PMM plasticity is suggested, which allows accounting for the presence of axial load due to prestressing (i.e., P) and the bi-directional bending in both main section axis (i.e., MM). To model the prestressing loading induced by the unbonded post-tension system, an axial force can be applied in the centroid of the considered section together with proper bending moments attributed to the identified sections to simulate the position of the tendons (Noble, 2015) (i.e., external sections and intermediate ones considered in the diffused plasticity). From a mechanical point of view, the stress induced on each tendon by the prestressing force reduces yielding and ultimate stress of the steel material available for additional external loads (i.e., traffic loads). Thus, these mechanical properties are reduced by a quantity equal to the prestressing force times the cross area of the tendons. Concerning the mechanical nonlinearities, each fiber should be modelled in elastic and post-elastic fields, by assigning a proper constitutive law for each material typology. About this aspect, the selection of the constitutive laws depends on the analyst's preference and on the adopted software. As more practical options (and according to the authors' selection), the Mander model, as reported in the reference building code (Eurocode 2, 2004) , can be used as concrete constitutive law for concrete fibers, while steel reinforcements can be simulated through a perfectly elastoplastic model.

According to the above-reported modelling strategy, some considerations can be provided. First, the definition of a nonlinear numerical model allows the reduction of the number of input parameters in the proposed ML model. Indeed, running several analyses under different prestressing load conditions (i.e., F_0) can provide the necessary output values to be used in the ML model (i.e., $\Delta\varepsilon^{(i,j)}$), which accounts for the nonlinear nature of the investigated problem. Second, the proposed numerical model could be considered as simplified (e.g., simulation of the unbonded strands as external and punctual actions). If on one hand, this could represent a formal limitation of the proposed modelling strategy, on the other hand, this strongly lightens the computational time of analysis increasing the number of simulations for providing a consistent dataset for ML model training and test. For any cases, the quality of the model can be always assessed and validated towards experimental results (as done in the present study and as later shown). Finally, a clear simplification is hidden in the proposed model, because the physical variation of F_0 to F_1 could be due to other effects (e.g., material degradation and environmental effects), which were simulated in the proposed model only by accounting for the variation of E_c. However, the aim of the proposed ML model is exactly that of avoiding complex simulations while predicting overall prestressing load effects through a simple and effective tool.

On this basis, the first step for model generation is to define E_c, F_0 and a fixed external load to compute strain increments $\Delta\varepsilon_{model}^{(i,j)}$ due to the application of fixed external load itself while the considered prestressing force is constant. To this scope, the analysis is divided into two steps: (a) application of self-weight load (e.g., dead), F_0 and related sectional moments; (b) application of the external load on the deformed configuration attained at the end of step (a). In both steps, geometric nonlinearities (i.e., P-Δ) are considered, solving then the equilibrium equations in the deformed configuration of the structure. According to this approach, the output of the analysis is the strain increment $\Delta\varepsilon_{model}^{(i,j)}$, which for the j^{th} generic fiber of the i^{th} section can be computed as follows:

$$\Delta\varepsilon_{model}{}^{(i,j)} = \varepsilon_{(b)}{}^{(i,j)} - \varepsilon_{(a)}{}^{(i,j)} \tag{42}$$

where $\varepsilon_{(a)}{}^{(i,j)}$ and $\varepsilon_{(b)}{}^{(i,j)}$ are the absolute strain values of step (a) and step (b), respectively. The difference between $\varepsilon_{(b)}{}^{(i,j)}$ and $\varepsilon_{(a)}{}^{(i,j)}$ is required because strain values of the numerical FE model are absolute, and experimental strain measures are relative to the time in which they started measuring (after the application of the other loads).

3.3.2. Data generation

To consider the uncertainties related to input values F_0 and E_c, different strategies could be used. If available, literature-based continuous distributions could be adopted (e.g., normal, lognormal) and sampling techniques could be used (e.g., see Nettis *et al*., 2024), while in the case of missing information, a range of values can be accounted for by considering uniform distributions (Nettis *et al*., 2023b). The values to consider should be characterized by physical sense, to characterize a likely sample data for training and testing the ML algorithm. Starting from a generic value of F_0, defined as "initial state" (i.e., at the time of onsite strain-sensors installation), the results of the analyses given a fixed external load can be stored, $\Delta\varepsilon_{model}{}^{(i,j)}$, with the aim to compute the strain increments $\Delta\varepsilon^{(i,j)}$. The values of this latter at different sections are calculated under the initial assumption that $F_1 = F_0$, simulating the case in which no prestressing force reduction occurs. Hence, values of $\Delta\varepsilon^{(i,j)}$, which is the input of the ML algorithms, can be computed as:

$$\Delta\varepsilon^{(i,j)} = \Delta\varepsilon_{F_1}{}^{(i,j)} - \Delta\varepsilon_{F_0}{}^{(i,j)} \tag{43}$$

where $\Delta\varepsilon_{F_k}{}^{(i,j)}$ is $\Delta\varepsilon_{model}{}^{(i,j)}$ derived by Equation (42) under a F_k value, and $\Delta\varepsilon^{(i,j)}$ is equal to 0 for each j^{th} fiber of each i^{th} section of the model. After defining the "initial state", F_0 is then reduced up to a desired percentage value, with the aim of defining different prestressing force reduction F_1. The maximum reduction rate of F_0 should be calibrated case-by-case, considering the demand to capacity ratio of the structure (Nettis *et al.,* 2024). In the end, it is worth specifying that to efficiently use the proposed method in practical applications, the input parameters at the "initial state" are needed. To this scope, onsite tests are required, both destructive (concrete specimens for assessing

E_c) and non-destructive (strain monitoring and saw-cuts tests for assessing F_0, Bagge *et al*., 2017).

3.3.3. ML surrogate model

Once data are simulated, a ML model can be trained to find the best relation between the input vector of F_0, E_c, and $\Delta\varepsilon^{(i,j)}$, and the output value, F_1. Obviously, different viable options can be employed, according to the available ML algorithms in the literature. This Section presents a description of the selected candidates for defining the proposed ML surrogate model, aiming at solving a regression problem in a supervised learning approach. Generally, in supervised learning approaches, the ML algorithms use labelled datasets to train the predict outcomes. The dataset generated in the previous step can be then used to train/test/validate a ML algorithm. Three main ML algorithms were adopted in this study, that is, ANN, RFR, and SVR, as detailed described in the next Subsections. ANN was selected for its ability to generalize problems, even though it presents many hyperparameters to be tuned. RFR is robust against overfitting and is simpler to set, given a smaller number of overall hyperparameters. SVR is a sort of compromise between ANN and RFR, because it is robust against overfitting but, at the same time, challenging in hyperparameter tuning (Mariniello *et al*., 2021).

3.3.3.1. Artificial Neural Network (ANN)

ANN is a computational model inspired by how the human brain works, and it is used for tasks such as pattern recognition, data classification, and predictive analytics. A typical ANN, shown in Fig. 77, is characterized by layers, and for each layer, one or more nodes (neurons) can be observed. The input and output layers are characterized by a number of neurons equal to the input and output values, respectively, while between these extreme layers, one or more hidden layers can be involved, able to perform the intermediate calculations and establish the input-output relationship. All nodes of each layer are connected to all the nodes of the subsequent layer, and for each connection, a specific weight is assigned. The special feature of ANN is the activation function, ψ_{NL}, which transforms the output of the neuron, a_u, toward the next layer by

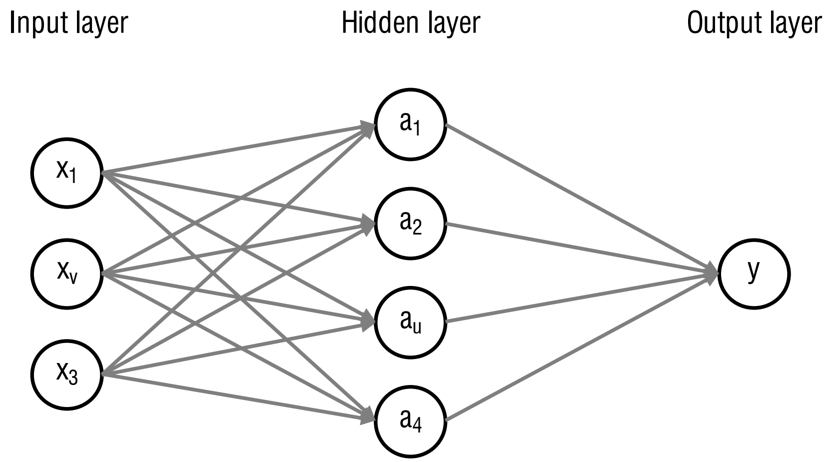

Fig. 77 - Example of ANN architecture.

inserting nonlinearities into the problem. From the mathematical point of view, the simple ANN reported in Fig. 77 presents an input layer made by 3 neurons, which can be written as a column vector, $[X] \in \mathbb{R}^{nx1}$ (with n equal to 3) with $x_v \in [X]$. The numerical value input for the u^{th} neuron of the hidden layer, a_u, is equal to:

$$a_u = \psi_{NL}\left(\sum_{v=1}^{n}(w_v \cdot x_v) + b_u\right) \tag{44}$$

where w_v is the weight associated to x_v and $w_v \in [W_1]$, $[W_1] \in \mathbb{R}^{1xn}$, $b_u \in \mathbb{R}$ is the bias associated with the activation of the neuron, and ψ_{NL} is a nonlinear function that computes the output of the neuron based on the passed values. In matrix form, considering all the *m* neurons in the hidden layer, the ANN can be written as:

$$[A] = \psi([W] \cdot [X] + [B]) \tag{45}$$

where $[W] \in \mathbb{R}^{nxm}$ (m is the number of neurons in the hidden layer), $[B] \in \mathbb{R}^{nx1}$ and $[A] \in \mathbb{R}^{1xm}$. To proceed to the output layer, each a_u value of $[A]$ matrix is weighted again via another weight matrix, $[W_2] \in \mathbb{R}^{mx1}$. In the end, the output value of the ANN, y, according to the input vector $[X]$, is equal to:

$$y = [W_2] \cdot \psi([W] \cdot [X] + [B]) \tag{46}$$

Regarding the activation function, several possibilities exist depending on the specific application (e.g., Sigmoid, Tanh, ReLU) and the considered layer (also the output layer can be characterized by the function ψ_{NL}). In the end, is worth highlighting that the performance of the ANN is evaluated through a loss function, selected on the base of the type of application (see Section 3.3.4).

The definition of a good ANN model consists of iteratively reducing the value of the loss function by updating the weights and bias values through an optimization algorithm (e.g., Gradient descent, Stochastic Gradient Descent, Adam). The use of ANN is justified for the ability of this model to generalize problems (for the case at hand, an ANN with 2 hidden layers was selected Pérez-Sala and Ruiz-Teran, 2023), even though many hyperparameters should be tuned, such as training epochs and batch size. Training epochs represent the number of epochs to train a model, in which an epoch is defined as an iteration over the sample of provided data. The batch size is the number of samples per batch of computation. Higher values of the above hyperparameters require higher computational resources. To determine optimal hyperparameters (number of neurons and their activation function in hidden layers, optimization algorithm, and number of epochs) for assuring the best performance of the model and for avoiding overfitting problems, the grid search approach with 10 k-fold cross-validation can be implemented, to assess a wide array of hyperparameters (Dang *et al.*, 2023; Wang *et al.*, 2023).

3.3.3.2. Random Forrest Regressor (RFR)

Random Forrest algorithms, first proposed by Breiman (2001), are ensemble learning methods designed for both regression and classification tasks and they present some differences if compared to ANNs. Generally, they are characterized by a limited number of hyperparameters and allow to management of different types of input features (e.g., both numerical and categorical), with higher efficiency even on small datasets. An extension of Random Forrest algorithms is RFR, typically applied for classification problems and useful for predicting numerical output. RFR is a meta estimator that employs different Decision Tree (DT) regressors (see Fig. 78a) on various sub-

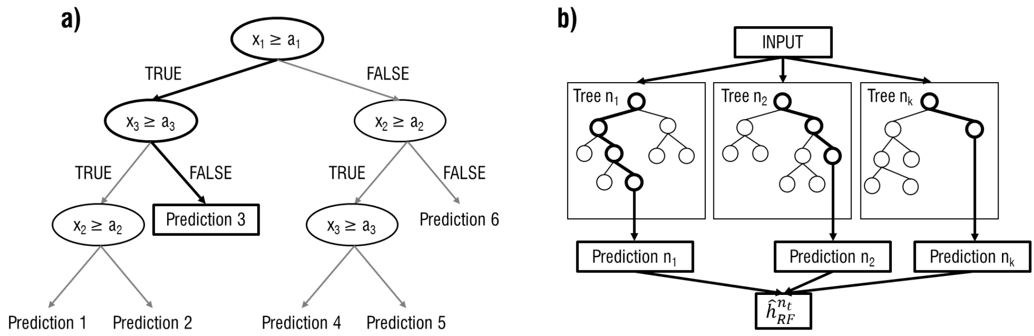

Fig. 78 - Example of: (a) Decision Tree, and (b) Random Forrest Regressor architecture.

samples of the dataset and uses averages to improve the predictive accuracy and control overfitting (Hastie *et al*., 2009). A typical scheme of RFR is reported in Fig. 78b. A DT is a nonparametric regression approach, which generates a tree-like graph composed by a root node, internal nodes and leaves. The root-node contains the sub-sample of data, the internal nodes represent the points in which the dataset is split based on certain features and criteria, while leaves (or terminal nodes) are the points reporting final output values for the predictions. Two main steps are performed to build a DT: (a) subdividing the training space in u distinct and nonoverlapping regions R_u; (b) perform the prediction, assuming that it is equal for each observation falling in the R_u region. Region R_u is determined through an iterative process (recursive binary splitting) that minimizes a loss function (e.g., Root Mean Squared Error, RMSE). This operation is performed in internal nodes, until no further subdivision is performed. The parameter used by DT to establish if a further subdivision is needed or not is the minimum size node, and it represents a hyperparameter. When a node exceeds the minimum size, it can be defined as an internal node, otherwise, it is a leaf. This workflow is called top-down strategy (Xu *et al.,* 2005) and in this way, DT can make the prediction by following the path from the root note to the leaves. From the mathematical point of view, the output of the RFR, $\hat{h}_{RF}^{nt}$, can be expressed by the following equation:

$$\hat{h}_{RF}^{n_t} = \frac{1}{n_t} \cdot \sum_{1}^{n_t} h_{n_t}(x) \tag{47}$$

where $h_{n_t}(x)$ is the individual prediction of a tree, n_t, for an input vector x. The variance of the average of n_t random variable, *var*, with a correlation coefficient ρ and standard deviation σ is expressed as:

$$var = \rho\sigma^2 + \frac{1-\sigma}{n_t} \cdot \sigma^2 \tag{48}$$

As for ANN, hyperparameter tuning including n_t, maximum number of levels in each decision tree, and minimum number of data points placed in a node before splitting is required.

3.3.3.3. Support Vector Regression (SVR)

SVR, reported in Fig. 79, is a specific type of Support Vector Machine (generally used for regression tasks through a binary classification algorithm formulated by

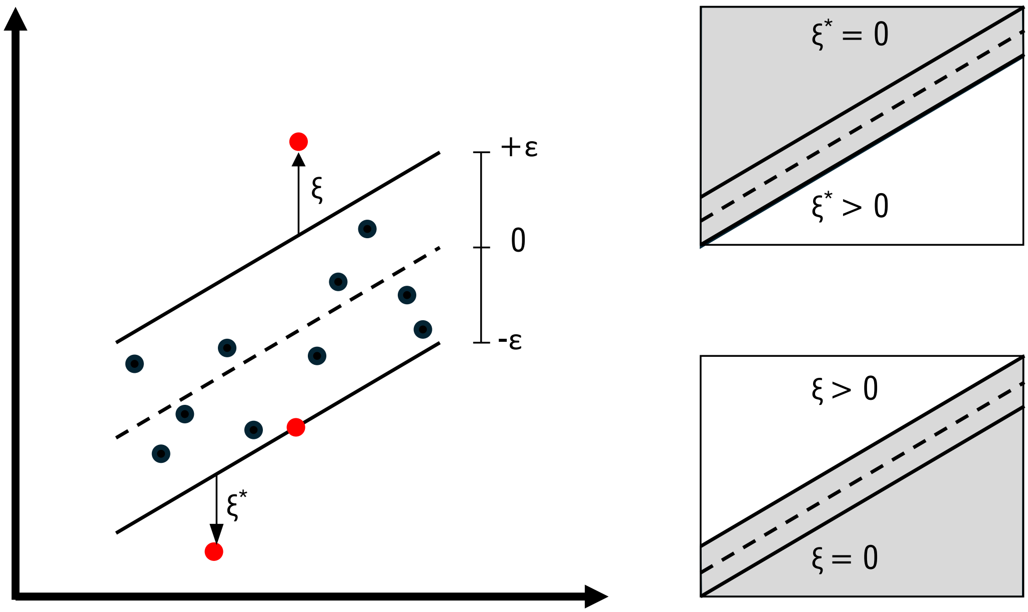

Fig. 79 - Schematic representation of SVR.

Vapnik, 2006), which is adequate for predicting continuous numerical values (Vapnik, 1998). SVR is built from training data, and it employs a regression function, *f*, to map training data as closely as possible to the numerical labels. For nonlinear regression tasks, given a set of *z* training data T_{SVR}, where $T_{SVR} = \{(x_c, y_c)\}_{c=1...z}$, $x_m \in \mathbb{R}^n$, $y_m \in \mathbb{R}$ and a set of functions F with Z_{par} set of parameters, where F $= \{f(x, \alpha), \beta_{plane} \in Z_{par} \mid f : \mathbb{R}^n \rightarrow \mathbb{R}\}$, the regression function can be expressed as:

$$f(x, \alpha) = \beta_{plane} \cdot \varphi(x) + b \tag{49}$$

where $\varphi(x)$ is a nonlinear function to linearly map input space into a high-dimensional feature space. If the error between predicted and real values is less than ε, *f* can predict *y* correctly. β_{plane} is the optimal separating hyperplane in SVR according to a minimization function:

$$min \frac{1}{2} ||w^2|| + C \frac{1}{l} \sum_{c=1}^{z} V(x, y, f) \tag{50}$$

where *V*(x, y, f) is Vapnik's ε-insensitive loss function:

$$V(x, y, f) = \begin{cases} 0 & if \ |f(x) - y| \leq \varepsilon \\ |f(x) - y| - \varepsilon & if \ |f(x) - y| > \varepsilon \end{cases} \tag{51}$$

which is employed to find a function that fits the current training data with a deviation less than or equal to ε, under these constraints:

$$\begin{cases} \beta_{plane} \cdot \varphi(x) + b - y_c \leq \xi_c^* + \varepsilon \\ y_c - \beta_{plane} \cdot \varphi(x) - b \leq \xi_c + \varepsilon \\ \xi_c, \xi_c^* \geq 0 \end{cases} \tag{52}$$

The terms ξ_c and ξ_c^* are defined as slack variables, which denotes the excess deviation in the upper and lower regions outside support vectors. The difference between prediction and real values are constrained in a region defined by the ε hyperparameter. Thus, ε can be considered as a tolerance and only predictions characterized by a residual greater than ε are penalized. The data on and outside the ε-boundary are called support vectors. *C* is a positive constant that defines the degree of penalization when a training error occurs. For large values of *C*, a complex model is obtained, able to avoid training errors with the risk of overfitting while, a small value of C leads to a model characterized by low complexity with a tendency to insufficiently fit training data (Balfer and Bajorath, 2015; Rodríguez-Pérez and Bajorath, 2022). Hence, the tuning of the C hyperparameter is critical for achieving a compromise between model accuracy and generalizability. Finally, the kernel function is involved together with the method of Lagrange to express the prediction function (e.g., radial basis kernel function). As for ANN and RFR, hyperparameter tuning is required starting from C, ε and kernel.

3.3.4. Comparison of results and use of eXplainability

The selection of a specific algorithm among the ones reported in Section 3.3.3 for the definition of the proposed ML surrogate model depends on the higher prediction accuracy provided by each proposal. It is worth also justifying the reasons for which ANN, RFR, and SVR were selected as candidates for this scope. In fact, ANN was selected for its ability to generalize problems, even though it presents many hyperparameters to be tuned. RFR was selected because it is robust against overfitting and is simpler to set, given a smaller number of overall hyperparameters. SVR is a sort of compromise between ANN and RFR, because it is robust again overfitting but at the same time challenging in hyperparameter tuning (Mariniello *et al*., 2021).

The predictive accuracy of the models can be assessed through the definition of some statistical metrics. Going into detail, different metrics can be defined, such as the coefficient of determination (R^2), Mean Squared Error (MSE_1), RMSE, Mean Signed Error (MSE_2) and Mean Absolute Error (MAE), which are all mathematically defined as follows:

$$R^2 = 1 - \frac{\sum_{m=1}^{p}(y_m - \bar{y}_m)^2}{\sum_{m=1}^{p}(y_m - \mu_\varepsilon)^2} \tag{53}$$

$$MSE_1 = \frac{1}{p}\sum_{m=1}^{p}(y_m - \bar{y}_m)^2 \tag{54}$$

$$MSE = \sqrt{MSE_1} = \sqrt{\frac{1}{p}\sum_{m=1}^{p}(y_m - \bar{y}_m)^2} \tag{55}$$

$$MSE_2 = \frac{1}{p}\sum_{m=1}^{p}(y_m - \bar{y}_m) \tag{56}$$

$$MAE = \frac{1}{p}\sum_{m=1}^{p}|y_m - \bar{y}_m| \tag{57}$$

where p is the number of data points, y_m is the experimental value, $\bar{y}_m$ is the predicted value, μ_ε is the average value of experimental values.

Generally, R^2 expresses the correlation among variables, and it is used to evaluate the goodness of fit of a regression model. MSE_2 represent the mean of the distances between experimental and predicted regression model values, and it accounts for the sign of the error. RMSE is the root of MSE_1 and presents the main advantage of having a value in the same unit measure of the response variable (in this sense, RMSE is preferred to MSE_1 for its straightforward interpretability). While higher values of R^2 are preferrable, the fitting is more accurate if lower values of RMSE are obtained. Regarding the values of MSE_2, it is not possible to define an optimal value, but a positive value leads to underestimate the ground truth and vice versa. Finally, MAE provides a more balanced representation of errors, considering the combination of positive and negative errors in absolute value. This makes MAE a robust choice when the direction of errors is not critical. For evaluating the algorithm to employ in the proposed ML surrogate model, all the above metrics (i.e., loss functions) can be used, but for the case at hand, the discriminant metrics for selecting the best model is the MSE_2. In fact, it is important to distinguish between positive and negative errors, because a smaller value of F_1 is conservative, reflecting then a positive value of the error. On the other hand, RMSE is the best way to assess the accuracy of the model, because as above reported, it is an overall metrics able to give an idea about the obtained output, in the same unit measure of the output itself.

Finally, given the nature of the proposed black-box models, a physical explanation of ML surrogate model can provide additional insights into the prediction. To this scope, eXplainability metrics could be exploited. Although different eXplainability techniques are available in the literature, a viable option is a model-agnostic interpretable method, such as SHapley Additive exPlanations (SHAP), Lundberg and Lee (2017). This latter can be used to deeply investigate the structure of ML models by analysing the relationship between the input variables and output of the model (called SHAP value). SHAP uses cooperative game theory to allocate credit for a model output among its input features. The idea is to consider each feature as a player and the dataset as a team. The players give their contribution to the result of the team. The influence of a feature is dependent on the complete set of features in the dataset and not on only a single feature. Thus, SHAP retrains the model overall feature combinations accounting for the feature under consideration, by calculating SHAP value using combinatorial calculus. The significance of a feature can be determined by estimating the average absolute value, which is compared with a target variable.

$$\gamma_o(\delta, r) = \sum_{S_N \subseteq N_d \setminus \{o\}} \frac{|S_N|!\,(|N_d| - |S_N| - 1)}{|N_d|!} [\delta_r(S_N \cup \{o\}) - \delta_r(S_N)] \quad (58)$$

Equation (58) describes mathematically the SHAP value, γ_o, of the input feature o. δ is the trained ML model, r is a generic record of the sample data, N_d, and S_N is a subset of N_d that does not include o. The two terms under the summation sign express the weighting function for the impact on each subset of features S, and the impact of removing the feature o, respectively.

For the case at hand, the importance of SHAP application is dual: (i) SHAP can highlight which parameters require an accurate evaluation because they present a higher impact on the output values; and (ii) SHAP can indicate the best combination of fibres and section to monitor based on significance of features, in order to reduce the cost of the sensors-based system to design.

3.4. Experimental tests on a scaled PSC box bridge and results

The framework described in Section 3.3 was applied to an experimental case study, and the steps performed are summarized in Fig. 80.

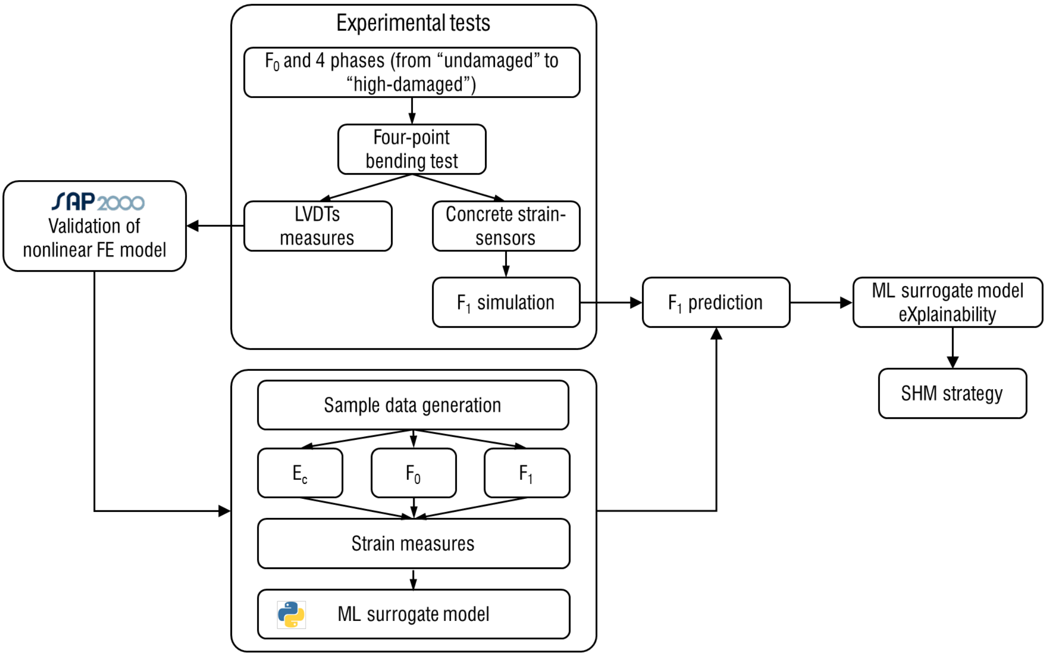

Fig. 80 - ML-based framework application on an experimental case.

3.4.1. Description of the specimen

The considered specimen was a scaled PSC box bridge tested in the ICITECH laboratory of the *Universitat Politècnica de València* (ICITECH, 2024). The use of a scaled model is justified by the necessity to simulate the prestressing loss in a controlled environment, besides the impossibility to create a real dimension specimen in laboratory or to produce controlled damage in a real bridge under service. At the same time, the investigation of one (or more) full-scale specimen would allow the generation of more reliable data in the next steps of the work. The specimen, shown in Fig. 81, is geometrically defined as a box-girder having length, L, equal to 6 m, supported by two hinged and a hinged-roller supports (see Fig. 81, right and left respectively). At both beam ends, the box section is solid for a length of 0.40 m (Fig. 81d), while in the middle the box section is lightened by expanded polystyrene (Fig. 81c). During the construction phase, three polyvinyl chloride tubes, diameter of 24 mm, were placed in the bottom part of the section, to subsequently insert unbonded prestressing bars. Given the use of a scaled model, it was not possible to reproduce a prestressing system like the one employed in real bridges, but tendons were simulated by three steel bars with 20 mm of diameter. The bars, 45 days after concrete casting, were placed into the housing and were anchored through bolts with steel plates interposed to the end faces of the beam after stringing operations, as shown in Fig. 82. Regarding construction materials, the concrete class used was C30/37 (according to Eurocode 2 [65]) with aggregates having maximum size of 20 mm, while steel used for both mild and prestressing reinforcement was B500C [65]. Mechanical properties of the concrete, compressive and tensile strength and Ec, were evaluated through tests on nine cubic specimens collected before casting the main specimen. Regarding concrete curing, both concrete specimen types were subjected to pouring water for the first three days after casting and, before performing mechanical tests, no shrinkage cracks were detected. The mechanical properties of concrete were evaluated 45 days after concrete casting, rather than 28 days as usual in the practice, to provide a representative description of the mechanical features of the specimen during the Four-point bending tests, which were carried out on the same day of the stringing operation of prestressing bars. On the other hand, the mechanical properties of the steel were assumed equal to the ones declared by the manufacturer (i.e., see mechanical properties of B500C steel, as reported in the Eurocode 2, 2004, with yielding and ultimate strength equal to 500 and 620 MPa, respectively, and ductility factor equal to 1.24). Test results of concrete tests are summarized in Table 15.

After defining the specimen, the beam was instrumented for two main reasons: (i) to calibrate a nonlinear FE model; (ii) to record strain measurements while simulating prestressing losses. Regarding the adopted monitoring system, several sensors were installed as shown in Fig. 83: (i) ten linear variable displacement transducer (LVDTs)

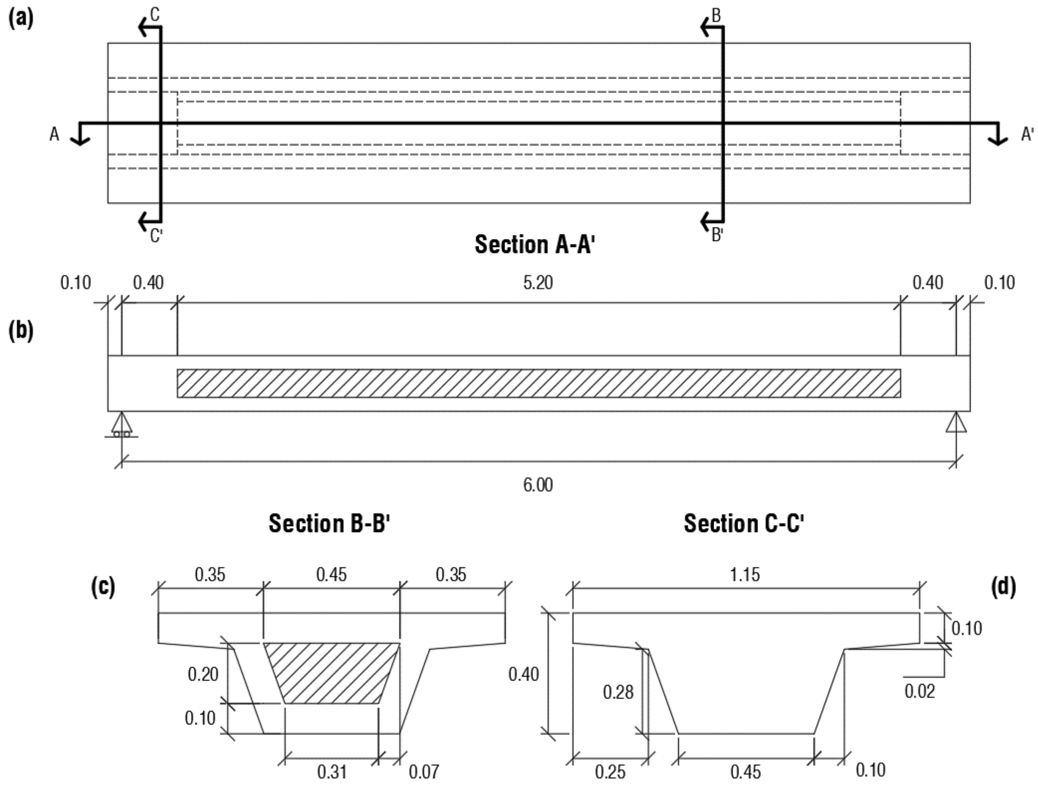

Fig. 81 - Geometry of lab-tested scaled PSC box bridge: (a) Top view, (b) Longitudinal section A-A', (c) Hollow cross-section B-B', (d) Solid cross-section C-C'.

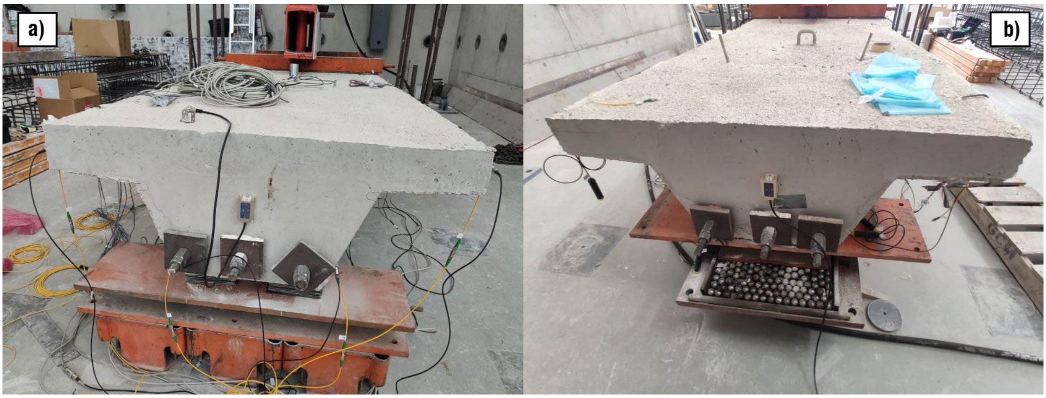

Fig. 82 - View of anchorages of prestressing bar on (a) fixed and (b) mobile support.

Table 15 - Results of mechanical tests through Ibertest universal machine, on nine concrete cylinders, three investigated after 14 days and three investigated after 45 days.

Compressive strength [MPa]		**Tensile strength [MPa]**	**Elastic modulus E_c [MPa]**
14 days	45 days	45 days	45 days
29.86	34.99	2.35	39464
29.28	31.34	3.01	36741
Discarded value	32.12	2.93	32412

were placed along the longitudinal development of the beam, one for each meter starting from the mobile support and considering both left and right side of the section, to measure the vertical displacements (Fig. 83b); (ii) twenty-one embedded strain gauges to monitor concrete deformations, subdivided among five placed on lower part of the section at two different cross-sections, glued to the bottom rebars and located at the middle, at a quarter of the span length (L/4 and L/2, which is 1.5 m and 3 m from the hinged support, respectively), and at mobile support, for a total of fifteen sensors (Fig. 83c); and three placed on each side of every prestressing steel bar to measure deformations and to derive both axial stress and prestressing force during stringing operations and investigation phases (i.e., Four-point bending test), for a total of six sensors (Fig. 83d). Although strain sensors are usually placed on the bottom and upper fibers of the same section, the selected location of the sensors was an engineering choice since, for the type of loading, the main strain increments were expected in the considered positions. In addition, a FBG sensor was placed for the entire length of the bridge, in the same vertical position of strain sensors and in the upper face to provide strain increments on top fibers. According to the definition of the specimen, the value of prestressing force applied to each bar was equal to 110 kN (and then, F_0 was equal to 330 kN), which resulted in a stress on each bar equal to 350 MPa. The final value of F_0 also included the instantaneous prestressing losses due to the elastic deformation of the concrete induced by the sequential strand stringing. It is worth noting that due to the application of the prestressing force and the performance of the entire experimental

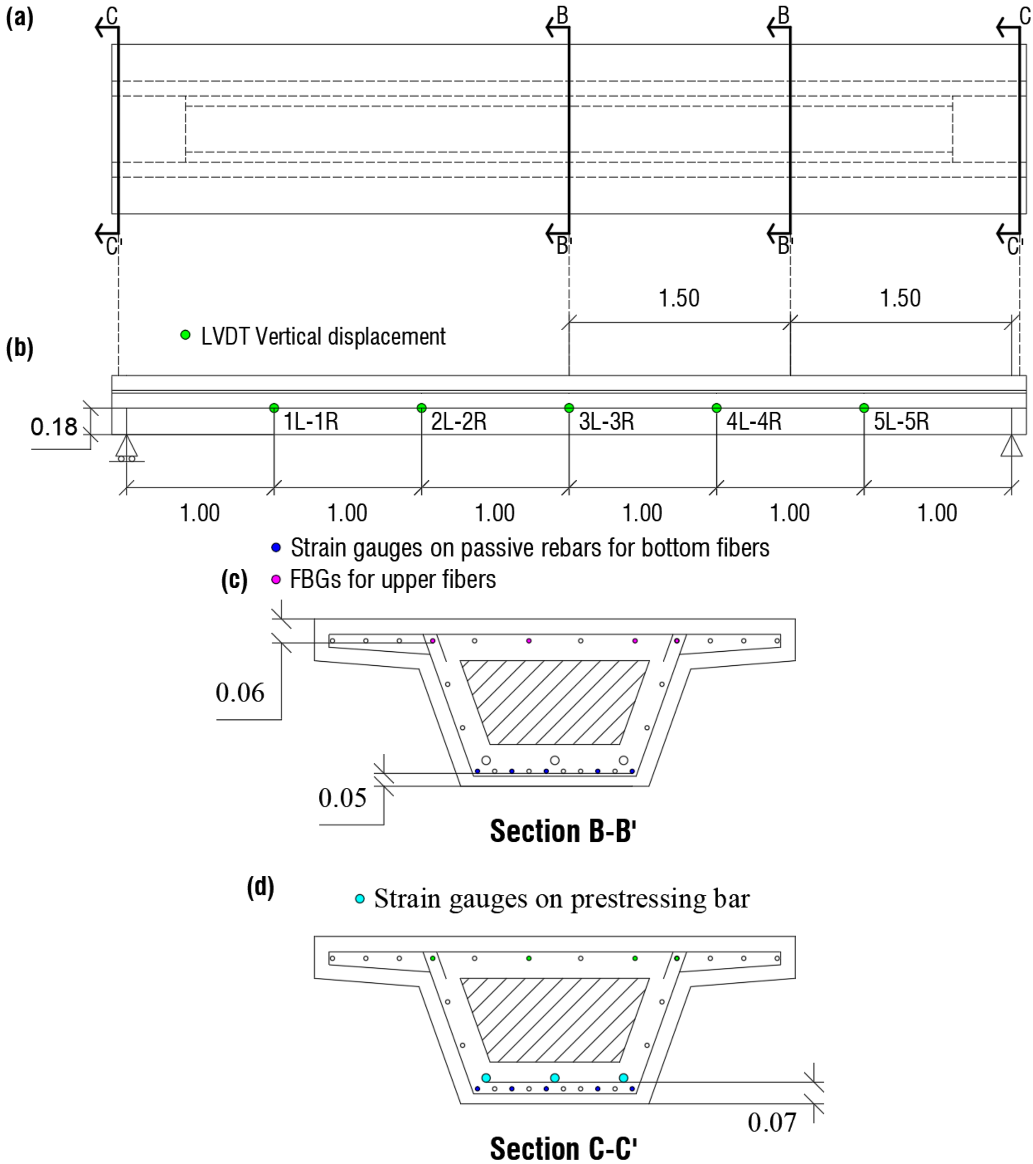

Fig. 83 - Position of installed sensors: (a) Top view, (b) Longitudinal view on left side, (c) Hollow cross-section B-B', (d) Solid cross-section C-C'.

campaign on the same day (i.e., the 45th day after the concrete casting), the early-age phenomena due to relaxation of the tendons and creep can be considered negligible.

3.4.2. Experimental setup and test

The laboratory tests were designed to assess the effects of prestressing variation due to the loss of functionality of steel strands on the box beam deformations through strain gauges. To this scope, the experimental campaign was subdivided into four phases: Phase 1, also named “undamaged”, in which the beam was loaded in its initial state; Phase 2, also named “low-damaged”, in which the prestressing loss was simulated by removing one of the three bars and the same loading was performed again; Phase 3, also named “moderate-damaged”, in which the prestressing loss was simulated by removing an additional bar (two of the three bars are removed) and the same loading was performed again; Phase 4, also named “high-damaged”, in which the loss of the whole prestressing force was simulated by the removal of the three post-tensioning bars and the same loading protocol was performed. For all cases, the loading was applied through a Four-point bending test in which the maximum applied load was set to 140 kN for Phases 1, 2, 3 and 4, although the test continued until failure in Phase 4, reaching a final value of load equal to 210 kN. The setup of the tests can be observed in Fig. 84, while schematic test configuration in terms of geometry and loading steps is shown in Fig. 85. In Fig. 86, the end sections in the four considered Phases are shown, with the progressive removal of the prestressing bars. The loading and the test were designed to ensure a quasi-elastic behaviour of the specimen from Phase 1 “un-damaged” to Phase 3 “damaged”, where also damage was incremental to avoid a significant effect of one test on the subsequent one. In addition, over the first three phases, the specimen did not exhibit either vertical cracks in the middle due to bending moment or residual displacements due to plastic deformation of materials. The absence of residual plastic deformation was verified by comparing sensor measurements at the beginning and at the end of the loading-unloading protocol of each phase, not observing differences in terms of deformation. Effects like creep, shrinkage, and strand relaxation were not considered, for the reasons reported in Section 3.3.1 (the application of the prestressing force and the entire experimental campaign were performed on the same day, minimizing the effects of early-age phenomena). In addition, considering the

Fig. 84 - Set up of the four-point bending test.

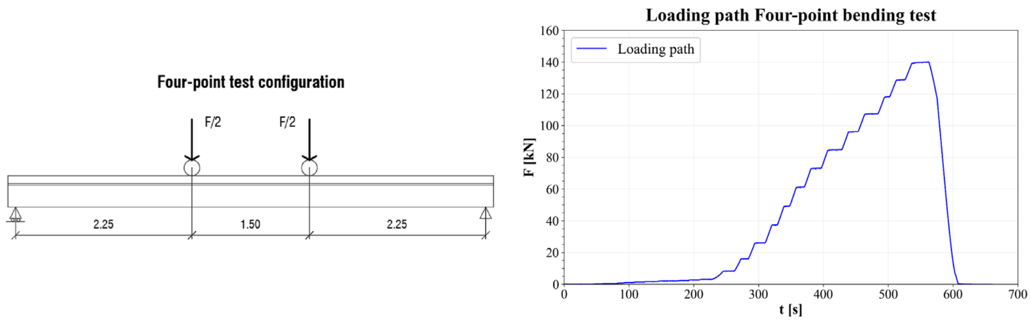

Fig. 85 - Four-point bending test: (from left to right) configuration (F/2 indicates half of the total force applied in those positions) and loading protocol of Phase 1.

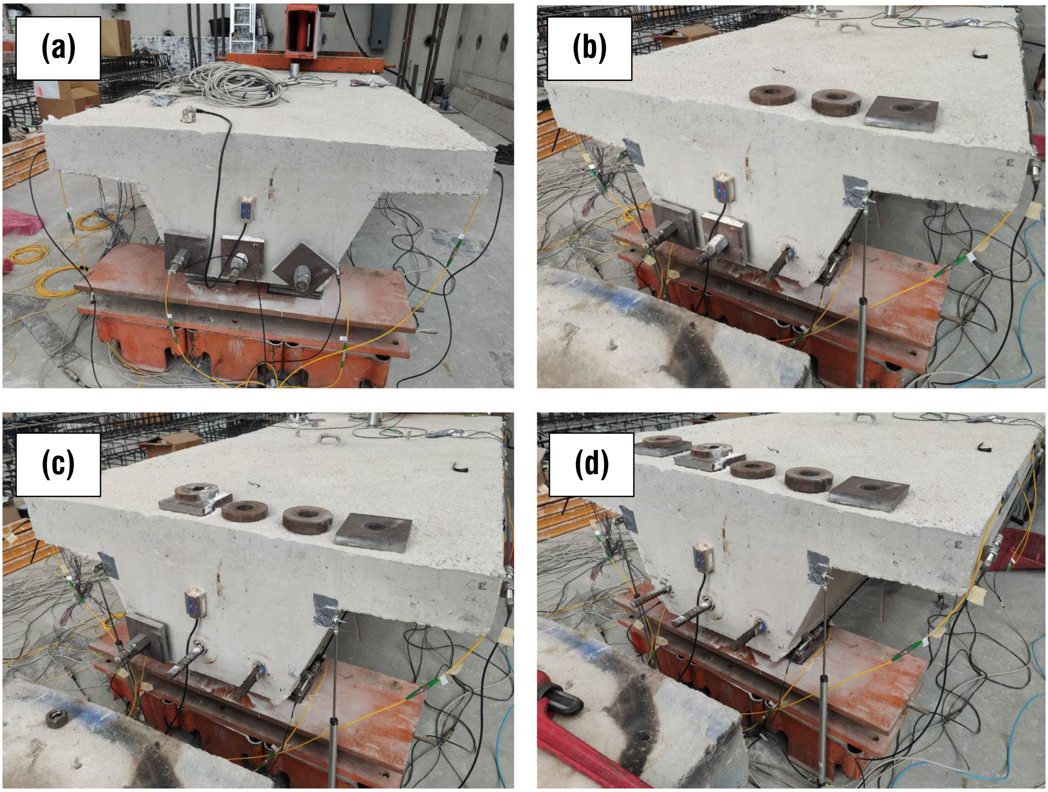

Fig. 86 - End section of the Box-Girder specimen, observed at Phase 1 (a), Phase 2 (b), Phase 3 (c) and Phase 4 (d).

3.4.3. Definition and calibration of the FE model

Having at disposal the data about experimental tests, a nonlinear numerical FE model of the specimen was carried out, by calibrating to the numerical output on the vertical displacements measured with LVDT sensors. The bridge was simulated through the SAP2000 structural software, v.25 (Computer and Structures, Inc, 2024), by using frame elements. The girder was divided in five frame elements of different length. The two external frames, indicated with grey elements in Fig. 87a , were characterized by a solid cross-section, Fig. 81c and Fig. 87b, with a length 0.40 m. The three central frames, indicated with blue elements in Fig. 87a, were characterized by a hollow cross-section, Fig. 81d and Fig. 87c, with different lengths of 1.85 m, 1.50 m,

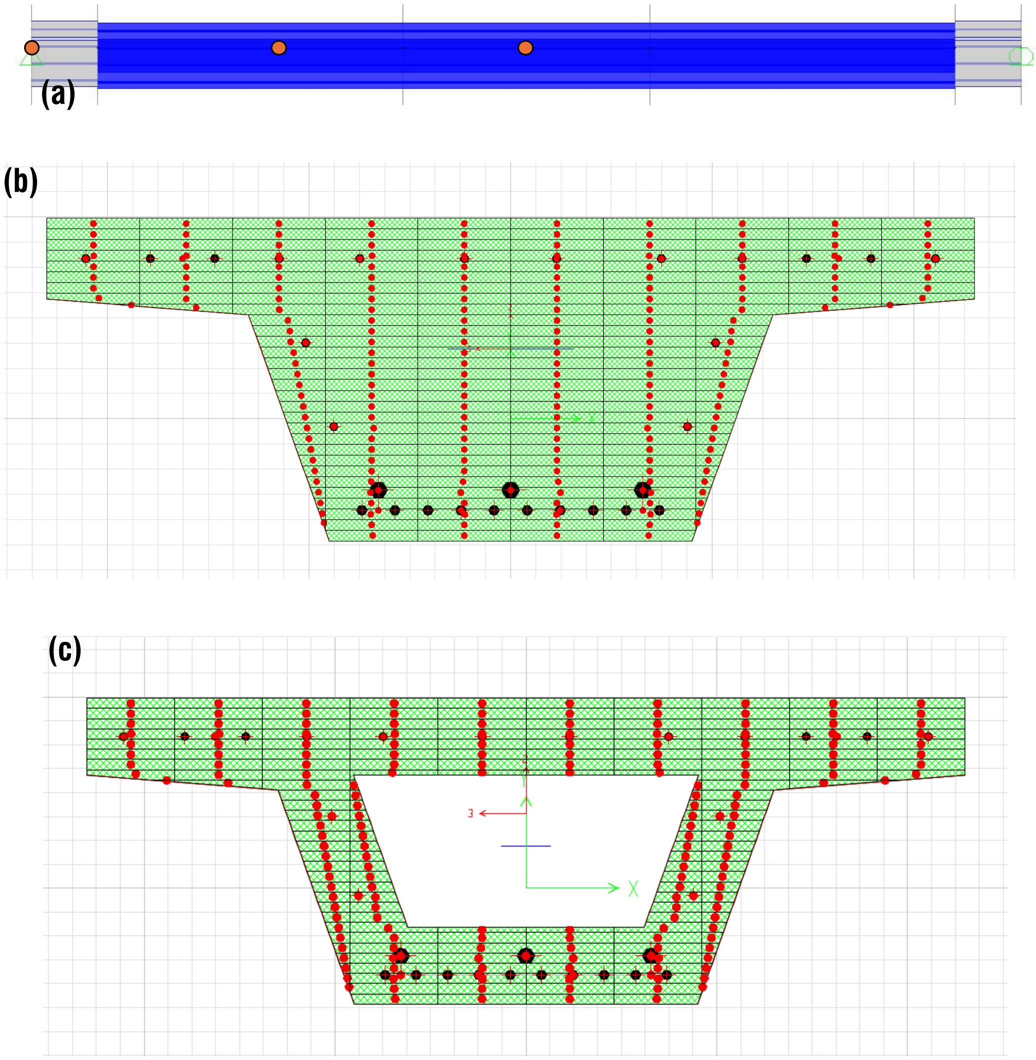

Fig. 87 - FE model in SAP2000: (a) frame elements of the FE model with plastic hinges (orange dots); (b) solid cross-section fiber definition; (c) hollow cross-section fiber definition.

and 1.85 m, respectively. The subdivision of the central part was set to simulate the position of the vertical loads of the Four-point bending test. External restraints were assigned to the external frames to simulate supports with proper degrees of freedom (i.e. one hinge and one hinged-roller supports).

Regarding the load applications, as schematically reported in Fig. 85 left, the loads were applied at a 2.25 m distance from the supports. Still, considering the frame a one-dimensional element, the vertical load condition of the four-point test was modelled by two vertical forces, whose values were half of the experimental load (i.e., 70 kN for 140 kN load step of Phase 1 “undamaged”). The axial load of the prestressing system was applied on both the sides of the beam (110 kN for each bar depending on the phase under investigation), accounting for bending moments (Noble *et al*., 2016) due to the eccentricity with respect to the centroid of the section (red local reference system in Fig. 87c), indicated with M_x and M_y around X and Y axes, respectively (see green reference system in Fig. 87c). Indeed, the prestressing bars were placed at a distance equal to 0.19 m and 0.18 m from the centroid of the section in the Y direction (green reference system in Fig. 87c) for hollow and solid section, respectively. Given the different position of the centroid for the two sections, an additional bending moment was considered at the end of frames with hollow cross-section in the FE model. Moreover, when simulating Phase 2 “low-damaged” and Phase 3 “moderate-damaged”, the absence of one or more prestressing bars generated an additional bending moment around the Y axis, which was applied only at the end of frames with solid section (considering that the centroid of the two sections differed only in the Y direction).
Concerning the nonlinear modelling, the diffused plasticity strategy mentioned in Section 3.3.1 regarded the number and distribution of plastic hinges in the beam (PMM type due to the interaction of prestressing force and bending moments). The behaviour of the plastic hinges was defined by the software considering the section, fibers and mechanical properties of materials. Solid and hollow cross-sections were divided as 10 fibers in X direction and 30 in the Y direction (see Fig. 87c) for a total number of 235 and 207 fibers, respectively. The selected number of fibers was fixed according to two main considerations: (a) the differences in terms of strain, obtained with a model characterized by a higher number of fibers than the current model were lower than 5%; (b) the discretization in fibers was set to match the position of strain gauges. Thus, plastic hinges were placed at girder mid-length (i.e., at 3.0 m) and at a distance equal to 1.5 m from hinged support for the hollow section, and at the end of the beam for the

solid section near the hinged support. The analysis on the FE model was subdivided into two steps: (i) application of external forces due to the prestressing system (i.e., axial loads and bending moments); (ii) application of Four-point bending test load in a force-controlled approach on the geometric configuration of the step (i). Both analyses considered geometrical nonlinearities (i.e., P-Δ).

The numerical calibration was performed by varying only one parameter, that is, the E_c value. To assess the accuracy of the numerical model, several comparisons between numerical and experimental results were performed. Vertical displacements were compared for each Phase using LVDT records on the left and right part of the box-girder. As for example, Fig. 88 reports the comparison between experimental and numerical results in the Phase 1 (i.e., "undamaged") and in Phase 2 (i.e., "low-damaged"), both for an intermediate load step of 60 kN, and for the last load step of 140 kN. As can be observed, there is a total agreement between numerical and experimental results, with low percentage differences both in the "undamaged" and "low-damaged" cases. Numerical results can be also checked in Table 16, where the differences both in percentage values and in millimetres for the ten LVDTs placed on the beam are reported. In detail, the experimental vertical displacements are higher than the numerical ones on average by 1.4% and 0.8% in Phase 1 ("undamaged") and Phase 2 ("low-damaged"), respectively, for a load step of 60 kN, and on average by 1.2% and 0.7% on Phase 1 ("undamaged") and Phase 2 ("low-damaged"), respectively, for a load step of 140 kN. This is an important achievement since confirms and justifies the type of simplified nonlinear numerical model used for the next steps. The same conclusion can be drawn by comparing experimental and numerical values of stress levels of prestressing bars during Phase 1, Phase 2, and Phase 3. Stress values were derived from strain measures and were equal to 429 MPa, 459 MPa and 493 MPa for Phase 1 "undamaged", Phase 2 "low-damaged", and Phase 3 "moderate-damaged", respectively (considering an initial stress value of 350 MPa at the bar stringing). During Phase 4 "high-damaged", stress values were available only for mild reinforcements, which were beyond the yielding tensile strength of steel, i.e., 500 MPa. The above values were

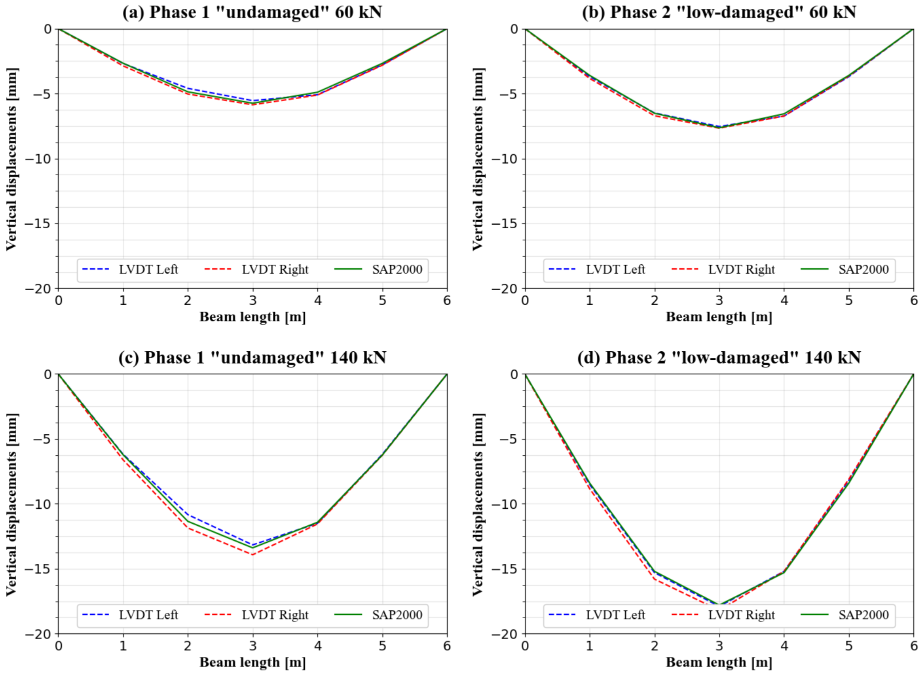

Fig. 88 - Comparison between numerical (step (ii) SAP2000) and experimental (Phase 1 "undamaged" and Phase 2 "low-damaged" LVDT) vertical displacement values for 60 kN (a – b) and 140 kN (c – d) steps. All the values are expressed in millimetres; therefore, all vertical deformed shapes are in 1000:1 scale with respect to beam length.

assessed also in the FE model, and a good agreement in terms of stress was observed, with a percentage difference of 2% on average.

Looking at the results in Fig. 88, it is worth noting that the values obtained by the numerical FE model are equal on the left and right sides, considering that the structure was modelled as a frame element. In addition, the calibration performed with a "trial-and-error" approach showed that the value of E_c was equal to 38150 MPa, which is in good agreement with experimental data reported in Table 16 (5% of difference with the average value of the three concrete cylindric specimens after 45 days, equal to 36200 MPa). The higher value of the calibrated E_c is balanced by the assumption of perfect external restraints, which in the FE model ensure null rotational stiffness. The balance between the ideal boundary conditions (FE model should experience higher deformations) and different mechanical properties (FE model should experience lower deformations) provided a deformation for the FE model comprised between the LVDT measurements on both sides of the beam, as shown in Fig. 88.

Table 16 - Comparison between numerical (step (ii) SAP2000) and experimental (Phase 1-undamaged and Phase 2-low-damaged LVDT) vertical displacement values for 60 kN and 140 kN steps.

Phase	Applied load [kN]	*F* [kN]	LVDT ID	Lab-test [mm]	SAP2000 [mm]	Difference [mm]	Difference [%]
1	60	330	1L	-2.576	-2.667	0.091	-3.53%
			1R	-2.755	-2.667	-0.088	3.19%
			2L	-4.844	-4.871	0.027	-0.56%
			2R	-5.303	-4.871	-0.432	8.15%
			3L	-5.639	-5.747	0.108	-1.92%
			3R	-5.964	-5.747	-0.217	3.64%
			4L	-5.018	-4.902	-0.116	2.31%
			4R	-5.043	-4.902	-0.141	2.80%
			5L	-2.665	-2.681	0.016	-0.60%
			5R	-2.694	-2.681	-0.013	0.48%
1	140	330	1L	-6.180	-6.215	0.035	-0.57%
			1R	-6.609	-6.215	-0.394	5.96%
			2L	-10.835	-11.351	0.516	-4.76%
			2R	-11.862	-11.351	-0.511	4.31%
			3L	-13.165	-13.392	0.227	-1.72%
			3R	-13.925	-13.392	-0.533	3.83%
			4L	-11.498	-11.423	-0.075	0.65%
			4R	-11.554	-11.423	-0.131	1.13%
			5L	-6.191	-6.248	0.057	-0.92%
			5R	-6.259	-6.248	-0.011	0.18%
2	60	220	1L	-3.548	-3.605	0.057	-1.61%
			1R	-3.685	-3.605	-0.080	2.17%
			2L	-6.840	-6.523	-0.317	4.63%
			2R	-7.064	-6.523	-0.541	7.66%
			3L	-7.667	-7.639	-0.028	0.37%
			3R	-7.795	-7.639	-0.156	2.00%
			4L	-6.634	-6.566	-0.068	1.03%
			4R	-6.634	-6.566	-0.068	1.03%
			5L	-3.530	-3.605	0.075	-2.12%
			5R	-3.487	-3.605	0.118	-3.38%

Phase	Applied load [kN]	F [kN]	LVDT ID	Lab-test [mm]	SAP2000 [mm]	Difference [mm]	Difference [%]
2	140	220	1L	-8.514	-8.413	-0.101	1.19%
			1R	-8.840	-8.413	-0.427	4.83%
			2L	-15.366	-15.227	-0.139	0.90%
			2R	-15.867	-15.227	-0.640	4.03%
			3L	-17.923	-17.786	-0.137	0.76%
			3R	-18.233	-17.786	-0.447	2.45%
			4L	-15.230	-15.298	0.068	-0.45%
			4R	-15.198	-15.298	0.100	-0.66%
			5L	-8.204	-8.402	0.198	-2.41%
			5R	-8.129	-8.402	0.273	-3.36%

3.4.4. Sample data generation

Given the calibrated nonlinear numerical FE model, new data were generated by varying some parameters in a schematic way. To this scope, SAP2000 OpenAPI was used, and, through Python programming language (Python Software Foundation, 2024) , several numerical FE models were created and analysed. The first varied parameter was E_c, which was randomly changed between 30000 MPa and 40000 MPa for 129 times (this interval of variation is justified later in this Section). After, considering the necessity to simulate the prestressing losses and the presence of three unbonded steel strands, a first hypothesis was fixed, that is, each bar was equivalent to a classical tendon made by three 7-wire strands to be able to progressively simulate the loss of a small percentage of post-tensioning. According to this assumption, the variation from F_0 to F_1 was simulated by eliminating a progressive number of wires from the three available unbonded steel strands, in order to define a progressive percentage drop rate. With this regard, a minimum value of absolute percentage drop rate equal to 0% was assumed (initial state), while a maximum value of absolute percentage drop rate equal to 40% was fixed. Obviously, higher values of percentage drop rate could be considered but, according to the available literature (e.g., Nettis *et al*., 2024), a percentage drop rate of 20% already might lead to capacity-demand ratios lower than the unity. Hence, the simulation of a prestressing loss of 40% can be assumed double an acceptable physical limit. Besides, it is important to train the ML surrogate model for real situations and not towards extreme limits of damage that are physically admissible. In addition, a percentage drop rate of 40% simulated a loss in F_0 assimilable to the 33% obtained in the laboratory test by removing one of the three bars (i.e. the calibration performed in this work is consistent for the creation of the ML surrogate models).

The logic behind the model generation aimed at defining different values of F_0 and F_1, to cover a large range of real applications. Let us define two values of percentage drop rate: (a) initial percentage drop rate, which represents the initial prestressing loss imposed on F_0 to vary this value in the ML model; (b) final percentage drop rate, which represents the final prestressing loss on F_0 that provide the value of F_1. Assuming a fixed value of E_c and a value of F_0 with a declared initial percentage drop rate, a progressive removal of one wire for each strand was simulated (i.e., a numerical FE model), until achieving a final percentage drop rate of 40%. For example, if the initial drop rate is 0%, the model is characterized by three groups of three 7-wires strands, each one containing 21 wires, and a final percentage drop rate of 40% can be achieved when each group of three strands is characterized by 13 wires (i.e., 9 models). If the initial drop rate is 10%, the model is characterized by three groups of strands, each one containing 19 wires, and a final percentage drop rate of 40% can be achieved when each group of three strands is characterized by 11 wires (i.e., 9 models). In this way, for achieving a final percentage drop rate of 40%, the value of F_0 was updated for values of initial percentage drop rate equal to 0% (from 21 wires to 13 wires), 10% (from 19 wires to 11 wires), 20% (from 17 wires to 10 wires), 30% (from 15 wires to 9 wires) and 40% (from 13 wires to 8 wires), and the final number of models was equal to 39 (counting also the first case without first wire removal).

Combining the 39 models with 129 values of E_c, a total of 5031 models were generated (the number of E_c values was set to achieve more than 5000 models and, for each model, six values of $\Delta\varepsilon^{(i,j)}$ (for a total number of 30186 $\Delta\varepsilon_{model}{}^{(i,j)}$, taking the average strain values of the j^{th} fiber in the i^{th} section) were extracted (according to the locations of strain gauges and FBG sensors installed for the reference laboratory test). The generated sample of data was then used for calibrating the ML surrogate model. In literature, the size of the sample data varies and upscales as the complexity of the ML application raises. In this case, the size of sample data was set according to problems of similar complexity, as shown in Parisi *et al*. 2022, which employed about 5000 models. Increasing the complexity of the problem, the size of sample data increases, as for example shown by Parisi *et al*. 2024, which adopted about 15000 models for training a graph neural network on a 2D truss-structure.

3.4.5. Definition of ML surrogate models and discussion of the obtained results

For each generated model, the analyses defined in Section 3.3.2 were performed and results in terms of input (F_0, E_c, $\Delta\varepsilon^{(i,j)}$) and output ($F_1$) parameters were stored. Hence, the training of the ML surrogate models (i.e., using all above-defined networks in Section 3.3.3) was performed through a machine equipped with a 11th Gen Intel® Core ™ i9-11980 HK @ 2.6 GHz (8 CPUs), 32 GBs DDR4 of RAM, and NVIDIA GeForce RTX 3080 GPU with 16 GBs. The sub-optimal values of hyperparameter tuning employed in all models and obtained via grid search are reported in Table 17, while training/test statistical metrics values are reported in Table 18.

As observed, the obtained results for all ML models provide a good accuracy with optimal values of the evaluation metrics, which justify the use of the proposed models. In addition, although R^2 values for each ML surrogate model overcame 0.99 in both training/test phases (see Fig. 89), some differences can be highlighted for the other statistical metrics in Table 18. MAE values were lower than other models for the ANN (0.0016/0.0017), although the MAE obtained by RFR in the training phase (0.0058) was close to that by ANN. As discussed in Section 3.3.4, MSE_2 and RMSE are the core statistical metrics. Given that a positive value of MSE_2 leads to underestimations of the output value, thus providing a conservative evaluation of F_1, ANN is the only ML Surrogate model to achieve this requirement (0.00061/0.00064), while negative values were obtained for RFR (0.0015/-0.0046) and SVR (-0.0014/-0.001). Still, ANN outperformed SVR and RFR by considering RMSE (ANN: 0.0019/0.0021, RFR: 0.0938/0.03301, SVR: 0.0255/0.0257), and MSE_1 (ANN: 4.12E-06/4.57E-06, RFR: 0.0088/0.1090, SVR: 0.0006/0.0006) This result was expected given the ability of ANN to generalize

Table 17 - Hyperparameter tuning for each ML algorithm.

Model	Hyperparameter	Value
ANN	Neurons in 1st hidden layer	64
	Activation function of 1st hidden layer	ReLU
	Neurons in 2nd hidden layer	256
	Activation function of 2nd hidden layer	TanH
	Optimizer	Adam
	Epochs	600
	Loss function	MSE_1
RFR	Number of trees in the Forrest	100
	Maximum number of levels in each decision tree	10
	Minimum number of samples required to be at a leaf node	6
SVR	C	0.2
	ε	0.05
	Kernel	Rbf

Table 18 - Evaluation metrics results for training and test dataset of each ML surrogate model.

Set	Metric	ANN	RFR	SVR
Training	R^2	0.9999	0.9999	0.9945
	MAE	0.0016	0.0058	0.0216
	MSE_1	4.12E-06	0.0088	6.5E-04
	RMSE	0.0019	0.0938	0.0255
	MSE_2	6.13E-04	1.53E-03	-1.42E-03
Test	R^2	0.9999	0.9999	0.9845
	MAE	0.0017	0.0229	0.0213
	MSE_1	4.57E-06	0.1090	6.5E-04
	RMSE	0.0021	0.3301	0.0257
	MSE_2	6.44E-04	-4.58E-03	-1.00E-03

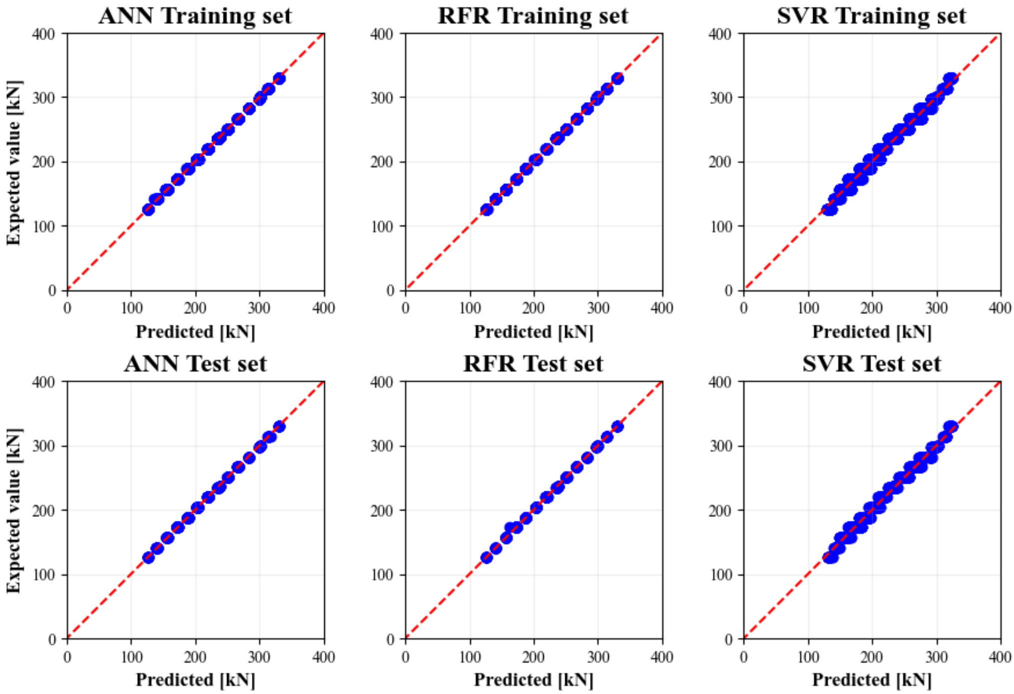

Fig. 89 - ML surrogate models comparisons between predicted and expected value (F_1) on training set (top row) and test set (bottom row). Red dashed line shows R^2.

problems. Using the RMSE to evaluate the capability of the model to predict prestressing losses (same unit measure), the obtained value by using ANN represent a lower bound in terms of prediction (i.e., the proposed model is able to predict low prestressing losses, up to 1.9 N)

After defining the three ML models, the choice of the surrogate was performed by checking the predictive capacity of each model toward the experimental tests. To this scope, all models were applied to predict the experimental values obtained in Phase 2, "low-damaged", which was characterized by the removal of one bar over three, with a F_0 equal to 330 kN and a F_1 equal to 220 kN. The results are shown in Table 19, where all models presented overall satisfying results. Nevertheless, the surrogate model made by ANN confirmed the best accuracy, having a percentage difference in terms of F_1 of 0.3%. It is worth noting that also RFR presented very good results, with a percentage

Table 19 - ML surrogate models F_1 calculated values on Phase 2 "low-damaged" measurements.

ML Surrogate model	F_1 calculated [kN]	F_1 experimental [kN]	Difference [%]
ANN	219.43	220	0.3%
RFR	219.13	220	0.4%
SVR	209.78	220	4.6%

difference of 0.4% in terms of F_1. It is worth noting that, although ANN presented high accuracy (see hyperparameter tuning shown in Fig. 90) there was no evidence of overfitting problems. In fact, as performed in several existing papers (e.g., Mangalathu *et al*., 2019) , by assessing the performance of the proposed ML model to the training and test data, properly split, the overfitting problem can occur if the model performs significantly better on the training set than the test set. To check this aspect, two main controls were performed: (a) definition of k-fold cross-validation to evaluate the model performance; and (b) comparison of the loss function between training and test datasets. Regarding the k-fold cross-validation, a 10 k-fold subdivision was considered and statistical metrics results for each fold are reported in Table 20, together with the related mean and standard deviation (mean values for training set are the same reported in Table 18 for ANN). Regarding the loss function, the MSE_1 metric was used, and the results are shown in Fig. 91a for ANN. Loss function for training and test datasets were similar, confirming the absence of overfitting for the proposed surrogate model. Still, Fig. 91b reports the residues for the test dataset, to denote a normal-like distribution of this quantity, which suggests that errors are random and not correlated. Finally, an eXplainability approach was used on the proposed ML surrogate model to assess the influence of each considered parameter on the simulated prestressing loss. It is worth reminding that this step is important because it can provide some insights about the most influent concrete strain values on the results, which in turn can suggest how to design sensors-based systems aimed at monitoring the prestressing losses. With this goal in mind, the SHAP method was employed through SHAP Python package, and the results are shown in Fig. 92 and Fig. 93. In particular, Fig. 92 reports the summary

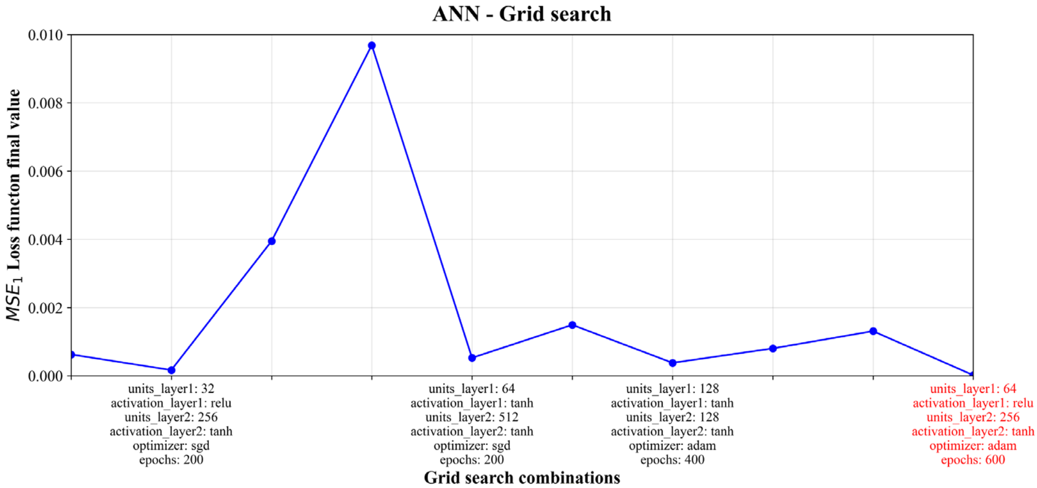

Fig. 90 - Loss function (MSE_1) values for some of the combinations of ANN hyperparameters used to select the best hyperparameter set (red one) reported in Table 16. In the abscissa, only few sets of hyperparameters (i.e., the more accurate) were reported, for the sake of clarity.

Table 20 - ANN K-fold cross-validation metrics results on training and validation sets.

Set	Metric	k-fold										Avg.	Std.
		1	2	3	4	5	6	7	8	9	10		
Training	R^2	0.9999	0.9999	0.9999	0.9999	0.9999	0.9999	0.9999	0.9999	0.9999	0.9999	0.9999	4E-05
	MAE	0.0025	0.0022	0.0015	0.0019	0.0013	0.0016	0.0022	0.0012	0.0008	0.0008	0.0016	5E-04
	MSE_1	8E-06	7E-06	3E-06	5E-06	3E-06	4E-06	7E-06	3E-06	1E-06	1E-06	4E-06	2E-06
	RMSE	0.0029	0.0025	0.0017	0.0022	0.0017	0.0019	0.0026	0.0017	0.0011	0.0011	0.0019	5E-04
	MSE_2	2E-03	-2E-03	-3E-04	2E-03	-1E-03	-1E-03	2E-03	-7E-05	-1E-04	-1E-04	6E-04	1E-03
Validation	R^2	0.9999	0.9999	0.9999	0.9999	0.9999	0.9999	0.9999	0.9999	0.9999	0.9999	0.9999	4E-05
	MAE	0.0026	0.0021	0.0016	0.0020	0.0014	0.0017	0.0022	0.0012	0.0009	0.0009	0.0017	5E-04
	MSE_1	8E-06	6E-06	5E-06	5E-06	3E-06	4E-06	7E-06	3E-06	1E-06	2E-06	4E-06	2E-06
	RMSE	0.0029	0.0025	0.0023	0.0023	0.0018	0.0021	0.0026	0.0018	0.0012	0.0014	0.0021	5E-04
	MSE_2	3E-03	-2E-03	-3E-04	-2E-03	1E-03	-1E-03	2E-03	-2E-04	-2E-04	-1E-04	6E-04	1E-03

plot with input features in ordinate, ranked on the base of their influence on the results, and in abscissa the value of the impact of each feature on the predictive capacity of the model. A red color indicates increasing output value while a blue color denotes decreasing output value. As expected, the most influential value is F_0. The second and the

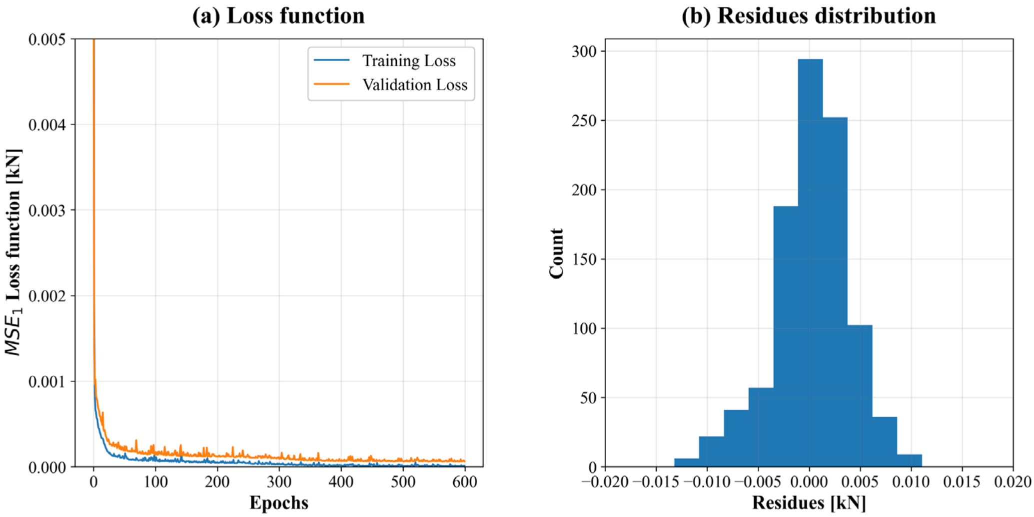

Fig. 91 - ANN (a) loss function values, (b) residues distribution of test data.

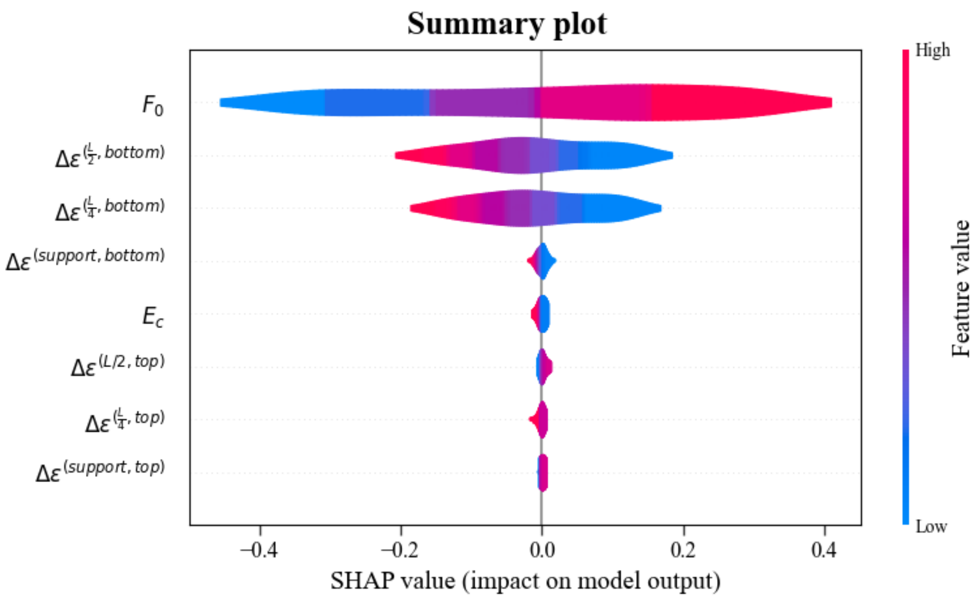

Fig. 92 - SHAP results for F_1 output feature.

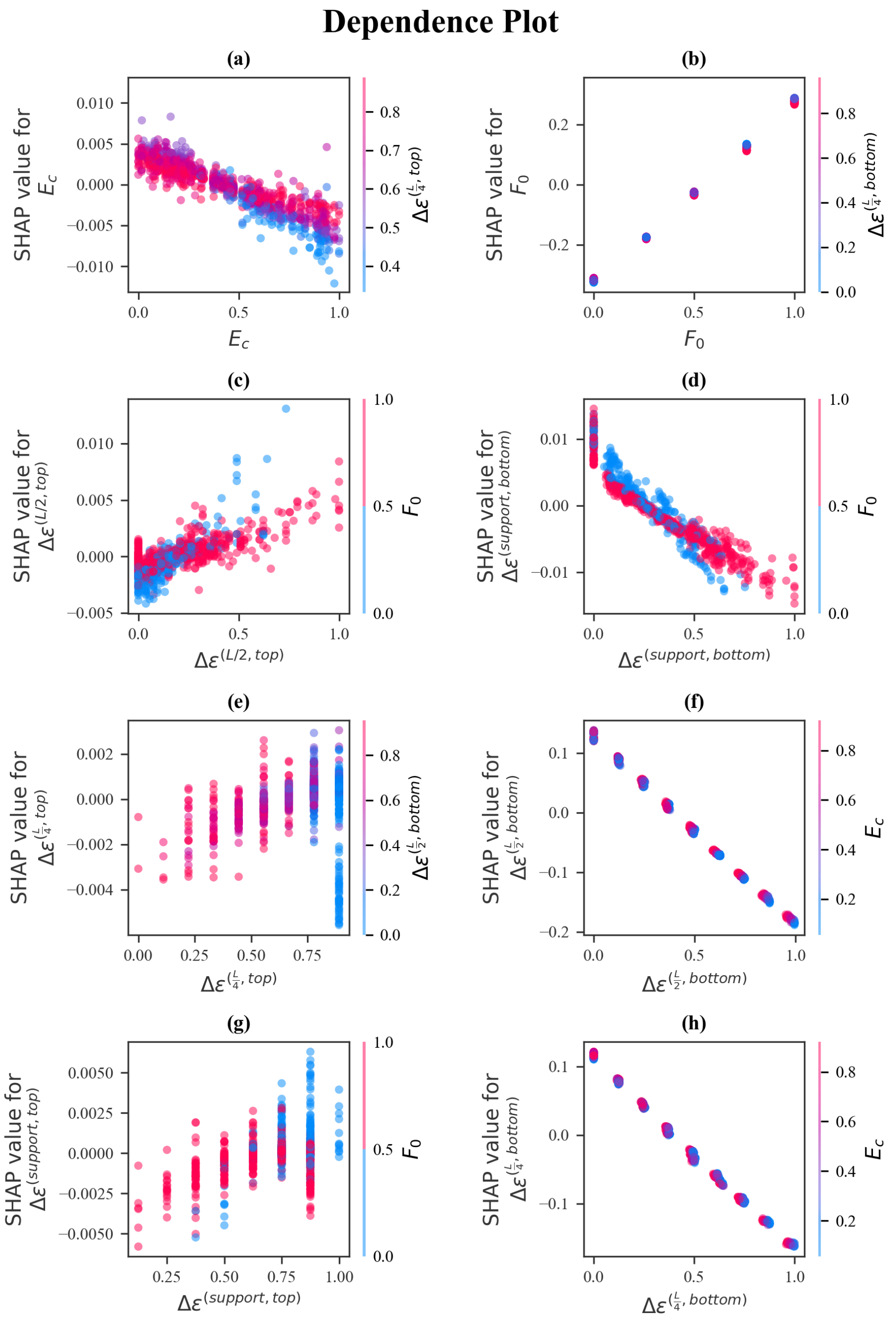

Fig. 93 - Dependence plot, on abscissa input feature, on ordinate its SHAP value on output feature and colormap shows the values of the input variable that may have an interaction effect with the plotted input feature.

third influent parameters are the strain measures at the bottom fiber of the *L*/2 section, $\Delta\varepsilon^{(L/2,\ bottom)}$, and bottom fiber of *L*/4 section, $\Delta\varepsilon^{(L/4,\ bottom)}$. The density of the red color changes when F_0 increases, from which it can be deduced that F_1 increases as F_0 increases. On the contrary, an increment in $\Delta\varepsilon^{(L/2,\ bottom)}$ and $\Delta\varepsilon^{(L/4,\ bottom)}$ correspond to an F_1 decrease, and this is an important achievement, because the proposed model allows characterizing the relation between strain in some specific points and loss of prestressing force. Fig. 93 reports the SHAP dependence plot, aiming at interpreting the effects of each feature and their interactions within the model. The plots provide a bi-dimensional view showing the relationship between the value of a feature (abscissa) and its SHAP value (ordinate), reporting then the contribution of each feature to the predictions. The obtained magnitude of values on the ordinates for each input parameter confirms the outcomes in Fig. 92, while abscissa values are reported in the normalized scale used for ANN training. A negative trend in the graphs (e.g., Fig. 93d, Fig. 93f and Fig. 93h) implies that as the input value increases the output value, F_1, decreases. Conversely a positive trend in the graph (e.g., Fig. 93b), as the input value increases the output value, F_1, increases. Hence, as $\Delta\varepsilon^{(L/2,\ bottom)}$, $\Delta\varepsilon^{(L/4,\ bottom)}$ and $\Delta\varepsilon^{(support,\ bottom)}$ increase, F_1 decreases. On the other hand, as F_0 increases, F_1 tends to increase. The input variable that may have an interaction effect with the plotted feature is represented in the colormap. If an interaction effect is present between two features, a distinct vertical pattern of colouring is shown. Fig. 93b shows the impact on F_0 -related SHAP value given the variation of $\Delta\varepsilon^{(L/4,\ bottom)}$. For F_0 values above 0.5, a reduction in $\Delta\varepsilon^{(L/4,\ bottom)}$ increases the SHAP value of F_0, while for F_0 values below 0.5, an increase in $\Delta\varepsilon^{(L/4,\ bottom)}$ value decreases the SHAP value of F_0. This is physically true because lower strain increments suggest a higher F_1 value, and thus a lower prestressing force reduction. Conversely, Fig. 93f and Fig. 93h show that for input feature values $\Delta\varepsilon^{(L/2,\ bottom)}$ and $\Delta\varepsilon^{(L/4,\ bottom)}$ above 0.5, a decrement in E_c reduces the SHAP value of the input feature. For the same features, while their values are below 0.5, an increment in E_c increases the SHAP value. The mathematical relation proposed by the ANN is simple to capture, because higher values of E_c correspond to lower strain increments, and thus a lower prestressing force reduction.

From the obtained results, some considerations can be finally provided. The proposed ANN-based surrogate model can be employed for the purpose of prestressing loss prediction in PSC box-girder bridges, and the use of eXplainability revealed that the best solution for defining a SHM sensor-based system consists of using strain gauges in the bottom fibers of sections at $L/2$ and $L/4$ of the beam. After that, additional sensors can be not necessary. Regarding the mechanical parameters of the concrete characterizing the bridge, the influence of E_c was negligible. On the other hand, the above consideration is not absolute, because the value of E_c is strictly correlated to the values of $\Delta\varepsilon^{(i,j)}$. Finally, as expected, an accurate evaluation of F_0 value is required to accurately predict the F_1 value and then, the subsequent prestressing loss.

3.5. Conclusions

In this Chapter, a framework to define a Machine Learning (ML)-based surrogate model able to predict the prestressing losses of unbonded strands in prestressed concrete (PSC) box-girder bridges is proposed. The developed surrogate model aims to support a reliable structural assessment and monitoring of PSC box-girder bridges. The structural safety management of these structures involves the characterization of the health state of internal unbonded tendons (which are often inaccessible), the continuous record of the effective prestressing force reduction over time, and the design of an effective structural health monitoring (SHM) system. To these scopes, the proposed framework is based on the results obtained by experimental tests on a scaled PSC box bridge, made in the ICITECH laboratory of the *Universitat Politècnica de València*. The scaled box-girder specimen, instrumented with linear variable displacement transducer sensors and strain gauges, was tested under a Four-point bending test on different phases, accounting for an undamaged phase (i.e., Phase 1) and three progressive damaged phases (i.e., Phases 2, 3, 4). From the obtained results, a simple but effective nonlinear Finite Element (FE) model was developed and validated. In particular, both undamaged and damaged phases were assessed for the calibration, obtaining average percentage differences equal to 1% and 2% for displacement and stress values, respectively. Using the defined modelling approach and including variability for geometrical and mechanical properties, i.e., the elastic modulus of concrete (E_c) and prestressing force at the "initial state" (F_0), a sample dataset was generated by defining 5031 FE models. Using the above data, three ML algorithms were trained (Artificial Neural Network, ANN, Random Forrest Regressor, and Support Vector Regression) to relate the prestressing losses (i.e., F_1) to the input variables (i.e., E_c, F_0, and the strain variation in different sections, $\Delta\varepsilon^{(i,j)}$). By using adequate evaluation metrics, the prediction provided by ANN resulted the most accurate, revealing the best algorithm to define the ML surrogate model. In addition, input variables were ranked through an eXplainability approach to evaluate their impact on the target variable prediction. The results can be summarized as follows:

- A correct definition of F_0 is required in the "initial state", that is the time of investigation.

- The value of E_c presents a low impact on the overall results, even though its role is fundamental in the definition of $\Delta\varepsilon^{(i,j)}$.

- An effective sensors-based SHM system, aimed at assessing prestressing losses, can be employed for this typology of bridge by placing strain gauges at the bottom fibers of $L/2$ and $L/4$ sections (L is the length of the beam).

The results presented in this study suggest that the proposed ML surrogate model allows overcoming the limitations characterizing the traditional non-destructive methods, which require periodic and expensive onsite tests. In fact, to derive the current prestressing losses, it is necessary to characterize the values of F_0 and E_c in the "initial state" and ensure continuous strain monitoring in the specific points above indicated. One limitation of the study is represented by the scaled model, which presents some simplifications in its manufacturing. In fact, the scaled bridge presents a beam section designed according to the indication by Agarwal *et al*. (2022), but other quantities were not scaled (as for example made by Losanno *et al*., 2023). Moreover, the realization of other specimens with different geometrical and mechanical feature could improve the dataset at the base of the proposed ML model, which at the current state was numerically generated. In addition, those data could be used also for elaborating different type of predicting models, such as by employing more classical probabilistic-based approaches.

FINAL REMARKS

The structural safety of existing bridges is a primary concern for road and railway management companies and public institutions, which have the role of continuously assessing the health state of bridge portfolios to reduce the risk associated with these structures for safeguarding human life and minimizing economic losses. When referring to bridge portfolios, the main challenge is to individuate the worst cases and, subsequently, to perform structure-specific analysis (e.g., structural health monitoring - SHM, on-site inspection campaign or detailed assessment via modelling and analysis) to plan future actions, such as demolition/reconstruction, retrofit interventions or traffic limitations. This is the logic behind current trends in risk-prioritization of existing bridge portfolios, such as the one proposed by the Italian government that, after the collapses of some important bridges in the recent past, released in 2020 new guidelines (IG) for the structural safety of existing bridges and viaducts. A multi-level approach is proposed, oriented to perform firstly a large-scale screening of bridge portfolios and after, on worst cases, a structure-specific analysis. This approach can be decisive in driving the few available resources towards bridges with higher risks. However, although effective as standardized methodology at a national scale, IG propose traditional monitoring procedures (necessary and hardly replaceable), which involves time- and cost-consuming activities which hinder their wide and timely application to a bridge portfolio scale, given the thousands of bridges presenting Medium to High warning class. Still, new cutting-edge technologies, new if compared to the well consolidated traditional monitoring techniques, can be explored with the goal to lighten management costs and to support reliable prioritization schemes of the IG, on a near-continuous basis.

Overall conclusion and key findings

This dissertation investigates procedures for an efficient large-scale assessment of bridge portfolios and to enhance single-structure Structural Health Monitoring (SHM) exploiting new sources of data and techniques after the identification of the most recurrent structural typology on the Italian bridge stock (i.e., simply supported concrete girder bridges).

- Chapter 1 describes remote sensing techniques for Earth observation purposes with a focus on Synthetic Aperture Radar (SAR) sensors, satellite constellations deployed with this payload, and elaboration algorithms of acquired SAR images (i.e., Differential Interferometry Synthetic Aperture Radar, DInSAR, and Multi-Temporal Interferometry Synthetic Aperture Radar, MTInSAR). From the literature review on the principles of SAR sensors and on the application of InSAR algorithms valuable considerations are derived regarding this remote-sensing technique. SAR sensors collect data regardless the atmospheric and lightning condition of the scene, providing a new SAR image once every two weeks, satisfying the requirement of a near-continuous monitoring. The image stacks, spanning the entire constellation activity period, characterized by a few meter resolution and hundreds of kilometres in size (hence adequate as cost-effective solution), can be processed by InSAR algorithms to detect displacements related to scatterers on the Earth surface. These scatterers, mostly characterizing parts of man-made structures (e.g., buildings and bridges), identified by their attributes as displacement time history along the Line-of-Sight (LoS), velocity over the entire period along the same direction, coherence and spatial position can be exploited for structural assessment of built heritage.

  A framework is proposed based on MTInSAR data, poor structural information (already at disposal by transportation management authorities) and temperature data to describe bridge behaviour over the time and compare it with displacement thresholds related to service conditions, obtained with simple analytical models. The proposed early warning system, composed of a series of standardized and scalable steps and implemented in a Python module to enhance its scalability to bridge portfolios, aims to identify the causes of such displacements (enclosed in scenarios) with the goal of: (i) provide structural interpretation of remote-sensed measurements, (ii) support the planning of further actions (e.g., specific bridge sensors-based monitoring, traffic restrictions) in response to the identified displacement scenario. The procedure, which is applied to simply supported concrete girder bridges (most spread bridge typology in Italy as demonstrated in the Introduction), is tested on two different case studies affected by different pathologies (e.g., increasing material degradation/gravity loads, differential displacements and subsidence), demonstrating its effectiveness as early warning system for the purpose of bridge portfolio analysis and structural risk prioritization, also according to the framework proposed by the recent IG (at least for the structural-foundational risk). Moreover, a GIS plugin named BAS-MTInSAR is developed to foster the use of this cutting-edge technology by practitioners. Its user-friendly Graphic User Interface, structure and functionalities are demonstrated achieving a satisfactory level of automation of the proposed framework.

- Chapter 2 deals with another remote-sensing technique based on the use of Unmanned Aerial Vehicles (UAV). UAVs employment is increasing in several application areas thanks to the ability of autonomous flight (i.e., through a preliminary flight plan) and different payloads ranging from thermal cameras to LiDAR sensors to optical cameras. Georeferenced images acquired with a consistent overlay can be processed by commercial software such as Agisoft Metashape to retrieve different digital products used for three-dimensional modelling and measurements. One of these digital products is the Digital Surface Model (DSM) which can be employed to monitor another risk related to structures, that is displacements induced by the geomorphological context (i.e., geological risk described in the IG). Traditional SHM systems (i.e., sensors-based) can be costly due to high management costs, while alternative option such as involving a pool of experts who periodically monitor the focused area is both inefficient (timely assessment over time) and expensive. Therefore, pursuing the goal of employing new cost-effective technologies the UAV photogrammetry can be used and combined with MTInSAR data in a probabilistic-based approach to monitor existing built heritage (both buildings and infrastructures) and evaluate the influence of potential landslides.

The proposed framework exploits the advantages of both remote sensing techniques to pay off their shortcomings. As discussed in the previous Chapter 1, MTInSAR data lack of scatterers in unurbanized areas ,where bridges are typically located, thus limiting the monitoring of displacement in their surroundings related to geological hazards. On the other hand, although DSM easily cover large areas around the structure under investigation, are less accurate than MTInSAR displacement time series which are on a millimetre scale. Given the different accuracy and uncertainties of the two measurements, the statistical distributions of spatiotemporal velocities (i.e., a normalized measure of displacements) detected with both techniques are used in the evaluation under two assumptions: (a) normal distribution of data; (b) displacements recorded by UAV photogrammetry further from the structure are less likely to influence it. Statistical distributions are processed separately and compared with a threshold value by means of a limit-state (LS) function. Performing this step for each technique, the probabilities of exceeding (PoE) the LS can be computed, and the comparisons between those probabilities are framed within three scenarios, which can suggest the occurrence of subsidence phenomena.

The framework is first validated on the case study of Pomarico landslide, and then applied for the purpose of risk prediction on the multi-span bridge analysed with the MTInSAR framework in the previous Chapter 1. At the end of the application, several advantages can be highlighted: (i) the obtained results successfully identified the Pomarico landslide and provided a qualitative information on the evolution of a geological risk affecting the focused structure; (ii) the obtained results provide a warning, which can be implemented in reliable structural risk mitigation plans in areas prone to widespread terrain motions, accounting for geological risks and highlighting the necessity (or not) of new detailed monitoring campaigns enhancing rational administration of resources for safety assessment; (c) the entire process is simple and economic (MTInSAR data could be free, while UAV surveys can be performed by using low-cost drones) and can improve the current practices of onsite inspections, by ensuring continuous monitoring for the existing built stock.

- Chapter 3 is no longer focused on the use of remote sensing techniques for structural risk assessment of bridge portfolios, but on the use of a sensor-based system for the same objective. While the cutting-edge technologies explored so far can be used to remotely detect anomalies, in some cases difficult to perceive through visual inspections, the use of sensor monitoring systems can be used to study evolutionary trends of possible degradation phenomena. As discussed in the Introduction of the thesis, two construction materials are widely used in Italy to build bridges, that is reinforced concrete and prestressed concrete (PSC). This latter, although brings several advantages as described in this Chapter, suffers from time dependent phenomena related to concrete and harmonic steel, used for tendons, that reduce the prestressing force over time. This occurrence, although accounted for in the design phase, could happen in case of degradation phenomena too. For example, corrosion can reduce both the mechanical properties (i.e., ultimate strength and ultimate strain) and the cross-sectional area and mass of the steel strands, leading in worst cases to wires rapture. In this case, total prestressing force of tendons at the anchorage is reduced as well as the bearing capacity of structural elements.

  For certain types of sections of PSC girder bridges, as the box-girder ones, the visual inspection proposed by the IG poses some difficulties. For this specific type of section, tendons are placed inside of the beam limiting their inspection only in case of manholes planned during the design phase. Over time, several

SHM approaches were proposed by the scientific community to identify the residual prestressing force at the anchorage of the beam and based on literature review concrete strain sensor can be a cost-effective solution. Still, some limitations regarding local measures (i.e. dependencies with paste-aggregate interactions and cracking) and the unbonded condition of tendons inside the box-girder can prevent a straightforward estimate of prestressing force. Valuable support can be provided by Machine Learning (ML) regression algorithms in a model-driven approach.

On this basis, a framework based on ML regression algorithms, FE modelling and concrete strain measures is proposed to predict the prestressing force and its reduction over-time. Among literature ML algorithms Artificial Neural Network (ANN), Random Forrest Regressor (RFR) and Support Vector Regression (SVR) are explored to identify the best ML surrogate model for the case at hand. These ML algorithms are trained on sample data generated from a calibrated nonlinear FE model with diffused plasticity approach and fiber discretization of the bridge deck. Sample data are generated by varying some parameters in a schematic way (i.e., initial prestressing force, current prestressing force, and concrete elastic modulus). The FE modelling strategy, validated on experimental campaign took in ICITECH laboratories of the Universitat Politècnica de València, represents a trade-off between computational effort in the generation and analysis of thousand of models and precision of the measurements. Each ML algorithm is trained considering a k-fold cross-validation for hyperparameter tuning and to avoid overfitting. Literature statistical parameters as Mean Signed Error (desired negative values to underestimate the output of the model in a conservative way) and Root Mean Squared Error (in the same unit measure of the response variable for a straightforward interpretability) are used to select the best ML surrogate model. Given the nature of the proposed models as black-box, a physical explanation of ML surrogate model can provide additional insights into the prediction. To this scope, eXplainability metrics are exploited as Shapley Additive exPlanations (SHAP). For the case at hand, the importance of SHAP application is dual: (i) SHAP can highlight which parameters require an accurate evaluation because they present a higher impact on the output values; and (ii) SHAP can indicate the best combination of fibres and section to monitor based on significance of features, to reduce the cost of the sensors-based system to install.

The framework is applied to a scaled PSC box bridge experimentally tested at ICITECH. The beam, instrumented with Linear Variable Displacement Transducers (LVDTs), strain-gauges, and Fiber Bragg Gratings (FBGs) is tested under four-point bending moment test considering both "undamaged" and "damaged" scenarios (i.e., achieved by consecutively removing dywidag steel bars used as prestressing system at the end of each loading test). Experimental vertical displacements are used to calibrate and validate the nonlinear FE model with diffused plasticity approach and fibers, while experimental strain data are used as input of the trained ML surrogate models. ANN is reported as the best ML surrogate model, compared to RFR and SVR, given the negative values of MSE and lowest values of RMSE (in both training and validation phase). This result was expected prior the application, given its ability to generalize problems, even though it presents many hyperparameters to be tuned. The application of the ML surrogate model to the experimental values of the case study reported the current prestressing force with a 0.3% difference, thus showing potentials of the combination of traditional sensor-based SHM systems and ML algorithms.

Finally, the eXplainability approach provided valuable insights regarding the design of a sensors-based SHM systems aimed at monitoring the prestressing losses: (i) a correct definition of initial prestressing force is required; (ii) the value of the elasticity modulus of the concrete presents a low impact on the overall results, even though its role is fundamental in the definition of strain increments; (iii) an effective sensors-based system of strain-gauges can be applied at bottom fibers of *L*/2 and *L*/4 sections (*L* is the length of the beam), for prestressing losses assessment. Moreover, the SHAP approach highlighted the relations between input variables providing a satisfactory learning of the physical process by the black-box model.

Future research

Based on the presented outcomes, recommendations for future research on the considered topics are proposed.

- The proposed frameworks for bridge structural risk assessment and early-warning rely on the availability of knowledge data about the structure/s to be analysed. As evidenced in these studies, initial knowledge is a crucial variable for the accuracy of the assessment process. In future, the availability of data is expected to increase. Consistently with the technological advances in geomatics, the deployment of new satellite platforms will provide open-access or low-cost images characterized by higher resolution with high potential in data extraction for structural assessment purposes. In this process, expertise in geomatic and informatic for data mining will contaminate conventional structural engineering.
  Data-sharing should be encouraged. In Italy, the innovative platform AINOP (MIT, 2024) aims at storing and increasing the availability of knowledge data about public infrastructures. The platform is designed to allocate contributions by privates which can signal disruptions or damages in public infrastructure assets. The sharing of the data with researchers, together with private structural engineers, will be essential to increase the safety of infrastructure systems in the name of the public interest.

- The advances about the use of Multi-Temporal Interferometry Synthetic Aperture Radar (MTInSAR) data for structural assessment of existing bridges through displacement scenarios enrich an extended literature on the theme mostly focused on single structures with known problems or already collapsed. Based on the limitations highlighted in the conclusion of Chapter 1, promising advances can be achieved combining different satellite constellation data to improve the timeliness of early-warning, enhancing the range of tools at the disposal by transportation authorities. Moreover, new satellite constellation as IRIDE (Planetek, 2023) travelling outside of a near polar orbit will contribute to reconstruct displacement components in each direction of the proposed Mobile-Local Reference Coordinate System by the data fusion with present satellite platforms. In the end, proposing new simplified models for threshold evaluations, the proposed framework could be extended to other bridge typologies for a complete portfolio assessment.

- The combination of MTInSAR data and Unmanned Aerial Vehicle (UAV) Photogrammetry is one of the few examples of data fusion between these remote-sensing techniques as evidenced in the review on the state-of-the-art. The validation of the proposed probabilistic-based approach on a real landslide shows promising in geological risk assessment in the IG. UAV is a key technology on which transportation authorities are investing as demonstrated by the smart road program of ANAS S.p.A. (ANAS, 2024b). Given the ability of UAV to perform autonomous flights, the development of more powerful payloads in the future, and recent advances in computer vision for detecting common defect on existing bridges (e.g., Cardellicchio *et al*., 2023), this technique can deeply change the paradigm of transportation network management and assessment. As with the use of MTInSAR data, different expertises are required to employ such Structural Health Monitoring (SHM) strategies, and thus their dissemination depends on the sensitivity of the technical-scientific context to knowledge other than that of the cultural matrix of origin and the more or lesser aptitude to assimilate its innovative content.

- The proposed methodology for estimating the prestressing force reduction via ML algorithms and strain sensors is promising in the filed of structural risk assessment of prestressed concrete girder bridges. Still, some limitations are highlighted due to the laboratory test rather than on-field application. For this reason, data availability and cooperation between researchers and stakeholders is fundamental to achieve a higher level of results in integrating traditional and cutting-edge technologies. In addition, the future development of new ML algorithms will improve the quality of predictions based on experimental measurements.

- The future of the management of exiting infrastructure assets will be governed by digital database connected to automatic algorithms for the real-time calculation and update of the structural-foundational, seismic, geological/hydraulic risk and global warning classification. The data stored in cloud system and accessible through Geographical Information Systems (GIS) and Building Information Models can help data analysis to address inspections and retrofit interventions. Based on the proposed routines and future developments aimed at extending their applicability to other bridge typologies, applications and more refined GIS plugins will be developed to foster the adoption of these algorithms by the transportation authorities' operators. An example is the alpha version of BAS-MTInSAR (Calò *et al*., 2024b; Calò *et al*., 2024c) developed by the author.

ACKNOWLEDGEMENTS

This study was conducted as part of the Industrial PhD research program sponsored by Italian Ministry of University and Research, within the project ‘PON-Ricerca e Innovazione-2014–2020, CUP Code (D.M. 10/08/2021, n. 1061): D95F21002340006. Greetings to Planetek Italy for processing the raw data from the COSMO-SkyMed constellation and making it available for the development of the research work. ICITECH Laboratories of the Universitat Politècnica de València provided a wide range of experimental data on the scaled prestressed concrete box girder bridge and welcomed me into their group during the abroad experience. To them goes my heartfelt thanks.

Last, not least, I would like to express my gratitude to the research team that has supported me over the past 3 years. Their contribution has been fundamental to the development of the scientific content described in the thesis and to my personal growth.

LIST OF FIGURES

LIST OF TABLES

LIST OF ABBREVIATIONS

ASC .... Ascending track
Co .... Commercial
COH .... Coherence criterion
DSC .... Descending track
E .... East
H_GEO .... Height criterion
IR .... Infrared
Lat .... Latitude
Lon .... Longitude
N .... North
POS .... Positioning criterion
RAR .... Real Aperture Radar
Re .... Restrained
S .... South
SAR .... Synthetic Aperture Radar
T... Transverse direction
UV .... Ultraviolect
V_LOS .... Velocity along the Line-of-Sight criterion
W .... West

LIST OF ACRONYMS

a.s.l.	Above sea level
A-D	Application-dependent
ANAS	Autonomous National Agency of Highways
ANN	Artificial Neural Network
BAS-MTInSAR	Artificial Neural Network
CSK	COSMO-SkyMed
DInSAR	Differential Interferometry Synthetic Aperture Radar
DS	Distributed Scatterer
DSMs	Digital Surface Models
DT	Decision Tree
EO	Earth Observation
ERS	European Remote-Sensing
ESA	European Space Agency
F&O	Free and open
FBG	Fiber Bragg Gratings
FE	Finite Element
FLIR	Forward Looking InfraRed
GCPs	Ground Control Points
GEO	Geostationary Earth orbit
GIS	Geographic information System
IG	Italian Guidelines
InSAR	Interferometry via satellite-based Synthetic Aperture Radar
JERS	Japanese Earth Resources Satellite
JPD	Joint Probability Distribution
LEO	Low Earth orbit

LiDAR .... Light Detection And Ranging
LL.GG. .... Linee Guida
LoS .... Line-of-Sight
LS .... Limit State function
LVDT .... Linear Variable Displacement Transducer
MEO .... Medium Earth orbit
MIT .... Italian Ministry of Infrastructures and Transporation
ML .... Machine Learning
M-LCRS .... Mobile-Local Coordinate Reference System
MTInSAR .... Multi-Temporal Interferometry Synthetic Aperture radar
NASA .... National Aeronautics and Space Administration
NASDA .... National Space Development Agency
NPO .... Near Polar orbit
OSM .... OpenStreetMap
PO .... Polar orbit
PoE .... Probability of exceeding
PS .... Persistent Scatterer
PSC .... Prestressed concrete
RC .... Reinforce concrete
RFR .... Random Forrest Regressor
RS .... Restrained scientific
RTK .... Real Time Kinematic
SB .... Small Baseline
SEASAT .... Sea Satellite
SEN1 .... Sentinel-1
SHAP .... SHapley Additive exPlanations
SHM .... Structural Health Monitoring
SLC .... Single-Look Complex
SO .... Specific objectives
SP .... Scientific proposal

SPINUA .... Stable Point INterferometry even over Un-urbanized Areas
SSO .... Sun-synchronous orbit
STL .... Seasonal Trend decomposition based on LOESS
SVR .... Support Vector Regression
TCD .... Tree Cover Density
TDB .... To be decided
UAV .... Unmanned Aerial Vehicle

LIST OF SYMBOLS

[A] .... Matrix of values of neurons of hidden layer of ANN
[B] .... Bias column vector of hidden layer of neurons of ANN
[W] ....Weight matrix of the column input vector of the ANN
[W_1] ....Weight row vector of the column input vector of the ANN
[W_2] ....Weight row vector of the output of hidden layer of ANN
[X] .... Column vector describing the input layer of the ANN
AB1 .... First abutment
AB2 .... Second abutment
A_{mp} .... *Amplitude*
A_T .... Average annual temperature
a_u ....Input value of the uth neuron of the hidden layer of the Artificial Neural Network
B .... Magnetic field
B_T .... Amplitude of the cosine temperature model
b_u . Bias associated with the activation of the uth neuron of the hidden layer of the ANN
C ....
Positive constant defining the degree of penalization when a training error occurs in SVR algorithms
d .... Distance travelled by the wave in a complete cycle
d_0 .... Intercept of the Least Squared Regression
d_L ....Displacement along the Longitudinal direction
d_{LoS} ....Displacement along the Line-of-Sight
d_M .... Displacement measured in the [$-\pi$; $+\pi$] range
d_{Real} ....Real displacement
DSM1 ....Digital Surface Model at the start of the observation period
DSM2 .... DSM1 Digital Surface Model at the end of the observation period

d_T .... Displacement along the Transversal direction
d_{Term} .... Maximum thermal displacement
d_V .... Displacement along the Vertical direction
$d_{vi,MTInSAR}$ ....
Vertical component of i^{th} PS recorded via Multi-Temporal Interferometry Synthetic Aperture Radar
$d_{vj,UAV}$ .... Vertical component of i^{th} cell of the DSM
E_c .... Elastic modulus of concrete
E_I .... Electromagnetic field
F .... Set of function of Support Vector Regression
$f(x, \alpha)$ .... Regression function of Support Vector Regression
F_0 .... Initial prestressing force at the time of sensor installation
F_1 .... Current prestressing force
$F_{Traffic}$ .... Concentrated force corresponding to the axial load of two axels
f_λ .... Frequency of the wave
g .... Generic limit state function
G .... Shear modulus
h .... Height of deck section
$h_{nt}(x)$ .... Value of the output prediction of a Decision Tree
$\hat{h}_{RF}^{n_t}$ .... Output value of the Random Forrest Regressor
$H_{x,DSM}$ ....
Shortest distance from the external side of the subarea of the Digital Surface Model to the centroid of the structure
J_{deck} .... Moment of inertia around deck transverse axis
k_λ .... Wavenumber
L .... Longitudinal direction parallel to bridge/sub-region main longitudinal axis
L_{beam} .... Lenght of the antenna
L_{prog} .... Progressive length of the sub-region from the fixed suppor
L_{tot} .... Span length
m .... Day of the year expressed in months

MAE ....Mean Absolute Error
MM .... Bending moment in both main section directions
m_{PSs} .... Number of Persistent Scatterers
MSE_1 .... Mean Squared Error
MSE_2 .... Mean Signed Error
N_d .... Ensemble of sample data
n_{noise} ....Phase component due to noise
n_t .... Number of trees
p ....Number of data points
P ....Prestressing
$PoE_{MTInSAR}$ ....
Probability of exceeding obtained from Multi-Temporal Interferometry Synthetic Aperture Radar
PoE_{UAV} ....
.......Probability of exceeding obtained from Unmanned Aerial Vehicle photogrammetry
Q .... Demand to which the system is subjected
R ....Capacity of the system
r .... Distance between the target and the sensor
r .... Generic record of the sample data
r' ....Range direction
R^2 ....R squared score of Least Square Regression
R_{es} .... Remainder component of displacement time series
R_L .... Longitudinal rotation matrix
R_T .... Transverse rotation matrix
R_u ....Distinct and nonoverlapping region of the training space of the Decision Tree
R_V ....Vertical rotation matrix
S11 .... Sub-region 1 of 1st span
S12 .... Sub-region 2 of 1st span
S13 .... Sub-region 3 of 1st span
S31 .... Sub-region 1 of 3rd span

S32 .... Sub-region 2 of 3rd span
S33 .... Sub-region 3 of 3rd span
S_{eas} .... Seasonal component of displacement time series
S_N .... Subset of sample data
$T(m)$ .... Cosine temperature model
T_0 .... Start of the observation period
T_1 .... End of the observation period
T_{MAX} .... Maximum temperature
T_{MIN} .... Minimum temperature
T_r .... Trend component of displacement time series
T_{start} .... Temperature on the first acquisition date
T_{REF} .... Temperature on the first acquisition date
T_{SVR} .... Training data of Support Vector Regression
u ....
Number of distinct and nonoverlapping regiongs of the training space of the Decision Tree
U .... Vertical direction in WGS84 Reference System
V .... Vertical direction defined by a normal vector to road pavement
V(x, y, f) .... Vapnik's ε-insensitive loss function
var .... Variance of the average of n_t random variable
V_{LoS} .... Velocity along the Line-of-Sight
$V_{vi,MTInSAR}$ ....
Velocity of the vertical component of i^{th} PS recorded via Multi-Temporal Interferometry Synthetic Aperture Radar
$V_{vj,UAV}$ .... Velocity of the vertical component of i^{th} cell of the DSM
v_λ .... Velocity of the wave
w_v ....
Weight associated to the v^{th} element of the column input vector of the Artificial Neural Network
w_z .... Weight of the z^{th} subarea of the Digital Surface Model

x .... Input vector of the Random Forrest Regressor
x' .... Azimuth direction
x_v .... Element of the column input vector of the Artificial Neural Network
y .... Value of the output layer of the Artificial Neural Network
y_m .... Experimental value
Z .... Direction of propagation of electromagnetic wave
Z_{par} .... Set of parameters of Support Vector Regression
α .... Azimuth angle
α_{atm} .... Phase component due to the atmosphere
α_{CTE} .... Coefficient of thermal expansion for the concrete
β .... Pitch angle
β_{index} .... Reliability index
$\beta_{MTInSAR}$ ....
... Reliability index for the Multi-Temporal Interferometry Synthetic Aperture Radar data
β_{plane} .... Optimal separating hyperplane in Support Vector Regression
$\beta_{UAV,z}$ .... Reliability index for the z^{th} subarea of the Digital Surface Model
γ .... Roll angle
γ_o .... SHAP value of the input feature o
δ .... Trained Machine Learning model
δ .... Yaw angle
$\Delta_{azimuth}$ .... Azimuth resolution
Δ_i .... Difference between two cumulative vertical displacements
δ_i .... Vertical cumulative displacement
$\delta_{mid\ span}$ .... Vertical cumulative displacement at mid span
Δ_{range} .... Slant range resolution
ΔT_C .... Constant temperature delta
ΔT_L .... Linear temperature delta
ΔT_{MAX} .... Maximum temperature delta
ΔT_{MIN} .... Minimum temperature delta
$\Delta\varepsilon^{(i,j)}$ .... Strain variation for the j^{th} fiber and the i^{th} section

$\Delta\varepsilon_{F_k}^{(i,j)}$ .... Strain increment at j^{th} fiber of the i^{th} section under a generic F_k value

$\Delta\varepsilon_{model}^{(i,j)}$ .... Strain increments for the j^{th} fiber at the i^{th} section due to the application of a fixed external load

$\Delta\varphi$ .... Phase difference

$\Delta\varphi^{atmosphere}$ .... Phase difference due to different atmospheric conditions

$\Delta\varphi^{displacement}$ .... Phase difference due to the displacement

$\Delta\varphi^{noise}$ .... Phase difference due to the decorrelation noise

$\Delta\varphi^{orbit}$ .... Phase difference due to theinaccurate knowledge of the oribit

$\Delta\varphi^{topography}$ .... Phase difference due to the topography

ε .... Quantity to compare with error between predicted Support Vector Regression and real values

ϑ .... Incidence angle

ϑ_G .... Ground slope measured from horizontal plane

λ .... Wavelength of the sensor

μ .... Slope of the Least Square Regression

$\mu_{MTInSAR}$ .... Mean of the velocity values of vertical displacement recorded via Multi-Temporal Interferometry Synthetic Aperture Radar

$\mu_{UAV,z}$ .... Mean of the velocity values of the vertical displacement of the z^{th} subarea

μ_ε .... Average value of experimental values

ξ_c^* .... Slack variable

ξ_m .... Slack variable

ρ .... Correlation coefficient of n_t random variable

σ .... Standard deviation of n_t random variable

$\sigma_{MTInSAR}$ .... Standard deviation of the velocity values of vertical displacement recorded via Multi-Temporal Interferometry Synthetic Aperture Radar

$\sigma_{UAV,z}$ ....
Standard deviation of the velocity values of the vertical displacement of the zth subarea
Φ ....Cumulative distribution function
φ .... Phase
$\varphi(x)$..
Nonlinear function to linearly map input space into a high-dimensional feature space in Support Vector Regression
ϕ_T ....Phase shift of the cosine temperature model
ψ ....Phase component due to the reflectivity of the target
ψ_{NL} ....
Nonlinear function that computes the output of the neuron of the hidden layer of the ANN
ω ....Frequency of the cosine temperature model
ω_λ ....Wave angular frequency
$\bar{y}_m$ .... Predicted value

BIBLIOGRAPHY

Fondo Ambiente Italiano (2022) *Ponte di Annibale sul Savuto*. Available at: https://fondoambiente.it/luoghi/ponte-di-annibale?ldc

Calvi, G.M. *et al*. (2018) 'Once upon a Time in Italy: The Tale of the Morandi Bridge', *Structural Engineering International*, 29(2), pp. 198–217. https://doi.org/10.1080/10168664.2018.1558033

Lanari, R. *et al*. (2020) 'Comment on "Pre-Collapse Space Geodetic Observations of Critical Infrastructure: The Morandi Bridge, Genoa, Italy" by Milillo et al. (2019)', *Remote Sensing*, 12(24), p. 4011. https://doi.org/10.3390/rs12244011

Milillo, P. *et al*. (2019) 'Pre-Collapse space geodetic observations of critical infrastructure: the Morandi Bridge, Genoa, Italy', *Remote Sensing*, 11(12), p. 1403. https://doi.org/10.3390/rs11121403

Farneti, E. *et al*. (2022) 'A method for structural monitoring of multispan bridges using satellite InSAR data with uncertainty quantification and its pre-collapse application to the Albiano-Magra Bridge in Italy', *Structural Health Monitoring*, 22(1), pp. 353–371. https://doi.org/10.1177/14759217221083609

Borzi, B. *et al*. (2015) 'Seismic vulnerability of the Italian Roadway Bridge stock', *Earthquake Spectra*, 31(4), pp. 2137–2161. https://doi.org/10.1193/070413eqs190m

Fiorillo, G. and Ghosn, M. (2017) 'Fragility analysis of bridges due to overweight traffic load', *Structure and Infrastructure Engineering*, 14(5), pp. 619–633. https://doi.org/10.1080/15732479.2017.1380675

Nettis, A. *et al*. (2022) 'Displacement-based seismic performance assessment of multi-span steel truss bridges', *Engineering Structures*, 254, p. 113832. https://doi.org/10.1016/j.engstruct.2021.113832

Sangiorgio, V. *et al*. (2022) 'Analytical fault tree and diagnostic aids for the preservation of historical steel truss bridges', *Engineering Failure Analysis*, 133, p. 105996. https://doi.org/10.1016/j.engfailanal.2021.105996

Sbarbaro, A (2018) *Collapse of the Polcevera bridge in Genova (Italy)*. Available at: https://it.wikipedia.org/wiki/Crollo_del_viadotto_Polcevera#/media/File:Ponte_Morandi_Genova_Campi_014.jpg

Delle Luche, R (2022) *Collapse of a bridge in Albiano Magra (Massa-Carrara, Italy)*. Available at: https://www.ansa.it//webimages/news_base/2020/4/20/31414011c7436cc815ca71d3106fbe8e.jpg

ANAS, Azienda Nazionale Autonoma delle Strade Statali (2024a) *Sito istituzionale Anas S.p.A.*. Available at: https://www.stradeanas.it/it

AASHTO, American Association of State Highway and Transportation Officials (2018) *The Manual for Bridge Evaluation*. 3rd edn. Washington: American Association of State Highway and Transportation Officials, 2018. ISBN: 978-1-56051-683-5

ANSFISA, Agenzia nazionale per la sicurezza delle ferrovie e delle infrastrutture stradali e autostradali (2022) *Istruzioni Operative per L'applicazione delle Linee Guida per la Classificazione e Gestione del Rischio, la Valutazione della Sicurezza ed il Monitoraggio dei Ponti Esistenti*.

MIT, Ministero delle Infrastrutture e dei Trasporti (2020) *Linee Guida per la Classificazione e Gestione del Rischio, la Valutazione della Sicurezza ed il Monitoraggio dei Ponti Esistenti*.

Fabre (2024) *Consorzio Fabre*. Available at: https://www.consorziofabre.it/

Salvatore, W. *et al*. (2024) 'Application of Italian Guidelines for structural-foundational and seismic risk classification of bridges: the Fabre experience on a large bridge inventory', *Procedia Structural Integrity*, pp. 1/16. https://doi.org/10.1016/j.prostr.2024.09.009

Calò, M. *et al*. (2023) 'Multi source Interferometry Synthetic Aperture Radar for monitoring existing bridges: a case study', *Ce/Papers*, 6(5), pp. 787/793. https://doi.org/10.1002/cepa.2058.

Calò, M. *et al*. (2024a) 'A MTInSAR-based early warning system to appraise deformations in simply supported concrete girder bridges', *Structural Control and Health Monitoring*, p. 8978782. https://doi.org/10.1155/2024/8978782

Calò, M. *et al*. (2024b) 'BMS-INSAR: GIS PLUGIN FOR BRIDGE PORTFOLIO SERVICE DISPLACEMENT ANALYSIS THROUGH MTINSAR DATA', *18th World Conference on Earthquake Engineering at: Milan, June 30 - July 5*.

Calò, M. *et al*. (2024c) 'A GIS plugin for the assessment of deformations in existing bridge portfolios via MTInSAR', *Remote Sensing*, 16(22), 4293. https://doi.org/10.3390/rs16224293

Calò, M. *et al*. (2024d) 'Probabilistic-based assessment of subsidence phenomena on the existing built heritage by combining MTInSAR data and UAV photogrammetry', *Structure and Infrastructure Engineering*, pp. 1/16. https://doi.org/10.1080/15732479.2024.2423032

Calò, M. *et al*. (2024e) 'An ML-based framework for predicting prestressing force reduction in reinforced concrete box-girder bridges with unbonded tendons', *Engineering Structures*, 325, 119400*.* https://doi.org/10.1016/j.engstruct.2024.119400

Nettis, A. *et al*. (2024) 'Corrosion-induced fragility of existing prestressed concrete girder bridges under traffic loads', *Engineering Structures*, 314, p. 118302. https://doi.org/10.1016/j.engstruct.2024.118302

Paravano, A. et al. (2024) 'The Impact of the New Space Economy on Sustainability: the ESA Business Application Programme case', *Acta Astronautica* [Preprint]. https://doi.org/10.1016/j.actaastro.2024.05.046

ESA, European Space Agency (2020a) *Types of orbits*. Available at: https://www.esa.int/Enabling_Support/Space_Transportation/Types_of_orbits

NASA, Hubble Site (2022) *The Electromagnetic Spectrum*. Available at: https://hubblesite.org/contents/articles/the-electromagnetic-spectrum

ESA, European Space Agency (2021) *SEASAT*. Available at; https://earth.esa.int/eogateway/missions/seasat

ESA, European Space Agency (2020b) *ERS*. Available at: https://earth.esa.int/eogateway/missions/ers

ESA, European Space Agency (2020c) *JERS-1*. Available at: https://earth.esa.int/eogateway/missions/jers-1

CSA, Canadian Space Agency (2024) *RADARSAT Constellation Mission*. Available at: https://www.asc-csa.gc.ca/eng/satellites/radarsat/

ESA, European Space Agency (2024) *Sentinel-1*. Available at: https://www.esa.int/Applications/Observing_the_Earth/Copernicus/Sentinel-1

DLR, Deutsches Zentrum für Luft- und Raumfahrt (2024) *TerraSAR-X*. Available at: https://www.dlr.de/en/research-and-transfer/projects-and-missions/terrasar-x

ASI, Agenzia Spaziale Italiana (2019) *COSMO-SkyMed*. Available at: https://www.asi.it/scienze-della-terra/cosmo-skymed/

ESA, European Space Agency (2022a) *COSMO-SkyMed Second Generation*. Available at: https://earth.esa.int/eogateway/missions/cosmo-skymed-second-generation

Planetek, Planetek (2023) *Costellazione ride*. Available at: https://www.planetek.it/progetti/costellazione_iride

SERVIR Global Science (2019) *The SAR handbook*. 1st ed. SERVIR Global Science Coordination Office: Huntsville, AL. https://doi.org/10.25966/nr2c-s697

Prats-Iraola, P. *et al*. (2015) 'Role of the orbital tube in interferometric spaceborne SAR missions', *IEEE Geoscience and Remote Sensing Letters*, 12(7), pp. 1486–1490. https://doi.org/10.1109/lgrs.2015.2409885.

Franceschetti, G., and Lanari, R. (1999) *Synthetic Aperture Radar Processing*. 1st ed. CRC Press: Boca Raton. https://doi.org/10.1201/9780203737484

Zalite, K. *et al*. (2014) 'Effects of inundated vegetation on X-Band HH–VV backscatter and phase difference', *IEEE Journal of Selected Topics in Applied Earth Observations and Remote Sensing*, 7(4), pp. 1402–1406. https://doi.org/10.1109/jstars.2013.2279552

Luo, X. *et al*. (2017) 'A novel technique to compute the revisit time of satellites and its application in remote sensing satellite optimization design', *International Journal of Aerospace Engineering*, 1, pp. 1–9. https://doi.org/10.1155/2017/6469439

ESA, European Space Agency (2022b) *Mission ends for Copernicus Sentinel-1B satellite*. Available at: https://www.esa.int/Applications/Observing_the_Earth/Copernicus/Sentinel-1/Mission_ends_for_Copernicus_Sentinel-1B_satellite

Fiorentino, C. and Virelli, M. (2016) 'COSMO-SkyMed Mission and Products Description', *Agenzia Spaziale Italiana*, 2, pp. 1-151. https://earth.esa.int/eogateway/documents/20142/37627/COSMO-SkyMed-Mission-Products-Description.pdf

REA-CNR, DPC, ReLUIS. (2021) *Linee Guida per l'utilizzo dei dati interferometrici satellitari ai fini dell'interpretazione del comportamento strutturale delle costruzioni, Linee Guida per L'utilizzo Dei Dati Interferometrici Satellitari Ai Fini Dell'interpretazione Del Comportamento Strutturale Delle Costruzioni*, [Version 1].

Bovenga, F. *et al*. (2004) 'SPINUA: A Flexible Processing Chain for ERS / Envisat Long Term Interferometry', *Proceedings of the 2004 Envisat & ERS Symposium (ESA SP-572)*, 6-10 September 2004.

Ferretti, A. *et al*. (2001) 'Permanent scatterers in SAR interferometry', *IEEE Transactions on Geoscience and Remote Sensing*, 39(1), pp. 8–20. https://doi.org/10.1109/36.898661

TRE ALTAMIRA (2009) *Analisi di dati radar satellitari mediante la tecnologia PSInSAR, Manuale d'uso*.

Ferretti, A. *et al*. (2011) 'A new algorithm for processing interferometric DataStacks: SqueeSAR', *IEEE Transactions on Geoscience and Remote Sensing*, 49(9), pp. 3460–3470. https://doi.org/10.1109/tgrs.2011.2124465

Hooper, A. *et al* (2004) 'A new method for measuring deformation on volcanoes and other natural terrains using InSAR persistent scatterers', *Geophysical Research Letter*, 31(23), 611–615. https://doi.org/10.1029/2004GL021737

Hooper A. *et al* (2013) *StaMPS/MTI Manual*. Version 3.3b1, *School of Earth and Environment University of Leeds*, Version 3.3b1. School of Earth and Environment University of Leeds, Leeds, UK, 2013

Berardino, P. *et al*. (2002) 'A new algorithm for surface deformation monitoring based on small baseline differential SAR interferograms', *IEEE Transactions on*

Geoscience and Remote Sensing, 40(11), pp. 2375–2383. https://doi.org/10.1109/tgrs.2002.803792

Nitti, D.O. *et al*. (2011) 'Impact of DEM-Assisted coregistration on High-Resolution SAR interferometry', *IEEE Transactions on Geoscience and Remote Sensing*, 49(3), pp. 1127–1143. https://doi.org/10.1109/tgrs.2010.2074204

Belmonte, A. *et al*. (2017) 'Unwrapping-free interpolation of sparse DInSAR phase data: experimental validation', *International Journal of Remote Sensing*, 38(4), pp. 1006–1022. https://doi.org/10.1080/01431161.2016.1275055

Infante, D. *et al*. (2019) 'Integrated Procedure for Monitoring and Assessment of Linear Infrastructures Safety (I-PRO MONALISA) affected by Slope Instability', *Applied Sciences*, 9(24), p. 5535. https://doi.org/10.3390/app9245535

Luo, S. *et al*. (2021) 'An improved method for automatic identification and assessment of potential geohazards based on MT-INSAR measurements', *Remote Sensing*, 13(17), p. 3490. https://doi.org/10.3390/rs13173490

Blasco, J.M.D. *et al*. (2019) 'Measuring Urban Subsidence in the Rome Metropolitan Area (Italy) with Sentinel-1 SNAP-StaMPS Persistent Scatterer Interferometry', *Remote Sensing*, 11(2), p. 129. https://doi.org/10.3390/rs11020129.

Orellana, F. *et al*. (2020) 'DINSAR for Road Infrastructure Monitoring: Case Study Highway Network of Rome Metropolitan (Italy)', *Remote Sensing*, 12(22), p. 3697. https://doi.org/10.3390/rs12223697

Fiorentini, N. *et al*. (2020) 'Surface motion prediction and mapping for road infrastructures management by PS-INSAR measurements and machine learning algorithms', *Remote Sensing*, 12(23), p. 3976. https://doi.org/10.3390/rs12233976

Macchiarulo, V. *et al*. (2022) 'Monitoring deformations of infrastructure networks: A fully automated GIS integration and analysis of InSAR time-series', *Structural Health Monitoring*, 21(4), pp. 1849–1878. https://doi.org/10.1177/14759217211045912

Di Carlo, F. *et al*. (2021) 'On the integration of multi-temporal synthetic aperture radar interferometry products and historical surveys data for buildings structural monitoring', *Journal of Civil Structural Health Monitoring*, 11(5), pp. 1429–1447. https://doi.org/10.1007/s13349-021-00518-4

Miano, A. *et al*. (2021) 'The use of satellite data to support the structural health monitoring in areas affected by slow-moving landslides: a potential application to reinforced concrete buildings', *Structural Health Monitoring*, 20(6), pp. 3265–3287. https://doi.org/10.1177/1475921720983232

Infante, D. *et al*. (2019) 'Assessment of building behavior in slow-moving landslide-affected areas through DInSAR data and structural analysis', *Engineering Structures*, 199, p. 109638. https://doi.org/10.1016/j.engstruct.2019.109638

Milillo, P. *et al*. (2016) 'Space geodetic monitoring of engineered structures: The ongoing destabilization of the Mosul dam, Iraq', *Scientific Reports*, 6(1). https://doi.org/10.1038/srep37408

Scaioni, M. et al. (2018) 'Geodetic and Remote-Sensing sensors for dam deformation monitoring,' Sensors, 18(11), p. 3682. https://doi.org/10.3390/s18113682

Peduto, D., Elia, F. and Montuori, R. (2018) 'Probabilistic analysis of settlement-induced damage to bridges in the city of Amsterdam (The Netherlands)' *Transportation Geotechnics*, 14, pp. 169–182. https://doi.org/10.1016/j.trgeo.2018.01.002

Nettis, A. *et al*. (2023a) 'Satellite-based interferometry for monitoring structural deformations of bridge portfolios', *Automation in Construction*, 147, p. 104707. https://doi.org/10.1016/j.autcon.2022.104707

Del Soldato M. *et al*. (2016) 'A multi-sensor approach for monitoring a road bridge in the Valencia harbor (SE Spain) by SAR Interferometry (InSAR)', *Rendiconti Online Della Società Geologica Italiana*, 41, pp. 235–238. https://doi.org/10.3301/rol.2016.137

Hoppe, E.J. *et al*. (2019) 'Deformation monitoring of posttensioned bridges using High-Resolution satellite Remote sensing', *Journal of Bridge Engineering*, 24(12). https://doi.org/10.1061/(asce)be.1943-5592.0001479

Giordano, P. *et al*. (2022) 'Damage detection on a historic iron bridge using satellite DInSAR data', *Structural Health Monitoring*, 21(5), pp. 2291–2311. https://doi.org/10.1177/14759217211054350

Markogiannaki, O. *et al*. (2021) 'Monitoring of a landmark bridge using SAR interferometry coupled with engineering data and forensics', *International Journal of Remote Sensing*, 43(1), pp. 95–119. https://doi.org/10.1080/01431161.2021.2003468

Huang, Q. *et al*. (2017) 'Displacement monitoring and modelling of a high-speed railway bridge using C-band Sentinel-1 data', *ISPRS Journal of Photogrammetry and Remote Sensing*, 128, pp. 204–211. https://doi.org/10.1016/j.isprsjprs.2017.03.016

Huang, Q. *et al*. (2018) 'Displacement monitoring and health evaluation of two bridges using Sentinel-1 SAR images', *Remote Sensing*, 10(11), p. 1714. https://doi.org/10.3390/rs10111714

Lazecky, M. *et al*. (2017) 'Bridge displacements monitoring using Space-Borne X-Band SAR interferometry', *IEEE Journal of Selected Topics in Applied Earth Observations and Remote Sensing*, 10(1), pp. 205–210. https://doi.org/10.1109/jstars.2016.2587778

Jung, J. *et al*. (2019) 'Long-Term deflection monitoring for bridges using X and C-Band Time-Series SAR interferometry', *Remote Sensing*, 11(11), p. 1258. https://doi.org/10.3390/rs11111258

Cusson, D. *et al*. (2018) 'Satellite-Based INSAR monitoring of highway bridges: validation case study on the North Channel Bridge in Ontario, Canada', *Transportation Research Record Journal of the Transportation Research Board*, 2672(45), pp. 76–86. https://doi.org/10.1177/0361198118795013

Selvakumaran, S. *et al*. (2018) 'Remote monitoring to predict bridge scour failure using Interferometric Synthetic Aperture Radar (InSAR) stacking techniques', *International Journal of Applied Earth Observation and Geoinformation*, 73, pp. 463–470. https://doi.org/10.1016/j.jag.2018.07.004

Milillo, P. et al. (2020) 'Reply to Lanari, R., et al. Comment on “Pre-Collapse Space Geodetic Observations of Critical Infrastructure: The Morandi Bridge, Genoa, Italy” by Milillo et al. (2019)', *Remote Sensing*, 12(24), p. 4016. https://doi.org/10.3390/rs12244016

Copernicus (2024) *Copernicus Open Access Hub*. Available at: https://sci-hub.copernicus.eu/

Mahaffy, J.M. (2012) 'Lecture Notes – Trigonometric functions', pp. 1–12. https://jmahaffy.sdsu.edu/courses/f11/math122/beamer_lectures/trig-04.pdf

OSM, OpenStreetMap (2024) *OpenStreetMap*. Available at: https://www.openstreetmap.org/#map=6/42.088/12.564

Talledo, D.A. *et al*. (2022) 'Satellite radar interferometry: Potential and limitations for structural assessment and monitoring', *Journal of Building Engineering*, 46, p. 103756. https://doi.org/10.1016/j.jobe.2021.103756

Mele, A. *et al*. (2022) 'On the Joint Exploitation of Satellite DInSAR Measurements and DBSCAN-Based Techniques for Preliminary Identification and Ranking of Critical Constructions in a Built Environment', *Remote Sensing*, 14(8), p. 1872. https://doi.org/10.3390/rs14081872

Cleveland, R.B. *et al*. (1990) 'STL: A seasonal-trend decomposition procedure based on loess', *Journal of Official Statistics*, 6(1), pp. 3-73.

Goel, K. *et al*. (2014) ' Thermal dilation monitoring of complex urban infrastructure using high resolution SAR data', *IEEE Geoscience and Remote Sensing Symposium*, pp. 954-957. https://doi.org/10.1109/IGARSS.2014.6946584

Ponzo, F.C. *et al*. (2024) 'DInSAR–SBAS satellite monitoring of infrastructures: how temperature affects the "Ponte della Musica" case study', *Journal of Civil Structural Health Monitoring, 14, pp. 745-761*. https://doi.org/10.1007/s13349-023-00751-z

MIT, Ministero delle Infrastrutture e dei Trasporti (2018) *Aggiornamento delle <<Norme tecniche per le costruzioni>>*.

Bordoni, M. *et al.* (2017) 'A methodology for ground motion area detection (GMA-D) using A-DInSAR time series in landslide investigations', CATENA, 163, pp. 89–110. https://doi.org/10.1016/j.catena.2017.12.013

DePrekel, K., Bouali, E.H. and Oommen, T. (2018) 'Monitoring the impact of groundwater pumping on infrastructure using Geographic Information System (GIS) and Persistent Scatterer interferometry (PSI)', Infrastructures, 3(4), p. 57. https://doi.org/10.3390/infrastructures3040057

Meisina, C. *et al*. (2008) 'Geological interpretation of PSINSAR data at regional scale', Sensors, 8(11), pp. 7469–7492. https://doi.org/10.3390/s8117469

Ciampoli, L.B. *et al*. (2019) 'Automatic network level bridge monitoring by integration of InSAR and GIS catalogues'. Proceedings of SPIE OPTICAL METROLOGY [Preprint]. https://doi.org/10.1117/12.2527299

Vaccari, A. *et al*. (2018) 'Integrating remote sensing data in decision support systems for transportation asset management', Transportation Research Record Journal of the Transportation Research Board, 2672(45), pp. 23–35. https://doi.org/10.1177/0361198118786645

Chaurasia, R. and Mohindru, V. (2021) 'Unmanned Aerial Vehicle (UAV): A Comprehensive Survey', *Unmanned Aerial Vehicles for Internet of Things. https://doi.org/10.1002/9781119769170.ch1*-z

Sharma, A. *et al*. (2020) 'Communication and networking technologies for UAVs: A survey', *Journal of Network and Computer Applications*, 168, p. 102739. https://doi.org/10.1016/j.jnca.2020.102739

Rajan, J., et al. (2021) 'Disaster management using unmanned aerial vehicles', in Elsevier eBooks, pp. 129–155. https://doi.org/10.1016/b978-0-12-820276-0.00013-3

Samad, A.M. *et al*. (2013), 'The potential of Unmanned Aerial Vehicle (UAV) for civilian and mapping application', *IEEE 3rd International Conference on System Engineering and Technology, Shah Alam, Malaysia*, pp. 313-318. https://doi.org/10.1109/ICSEngT.2013.6650191

Montambault, S. *et al*. (2010) 'On the application of VTOL UAVs to the inspection of power utility assets', *2010 1st International Conference on Applied Robotics for the Power Industry, Montreal, QC, Canada*, pp. 1-7. https://doi.org/10.1109/CARPI.2010.5624443

Tsouros, D.C. *et al*. (2019) 'A Review on UAV-Based Applications for Precision Agriculture', *Information*, 10(11), p. 349. https://doi.org/10.3390/info10110349

DJI (2024) *DJI Store*. Available at: https://www.dji-store.it/

Wang, X. *et al*. (2023) 'Rapid seismic assessment of bridges using UAV aerial photogrammetry', *Engineering Structures*, 279, p. 115589. https://doi.org/10.1016/j.engstruct.2023.115589

Nex, F. and Remondino, F. (2014) 'UAV for 3D mapping applications: a review', *Applied Geomatics*, 6, pp. 1-15. https://doi.org/10.1007/s12518-013-0120-x

Eugster, H., and Nebiker, S. (2008) 'UAV-based augmented monitoring– real-time georeferencing and integration of video imagery with virtual globes', *Int. Archives of Photogrammetry, Remote Sensing and Spatial Information Sciences, Beijing, China*, 37(B1), pp. 1229–1235.

Colomina, I. and Molina, P. (2014) 'Unmanned aerial systems for photogrammetry and remote sensing: A review', *ISPRS Journal of photogrammetry and remote sensing*, 92, pp. 79-97. https://doi.org/10.1016/j.isprsjprs.2014.02.013

Remondino, F. *et al*. (2012) 'UAV photogrammetry for mapping and 3d modelling–current status and future perspectives', *The International Archives of the Photogrammetry, Remote Sensing and Spatial Information Sciences*, 38, pp. 25-31. https://doi.org/10.5194/isprsarchives-XXXVIII-1-C22-25-2011

Agisoft (2024) *Agisoft*. Available at: https://www.agisoft.com/

Kim, I.-H. *et al*. (2018) 'Application of crack identification techniques for an aging concrete bridge inspection using an unmanned aerial vehicle', *Sensors*, 18(6), p. 1881. https://doi.org/10.3390/s18061881

Duque, L. *et al* (2018) 'Bridge Deterioration Quantification Protocol using UAV', *Journal of Bridge Engineering*, 23(10). https://doi.org/10.1061/(asce)be.1943-5592.0001289

Lei, B. *et al*. (2018) 'New crack detection method for bridge inspection using UAV incorporating image processing', *Journal of Aerospace Engineering*, 31(5). https://doi.org/10.1061/(asce)as.1943-5525.0000879

Castellazzi, G. *et al*. (2015) 'From laser scanning to finite element analysis of complex buildings by using a Semi-Automatic procedure', *Sensors*, 15(8), pp. 18360–18380. https://doi.org/10.3390/s150818360

Barazzetti, L. *et al*. (2015) 'BIM FROM LASER CLOUDS AND FINITE ELEMENT ANALYSIS: COMBINING STRUCTURAL ANALYSIS AND GEOMETRIC COMPLEXITY', *Int. Arch. Photogramm. Remote Sens. Spatial Inf. Sci.*, XL-5/W4, pp. 345–350, https://doi.org/10.5194/isprsarchives-XL-5-W4-345-2015, 2015

Morgenthal, G. *et al*. (2019) 'Framework for automated UAS-based structural condition assessment of bridges', *Automation in Construction*, 97, pp. 77–95. https://doi.org/10.1016/j.autcon.2018.10.006

Wang, X. *et al*. (2023) 'Rapid seismic risk assessment of bridges using UAV aerial photogrammetry', *Engineering Structures*, 279, p. 115589. https://doi.org/10.1016/j.engstruct.2023.115589

Devoto, S. *et al*. (2020) 'Advantages of using UAV digital photogrammetry in the study of slow-moving coastal landslides', *Remote Sensing*, 12(21), p. 3566. https://doi.org/10.3390/rs12213566

Özcan, O. and Özcan, O. (2021) 'Multi-temporal UAV based repeat monitoring of rivers sensitive to flood ', Journal of Maps, 17(3), pp. 163-170. https://doi.org/10.1080/17445647.2020.1820387

Meng, Q. *et al*. (2021) 'Time-series analysis of the evolution of large-scale loess landslides using InSAR and UAV photogrammetry techniques: A case study in Hongheyan, Gansu Province, Northwest China', *Landslides*, 18, pp. 251-265. https://doi.org/10.1007/s10346-020-01490-8

Casagli, N. *et al*. (2017) 'Spaceborne, UAV and ground-based remote sensing techniques for landslide mapping, monitoring and early warning', *Geoenvironmental Disasters*, 4, pp. 1-23. https://doi.org/10.1186/s40677-017-0073-1

Martins, B. H. *et al* (2020) 'Ground surface deformation detection in complex landslide area—Bobonaro, Timor-Leste—Using SBAS DinSAR, UAV photogrammetry, and field observations', *Geosciences*, 10(6), p. 245. https://doi.org/10.3390/geosciences10060245

Eker, R. and Aydın, A. (2021) 'Long-term retrospective investigation of a large, deep-seated, and slow-moving landslide using InSAR time series, historical aerial photographs, and UAV data: The case of Devrek landslide (NW Turkey)', *Catena*, 196, p. 104895. https://doi.org/10.1016/j.catena.2020.104895

Romeo. S. *et al*. (2022) 'Investigation and preliminary assessment of the Casamicciola landslide in the island of Ischia (Italy) on November 26', *Landslides,* 20, pp. 1265-1276. https://doi.org/10.1007/s10346-023-02064-0

Vassallo, R. *et al*. (2016) 'Relationships between rain and displacements of an active earthflow: a data-driven approach by EPRMOGA', *Natural Hazards*, 81, pp. 1467-1482. https://doi.org/10.1007/s11069-015-2140-9

Galeandro, A. *et al*. (2013) 'Hydraulic stream network conditioning by a tectonically induced, giant, deep-seated landslide along the front of the Apennine chain (south Italy)', *Natural Hazards and Earth System Sciences*, 13(5), pp. 1269-1283. https://doi.org/10.5194/nhess-13-1269-2013

Novak, A.S., and Collins, K.R. (2013) *Reliability of Structures*. 2nd ed. CRC Press: London.

Joint Committee of Structural Safety (2001). Joint Committee of Structural Safety. Available at: https://www.jcss-lc.org/

Doglioni, A.*et al*. (2020) 'The landslide of Pomarico, South Italy, occurred on January 29th 2019', *Landslides*, 17, pp. 2137-2143. https://doi.org/10.1007/s10346-020-01455-x

Tyson, D. (2009) 'The history of prestressed concrete: 1888 to 1963', *K-State Electronic Theses, Dissertations, and Reports: 2004*, KANSAS STATE UNIVERSITY: Lawrence: USA.

Ledesma, T. and WSP USA (2019) *Replaceable grouted External Post-Tensioned tendons*. technical report FHWA-HIF-19-067. Federal Highway Administration. https://www.fhwa.dot.gov/bridge/concrete/hif19067.pdf

Naito, C. *et al*. (2010) 'Forensinc Extimation of a Noncomposite Adjacent Precast Prestressed Concrete Box Beam Bridge', *Journal of Bridge Engineering*, 15(4), pp. 408-418. https://doi.org/10.1061/(ASCE)BE.1943-5592.0000110

Corven, J. (2015) 'Post-Tensioned Box Girder Design Manual', *Federal Highway Administration*. https://www.fhwa.dot.gov/bridge/concrete/hif15016.pdf

Bažant, Z.P. and Jirásek, M. (2018) 'Paradigms of application, phenomena affecting creep deformations, and comparisons to measurements on structures', *Solid mechanics and its applications*, pp. 205–268. https://doi.org/10.1007/978-94-024-1138-6_7

Chávez, A.A. *et al.* (2024) 'Assessment of residual prestress in existing concrete bridges: The Kalix bridge', *Engineering Structures*, 311, p. 118194. https://doi.org/10.1016/j.engstruct.2024.118194

Kim, D. *et al.* (2023) 'An experimental study on the deterioration behaviour of external tendons due to corrosion', *KSCE Journal of Civil Engineering*, 27(12), pp. 5319–5328. https://doi.org/10.1007/s12205-023-0316-5

Sconocchia, G.G. *et al.* (2024) 'Insights into structural assessment and long-term effects of a post-tensioned multispan concrete box girder bridge with vertically prestressed internal joints', *Structures*, 63, p. 106396. https://doi.org/10.1016/j.istruc.2024.106396

Yang, M. *et al*. (2020) 'Refined calculation of time-dependent prestress losses in prestressed concrete girders', *Structure and Infrastructure Engineering*, 16(10), pp. 1430–1446. https://doi.org/10.1080/15732479.2020.1712438

Huang, H., Huang, S.-S. and Pilakoutas, K. (2018) 'Modeling for Assessment of Long-Term behavior of prestressed Concrete Box-Girder bridges', *Journal of Bridge Engineering*, 23(3). Available at: https://doi.org/10.1061/(asce)be.1943-5592.0001210.

ACI Committee 318 (2022) *Building Code Requirements for Structural Concrete and Commentary (ACI 318-19)*.

Tu, B., *et al*. (2019) 'Time-Dependent reliability and redundancy of corroded prestressed concrete bridges at material, component, and system levels', *Journal of Bridge Engineering*, 24(9). https://doi.org/10.1061/(asce)be.1943-5592.0001461

Bažant, Z.P. and Yu, Q. (2012) 'Relaxation of prestressing steel at varying strain and temperature: viscoplastic constitutive relation,', *Journal of Engineering Mechanics*, 139(7), pp. 814–823. Available at: https://doi.org/10.1061/(asce)em.1943-7889.0000533

Losanno, D., Galano, S. and Parisi, F. (2023a) 'Influence of strand rupture on flexural behavior of reduced-scale prestressed concrete bridge girders with different prestressing levels', *Engineering Structures*, 301, p. 117358. Available at: https://doi.org/10.1016/j.engstruct.2023.117358

Losanno, D. *et al.* (2023b) "Experimental Investigation on Nonlinear Flexural Behavior of Post-Tensioned Concrete Bridge Girders with Different Grouting Conditions and Prestress Levels', *Journal of Bridge Engineering*, 29(3). Available at: https://doi.org/10.1061/jbenf2.beeng-6466

P. Zia, *et al*. (1979) 'Estimating prestress losses', *Concrete International*, 1, p. 6.

Franceschini, L. *et al.* (2021) 'Analytical method for the evaluation of the residual service life of prestressed concrete beams subjected to corrosion deterioration', *Structural Concrete*, 23(1), pp. 121–137. https://doi.org/10.1002/suco.202100245

Ministerio de Transportes Y Movilidad Sostenible (2022) *Mitma presenta los informes provisionales sobre las causas del colapso del viaducto del Castro de la A-6 sentido A Coruña*. Available at: https://www.transportes.gob.es/el-ministerio/sala-de-prensa/noticias/mar-15112022-1613

He, Z.-Q. *et al*. (2021) 'Crack-based serviceability assessment of post-tensioned segmental concrete box-girder bridges', *Structures*, 30, pp. 1097–1108. Available at: https://doi.org/10.1016/j.istruc.2021.01.062

Sousa, H. *et al*. (2014) "Assessment and management of concrete bridges supported by monitoring Data-Based Finite-Element Modeling," *Journal of Bridge Engineering*, 19(6). Available at: https://doi.org/10.1061/(asce)be.1943-5592.0000604.

Comisu, C.-C. *et al*. (2017) 'Structural health monitoring system of bridges', *Procedia Engineering*, 199, pp. 2054–2059. Available at: https://doi.org/10.1016/j.proeng.2017.09.472

He, Z. *et al*. (2022) 'Integrated structural health monitoring in bridge engineering', *Automation in Construction*, 136, p. 104168. Available at: https://doi.org/10.1016/j.autcon.2022.104168

Sousa, H. *et al.* (2011) 'Design and implementation of a monitoring system applied to a long-span prestressed concrete bridge', *Structural Concrete*, 12(2), pp. 82–93. https://doi.org/10.1002/suco.201000014

Dall'Asta, A. and Dezi, L. (1996) 'Discussion on "Prestress force effect on vibration frequency of concrete bridges" by Saiidi M. et al. ', *Journal of Structural Engineering*, 122(4). https://doi.org/10.1061/(ASCE)0733-9445(1996)122:4(459)

Abraham, M.A. *et al*. (1995) 'Loss of prestress prediction based on nondestructive damage location algorithms', *Proceedings of SPIE, the International Society for Optical Engineering/Proceedings of SPIE* [Preprint]. https://doi.org/10.1117/12.207717

Bonopera, M. *et al.* (2018) 'Prestress force effect on fundamental frequency and deflection shape of PCI beams', *Structural Engineering and Mechanics*, 67(3), p. 255. https://doi.org/10.12989/sem.2018.67.3.255

De Angelis, A. *et al*. (2024) "Identification of modal parameters of scaled bridge PC beams by OMA Dynamic Tests," *Journal of Bridge Engineering*, 29(8). Available at: https://doi.org/10.1061/jbenf2.beeng-6763

Hamed, E. and Frostig, Y. (2006) 'Natural frequencies of bonded and unbonded prestressed beams–prestress force effects', *Journal of Sound and Vibration*, 295(1–2), pp. 28–39. https://doi.org/10.1016/j.jsv.2005.11.032

Limongelli, M.P. *et al*. (2016) 'Damage detection in a post tensioned concrete beam – Experimental investigation', *Engineering Structures*, 128, pp. 15–25. Available at: https://doi.org/10.1016/j.engstruct.2016.09.01

Park, G. *et al.* (2003) 'Overview of Piezoelectric Impedance-Based Health Monitoring and Path forward', *The Shock and Vibration Digest*, 35(6), pp. 451–463. https://doi.org/10.1177/05831024030356001

Rabelo, D. *et al*. (2015) 'Impedance-Based Structural Health Monitoring incorporating compensation of temperature variation effects', *Proceedings of the 23rd International Congress of Mechanical Engineering* [Preprint]. https://doi.org/10.20906/cps/cob-2015-1903

Huynh, T.-C. and Kim, J.-T. (2014) 'Impedance-Based cable force monitoring in Tendon-Anchorage using portable PZT-Interface technique', *Mathematical Problems in Engineering*, 2014, pp. 1–11. https://doi.org/10.1155/2014/784731

Chen, S.-Z. *et al.* (2017) 'Prestressing force monitoring method for a box girder through distributed long-gauge FBG sensors', *Smart Materials and Structures*, 27(1), p. 015015. https://doi.org/10.1088/1361-665x/aa9bbe

Kim, S. *et al.* (2015) 'A Sensor-Type PC Strand with an Embedded FBG Sensor for Monitoring Prestress Forces', *Sensors*, 15(1), pp. 1060–1070. https://doi.org/10.3390/s150101060

Mckeeman, I. *et al.* (2016) 'First-time demonstration of measuring concrete prestress levels with metal packaged fibre optic sensors', *Smart Materials and Structures*, 25(9), p. 095051. https://doi.org/10.1088/0964-1726/25/9/095051

Liu, C. *et al*. (2015) 'A wireless strain sensor network for structural health monitoring,' *Shock and Vibration*, 2015, pp. 1–13. https://doi.org/10.1155/2015/740471

Jo, H. *et al.* (2013) 'Develoment of high-sensitivity wireless strain sensor for structural health monitoring', *Smart Structures and Systems*, 11(5), pp. 477–496. https://doi.org/10.12989/sss.2013.11.5.477

Abdel-Jaber, H. (2017) 'Comprehensive strain-based methods for monitoring prestressed concrete beam-like elements', *Ph.D. Thesis: Princeton University*.

Bonopera, M. and Chang, K.-C. (2021) 'Novel method for identifying residual prestress force in simply supported concrete girder-bridges', *Advances in Structural Engineering*, 24(14), pp. 3238–3251. Available at: https://doi.org/10.1177/13694332211022067

Abdel-Jaber, H. and Glisic, B. (2019) 'Monitoring of prestressing forces in prestressed concrete structures—An overview', *Structural Control and Health Monitoring*, 26(8). https://doi.org/10.1002/stc.2374

Xiong, C. *et al*. (2024) 'A novel YOLOv8-GAM-Wise-IoU model for automated detection of bridge surface cracks', *Construction and Building Materials*, 414, p. 135025. https://doi.org/10.1016/j.conbuildmat.2024.135025

Wan, H. *et al.* (2023) 'A novel transformer model for surface damage detection and cognition of concrete bridges', *Expert Systems With Applications*, 213, p. 119019. https://doi.org/10.1016/j.eswa.2022.119019

Mei, Q. *et al*. (2019) 'Indirect health monitoring of bridges using Mel-frequency cepstral coefficients and principal component analysis', *Mechanical Systems and Signal Processing*, 119, pp. 523–546. https://doi.org/10.1016/j.ymssp.2018.10.006

Sakiyama, F.I. *et al.* (2022) 'Quantifying the extent of local damage of a 60-year-old prestressed concrete bridge: A hybrid SHM approach', *Structural Health Monitoring*, 22(1), pp. 496–517. https://doi.org/10.1177/14759217221079295

Svendsen, B.T. *et al.* (2021) 'A data-based structural health monitoring approach for damage detection in steel bridges using experimental data', *Journal of Civil Structural Health Monitoring*, 12(1), pp. 101–115. https://doi.org/10.1007/s13349-021-00530-8

Chen, S. *et al.* (2021) 'Life-cycle modelling of concrete cracking and reinforcement corrosion in concrete bridges: A case study', *Engineering Structures*, 237, p. 112143. https://doi.org/10.1016/j.engstruct.2021.112143

Mangalathu, S. *et al*. (2018) 'Artificial neural network based multi-dimensional fragility development of skewed concrete bridge classes', *Engineering Structures*, 162, pp. 166–176. https://doi.org/10.1016/j.engstruct.2018.01.053

Mo, R. *et al.* (2023) 'Bridge seismic fragility model based on support vector machine and relevance vector machine', *Structures*, 52, pp. 768–778. https://doi.org/10.1016/j.istruc.2023.03.179

Opabola, E.A. and Mangalathu, S. (2022) 'Seismic fragility assessment of bridges with as-built and retrofitted splice-deficient columns', *Bulletin of Earthquake Engineering*, 21(1), pp. 583–603. https://doi.org/10.1007/s10518-022-01521-w

Soleimani, F. and Liu, X. (2021) 'Artificial neural network application in predicting probabilistic seismic demands of bridge components', *Earthquake Engineering & Structural Dynamics*, 51(3), pp. 612–629. https://doi.org/10.1002/eqe.3582

Dang, N.-L. *et al.* (2023) 'A hybrid method for strand looseness identification in post-tensioned system using FEM and ANN', *Journal of Civil Structural Health Monitoring*, 13(6–7), pp. 1287–1311. https://doi.org/10.1007/s13349-023-00704-6

Mariniello, G. *et al.* (2021) 'Layout-aware Extreme Learning Machine to Detect Tendon Malfunctions in Prestressed Concrete Bridges using Stress Data', *Automation in Construction*, 132, p. 103976. https://doi.org/10.1016/j.autcon.2021.10397

Kim, J. and Park, S. (2019) 'Field applicability of a machine learning–based tensile force estimation for pre-stressed concrete bridges using an embedded elasto-magnetic sensor', *Structural Health Monitoring*, 19(1), pp. 281–292. https://doi.org/10.1177/1475921719842340

Nguyen, T.-T. *et al.* (2022) 'Deep learning-based autonomous damage-sensitive feature extraction for impedance-based prestress monitoring', *Engineering Structures*, 259, p. 114172. https://doi.org/10.1016/j.engstruct.2022.114172

Lundberg, S.M. and Lee, S.-I. (2017) 'A unified approach to interpreting model predictions', *arXiv (Cornell University)* [Preprint]. https://doi.org/10.48550/arxiv.1705.07874

ICITECH – Instituto Universitario de Ciencia y Tecnología del Hormigón – UPV (2024) *Welcome*. Available at: https://icitech.webs.upv.es/index.php/en/presentation/

Hou, P. *et al.* (2024) 'Investigation on mechanical performance of prestressed concrete box-girder bridge strengthened using composite trusses with different shapes', *Structural Concrete*, 25(3), pp. 1620–1636. https://doi.org/10.1002/suco.202300183

Pérez-Sala, J.C. and Ruiz-Teran, A.M. (2023) 'Numerical analysis of precast concrete segmental bridge decks', *Engineering Structures*, 275, p. 115277. https://doi.org/10.1016/j.engstruct.2022.115277

Noble, D. *et al*. (2015) 'The effect of prestress force magnitude and eccentricity on the natural bending frequencies of uncracked prestressed concrete beams', *Journal of Sound and Vibration*, 365, pp. 22–44. Available at: https://doi.org/10.1016/j.jsv.2015.11.047

Eurocode 2 (2004). *Eurocode 2: Design of concrete structures - Part 1-1: General rules and rules for buildings*, EN 1992-1-1:2004.

Nettis, A. *et al*. (2023b) 'Seismic risk-informed prioritisation of multi-span RC girder bridges considering knowledge-based uncertainty', *Bulletin of Earthquake Engineering*, 22(2), pp. 693–729. https://doi.org/10.1007/s10518-023-01783-y

Bagge, N., Nilimaa, J. and Elfgren, L. (2017) 'In-situ methods to determine residual prestress forces in concrete bridges', *Engineering Structures*, 135, pp. 41–52. Available at: https://doi.org/10.1016/j.engstruct.2016.12.059

Wang, Y. *et al.* (2023) 'Machine learning-driven probabilistic seismic demand model with multiple intensity measures and applicability in seismic fragility analysis for nuclear power plants', *Soil Dynamics and Earthquake Engineering*, 171, p. 107966. https://doi.org/10.1016/j.soildyn.2023.107966

Breiman, L. (2001) 'Random Forests', *Machine Learning*, 45, pp. 5–32. https://doi.org/10.1023/A:1010933404324

Hastie, T. *et al*. (2009) *The elements of statistical learning: Data Mining, Inference, and Prediction, Second Edition*. Springer Science & Business Media. https://doi.org/10.1007/978-0-387-84858-7

Xu, M. *et al.* (2005) 'Decision tree regression for soft classification of remote sensing data', *Remote Sensing of Environment*, 97(3), pp. 322–336. https://doi.org/10.1016/j.rse.2005.05.008

Vapnik, V. (2006) *Estimation of dependences based on empirical data*. Springer Science & Business Media.

Vapnik, V.N. (1998) *Statistical learning theory*. Wiley-Interscience.

Balfer, J. and Bajorath, J. (2015) 'Systematic artifacts in support vector Regression-Based compound potency prediction revealed by statistical and activity landscape analysis', *PLoS ONE*, 10(3), p. e0119301. https://doi.org/10.1371/journal.pone.0119301

Rodríguez-Pérez, R. and Bajorath, J. (2022) 'Evolution of support vector machine and regression modeling in chemoinformatics and drug discovery', *Journal of*

Computer-Aided Molecular Design, 36(5), pp. 355–362. https://doi.org/10.1007/s10822-022-00442-9

Computer and Structures, Inc (2024) *SAP2000, Advanced 25.Structural Analysis Program-Manual – Computer and Structures, Inc, Berkeley, California, USA*. Available at: https://www.csiamerica.com/products/sap2000

Python Software Foundation (2024) *Python: A Dynamic, Open-Source Programming Language*. Available at: https://www.python.org/

Parisi, F. *et al.* (2024) 'On the use of mechanics-informed models to structural engineering systems: Application of graph neural networks for structural analysis', *Structures*, 59, p. 105712. https://doi.org/10.1016/j.istruc.2023.105712

Parisi, F. *et al.* (2022) 'Automated location of steel truss bridge damage using machine learning and raw strain sensor data', *Automation in Construction*, 138, p. 104249. https://doi.org/10.1016/j.autcon.2022.104249

Mangalathu, S. *et al.* (2019) 'Rapid seismic damage evaluation of bridge portfolios using machine learning techniques', *Engineering Structures*, 201, p. 109785. https://doi.org/10.1016/j.engstruct.2019.109785

Agarwal, P., Pal, P. and Pradeep, K.M. (2022) 'Box-Girder Bridges - Modelling and Analysis', *International Journal for Engineering Modelling*, 35(1). https://doi.org/10.31534/engmod.2022.1.ri.02m

MIT, Ministero delle Infrastrutture e dei Trasporti (2024) *AINOP - Archivio Informatico delle Opere Pubbliche*. Available at: https://ainop.mit.gov.it/portale#/

ANAS, Azienda Nazionale Autonoma delle Strade Statali (2024b) *Smart road e smart mobility*. Available at: https://www.stradeanas.it/it/smartroad

Cardellicchio, A. *et al.* (2023) 'On the use of YOLOv5 for detecting common defects on existing RC bridges', *SPIE Optical Metrology, 2023, Munich, Germany* [Preprint]. https://doi.org/10.1117/12.2673655

CURRICULUM

Mirko Calò

Contact

Date of Birth: 15/09/1995
Nationality: Italian
Phone: +39 3489696771
Email: mirko.calo@poliba.it; mirko.calos3@gmail.com
LinkedIn: https://www.linkedin.com/in/mirko-cal%C3%B2-697137242/
ResearchGate: https://www.researchgate.net/profile/Mirko-Calo
ORCiD: https://orcid.org/0000-0003-4148-5959

About — December 2024

Current job — **PhD Candidate**, Doctor of Philosophy in Risk and Environmental, Territorial and Building Development, XXXVII Cycle, SSD: CEAR-07/A, Structural Engineering
DICATECh Department, Polytechnic University of Bari,
Via Edoardo Orabona, 4, 70126, Bari, Italy

Main Interests — Structural assessment of existing bridges and viaduct
Risk assessment
Programming
Innovative approaches for assessment and management of existing construction heritage (satellite remote sensing, unmanned aerial vehicle photogrammetry, Machine Learning and GIS)

Education

01/2022 – 12/2024
Bari, Italy

Doctor of Philosophy studies, Course of Civil, Environmental and Building Risk and Development, XXXVII Cycle,
Polytechnic University of Bari
Thesis Title: "*Cost-effective monitoring of structural risk of bridges supported by cutting edge technologies*"
Tutors: Prof. Eng Giuseppina Uva, Dr. Sergio Ruggieri, Dr. Andrea Nettis, Prof. Eng. J.M. Adam
Main studies: Cost-effective techniques for SHM monitoring of bridges, FE modelling, structural assessment

02/2024 – 07/2024
Valencia, Spain

PhD visiting
Universitat Politècnica de València – ICITECH
Structural monitoring of prestressing force reduction on prestressed concrete bridges through installed sensors and Machine Learning algorithms

02/2023 – 07/2023 Bari, Italy	**PhD visiting** **Planetek Italia** Data-driven structural assessment approach for existing bridges via satellite-based persistent scatterer interferometry
01/2022 – 12/2022 Italy	**Bridge inspections** **Consorzio FABRE**
09/2018 – 10/2021 Bari, Italy	**Master's degree of Civil Engineering, curriculum Structural Engineering** Polytechnic University of Bari, grade 110/110 cum laude. Thesis Title: "Modellazione tipologico-meccanica della risposta sismica di edifici esistenti in c.a. e analisi dinamiche non lineari" (in Italian), Seismic engineering. Tutor: Prof. Eng. Giuseppina Uva. Main studies: Seismic engineering, nonlinear behavior of structures
09/2014 – 07/2018 Taranto, Italy	**Bachelor's degree of Civil and Environmental Engineering** Polytechnic University of Bari, grade 102/110. Thesis Title: "Verifica della rete acquedottistica del comune di Pulsano mediante il software EPANET" Tutor: Prof. Eng. Michele Mossa
07/2014 Taranto, Italy	**High School Diploma** Liceo Scientifico "G. Battaglini", grade 72/100

Professional qualification

02/2022 Bari, Italy	**Civil engineer qualifying examination**

Teaching and tutoring

2024-2025 Bari, Italy	Course: "**Costruzioni in zona sismica**" (LM-23), SSD: CEAR-07/A, Polytechnic University of Bari, 40 hours, Tutor: Prof. Eng. Giuseppina Uva
2023-2024 Bari, Italy	Course: "**Costruzioni in zona sismica**" (LM-23), SSD: CEAR-07/A, Polytechnic University of Bari, 40 hours, Tutor: Prof. Eng. Giuseppina Uva
2022-2023 Bari, Italy	Course: "**Costruzioni in zona sismica**" (LM-23), SSD: CEAR-07/A, Polytechnic University of Bari, 40 hours, Tutor: Prof. Eng. Giuseppina Uva Course: "**Tecnica delle costruzioni**" (L-7), SSD: CEAR-07/A, Polytechnic University of Bari, 40 hours, Tutor: Prof. Eng. Saverio Spadea
2021-2022 Bari, Italy	Course: "**Costruzioni in zona sismica** (LM-23)", SSD: CEAR-07/A, Polytechnic University of Bari, 40 hours, Tutor: Prof. Eng. Giuseppina Uva Course: "**Tecnica delle costruzioni**" (L-7), SSD: CEAR-07/A, Polytechnic University of Bari, 40 hours, Tutor: Prof. Eng. Rita Greco

Techincal skills

Spoken languages	Italian (Mother), English (B2)
Programming languages	Python, VBA, Matlab, Tcl, SQL, CSS, HTML
Strucutral analysis software	Sap2000, Etabs, CSIBridge, OpenSees, Strauss, Edilus
CAD and Graphic	AutoCAD, Archicad, Photoshop
Strucutral analysis software	Sap2000, Etabs, CSIBridge, OpenSees, Strauss, Edilus

Soft skills

Curiosity, self-motivation, resilience, problem solving, fast learning, reverse engineering, teamwork.

Other interests

PhD students' representative: Departmental Council for Civil, Environmental, Land, Building and Chemical Engineering since October 2022.
Cars and motorbikes
Technology and computers
Team sports: Soccer, padel

Publications

Journal papers

Calò, M., Ruggieri, S., Nettis, A., Uva, G. (2024) 'A MTInSAR-based early warning system to appraise deformations in simply supported concrete girder bridges', *Structural Control and Health Monitoring*, p. 8978782. https://doi.org/10.1155/2024/8978782

Calò, M., Ruggieri S., Doglioni, A., Morga, M., Nettis, A., Simeone, V., Uva, G. (2024) 'Probabilistic-based assessment of subsidence phenomena on the existing built heritage by combining MTInSAR data and UAV photogrammetry', *Structure and Infrastructure Engineering*, pp. 1-16. DOI: 10.1080/15732479.2024.2423032

Calò, M., Ruggieri S., Buitrago, M., Nettis, A., Adam, J.M., Uva, G. (2024) 'An ML-based framework for predicting prestressing force reduction in reinforced concrete box-girder bridges', *Engineering Structures*, 325, 119400. DOI: 10.1016/j.engstruct.2024.119400

Calò, M., Ruggieri S., Nettis, A., Uva, G. (2024) 'A GIS plugin for the assessment of deformations in existing bridge portfolios via MTInSAR', *Remote Sensing*, 16(22), 4293. DOI: 10.3390/rs16224293

Ruggieri, S., **Calò, M.**, Cardellicchio, A., Uva, G. (2022) 'Analytical-mechanical based framework for seismic overall fragility analysis of existing RC buildings in town compartments', *Bulletin of Earthquake Engineering*, 20(4), pp. 8179–8216. DOI: 10.1007/s10518-022-01516-7

Conference papers

Calò, M., Ruggieri, S., Nettis, A., Uva G. (2023) 'Multi source Interferometry Synthetic Aperture Radar for monitoring existing bridges: a case study', *Ce/Papers*, 6(5), pp. 787/793. DOI:10.1002/cepa.2058

Ruggieri, S., Nettis, A., **Calò, M.**, Nettis, Al., Cardellicchio, A., Uva, G. (2023) 'Towards a new vision of civil engineering: digital innovation applications for the Structural Health Management of existing bridge portfolios', *iNDiS 2023 - International scientific conference planning, design, construction and building renewal At: Novi Sad, Serbia, November 16-17, 2023*.

Morga, M., **Calò, M.**, Nettis, A., Ruggieri, S., Doglioni, A., Simeone, V., Uva, G. (2024) 'On the use of MTInSAR data and UAV photogrammetry to monitor the behavior of existing bridge portfolios', *Procedia Structural Integrity, 2024*, 62, pp 924-931. https://doi.org/10.1016/j.prostr.2024.09.124

Salvatore, W. ***et al***. (2024) 'Application of Italian Guidelines for structural-foundational and seismic risk classification of bridges: the Fabre experience on a large bridge inventory', *Procedia Structural Integrity, 2024*, 62, pp 1-8. https://doi.org/10.1016/j.prostr.2024.09.009

Calò, M., Ruggieri, S., Nettis, A., Uva G. (2024) 'BMS-INSAR: GIS PLUGIN FOR BRIDGE PORTFOLIO SERVICE DISPLACEMENT ANALYSIS THROUGH MTINSAR DATA', *18th World Conference on Earthquake Engineering at: Milan, June 30 - July 5, 2024*.

La borsa di dottorato è stata cofinanziata con risorse del
Programma Operativo Nazionale Ricerca e Innovazione 2014-2020, risorse FSE REACT-EU
Azione IV.4 “Dottorati e contratti di ricerca su tematiche dell’innovazione”
e Azione IV.5 “Dottorati su tematiche Green”

UNIONE EUROPEA
Fondo Sociale Europeo
Ministero dell'Università e della Ricerca
PON RICERCA E INNOVAZIONE 2014 - 2020
REACT EU